

2001

A study of the heat transfer and fluid mechanics of the turbulent separating and reattaching flow past a backward facing step using large eddy simulation

Ravikanth V. R. Avancha
Iowa State University

Follow this and additional works at: <https://lib.dr.iastate.edu/rtd>

 Part of the [Mechanical Engineering Commons](#)

Recommended Citation

Avancha, Ravikanth V. R., "A study of the heat transfer and fluid mechanics of the turbulent separating and reattaching flow past a backward facing step using large eddy simulation " (2001). *Retrospective Theses and Dissertations*. 625.
<https://lib.dr.iastate.edu/rtd/625>

This Dissertation is brought to you for free and open access by the Iowa State University Capstones, Theses and Dissertations at Iowa State University Digital Repository. It has been accepted for inclusion in Retrospective Theses and Dissertations by an authorized administrator of Iowa State University Digital Repository. For more information, please contact digirep@iastate.edu.

INFORMATION TO USERS

This manuscript has been reproduced from the microfilm master. UMI films the text directly from the original or copy submitted. Thus, some thesis and dissertation copies are in typewriter face, while others may be from any type of computer printer.

The quality of this reproduction is dependent upon the quality of the copy submitted. Broken or indistinct print, colored or poor quality illustrations and photographs, print bleedthrough, substandard margins, and improper alignment can adversely affect reproduction.

In the unlikely event that the author did not send UMI a complete manuscript and there are missing pages, these will be noted. Also, if unauthorized copyright material had to be removed, a note will indicate the deletion.

Oversize materials (e.g., maps, drawings, charts) are reproduced by sectioning the original, beginning at the upper left-hand corner and continuing from left to right in equal sections with small overlaps.

Photographs included in the original manuscript have been reproduced xerographically in this copy. Higher quality 6" x 9" black and white photographic prints are available for any photographs or illustrations appearing in this copy for an additional charge. Contact UMI directly to order.

**ProQuest Information and Learning
300 North Zeeb Road, Ann Arbor, MI 48106-1346 USA
800-521-0600**

UMI[®]

**A study of the heat transfer and fluid mechanics of the turbulent
separating and reattaching flow past a backward facing step using
large eddy simulation**

by

Ravikanth V. R. Avancha

A dissertation submitted to the graduate faculty
in partial fulfillment of the requirements for the degree of

DOCTOR OF PHILOSOPHY

Major: Mechanical Engineering

Program of Study Committee:
Richard H. Pletcher, Major Professor
Gerald M. Colver
Ganesh R. Rajagopalan
Eugene S. Takle
John C. Tannehill

Iowa State University

Ames, Iowa

2001

Copyright © Ravikanth V. R. Avancha, 2001. All rights reserved.

UMI Number: 3034169

UMI[®]

UMI Microform 3034169

**Copyright 2002 by ProQuest Information and Learning Company.
All rights reserved. This microform edition is protected against
unauthorized copying under Title 17, United States Code.**

**ProQuest Information and Learning Company
300 North Zeeb Road
P.O. Box 1346
Ann Arbor, MI 48106-1346**

**Graduate College
Iowa State University**

**This is to certify that the doctoral dissertation of
Ravikanth V. R. Avancha
has met the dissertation requirements of Iowa State University**

Signature was redacted for privacy.

Committee Member

Signature was redacted for privacy.

Major Professor

Signature was redacted for privacy.

For the Major Program

TABLE OF CONTENTS

NOMENCLATURE	xiii
ABSTRACT	xx
CHAPTER 1 INTRODUCTION	1
1.1 Motivation	1
1.2 Survey of Literature	3
1.2.1 Review of large eddy simulations	3
1.2.2 Review of RANS simulations	7
1.2.3 Review of experimental studies	10
1.2.4 Summary	14
1.3 Survey of Relevant Previous Work by Members of the ME CFD Research Group at Iowa State University	15
1.4 Objectives	17
1.5 Dissertation Organization	17
CHAPTER 2 MATHEMATICAL FORMULATION	19
2.1 Conservation Principles and Governing Equations	19
2.1.1 Conservation of mass	20
2.1.2 Conservation of momentum	20
2.1.3 Conservation of energy	22
2.1.4 Closure	23
2.1.5 Generic conservation equation	26

2.2	Form of Governing Equations Used in this Study	27
2.2.1	Non-dimensionalization	28
2.3	Filtering Procedure	29
2.3.1	Types of filters	33
2.3.2	Favre filtering	34
2.4	Favre Filtered Compressible Governing Equations	34
2.5	Sub-grid Scale Models	37
2.5.1	Smagorinsky sub-grid scale model	37
2.5.2	Dynamic sub-grid scale models	39
CHAPTER 3 NUMERICAL FORMULATION		44
3.1	The Finite Volume Approach	44
3.2	The Cell Centered Algorithm	47
3.3	The Colocated Grid Approach	48
3.4	Cartesian Grid Limitation	51
3.5	Spatial Discretization	51
3.6	Evaluation of Inviscid Fluxes	53
3.6.1	Second and fourth-order central differences	53
3.7	Viscous Flux Calculation	55
3.8	Unsteady Terms and Preconditioning	56
3.9	Primitive Variables and Linearization	58
3.10	Coupled Strongly Implicit Procedure	61
3.11	Convergence Criteria	62
3.12	Boundary Conditions	63
3.13	Navier-Stokes Characteristic Boundary Conditions (NSCBC)	63
3.13.1	Steps to provide NSCBC conditions	66
3.14	Boundary Conditions for the Flow Past a Backward-Facing Step	72

3.14.1	Streamwise boundary conditions	73
3.14.2	Wall-normal boundary conditions	75
3.14.3	Spanwise boundary conditions	77
CHAPTER 4	LES OF ISOTHERMAL TURBULENT FLOW	78
4.1	Introduction	78
4.2	Problem Description	78
4.3	Large Eddy Simulation of Turbulent Flow in a Channel	80
4.3.1	Problem description, simulation details, and results	82
4.4	Simulation Details: Flow Past a Backward-Facing Step	84
4.5	Results and Discussion	87
4.5.1	Mean velocity distributions	87
4.5.2	Reattachment length	88
4.5.3	Spanwise averaged coefficients of friction and pressure	90
4.5.4	Velocity fluctuations and turbulent kinetic energy	91
4.5.5	Reynolds shear stresses	93
4.5.6	Triple velocity correlations	93
4.5.7	Effect of subgrid scale model	93
4.6	Significance of the Study	100
CHAPTER 5	LES OF TURBULENT FLOW WITH HEAT TRANSFER	
	AND PROPERTY VARIATIONS	103
5.1	Introduction	103
5.2	Problem Description and Simulation Details	103
5.3	Results and Discussion	105
5.3.1	Mean velocity and mean temperature distributions	105
5.3.2	Velocity and temperature fluctuations	123
5.3.3	Cross-correlations of the velocity and temperature fluctuations	128

5.3.4	Density fluctuations	130
5.4	Summary	131
CHAPTER 6	CONCLUSIONS AND RECOMMENDATIONS	134
6.1	Summary and Contributions	134
6.2	Recommendations for Future Work	137
APPENDIX A	JACOBIAN MATRICES FOR FAVRE FILTERED SYSTEM	
	OF EQUATIONS	139
APPENDIX B	AN ESTIMATE OF FLUID BULK TEMPERATURE	142
APPENDIX C	AN ESTIMATE OF BUOYANCY EFFECTS	144
APPENDIX D	COMPARISON OF TURBULENT TRANSPORT TERMS	
	BASED ON REYNOLDS- AND FAVRE-AVERAGED FLUCTUATIONS .	145
APPENDIX E	PARALLELIZATION AND OPTIMIZATION OF A LARGE	
	EDDY SIMULATION CODE USING OpenMP FOR SGI Origin2000 PER-	
	FORMANCE	153
BIBLIOGRAPHY		169
ACKNOWLEDGEMENTS		182

LIST OF FIGURES

Figure 3.1	Geometry of flow variables	48
Figure 3.2	Arrangement of unknowns for the colocated grid approach	49
Figure 3.3	Arrangement of unknowns for the staggered grid approach	49
Figure 3.4	Nomenclature for discretization	52
Figure 3.5	Waves entering and leaving the backward-facing step domain	67
Figure 4.1	Backward-facing step geometry	79
Figure 4.2	Law of the wall plot	84
Figure 4.3	Streamwise RMS velocity profile	85
Figure 4.4	Wall-normal RMS velocity profile	85
Figure 4.5	Spanwise RMS velocity profile	85
Figure 4.6	Streamline of mean velocity	88
Figure 4.7	Streamwise mean velocity profiles	89
Figure 4.8	Wall-normal mean velocity profiles	89
Figure 4.9	Spanwise mean velocity profiles	89
Figure 4.10	Temporal variation of the spanwise average reattachment locations	90
Figure 4.11	Coefficient of pressure	92
Figure 4.12	Coefficient of friction	92
Figure 4.13	Streamwise RMS velocity profiles	94
Figure 4.14	Wall-normal RMS velocity profiles	94
Figure 4.15	Spanwise RMS velocity profiles	94

Figure 4.16	Contour lines of turbulent kinetic energy	95
Figure 4.17	Reynolds shear stress: $-\langle u'v' \rangle_{tz}$	96
Figure 4.18	Reynolds shear stress: $-\langle u'w' \rangle_{tz}$	96
Figure 4.19	Reynolds shear stress: $-\langle v'w' \rangle_{tz}$	96
Figure 4.20	Skewness profiles: $\langle u'u'u' \rangle_{tz}$	97
Figure 4.21	Skewness profiles: $\langle u'u'v' \rangle_{tz}$	97
Figure 4.22	Skewness profiles: $\langle u'u'w' \rangle_{tz}$	97
Figure 4.23	Skewness profiles: $\langle u'v'v' \rangle_{tz}$	98
Figure 4.24	Skewness profiles: $\langle u'v'w' \rangle_{tz}$	98
Figure 4.25	Skewness profiles: $\langle u'w'w' \rangle_{tz}$	98
Figure 4.26	Skewness profiles: $\langle v'v'v' \rangle_{tz}$	99
Figure 4.27	Skewness profiles: $\langle v'v'w' \rangle_{tz}$	99
Figure 4.28	Skewness profiles: $\langle v'w'w' \rangle_{tz}$	99
Figure 4.29	Skewness profiles: $\langle w'w'w' \rangle_{tz}$	100
Figure 4.30	Plot of $e(x)$	101
Figure 4.31	Plot of $l(x)$	101
Figure 4.32	Streamwise profiles of the dynamic model coefficient	101
Figure 5.1	Backward-facing step geometry	104
Figure 5.2	Mean streamwise velocity	107
Figure 5.3	Mean wall-normal velocity	107
Figure 5.4	Mean spanwise velocity	107
Figure 5.5	Mean temperature	108
Figure 5.6	Mean temperature	108
Figure 5.7	Mean temperature	108
Figure 5.8	Bulk temperature	110
Figure 5.9	Wall temperature	110

Figure 5.10	Nusselt number	110
Figure 5.11	Mean streamwise velocity in wall coordinates	113
Figure 5.12	Mean streamwise velocity in wall coordinates	114
Figure 5.13	Mean temperature in wall coordinates	115
Figure 5.14	Mean temperature in wall coordinates	116
Figure 5.15	Mean streamwise velocity in semi-local coordinates	117
Figure 5.16	Mean streamwise velocity in semi-local coordinates	118
Figure 5.17	Mean temperature in semi-local coordinates	119
Figure 5.18	Mean temperature in semi-local coordinates	120
Figure 5.19	Mean Stanton number	122
Figure 5.20	Mean skin-friction	122
Figure 5.21	Mean Stanton number	124
Figure 5.22	Average of absolute skin-friction coefficient	124
Figure 5.23	Fluctuating skin-friction coefficient	124
Figure 5.24	Streamwise RMS velocity fluctuations	126
Figure 5.25	Wall-normal RMS velocity fluctuations	126
Figure 5.26	Spanwise RMS velocity fluctuations	126
Figure 5.27	RMS temperature fluctuations	127
Figure 5.28	RMS temperature fluctuations	127
Figure 5.29	RMS temperature fluctuations	127
Figure 5.30	Streamwise turbulent heat flux	129
Figure 5.31	Wall-normal turbulent heat flux	129
Figure 5.32	Spanwise turbulent heat flux	129
Figure 5.33	RMS density fluctuations	130
Figure 5.34	Variation in dynamic viscosity	132
Figure 5.35	Variation in thermal conductivity	132

Figure D.1	Streamwise turbulent heat flux	147
Figure D.2	Streamwise turbulent heat flux	147
Figure D.3	Wall-normal turbulent heat flux	148
Figure D.4	Wall-normal turbulent heat flux	148
Figure D.5	Spanwise turbulent heat flux	149
Figure D.6	Spanwise turbulent heat flux	149
Figure D.7	Streamwise turbulent heat flux	150
Figure D.8	Streamwise turbulent heat flux	150
Figure D.9	Wall-normal turbulent heat flux	151
Figure D.10	Wall-normal turbulent heat flux	151
Figure D.11	Spanwise turbulent heat flux	152
Figure D.12	Spanwise turbulent heat flux	152
Figure E.1	Law of the wall plot	158
Figure E.2	Streamwise rms statistics	158
Figure E.3	Scalability chart for $32 \times 32 \times 32$ grid showing wall-clock time for PFA, OpenMP (optimized) and OpenMP (pure vector code). Comparison of OMP and OMPV shows the need for cache optimization; for 8 processors the CPU time drops by a factor of 2 if optimized code is used.	163
Figure E.4	Channel geometry showing partitioned blocks tasked to processors .	164
Figure E.5	Scalability chart for 32^3 , 64^3 and 81^3 grids	166
Figure E.6	SGI MFLOPS across all processors for OpenMP LES code for 81^3 grid	166

LIST OF TABLES

Table 4.1	Grid spacing	83
Table 4.2	Grid resolution used by Akselvoll and Moin [1995]	86
Table B.1	Estimates of certain quantities for different heat flux values	143
Table C.1	Estimates of certain quantities to determine buoyancy effects	144
Table E.1	Code Performance on the CRAY T90	159
Table E.2	Single CPU performance on the Origin2000	161

DEDICATION

I would like to dedicate this thesis to my parents for having always encouraged me in my academic pursuits, and importantly for having imbued me with a set of values that will always be a part of who I am.

NOMENCLATURE

Roman Symbols

$[A]$	banded block septa-diagonal matrix in CSIP
$[A]$	x-direction flux vector Jacobian ($= \partial \mathbf{E} / \partial \mathbf{U}$)
$[A_{inv}]$	x-direction inviscid flux vector Jacobian ($= \partial \mathbf{E}_{inv} / \partial \mathbf{U}$)
$[A_{vis}]$	x-direction viscous flux vector Jacobian ($= \partial \mathbf{E}_{vis} / \partial \mathbf{U}$)
A^+	constant in Van Driest damping formula
A_c	channel cross-sectional area ($= L_y L_z$)
B	body force vector
$[B]$	y-direction flux vector Jacobian ($= \partial \mathbf{F} / \partial \mathbf{U}$)
$[B_{inv}]$	y-direction inviscid flux vector Jacobian ($= \partial \mathbf{F}_{inv} / \partial \mathbf{U}$)
$[B_{vis}]$	y-direction viscous flux vector Jacobian ($= \partial \mathbf{F}_{vis} / \partial \mathbf{U}$)
$[C]$	z-direction flux vector Jacobian ($= \partial \mathbf{G} / \partial \mathbf{U}$)
$[C_{inv}]$	x-direction inviscid flux vector Jacobian ($= \partial \mathbf{G}_{inv} / \partial \mathbf{U}$)
$[C_{vis}]$	x-direction viscous flux vector Jacobian ($= \partial \mathbf{G}_{vis} / \partial \mathbf{U}$)
C_d, C_i	dynamic subgrid-scale model coefficients
C_{ij}	Cross subgrid-scale stress tensor
C_f	friction coefficient ($= 2\tau_w / (\rho_{ref} U_{ref}^2)$)
C_s	Smagorinsky subgrid-scale model coefficient
c	speed of sound ($= \sqrt{\gamma RT}$)

C_p	constant pressure specific heat, coefficient of pressure
C_v	constant volume specific heat
D	Van Driest damping function
D_h	hydraulic diameter ($= 4\delta$)
E	least-squares error term
Ec	Eckert number ($= U_{ref}^2 / C_p^* T_{ref}$)
E_t	total energy ($= \rho e + \rho u_i u_i / 2$)
$\mathbf{E}, \mathbf{F}, \mathbf{G}$	flux vectors
e	specific internal energy ($= C_v T$)
f_i	body force vector
G	filter function
g	gravitational constant
\mathcal{H}_{ij}	resolved turbulent heat flux vector
h	step height, heat transfer coefficient, or specific enthalpy
$\vec{i}, \vec{j}, \vec{k}$	unit vectors for Cartesian coordinate system
K	bulk viscosity
k	wave number, thermal conductivity, or pseudo time index
L_{ij}	Leonard subgrid-scale stress tensor
$[\mathcal{L}]$	lower triangular block septa-diagonal matrix in CSIP
\mathcal{L}_{ij}	resolved turbulent stress tensor
\mathcal{L}_i	amplitude variation of characteristic wave associated with each characteristic velocity λ_i
L_{ref}	reference length
L_x, L_y, L_z	dimensions of channel, or of step in the respective coordinate directions
M	Mach number
\dot{m}	mass flow rate

Nu	Nusselt number ($= hL_y/k$)
n	physical time index
\bar{n}	unit normal vector
n_i	unit normal vector, $i = 1,2,3$
$[\mathcal{P}]$	auxiliary block septa-diagonal matrix in CSIP
P_i	force per unit area (a vector), $i=1,2,3$
Pr	Prandtl number ($= \mu c_p/k$)
Pr_T	turbulent Prandtl number
p	thermodynamic pressure
\bar{p}	mechanical pressure
Q_j	subgrid-scale turbulent heat flux vector
Q_j^L	Leonard component of subgrid-scale heat flux vector
Q_j^C	Cross component of subgrid-scale heat flux vector
Q_j^R	Reynolds component of subgrid-scale heat flux vector
Q_{ij}	sub-test scale heat flux vector
q_w	nondimensional wall heat flux ($= q_w^*/[k_{ref}/T_{ref}L_{ref}]$)
Q^+	alternate normalization for the wall heat flux, $q_w^*/(\rho_{ref}U_{ref}C_pT_{ref})$
q_i, q_j	heat flux vector
R	gas constant
R_{ij}	Reynolds subgrid-scale stress tensor
$[R], [\mathcal{R}]$	residual vector
Ra	Rayleigh number
Re	generic Reynolds number
Re_h	Reynolds number based on step height ($= \rho_{ref}U_{ref}h/\mu_{ref}$)
Re_τ	Reynolds number based on friction velocity ($= \rho_{ref}u_\tau h/\mu_{ref}$)
S_{ij}	strain rate tensor

St	Stanton number ($= Nu / [Re Pr]$, or $h / [\rho_{ref} U_{ref} C_p]$)
T	thermodynamic temperature
T_{bulk}	bulk temperature
$[T]$	time derivative Jacobian ($= \partial \mathbf{W} / \partial \mathbf{U}$)
T_τ	friction temperature ($= q_w / [\rho_w C_p u_\tau]$)
T_{wall}	wall temperature
\mathcal{T}_{ij}	sub-test scale stress tensor
t	physical time
$[U]$	vector of primitive variables $[p, u, v, w, T]^T$
$[\mathcal{U}]$	upper triangular block septa-diagonal matrix in CSIP
u_τ	friction velocity ($= \sqrt{\tau_w / \rho_w}$)
u_τ^*	semi-local friction velocity ($= \sqrt{\tau_w / \rho(y)}$)
u, v, w	Cartesian velocity components in x, y, z directions
u_i	velocity vector, $i=1,2,3$
u^+	velocity in wall coordinates ($= u / u_\tau$)
u^*	velocity in semi-local coordinates ($= u / u_\tau^*$)
\mathbf{W}	vector of conserved variables $[\rho, \rho u, \rho v, \rho w, \rho T]^T$
x, y, z	Cartesian coordinates
y^+	distance to wall in wall coordinates ($= \delta_y u_\tau / \nu_w$)
y^*	distance to wall in semi-local coordinates ($= \delta_y u_\tau^* / \nu(y)$)
x_r	mean reattachment length

Greek Symbols

α	ratio of filter widths ($= \widehat{\Delta} / \Delta$)
α_τ	eddy-diffusivity

β_{ij}	stress tensor
Γ	time derivative preconditioning matrix
γ	ratio of specific heats
Δ	grid filter width
$\hat{\Delta}$	test filter width
δ	channel half-height or Kronecker delta
δ_y	distance to closest wall
ϵ	dissipation rate per unit mass
κ	von Karman constant
λ	second coefficient of viscosity or eigenvalue
λ_i	characteristic velocity
μ	molecular dynamic viscosity
μ_τ	subgrid-scale turbulent viscosity
ν	molecular kinematic viscosity ($= \mu/\rho$)
ν_τ	subgrid-scale turbulent kinematic viscosity ($= \mu_t/\rho$)
ρ	thermodynamic density
σ_{ij}	shear stress tensor
τ	pseudo time
τ_{ij}	subgrid-scale stress tensor
ϕ	scalar quantity, such as temperature, species concentration or a generic variable

Subscripts

b	bulk property
c	cut-off frequency
con	conduction contribution

<i>inv</i>	inviscid contribution
<i>i, j, k</i>	indices for Cartesian coordinates
<i>m</i>	molecular
<i>ref</i>	reference quantity
<i>res</i>	resolved contribution
<i>rms</i>	root-mean-square
<i>s</i> or <i>sgs</i>	subgrid-scale contribution
<i>v</i> or <i>vis</i>	viscous contribution
<i>w</i>	wall value
<i>x, y, z</i>	associated with Cartesian direction
<i>tur</i>	turbulent contribution

Superscripts and Other Symbols

*	dimensional variable or semi-local coordinates
+	wall coordinates
'	fluctuation with respect to ensemble average, or unresolved or subgrid-scale component of filtered quantity
"	fluctuation with respect to Favre ensemble average, or unresolved or subgrid-scale component of Favre filtered quantity
~	vector quantity
—	resolved or large scale component of filtered quantity
~	resolved or large scale component of Favre filtered quantity
^	test filtered quantity
<>	ensemble averaged quantity
<> _{zt}	ensemble averaged in <i>z</i> direction and time

Abbreviations

CFD	computational fluid dynamics
CV	control volume
DNS	direct numerical simulation
FD	finite difference
FV	finite volume
LES	large eddy simulation
NS	Navier-Stokes
NSCBC	Navier-Stokes characteristic boundary conditions
RANS	Reynolds-averaged Navier-Stokes
RMS	root mean square
SGS	subgrid-scale

ABSTRACT

The heat transfer and fluid mechanics of a turbulent separating and reattaching flow past a single-sided backward-facing step are studied using large eddy simulation. Three-dimensional simulations of isothermal flows and flows with heat transfer causing significant property variations are performed. A fully coupled, time-derivative preconditioned, colocated-grid, central differenced, compressible, finite volume formulation was developed to conduct the simulations. A sixth-order compact filter was used to prevent pressure-velocity decoupling. A dynamic subgrid scale model was used to model the effects of the smaller eddies. Navier-Stokes characteristic boundary conditions designed by Poinsoot and Lele were used to provide boundary conditions.

The isothermal turbulent flow past the step, at a Reynolds number of 5,540 (based on the step height and upstream centerline velocity) and a Mach number of 0.006, was simulated to validate the formulation. Periodic boundary conditions in the spanwise direction for all variables were employed. All solid walls were maintained at the reference temperature of 293 K and no slip velocity boundary conditions were used. Inflow conditions were provided from an independent large eddy simulation of a turbulent plane channel flow. From the simulations, the mean reattachment point was located at $x/h=6.1$ as opposed to $x/h=6.51$ from the recent experiments of Kasagi and Matsunaga. Excellent agreement with the experiments in the mean quantities and turbulent statistics was obtained.

Subsequently, the bottom wall downstream of the step was supplied with uniform wall heat flux levels of 1.0, 2.0, and 3.0 kW/m², while all other walls were insulated. The viscous sub-layer played a critical role in controlling the heat transfer rate. Dramatic variation of

the wall temperatures in the recirculation region was observed. The simulations captured the presence of a second counter-rotating eddy that affected the Nusselt number profiles. Streamwise and wall-normal turbulent heat fluxes were of the same order of magnitude. The Reynolds analogy did not hold in the recirculation region. However, the Stanton number profiles showed a striking similarity with the fluctuating skin-friction profiles.

CHAPTER 1 INTRODUCTION

1.1 Motivation

Flows with separation and reattachment occur commonly in critical components of many engineering systems like gas turbine engines, heat exchangers, combustors, and electronic equipment. Such flows cause large variations of the local heat transfer coefficient as well as augment overall heat transfer. Conventional turbulence modeling methods, such as the Reynolds averaged Navier-Stokes (RANS) approach, have proved to be generally inadequate in predicting the effects of turbulent separating and reattaching flows with heat transfer.

Turbulent flows are inherently time dependent and three-dimensional in nature. They have a continuous spectrum of relevant length and time scales that need to be accurately captured. For any turbulent flow, the largest significant length scales are related to the domain size, and the small scales are related to the dissipative eddies where the viscous effects become predominant. Large eddy simulation (LES) is a method where the motion of the large eddies is computed explicitly, and the nonlinear interactions with the smaller eddies, which are assumed to be isotropic and universal, are modeled. In the realm of computational fluid dynamics, owing to the tremendous growth in computing power of processors, and decreasing costs of memory and storage, the simulation of complex turbulent flows using the LES method is a very active area of research, and has received a great deal of attention in the past decade.

The computation of complex flows, such as those occurring in certain critical components of gas turbine engines, is essential in extending the capability of the LES technique as a tool

to predict flows of engineering interest. Accurate turbulence models for transition flows, such as by-pass transition and transition in a separation bubble, in low pressure turbines operating at low Reynolds numbers have been elusive. Effects of transition often tend to result in deterioration of turbine performance. Direct and/or large eddy simulations, owing to little *ad hoc* modeling, can reveal aspects of fundamental physics of such flows and provide details that cannot be measured easily by experiments. Turbulence models used in RANS approaches can then be refined based on information obtained from direct or large-eddy simulations.

Specifically for this study, the research topic of interest is the flow transition in separation and reattachment with effects of heat transfer. The backward-facing step geometry is an excellent candidate for a study of the characteristics of flow separation and reattachment. Within the framework of a fairly simple geometry, the turbulent flow past a backward facing step, involving significant heat transfer, consists of distinctly different flow regimes that include flow separation, reversal and recovery, mixing, reattachment, and redeveloping velocity and thermal boundary layers, in the presence of a strong adverse pressure gradient. These various flow features constitute a complex flow one might encounter in a typical engineering application. Importantly, existing RANS approaches have not been successful in predicting all the flow features and heat transport mechanisms for this geometry. Since such methods rely to a great extent on the modeling aspects, large variations in the quality of simulations are observed depending on the model assumptions. As indicated earlier, little *ad hoc* modeling is employed in large eddy simulation, and the three-dimensional unsteady motion of the larger eddies is computed. Subgrid-scale modeling is used to account for the effects of the smaller eddies. Large eddy simulation, thus, offers a way to better understand and predict the heat transfer and fluid mechanics of the turbulent separating and reattaching flow past a backward facing step.

1.2 Survey of Literature

Specific attention is given to subsonic turbulent backward-facing step flows in this survey of literature. The survey is divided into three main parts. The first part specifically addresses large eddy simulations carried out for the backward facing step geometry. Section 1.2.2 provides a review of relevant RANS simulations and Section 1.2.3 reviews experiments conducted. Both of these sections are further subdivided for isothermal flow conditions and those involving heat transfer.

1.2.1 Review of large eddy simulations

To the best of the author's knowledge no prior large eddy simulations have been reported for the turbulent flow past a backward-facing step with heat transfer. To date all the large eddy simulations were carried out to study the isothermal turbulent flow for this geometry.

Akselvoll and Moin [1995] conducted the large eddy simulation of the flow past a backward-facing step with the objectives of assessing the performance of the dynamic sub-grid scale model, and the dynamic localization model [Ghosal et al., 1994] in a complex flow. They studied two cases: one at a Reynolds number (based on step height¹ and the freestream velocity) of 5,100, and another at a Reynolds number of 28,000.

For the low Reynolds number case, the domain included an inlet section of $0.3h$, a spanwise section of $4h$ and a downstream section of $20h$, with an expansion ratio of 1.2. The geometrical parameters and boundary conditions were chosen to match the DNS study by Le and Moin [1994] as well as the experimental study by Jovic and Driver [1995]. A separate LES calculation of a spatially developing boundary layer was performed to provide inflow boundary conditions at $0.3h$ upstream of the step corner. The thickness of the boundary layer at the step corner was about $1.2h$. The method of Le and Moin [1994] involved superimposing random velocity fluctuations on a mean velocity profile - and this method was

¹ h will be used in this chapter to refer to the step height

used to provide inflow boundary conditions for the large eddy simulation of the boundary layer. The mean velocity profile was obtained from a DNS of a spatially developing boundary layer by Spalart [1988].

The high Reynolds number case was designed to match the experiments of Adams et al. [1984]. Inflow conditions for this case was provided by the same method as employed by Le and Moin [1994]. The mean velocity profile was obtained by fitting a log-law through the experimental data of Adams et al. [1984].

Results from the low Reynolds number case were in good agreement with the DNS data for the first and second order statistics. They demonstrated that the effect of the subgrid scale model decreased with increasing grid resolution. They observed large discrepancies when they performed a calculation without the subgrid scale model. This was particularly apparent in the recirculation region where the subgrid scale shear stress and dissipation were the largest. Results from the high Reynolds number case were shown to be in good agreement with the experimental data except for the coefficient of skin friction. They attributed the discrepancies in the skin friction to either the inflow condition or inaccuracies associated with measurements in the recirculation region.

Friedrich and Arnal [1990], Arnal and Friedrich [1991, 1992] analyzed the turbulent flow past a single-sided backward-facing step using the subgrid scale models of Schumann [1977] and of Smagorinsky [1963]. A computational domain with an expansion ratio of 2 was used. Inflow conditions were provided from a fully developed turbulent channel large eddy simulation immediately upstream of the step. Uniform grids were used in all three coordinate directions. Approximate wall boundary conditions, similar to those employed by Schumann [1977], were used since the near-wall region could not be resolved sufficiently. The Reynolds number, based on inlet channel centerline velocity and step height, was 165,000. Results from the simulation were compared with experimental data from Durst and Schmitt [1985] at a Reynolds number of 113,000 and with the experimental data of Tropea [1982] at a Reynolds number of 11,000.

Disagreement with experiments in the reattachment length ($7.0h$ as compared to $8.6h$ [Tropea, 1982] and $8.5h$ [Durst and Schmitt, 1985]) and turbulent intensities was found. Only a marginal agreement in wall-normal velocity distribution was observed. Discrepancies between the experiments and LES were attributed to a combination of poor grid resolution, the use of artificial wall-boundary conditions, differences in flow condition upstream of the step, and problems with the subgrid scale model [Akselvoll and Moin, 1995].

This study was extended by Arnal and Friedrich [1991] in order to evaluate the effect of spatial resolution, with the Reynolds number and other parameters kept the same as in a previous study [Friedrich and Arnal, 1990]. Three different grid resolutions: $80 \times 16 \times 16$, $160 \times 32 \times 32$, $320 \times 48 \times 64$ were tested and reattachment lengths of $7.7h$, $7.3h$, and $7.2h$ respectively, were obtained. Importantly, the prescription of the inflow data from the channel LES was moved farther upstream by adding an inlet section of 4 step heights. This change might have improved the agreement with the reattachment length, but only marginally. They studied the effect of the aspect ratios of the control volumes and found that the use of cubical cells as opposed to rectangular cells greatly improved the reattachment length ($7.3h$ to $8.5h$). They also investigated the effect of changing the spanwise domain size from 2 to 8 step heights and monitoring the reattachment length to verify the quality of the solution. They found that with a spanwise width of 4–6 step heights, the reattachment length remained nearly the same. Le and Moin [1994], in their DNS study, found that a spanwise width of at least 4 step heights was essential to minimize the influence the periodic boundary condition.

Results from the LES by Akselvoll and Moin [1995] also showed the importance of resolving the flow around the corner of the step in the streamwise and wall-normal directions where large truncation errors with the singularity posed by the corner affected the quality of the results.

Morinishi and Kobayashi [1990] conducted large eddy simulations for turbulent flow past a backward-facing step with an expansion ratio of 1.5 and a Reynolds number of 46,000 (based on the step height and inlet velocity). Inflow conditions were provided from the LES

of a fully developed turbulent channel flow. Approximate wall-boundary conditions, designed to match the law of the wall, were used. While both uniform and non-uniform grids were used in the wall-normal direction, a uniform streamwise grid up to $15h$ was used, beyond which the grid was stretched. An inlet section of $2h$ was used and the streamwise extent of the domain was $30h$. A spanwise width of $2h$ was employed, which based upon the results of Arnal and Friedrich [1992] and Le and Moin [1994] was probably insufficient. A modified version of the Smagorinsky [1963] model was used, where the model constant C_s was determined as a function of two adjustable parameters [Yoshizawa, 1989].

With uniform wall-normal grid spacing and using $230 \times 30 \times 20$ grid points in the three coordinate directions, Morinishi and Kobayashi [1990] obtained a reattachment length of $9.2h$. Increasing the number of wall-normal grid points from 30 to 50, with a non-uniform distribution, altered the reattachment length to $7.2h$, which was in much better agreement with the experimental results of $7h \pm 1h$ of Kim et al. [1980]. The agreement in the mean velocity profiles and turbulent intensities with the experiments, however, was only marginal and the flow condition upstream was suggested by Morinishi and Kobayashi [1990] as a possible cause for the discrepancy. The reasons for the discrepancies were attributed to a combination of poor grid distribution/resolution, the use of approximate wall-boundary conditions, the use of the Smagorinsky model, and importantly, the short spanwise width. The width of the spanwise domain, is quite critical in that it should allow for spanwise vortex stretching, an important turbulence maintenance/sustenance mechanism. It is equally important to note that the assumption of the existence of the law of the wall in the recirculating region or even in the recovery region (which is implicit in the use of wall-functions) would be inappropriate.

Neto et al. [1993] used DNS and LES techniques to conduct a statistical and topological study of the flow past a backward-facing step. The structure-function model proposed by Métais and Lesieur [1992] was the subgrid scale model in their LES study. A uniform velocity profile with superimposed random “white noise” served as the inflow condition. Two cases were considered; one with an expansion ratio of 1.67 and a Reynolds number of 38,000, and

the other with an expansion ratio of 5 and Reynolds number of 6,000.

The mean velocity profile for the high Reynolds number case was obtained from an experimental study by Eaton and Johnston [1980] and for the low Reynolds number case a uniform mean velocity profile was assumed. Approximate wall-boundary conditions were prescribed at the walls. A grid of $130 \times 25 \times 40$ points in the three coordinate directions were used for the low Reynolds number case for both DNS and LES; for the high Reynolds number case LES, two grids ($90 \times 16 \times 16$ and $200 \times 30 \times 30$) were used and only the coarse grid was used for the DNS. Their numerical algorithm employed a third-order upwind biased discretization scheme for the convective terms, which has been shown to introduce numerical diffusion [Mittal and Moin, 1997]. Rather poor agreement with experimental data in Reynolds stresses, turbulent kinetic energy and mean velocity profiles was observed [Akselvoll and Moin, 1995].

Le and Moin [1994] showed that inflow conditions, imposed at the step corner, based on random numbers resulted in large errors in the solution. In addition, they showed that the law of the wall does not hold in the recovery region. Akselvoll and Moin [1995] demonstrated that the flow downstream was very sensitive to the upstream flow conditions. The aforementioned issues most likely were the reasons for the disagreement between the simulations and experiments in the case of Neto et al. [1993].

1.2.2 Review of RANS simulations

1.2.2.1 RANS simulations with heat transfer

The flow over a backward-facing step with heat transfer has been widely studied as a benchmark problem in heat transfer. The limitations of using the $k-\epsilon$ model in predicting the characteristics of separated flow with reattachment have been noted. Abrous and Emery [1996] reviewed all the submissions for this benchmark problem, and participants were asked to use any $k-\epsilon$ model they desired. Submissions were made by Hong et al. [1996], Chopin

[1996], Osied et al. [1996], Yim and Armaly [1996], Horstman et al. [1996], Griaznov and Sengupta [1996]. Abrous and Emery [1996] reported in their review that the results for the streamwise velocity and dissipation, amongst the contributors, agreed well. A wide scatter in the data for the dimensionless dissipation rate of turbulence was observed. Turbulent kinetic energy and wall-normal velocity profiles showed substantial differences. The Nusselt number predictions showed the greatest differences, and there did not appear to be any consistency in the computed points of maximum Nusselt number and the reattachment point. The reason for this was attributed to the marked differences in the computed wall temperatures. Upon comparison with the experimental results of Mori et al. [1986], it turned out that none of the methods were successful in producing a shape similar to the experiments. While the RNG turbulence model predicted the peak Nusselt numbers better, a substantial overprediction of the Nusselt number adjacent to the step and far downstream was observed. The standard $k-\epsilon$ model underpredicted the peak values. They concluded that the computations by Horstman et al. [1996] gave the best agreement with the peak Nusselt number but that the profile of Nusselt number distribution was also clearly unusual.

Abe et al. [1994] conducted RANS simulations for the separating and reattaching flow past a backward-facing step by modifying an existing low-Reynolds-number $k-\epsilon$ model. They state in their work that among existing low-Reynolds-number $k-\epsilon$ models, the model developed by Nagano et al. [1989] (referred to as the NT model) is regarded as the most reliable. However, since the NT model uses the friction velocity u_τ , it breaks down around the separating and reattaching points where $u_\tau = 0$. Therefore, they proposed a modification of the NT model where the principal improvement was the usage of the Kolmogorov velocity scale $u_\epsilon = (\nu\epsilon)^{1/4}$ instead of the friction velocity, u_τ , to account for the near-wall and low-Reynolds-number effects. This velocity scale does not become zero at the separating nor at the reattaching points in contrast to the friction velocity. They also reevaluated the model constants so that both attached and separated wall shear flows could be predicted accurately. They conducted flow- and thermal-field calculations with their $k-\epsilon$ model [Abe et al., 1994,

1995]. The calculated reattachment lengths and Stanton numbers were in agreement with the experimental data of Vogel and Eaton [1984].

Ciofalo and Collins [1989] note in their study that the use of conventional wall functions with a constant nondimensional thickness of the viscous sub-layer tends to under predict heat transfer rates near and downstream of the reattachment point of separated shear layers for Reynolds numbers, based on upstream velocity and step height, up to 10^5 . In addition, the sensitivity of the peak Nusselt number to the Reynolds number was over predicted.

Collins [1983] states that the use of a low-Reynolds-number $k-\epsilon$ model presented serious problems when applied to separated flows. It was reported to over predict heat transfer rates [Chieng and Launder, 1980] and under predict them in [Gooray et al., 1981]. With the standard form of the energy dissipation term in such models, severe underpredictions of heat transfer rates at low to middle Reynolds numbers, over predictions at high Reynolds numbers, and a general disagreement of the Nusselt number profiles along the walls were reported [Ciofalo and Collins, 1989].

Ciofalo and Collins [1989], therefore, proposed an approach that retained the classic wall functions and scaling based on the near-wall turbulent kinetic energy, but allowed the non-dimensional thickness of the viscous sub-layer to vary as a function of the local turbulence intensity. They reported better agreement with experimental heat transfer data for single backsteps and double symmetric expansions with their approach. A need for improvement in the heat transfer predictions upstream of reattachment was also suggested, since most wall function approaches fail to resolve the counter-rotating corner eddy.

1.2.2.2 RANS simulations for isothermal step flows

Kobayashi and Tagashi [1996] used the LES database of Morinishi and Kobayashi [1990] to investigate the behavior of turbulence models for the Reynolds stress and turbulent kinetic energy equations. They found that the algebraic stress model of Rodi [1976] described this

flow more accurately than the standard $k-\epsilon$ model and that the gradient diffusion model for the turbulent diffusion term could not accurately predict the turbulent energy distribution in the recirculating region. They applied a new diffusion model [Yoshizawa, 1982] and predicted the turbulent energy in the recirculating region better than with the diffusion model.

The ability of two-equation turbulence models to accurately predict separated flows was analyzed from a combined theoretical and computational standpoint by Thangam and Speziale [1992]. They concluded that the underpredictions of the reattachment points by 15-20% reported from different studies were in error due to inadequate resolution of the flow-field. They reported only a 12% underprediction with the experimental data of Kim et al. [1980], with use of the standard $k-\epsilon$ model with three-layer wall functions. By modifying the standard $k-\epsilon$ model to include an anisotropic eddy viscosity, they obtained a better prediction of the reattachment point owing to better prediction of the normal Reynolds stress differences. They also suggested a correction to the $C_{\epsilon 1}$ constant for the RNG $k-\epsilon$ model [Yakhot and Orszag, 1986] to better predict the reattachment point. In concluding remarks of the report, they indicated that the deficiencies of the two-equation models were well established, particularly in turbulent flows with body forces or Reynolds stress relaxation effects, and that consequently the findings from their study should not be interpreted as an unequivocal endorsement of two-equation models. From their critical evaluation they indicated that properly calibrated two-equation turbulence models, with an anisotropic eddy-viscosity, could yield results for the backward-facing step problem that would be superior to the results from older zero- or one-equation turbulence models.

1.2.3 Review of experimental studies

1.2.3.1 Experimental studies with heat transfer

The study by Vogel and Eaton [1984] was a comprehensive and combined study of the fluid dynamics and heat transfer in the turbulent separating and reattaching flow past a

backward facing step. A constant heat flux was supplied downstream of the step, and Stanton number profiles as a function of the Reynolds numbers and boundary layer thickness at separation were presented. They reported that the heat transfer rate strongly correlated with the fluctuating or instantaneous skin friction. The mean temperature profiles showed the existence of temperature gradients only close to the wall, within a y^+ of 50. They also demonstrated the importance of the near-wall region in controlling the heat transfer rate, and concluded that it was dominated by conduction. Through their measurements they showed the relative importance of different scalar transport mechanisms.

Mori et al. [1986] investigated the instantaneous behavior of the heat transfer coefficient and its relation to the corresponding time averaged value. The downstream bottom wall was supplied with a constant heat flux although the values of heat flux are not indicated in their study. The Reynolds number (based on the step height and freestream velocity) in their study was 20,000. The condition of the boundary layer at the inlet was laminar.

Armaly et al. [1981] and Kottke [1984] employed a photochemical reaction to simulating heat transfer by mass transfer. The final result from Kottke [1984] was an empirically derived general formula for the maximum mean transport of mass or heat away from the lower surface. Vogel and Eaton [1984] indicated that the turbulent transport within the flow was not clarified, nor would the reader be left with a theoretical basis upon which to build numerical models.

Aung and Goldstein [1972a,b] acquired data in an air flow behind a backward-facing step using a Mach-Zehnder interferometer. Local heat transfer coefficients in the separated region were found to be less than for attached boundary layers. The upstream surface was heated to the same level as the downstream surface, unlike other studies. The range of free-stream velocities was smaller, corresponding to a range of Reynolds numbers, based on the step height, from 700 - 1920. The thickness of the boundary layer at separation was one step height.

Seban [1964] measured velocity and temperature distributions downstream of a backward-facing step supplied with a constant wall heat flux. The mean reattachment point was found to be nearly $6h$ downstream of the step for an estimated Reynolds number of 76,000. Seban found large temperature gradients in the near-wall region downstream of the step and at about $1.2h$; 80% of the temperature drop from the wall to the freestream levels took place within $0.2h$. In an earlier effort Seban et al. [1959], determined the Nusselt number to depend on $Re^{0.8}$. In a later study Seban [1966] made the important point that the maximum heat transfer rate coincides with the point of low or zero skin friction, attributing this fact to high diffusivity along with a low thermal resistance typical of a newly developing layer.

A detailed review of heat transfer in separated and reattached flows, up to 1974, for all regimes of flow has been made by Fletcher et al. [1974]. Aung and Watkins [1978] specifically reviewed literature on subsonic, separated, thermal transport mechanisms, and did not find consistent trends in available data.

1.2.3.2 Experimental studies of isothermal step flows

Only two of the most relevant experimental studies will be addressed in this section. The most recent experiments conducted to investigate the turbulent fluid dynamics for the flow past a backward facing step were conducted by Kasagi and Matsunaga [1995]. Using a 3-D particle tracking velocimeter, detailed turbulence measurements were made in the separated and reattaching flow past a backward-facing step at a Reynolds number (based on the step height and centerline velocity) of 5540. A fully developed turbulent channel flow was established upstream of separation so that no predictive calculation would suffer from incompleteness or ambiguity in the upstream boundary conditions. A database of turbulence statistics was established over a fairly wide region of $-2h$ upstream to $12h$ downstream of the step. The mean reattachment point was $6.51h$ downstream of the step. From the calculated mean streamlines, they identified a secondary recirculation bubble behind the step, where

the flow was almost stagnant. The Reynolds normal and shear stresses had maximum values in the separating free shear layer upstream of reattachment. The mean and fluctuating velocities, Reynolds shear stress, and the turbulent energy budget were in good agreement with the DNS results of Le and Moin [1994] and this was somewhat surprising since there was considerable difference in the inflow conditions.

A study carried out by Eaton and Johnston [1980] is often used as a reference case to compare results with numerical simulations. The study was conducted in a single-sided, two-dimensional, sudden expansion duct flow with an expansion ratio of 1.67. The boundary layer thickness at separation was approximately $0.2h$. Profiles of mean velocity and longitudinal turbulence intensity were obtained for stations between $x/h=1$ and $x/h=12$. Three sets of data were obtained with laminar, transitional and turbulent boundary layers at separation. Eaton and Johnston [1980] found that the growth rate of the separated shear layer was more rapid with the laminar boundary layer case than the other two. The turbulence intensity was observed to decay rapidly in the reattachment zone, and the decay began one to two step heights upstream of reattachment. The structure of the large eddies in the reattaching shear layer were studied with both laminar and turbulent boundary layers at separation. They found large spanwise vortices that grew by pairing in the shear layer originating from a laminar boundary layer, while these vortices were not observed in the turbulent boundary layer case upstream of $x/h=6$. They attributed the shorter reattachment length in the laminar boundary layer case to the spanwise vortex structure and the rapid entrainment associated with pairing. They also reported a “flapping” motion of the shear layer in the wall-normal direction and its role in causing the impingement point to move back and forth over a distance of ± 1 step height. They believed this motion to be responsible for the low frequency unsteadiness in the reattachment region.

1.2.4 Summary

In summary, the following comments may be made:

1. The isothermal turbulent flow past the backward facing step has been studied quite extensively, by way of direct and large eddy simulations, RANS simulations and experiments. Recent DNS [Le and Moin, 1994] and LES studies by Akselvoll and Moin [1995] have shown good agreement with experimental results of Jovic and Driver [1995]. All of these studies, however, have a boundary layer of specific thickness at the point of separation, leaving open the issue of effect of the upstream condition on the mean reattachment length and the recirculation region. The state of the inflow condition has often been cited by the researchers, even for LES calculations, as a potential source of disagreement with experimental data. In order to remove any ambiguity concerning the upstream boundary conditions Kasagi and Matsunaga [1995] performed an experimental study with a fully developed channel flow as the inflow condition.
2. RANS calculations for the isothermal turbulent flow past a backward facing step with standard $k-\epsilon$ models do not predict the reattachment length well. Properly calibrated two-equation models, with anisotropic eddy viscosity, yield better predictions of the reattachment length [Thangam and Speziale, 1992]. The ASM model of Rodi [1976], and diffusion model of Yoshizawa [1986] have also yielded better predictions of the reattachment length. Details of turbulence intensities and Reynolds shear and normal stresses, however, are difficult to find in many RANS studies. RANS approaches remain very sensitive to the type of models used and the related modeling assumptions and model constants that need to be specified *a priori*, in addition to other *ad hoc* factors such as wall-damping functions; these can be serious limiting factors in predicting complex flows where information needed for modeling may not be available easily.

3. RANS simulations for the turbulent flow past a backward facing step with heat transfer have proven inadequate in predicting the effects of heat transfer largely because of modeling assumptions. Mean quantities, turbulence intensities, wall temperatures and Nusselt/Stanton numbers are all very strongly tied in with the ability to predict the near-wall behavior accurately. Few studies have considered property variations or density variations, both of which occur routinely when high levels of heat fluxes are involved.
4. Experimental studies for the isothermal flows and flows with heat transfer have provided valuable insight and information for use by numerical modelers for the turbulent flow past a backward facing step. However, intrusion of the flow by measuring devices due to their sizes, or simply the inability to measure all quantities of interest are possible limitations of experimental procedures. It must be noted that significant advances are being made in instrumentation methods, and with the fabrication of nano- and micro-scale devices, experimental methods might be able to expand their reach.

1.3 Survey of Relevant Previous Work by Members of the ME CFD Research Group at Iowa State University

Prior to this study, Wang [1995] developed a finite volume coupled formulation for the simulation of incompressible and compressible turbulent flows with and without heat transfer. This formulation was developed using colocated and staggered grids, and employed central differences and upwind schemes. No conclusive evidence that recommended an “ideal” scheme for the large eddy simulation of complex flows was found. In the colocated-grid framework, the central difference schemes were unstable for the turbulent incompressible planar channel flow. For more complex flows, the upwind colocated-grid scheme was not able to sustain the computation long enough [Wang, 1995]. The staggered grid algorithms performed satisfactorily for the incompressible channel flow case. However, for complex flows,

the staggered grid central difference schemes were found to be unstable. The combination of upwinding in the staggered grid framework seemed to yield the most robust algorithm.

Central difference schemes are preferred over upwind schemes for direct and large eddy simulations for the reasons indicated in Mittal and Moin [1997]. Colocated grid schemes have advantages over staggered grid schemes (see Section 3.3) but suffer from the problems associated with pressure-velocity decoupling. Dailey [1997] conducted large eddy simulations of compressible turbulent channel flows with variable property heat transfer in a colocated-grid framework with central difference schemes. Excellent agreement with DNS and experiments for simple turbulent flows (such as homogeneous, isotropic, decaying turbulence and smooth wall channel flows) was reported. However, for the LES of a ribbed channel flow, artificial diffusion terms had to be used to provide the necessary coupling. An excessive damping of turbulent fluctuations upon use of artificial diffusion was reported.

The failure of the the colocated grid schemes in the study by Wang [1995], and the instability of the central difference scheme in the colocated-grid framework were, therefore, some of the key issues that needed to be addressed urgently [Narayanan, 1998].

Narayanan [1998] successfully addressed the issue relating to the instability of the central difference schemes and traced the cause to the method used to compute the cell-face convective fluxes. Avancha and Pletcher [2000] successfully conducted turbulent channel flow simulations using the second- and fourth-order central difference schemes in a colocated-grid framework. Towards the development of a robust colocated-grid scheme, Narayanan [1998] adapted the momentum-interpolation (MI) correction proposed by Rhie and Chow [1983] to the fully-coupled, dual time-stepping approach. Subsequently, Narayanan [1998] conducted simulations of two-dimensional laminar flows and the large eddy simulation of isotropic decaying turbulence. However, the MI approach imposed a severe time step penalty that discouraged its use in complex flow simulation as the one in this study.

1.4 Objectives

The main objectives of this study were

1. Develop a robust colocated grid, central difference, finite volume scheme using a fully-coupled compressible formulation for the large eddy simulation of complex turbulent flows with heat transfer and property variations. The code developed by Wang [1995] was used as the starting point for this work.
2. Develop, or if available, implement, methods to provide inflow, outflow conditions suitable for direct and large eddy simulations of complex turbulent flows using finite volume fully-coupled compressible formulations.
3. Investigate the heat transfer and fluid dynamics of the turbulent flow past the backward facing step with heat flux levels resulting in significant property variations by way of large eddy simulations.
4. Create a database relevant for future fluid dynamics and heat transfer studies in this geometry to guide RANS modeling approaches.
5. Attempt to create an efficient parallel large eddy simulation code for distributed memory architecture (such as the SGI Origin2000) from existing vector code designed for use on the CRAY machines (C90, J90, T90, SV1).

1.5 Dissertation Organization

The governing equations of fluid flow and heat transfer, the filtering procedure applied to the governing equations and the filtered form of the governing equations used for large eddy simulations are described in Chapter 2. Subgrid scale modeling is also addressed in this chapter.

In Chapter 3, the finite volume method, the cell-centered algorithm and colocated-grid methodology are discussed. The spatial discretization of the governing equations with a discussion of the viscous and inviscid flux calculation procedures for second- and fourth-order central differences are presented. Time-derivative preconditioning, essential for the computation of low Mach number flows using a compressible formulation is then addressed. The coupled strongly implicit procedure used for the solution of the discretized system of equations, and the convergence criteria are presented. The treatment of boundary conditions using the Navier-Stokes characteristic boundary condition (NSCBC) strategy is discussed in detail and all the boundary conditions used for the turbulent flow simulations are presented.

Details of the large eddy simulation of the isothermal turbulent flow past a backward facing step are presented in Chapter 4. Large eddy simulation of a turbulent channel flow was conducted to provide inflow conditions for the step flow, and the details of this channel flow simulation are presented. A discussion of the results from the simulation of the step flow and the significance of this study are finally presented.

Chapter 5 deals with the large eddy simulation of the turbulent flow past a backward facing step with heat transfer and property variations. Details of the simulation, and an extensive discussion of the results are presented in this chapter.

Conclusions and recommendations for future work are made in Chapter 6.

CHAPTER 2 MATHEMATICAL FORMULATION

In this chapter, conservation principles are applied to a fixed finite volume of fluid, and the fundamental governing equations of fluid dynamics are deduced. The form of the governing equations used in this study are then presented. In order to facilitate large eddy simulation (LES) these equations are subsequently filtered and the Favre filtered set of governing equations is introduced. Subgrid scale (SGS) modeling, motivated by a need to close these equations, is then discussed. The integral conservation form of these equations, which is a starting point for most classes of finite volume methods, is finally presented.

2.1 Conservation Principles and Governing Equations

The basic governing equations of fluid dynamics are obtained by invoking the physical laws of conservation of mass, momentum, and energy. These physical principles are applied to a model of the flow. A fixed finite control volume is an especially appealing model as it produces the governing equations in integral conservation form. The partial differential equation form of these equations can be obtained, if needed, by taking the limit as the volume is shrunk to a point. In the presentation of these equations, the Cartesian tensor notation (also known in literature as Einstein summation convention) will be used. The material presented in this section has relied upon the book by Currie [1974].

2.1.1 Conservation of mass

The principle of mass conservation applied to a finite control volume results in the continuity equation, in integral conservation form,

$$\frac{\partial}{\partial t} \int_V \rho dV + \int_S \rho u_j n_j dS = 0 \quad (2.1)$$

Applying the Gauss divergence theorem to convert the surface integral to a volume integral, and taking the time derivative inside the integral since the limits of the integration are constant, results in

$$\int_V \left[\frac{\partial \rho}{\partial t} + \frac{\partial(\rho u_j)}{\partial x_j} \right] dV = 0 \quad (2.2)$$

Since the finite control volume is arbitrary, the only way the above integral can equal zero is for the integrand to be zero at every point within the control volume. Thus, the continuity equation in partial differential equation form is

$$\frac{\partial \rho}{\partial t} + \frac{\partial(\rho u_j)}{\partial x_j} = 0 \quad (2.3)$$

Besides expressing the fact that mass is conserved, an important implication of this equation is that the velocity is continuous. Hence, the equation is termed 'continuity' equation. For cases of fluid flow where density variations are negligible, the above equation reduces to

$$\frac{\partial u_j}{\partial x_j} = 0 \quad (2.4)$$

The fluid is then said to be *incompressible*. Thus, not only is its mass constant, but also its volume and hence, density.

2.1.2 Conservation of momentum

The principle of conservation of momentum is an application of Newton's second law of motion to an element of the fluid. Newton's law when applied to an elemental volume of fluid states that the inertia force (force due to acceleration of the element, or rate of change

of momentum) is equal to the net external force acting on the fluid. The external forces experienced by a fluid element are classified into body forces and surface forces. Examples of body forces are gravitational, electric and magnetic forces. Surface forces result from pressure and viscous stresses. Viscous stresses can be further classified into normal stresses and shear stresses.

$$\frac{\partial}{\partial t} \int_V u_i \rho dV + \int_S \rho u_i u_j n_j dS = \int_S P_i dS + \int_V \rho f_i dV \quad (2.5)$$

where P_i is the surface force per unit area and f_i is the body force per unit mass. In order to proceed further, more information about the surface force P_i is needed.

There are nine components of stress at any given point, and any particular component of the stress may be represented by the quantity β_{ij} , where the first subscript indicates that this stress component acts on the plane $x_i = \text{constant}$, and the second subscript indicates that it acts in the x_j direction. For any arbitrarily oriented surface whose unit normal has components n_i , the surface vector P_i can be related to the stress tensor β_{ij} , such that

$$P_i = \beta_{ji} n_j \quad (2.6)$$

The momentum equation, now is

$$\frac{\partial}{\partial t} \int_V \rho u_i dV + \int_S \rho u_i u_j n_j dS = \int_S \beta_{ji} n_j dS + \int_V \rho f_i dV \quad (2.7)$$

Applying the Gauss divergence theorem, and collecting terms yields

$$\int_V \left[\frac{\partial \rho u_i}{\partial t} + \frac{\partial (\rho u_i u_j)}{\partial x_j} - \frac{\partial (\beta_{ji})}{\partial x_j} - \rho f_i \right] dV \quad (2.8)$$

The arbitrariness of the choice of the control volume implies that the integrand must equal zero at every point. Thus,

$$\frac{\partial \rho u_i}{\partial t} + \frac{\partial (\rho u_i u_j)}{\partial x_j} = \frac{\partial \beta_{ji}}{\partial x_j} + \rho f_i \quad (2.9)$$

2.1.3 Conservation of energy

The principle of conservation of energy is an application of the first law of thermodynamics to a fluid element as it flows. The first law of thermodynamics, as applied to a fluid element, states that the rate of change of the total energy is equal to the sum of the rate at which work is done on the fluid by external forces and the rate at which heat transfer takes place, and can be expressed as

$$\int_V \left\{ \frac{\partial E_t}{\partial t} + \frac{\partial(E_t u_j)}{\partial x_i} \right\} dV = \int_S P_i u_i dS + \int_V \rho f_i u_i dV - \int_S q_i n_i dS \quad (2.10)$$

where E_t is the total energy and $E_t = \rho e + \frac{1}{2}\rho u_i u_i$. Applying the Gauss divergence theorem to convert surface integrals to volume integrals, and relating the force vector P_i to the stress tensor β_{ji} from Eq. (2.6), results in

$$\int_V \left\{ \frac{\partial}{\partial t}(\rho e + \frac{1}{2}\rho u_i u_i) + \frac{\partial}{\partial x_i} \left[(\rho e + \frac{1}{2}\rho u_i u_i) u_j \right] \right\} dV = \int_V \left[\frac{\partial(\beta_{ji} u_i)}{\partial x_i} + \rho f_i u_i - \frac{\partial q_i}{\partial x_i} \right] dV \quad (2.11)$$

Considering Eq. (2.11) to be of the form $\int_V \{ \quad \} = 0$, we note that the quantity inside the integrand must equal zero since the choice of the control volume is arbitrary. Thus the partial differential equation form of the energy equation is

$$\frac{\partial}{\partial t}(\rho e + \frac{1}{2}\rho u_i u_i) + \frac{\partial}{\partial x_i} \left[(\rho e + \frac{1}{2}\rho u_i u_i) u_j \right] = \frac{\partial(\beta_{ji} u_i)}{\partial x_i} + \rho f_i u_i - \frac{\partial q_i}{\partial x_i} \quad (2.12)$$

Eq. (2.12) can be simplified as follows:

1. The left hand side of Eq. (2.12) can be rewritten as

$$\frac{\partial}{\partial t}(\rho e) + \frac{\partial}{\partial t} \left[\frac{1}{2}(\rho u_i u_i) \right] + \frac{\partial}{\partial x_i}(\rho e u_j) + \frac{\partial}{\partial x_i} \left[\left(\frac{1}{2}\rho u_i u_i \right) u_j \right] \quad (2.13)$$

2. The second and fourth terms in Eq. (2.13) may be split into

$$\rho \frac{\partial}{\partial t} \left[\frac{1}{2}(u_i u_i) \right] + \left[\frac{1}{2}(u_i u_i) \right] \frac{\partial \rho}{\partial t} + \left[\frac{1}{2}(u_i u_i) \right] \frac{\partial \rho u_j}{\partial x_j} + \rho u_j \frac{\partial}{\partial x_j} \left[\left(\frac{1}{2}u_i u_i \right) \right] \quad (2.14)$$

3. In Eq. (2.14) replacing $\frac{\partial \rho u_j}{\partial x_j}$ by $\frac{\partial \rho}{\partial t}$, in view of the continuity equation, enables the elimination of the second and third terms.

4. The remaining terms of Eq. (2.14) can be rewritten as

$$\rho \frac{\partial}{\partial t} \left[\frac{1}{2} (u_i u_i) \right] = \rho u_i \frac{\partial u_i}{\partial t} \quad (2.15)$$

$$\rho u_j \frac{\partial}{\partial x_j} \left[\frac{1}{2} (u_i u_i) \right] = \rho u_j u_i \frac{\partial u_i}{\partial x_j} \quad (2.16)$$

5. Thus, the left hand side now takes the form

$$\frac{\partial(\rho e)}{\partial t} + \frac{\partial(\rho e u_j)}{\partial x_j} + \rho u_i \frac{\partial u_i}{\partial t} + \rho u_j u_i \frac{\partial u_i}{\partial x_j} \quad (2.17)$$

6. The first term on the right hand side of Eq. (2.12) can be written as

$$\frac{\partial(\beta_{ji} u_i)}{\partial x_i} = u_i \frac{\partial(\beta_{ji})}{\partial x_i} + \beta_{ji} \frac{\partial u_i}{\partial x_i} \quad (2.18)$$

7. The conservation of energy equation is now given by

$$\frac{\partial(\rho e)}{\partial t} + \frac{\partial(\rho e u_j)}{\partial x_j} + \rho u_i \frac{\partial u_i}{\partial t} + \rho u_j u_i \frac{\partial u_i}{\partial x_j} = u_i \frac{\partial(\beta_{ji})}{\partial x_i} + \beta_{ji} \frac{\partial u_i}{\partial x_i} + \rho f_i u_i - \frac{\partial q_i}{\partial x_i} \quad (2.19)$$

8. It can be seen that the third and fourth terms on the left hand side can be canceled by the first and third terms on the right side, as they collectively amount to the product of u_i with the momentum equation (Eq. 2.9).

9. Finally, the equation that expresses the conservation of thermal energy becomes

$$\frac{\partial(\rho e)}{\partial t} + \frac{\partial(\rho e u_j)}{\partial x_j} = \beta_{ji} \frac{\partial u_i}{\partial x_i} - \frac{\partial q_i}{\partial x_i} \quad (2.20)$$

2.1.4 Closure

Equations 2.3, 2.9, 2.20 represent five scalar equations which the fluid properties must satisfy as the fluid flows. The continuity and energy equations are scalar equations, and the

momentum equation is a vector equation representing three scalar equations. Two equations of state, the thermal and caloric equations of state may be added to bring the total number of equations to seven. However, the conservation laws have introduced seventeen unknowns. The unknowns are

1. two scalars: density ρ , and internal energy e
2. two vectors: velocity u_j , and heat flux q_j , each having three components
3. one tensor: stress tensor β_{ij} , that has nine independent components.

In order to close this system of equations, we need to further specify the stress tensor β_{ij} , and the heat flux vector q_j . *Constitutive equations* are used to relate the stress tensor to the rate of strain tensor (also known as deformation tensor), and the heat flux vector to the gradients of temperature.

The constitutive relation for stress in a Newtonian fluid is

$$\beta_{ij} = -p\delta_{ij} + \sigma_{ij} \quad (2.21)$$

where p is the thermodynamic pressure, δ_{ij} is the Kronecker delta, and σ_{ij} is called the shear stress tensor and depends only on the motion of the fluid. The sign convention used is that the normal stresses are positive when they are tensile in nature; hence the negative sign in front of the pressure term. The shear stress tensor is linearly related to the rate of strain tensor in the case of Newtonian fluids. The constitutive relation for the shear stress is given by

$$\sigma_{ij} = \lambda\delta_{ij}\frac{\partial u_k}{\partial x_k} + \mu\left(\frac{\partial u_i}{\partial x_j} + \frac{\partial u_j}{\partial x_i}\right) \quad (2.22)$$

By substitution of Eq. (2.22) in Eq. (2.21), the constitutive equation for the stress in a Newtonian fluid becomes

$$\beta_{ij} = -p\delta_{ij} + \lambda\delta_{ij}\frac{\partial u_k}{\partial x_k} + \mu\left(\frac{\partial u_i}{\partial x_j} + \frac{\partial u_j}{\partial x_i}\right) \quad (2.23)$$

The nine elements of the stress tensor β_{ij} are now expressed in terms of the pressure and velocity gradients, and two coefficients, namely, (1) μ , the *dynamic viscosity*, which is a proportionality factor between the shear stress and the velocity gradient and (2) λ , is termed the *second coefficient of viscosity*. Both μ and λ are determined empirically. The significance of λ will be shown in the next few equations. The average normal stress component is given by

$$\bar{p} = \frac{1}{3}(\beta_{11} + \beta_{22} + \beta_{33}) \quad (2.24)$$

The average normal stress is the mechanical pressure in the fluid and is equal to one-third of the trace of the stress tensor. Owing to the fact that the mechanical pressure can depend purely on the hydrostatic pressure or the hydrostatic pressure plus a component induced by the stresses due to motion of the fluid, it will in general be different from the thermodynamic pressure p . Using Eq. (2.23), the mechanical pressure will be related to the thermodynamic pressure as

$$p - \bar{p} = \left(\lambda + \frac{2}{3}\mu\right) \frac{\partial u_k}{\partial x_k} \quad (2.25)$$

The difference in thermodynamic pressure and mechanical pressure is thus proportional to the divergence of the velocity vector, and the proportionality factor $\lambda + \frac{2}{3}\mu$ is termed *bulk viscosity*, and denoted by K . For incompressible fluids, the value of λ is immaterial since, from Eq. (2.22), the term involving λ is zero in view of the continuity equation. For monoatomic gases, the bulk viscosity is zero, and therefore

$$\lambda = -\frac{2}{3}\mu \quad (2.26)$$

This relation is called *Stokes relation*. For polyatomic gases and for liquids, the departure from $K = 0$ is frequently small, and the Stokes relation is used. An example where K would be nonzero is in the case of shock waves. Since we do not encounter shock waves in this study, we can take advantage of the Stokes relation. The constitutive relation for the shear

stress therefore becomes,

$$\sigma_{ij} = \mu \left\{ \left(\frac{\partial u_i}{\partial x_j} + \frac{\partial u_j}{\partial x_i} \right) - \frac{2}{3} \frac{\partial u_k}{\partial x_k} \delta_{ij} \right\} \quad (2.27)$$

The constitutive relation for the heat flux vector is obtained from Fourier's law of heat conduction. Fourier's law of heat conduction states that the heat flux by conduction is proportional to the negative of the temperature gradient,

$$q_j = -k \frac{\partial T}{\partial x_j} \quad (2.28)$$

The equation of conservation of momentum, supplemented with the constitutive relations for a Newtonian fluid yield the Navier-Stokes equations.

In summary, the governing equations for Newtonian fluids, are written as follows,

$$\frac{\partial \rho}{\partial t} + \frac{\partial(\rho u_j)}{\partial x_j} = 0 \quad (2.29)$$

$$\frac{\partial \rho u_i}{\partial t} + \frac{\partial \rho u_i u_j}{\partial x_j} = -\frac{\partial p_i}{\partial x_i} + \frac{\partial \sigma_{ij}}{\partial x_j} + \rho f_i \quad (2.30)$$

$$\frac{\partial(\rho e)}{\partial t} + \frac{\partial(\rho e u_j)}{\partial x_j} = -p \frac{\partial u_k}{\partial x_k} + \sigma_{ij} \frac{\partial u_i}{\partial x_j} - \frac{\partial q_i}{\partial x_i} \quad (2.31)$$

$$p = \rho R T \quad (2.32)$$

$$e = C_v T = (C_p T - R T) \quad (2.33)$$

2.1.5 Generic conservation equation

It is useful to note that the conservation equations discussed until now can be considered as special cases of the generic conservation equation. In integral conservation form, the generic conservation equation is:

$$\frac{\partial}{\partial t} \int_V \rho \phi dV + \int_S \rho \phi u_i n_i dS = \int_S \Gamma \nabla \phi n_i dS + \int_V q_\phi dV \quad (2.34)$$

where ϕ could be any scalar quantity, such as species concentration, or temperature, amongst others. Γ is the diffusivity of the quantity ϕ , and q_ϕ is the source or sink of ϕ . In Cartesian

coordinates, and tensor notation, the differential form of the generic conservation equation is:

$$\frac{\partial(\rho\phi)}{\partial t} + \frac{\partial(\rho u_j \phi)}{\partial x_j} = \frac{\partial}{\partial x_j} \left(\Gamma \frac{\partial \phi}{\partial x_j} \right) + q_\phi \quad (2.35)$$

2.2 Form of Governing Equations Used in this Study

The governing equations, Eq. (2.29), Eq. (2.30), Eq. (2.31) can be written as follows, with the superscript '*' denoting dimensional quantities,

$$\frac{\partial \rho^*}{\partial t^*} + \frac{\partial(\rho^* u_j^*)}{\partial x_j^*} = 0 \quad (2.36)$$

$$\frac{\partial \rho^* u_i^*}{\partial t^*} + \frac{\partial \rho^* u_i^* u_j^*}{\partial x_j^*} = -\frac{\partial p^*}{\partial x_i^*} + \frac{\partial \sigma_{ij}^*}{\partial x_j^*} - \rho^* g \delta_{2i} \quad (2.37)$$

$$\frac{\partial}{\partial t^*} (\rho^* C_p^* T^*) + \frac{\partial}{\partial x_j^*} (\rho^* u_j^* C_p^* T^*) = \frac{\partial p^*}{\partial t^*} + u_j^* \frac{\partial p^*}{\partial x_j^*} + \sigma_{ij}^* \frac{\partial u_i^*}{\partial x_j^*} - \frac{\partial q_j^*}{\partial x_j^*} \quad (2.38)$$

The last term on the right hand side of Eq. (2.37) represents the effect of the gravitational force acting in the negative y direction. The particular form of Eq. (2.38) is obtained by substituting for the pressure p , and internal energy e , using their respective equations of state, and applying the product rule of calculus for the term $\frac{\partial(pu_i)}{\partial x_i}$. The energy equation, Eq. (2.38), is now cast in a form more consistent with the primitive variable $[p, u, v, w, T]$ solution approach adopted for this study.

The transport properties μ and k are functions of temperature. This variation is given by the power-law form of Sutherland's formula [Schlichting, 1979].

$$\frac{\mu^*}{\mu_{ref}} = \left(\frac{T^*}{T_{ref}} \right)^a \quad (2.39)$$

$$\frac{k^*}{k_{ref}} = \left(\frac{T^*}{T_{ref}} \right)^a \quad (2.40)$$

where a is assumed to be 0.71. The Prandtl number (Pr) and the specific heat at constant pressure (C_p^*) are treated as constants for the temperature range under consideration.

2.2.1 Non-dimensionalization

The above set of equations have been non-dimensionalized by defining appropriate reference quantities as described below,

$$\begin{aligned} x_i &= \frac{x_i^*}{L_{ref}} & u_i &= \frac{u_i^*}{U_{ref}} & t &= \frac{t^*}{(L_{ref}/U_{ref})} \\ \rho &= \frac{\rho^*}{\rho_{ref}} & p &= \frac{p^*}{\rho_{ref}U_{ref}^2} & T &= \frac{T^*}{T_{ref}} \\ \mu &= \frac{\mu^*}{\mu_{ref}} & k &= \frac{k^*}{k_{ref}} & R &= \frac{R^*}{(U_{ref}^2/T_{ref})} = \frac{1}{\gamma M_{ref}^2} \end{aligned}$$

where L_{ref} , U_{ref} , T_{ref} , and ρ_{ref} are the reference length, velocity, temperature, and density respectively.

Using the above definitions we get the following non-dimensional form of the NS equations,

$$\frac{\partial \rho}{\partial t} + \frac{\partial \rho u_j}{\partial x_j} = 0 \quad (2.41)$$

$$\frac{\partial \rho u_i}{\partial t} + \frac{\partial \rho u_i u_j}{\partial x_j} = -\frac{\partial p}{\partial x_i} + \frac{\partial \sigma_{ij}}{\partial x_j} - \left(\frac{Ra}{2\epsilon Pr Re^2} \right) \rho \delta_{2i} \quad (2.42)$$

$$\frac{\partial}{\partial t}(\rho T) + \frac{\partial}{\partial x_j}(\rho u_j T) = Ec \left(\frac{\partial p}{\partial t} + u_j \frac{\partial p}{\partial x_j} + \sigma_{ij} \frac{\partial u_i}{\partial x_j} \right) - \frac{\partial q_j}{\partial x_j} \quad (2.43)$$

where the non-dimensional viscous (or shear) stress tensor and heat conduction vector are given as,

$$\sigma_{ij} = \frac{\mu}{Re} \left(\frac{\partial u_i}{\partial x_j} + \frac{\partial u_j}{\partial x_i} - \frac{2}{3} \frac{\partial u_k}{\partial x_k} \delta_{ij} \right) \quad (2.44)$$

$$q_j = -\frac{k}{Pr Re} \left(\frac{\partial T}{\partial x_j} \right) \quad (2.45)$$

The following non-dimensional parameters appear as a result of the non-dimensionalization,

$$\begin{aligned} Re &= \frac{\rho_{ref} U_{ref} L_{ref}}{\mu_{ref}} & Pr &= \frac{\mu^* C_p^*}{k^*} \\ M_{ref} &= \frac{U_{ref}}{\sqrt{\gamma R^* T_{ref}}} & Ec &= \frac{U_{ref}^2}{C_p^* T_{ref}} \\ Ra &= \frac{2\epsilon g \rho_{ref}^2 L_{ref}^3 Pr}{\mu_{ref}^2} \end{aligned}$$

Ra is the Rayleigh number and ϵ is a temperature difference factor defined as $\frac{\Delta T}{2T_{ref}}$. For a low Mach number case, the Eckert number will be very small and the term containing the pressure work and dissipation can be safely neglected [Wang, 1995]. The ideal gas law in non-dimensional form becomes,

$$p = \rho RT \quad (2.46)$$

2.3 Filtering Procedure

Turbulent flows are inherently time dependent and three-dimensional in nature. They contain a continuous spectrum of time and length scales that need to be accurately captured unlike other multiple scale problems that have a finite number of relevant scales. For any flow, the large significant length scales are related to the domain size, and directly affected by the boundary conditions. The large scales of motion are thus peculiar to the problem at hand. The small scales are related to the dissipative eddies which primarily act as a sink for the turbulent kinetic energy. Viscous effects become predominant at the small scales of motion, and these scales of motion are assumed to be nearly universal, and thus independent of the geometry.

The underlying philosophy of LES is to compute only the large-scale motions of the flow and model the effect of the small scale motions on the evolution of the large scales. Thus, the concept of LES is strongly supported by the notion that the large and small scales of motion differ qualitatively.

A clear definition of what one wants to consider as the resolved and modeled scales of motion is therefore essential. The governing equations must be modified to appropriately account for the removal of energy from the resolved (large) scales. This removal of energy must mimic as closely as possible, the physical cascade process.

Suppose a flow simulation is conducted on a grid insufficient to resolve the large scales of motion, without modifying the governing equations, then one of the following situations

is likely to occur [Rogallo and Moin, 1984]:

- Considerable “damming” up of the turbulence energy in the large scales would occur if an energy conserving finite difference scheme on the convective term is used.
- The turbulence energy may reach a non-physical equilibrium distribution among the finite degrees of freedom.
- The numerical algorithm may become unstable as the smallest computed scales accumulate energy.
- In situations where the viscosity is not zero, nevertheless too small to allow accurate resolution of the dissipation scales, an energy-conserving algorithm collects energy at the smallest computed scales until the dissipation and cascade rates reach an equilibrium.

The modification of the governing equations is therefore essential in order to simulate the energy cascade process as appropriately as possible.

A space filtering operation [Leonard, 1974] is applied to the governing equations in order to obtain the “resolvable-scale” equations. The resolved or large-scale variable, denoted by a bar, is defined by the convolution integral

$$\bar{\phi}(\underline{x}, t) = \int_D \phi(\underline{x}', t) h(\underline{x} - \underline{x}'; \Delta) d\underline{x}' \quad (2.47)$$

where D is the entire domain, h is a suitably defined filter function in space, \underline{x} and \underline{x}' are space vectors and Δ is the characteristic filter width. The flow variable can now be thought of as being decomposed into two components, a large scale (or resolved) component (denoted by the overbar) and a subgrid-scale component (denoted by the prime)

$$\phi = \bar{\phi} + \phi' \quad (2.48)$$

By definition, the space Fourier transform of ϕ , denoted by $\hat{\phi}$ is given by

$$\hat{\phi}(\underline{k}, t) \stackrel{\text{def}}{=} \int_D \phi(\underline{x}, t) e^{i \underline{k} \underline{x}} d\underline{x} \quad (2.49)$$

where \underline{k} represents wave number vector, and $i = \sqrt{-1}$. By the convolution theorem, we have

$$\hat{\phi}(\underline{x}, t) = \hat{h}(\underline{k}) \hat{\phi}(\underline{k}, t) \quad (2.50)$$

Equation (2.50) is in Fourier space, and can best illustrate the effect of filtering. Any signal can be broken down into its frequency components by means of transforming it into Fourier space. Filtering actually means setting the Fourier coefficients of scales smaller than a cut-off scale to be zero. That is, the filtering operation corresponds to a weighted selection of certain scales (or wave numbers) in the flow. Thus, if $\hat{h} = 0$ for $|k_i| > k_c$, where k_c is a cut-off wave number, all the high wave number (high frequency) components of ϕ are filtered out by convoluting it with h . Such a filter is termed an “ideal low pass filter” [Holloway, 1958]. In addition to the ideal filter, box filters (“moving average” or “top hat filter”) and Gaussian filters are quite commonly used in turbulent flow simulations.

In order to ensure that the filtering operation will reproduce any spatially uniform and constant quantity, the following normalization condition is imposed

$$\int_D h(\underline{x}) d\underline{x} = 1 \quad (2.51)$$

The filtering operation also commutes with the spatial and temporal derivatives if the filter width is constant, the function is piecewise continuously differentiable, and has bounded support. That is, the filter function must vanish at the boundary of its support.

$$\overline{\frac{\partial \phi}{\partial x}} = \frac{\partial \bar{\phi}}{\partial x} \quad \overline{\frac{\partial \phi}{\partial t}} = \frac{\partial \bar{\phi}}{\partial t} \quad (2.52)$$

This commutative property enables the required evolution equations for the filtered fields to be obtained by applying the filtering operation to the Navier-Stokes equations. The following

relations true for Reynolds averaging are invalid in the case of filtering,

$$\overline{\overline{\phi}} \neq \overline{\phi} \quad (2.53)$$

$$\overline{\phi'} \neq 0 \quad (2.54)$$

$$\overline{\overline{\phi} \phi'} \neq 0 \quad (2.55)$$

For the case of the cut-off filter, the inequality sign in Eq. (2.54) and Eq. (2.55) has to be replaced with an equality sign since the single and double filtered quantities are identical, the reason being that for the cut-off filter the grid and subgrid scales do not overlap in spectral space.

Although the filter function could be any function satisfying the above constraints, the cut-off filter, the box filter and the Gaussian filter are typically used due to the natural way in which they integrate with the numerical solution procedures. Any of these filter functions can be expressed as

$$h(\underline{x}) = \prod_{i=1}^3 h_i(x_i) \quad (2.56)$$

where $h_i(x_i)$ is a one-dimensional filter. The Fourier transform of h is

$$\hat{h}(\underline{k}) = \prod_{i=1}^3 \hat{h}_i^{x_i}(k_i) \quad (2.57)$$

where

$$\hat{h}_i^{x_i}(k_i) \stackrel{\text{def}}{=} \int_D h_i(x_i) e^{-ik_i x_i} dx_i \quad (2.58)$$

For the case of an isotropic filter,

$$h_i(x_i) = G(x_i) \quad (2.59)$$

$$\hat{h}_i^{x_i}(k_i) = \hat{G}^{x_i}(k_i) \quad (2.60)$$

Equations (2.59, 2.60) state that the *same* one-dimensional filter function is used in the three coordinate directions. The definitions of the filter functions $G(x_i)$, and the respective Fourier transforms $\hat{G}^{x_i}(k_i)$, for the sharp Fourier cut-off filter, top-hat (or box) filter and the Gaussian filter are given in the following section.

2.3.1 Types of filters

1. **Sharp Fourier cut-off filter:** The sharp cut-off filter, in physical space and its Fourier transform are defined as

$$G(x_i) = 2 \frac{\sin[2\pi x_i/\Delta]}{2\pi x_i} \quad (2.61)$$

$$\hat{G}^{x_i}(k_i) = \begin{cases} 0 & |k_i| > k_c \\ 1 & |k_i| \leq k_c \end{cases} \quad (2.62)$$

where k_i is the wave vector component in the i direction, $k_c (= 2\pi/\Delta)$ is the cut-off wave number and Δ is the filter width. This filter is implicitly used in all spectral methods having finite frequency resolution.

2. **Top-hat filter:** The top-hat filter in physical space and its Fourier transform are given by,

$$G(x_i) = \begin{cases} 1/\Delta & |x_i| \leq \Delta/2 \quad (i = 1, 2, 3) \\ 0 & |x_i| > \Delta/2 \end{cases} \quad (2.63)$$

$$\hat{G}^{x_i}(k_i) = \frac{\sin[\Delta k_i/2]}{\Delta k_i/2} \quad (2.64)$$

where Δ is the filter width. This filter is most commonly used in simulations using finite volume or finite difference methods since the finite spatial resolution is implicitly equivalent to filtering out the sub-grid scales. The top-hat filter is used in this study.

3. **Gaussian filter:** The Gaussian filter, and its Fourier transform are given as,

$$G(x_i) = \frac{\sqrt{c/\pi}}{\Delta} \exp\left[-c\left(\frac{x_i}{\Delta}\right)^2\right] \quad (2.65)$$

$$\hat{G}^{x_i}(k_i) = \exp\left[-\frac{\Delta^2 k_i^2}{4c}\right] \quad (2.66)$$

In this case c is a parameter usually set to 6. In contrast to the sharp Fourier cut-off filter which completely cancels out the smaller scales, both the Gaussian and the top-

hat filters have continuous spectral characteristics and merely attenuate the smaller scales.

2.3.2 Favre filtering

For the LES of compressible flows, a density weighted filtering (also referred to as Favre filtering; named after Favre [1983] who introduced it), is employed. A considerably simpler set of filtered equations is obtained with the use of Favre filtering. Triple correlations like $\overline{\rho'u'v'}$, arising due to the fact that density is an additional unknown, would otherwise have to be modeled.

For a quantity ϕ the Favre filtered quantity $\tilde{\phi}$ is defined as,

$$\tilde{\phi} = \frac{\overline{\rho\phi}}{\bar{\rho}} \quad (2.67)$$

Thus, any variable can be decomposed in two ways,

$$\begin{aligned} \phi &= \tilde{\phi} + \phi'' \\ \phi &= \bar{\phi} + \phi' \end{aligned} \quad (2.68)$$

where $\bar{\phi}$ and ϕ' are the simple filtered large-scale and sub-grid scale fluctuations, respectively, and $\tilde{\phi}$ and ϕ'' are the Favre filtered counterparts. Also, as in the case of the simple filtering,

$$\tilde{\phi} \neq \bar{\phi} \quad \tilde{\phi}'' \neq 0 \quad \widetilde{\phi\phi''} \neq 0 \quad (2.69)$$

2.4 Favre Filtered Compressible Governing Equations

The compressible governing equations take the following form upon Favre filtering,

$$\frac{\partial \bar{\rho}}{\partial t} + \frac{\partial \bar{\rho} \tilde{u}_j}{\partial x_j} = 0 \quad (2.70)$$

$$\frac{\partial \bar{\rho} \tilde{u}_i}{\partial t} + \frac{\partial \bar{\rho} \tilde{u}_i \tilde{u}_j}{\partial x_j} = -\frac{\partial \bar{p}}{\partial x_i} + \frac{\partial \bar{\sigma}_{ij}}{\partial x_j} - \frac{\partial \tau_{ij}}{\partial x_j} - \left(\frac{Ra}{2\epsilon Pr Re^2} \right) \bar{\rho} \delta_{2i} \quad (2.71)$$

$$\frac{\partial}{\partial t}(\bar{\rho}\tilde{T}) + \frac{\partial}{\partial x_j}(\bar{\rho}\tilde{u}_j\tilde{T}) = -\frac{\partial\bar{q}_j}{\partial x_j} - \frac{\partial Q_j}{\partial x_j} \quad (2.72)$$

The filtered viscous stress tensor and the filtered heat conduction vector are given by,

$$\bar{\sigma}_{ij} = \frac{\mu}{Re} \left(\frac{\partial u_i}{\partial x_j} + \frac{\partial u_j}{\partial x_i} - \frac{2}{3} \frac{\partial u_k}{\partial x_k} \delta_{ij} \right) \quad (2.73)$$

$$\bar{q}_j = -\frac{k}{Pr Re} \left(\frac{\partial T}{\partial x_j} \right) \quad (2.74)$$

The assumption that the correlation between the fluid properties and the derivatives of the velocities is weak [Cebeci and Smith, 1974] is made use of in order to rewrite the expressions for the filtered stress tensor and the filtered heat conduction vector as

$$\hat{\sigma}_{ij} = \frac{\bar{\mu}}{Re} \left(\frac{\partial \tilde{u}_i}{\partial x_j} + \frac{\partial \tilde{u}_j}{\partial x_i} - \frac{2}{3} \frac{\partial \tilde{u}_k}{\partial x_k} \delta_{ij} \right) \quad (2.75)$$

$$\bar{q}_j = -\frac{\bar{k}}{Pr Re} \left(\frac{\partial \tilde{T}}{\partial x_j} \right) \quad (2.76)$$

The SGS stress tensor and the SGS heat flux vector given as,

$$\tau_{ij} = \bar{\rho}(\widetilde{u_i u_j} - \tilde{u}_i \tilde{u}_j) \quad (2.77)$$

$$Q_j = \bar{\rho}(\widetilde{u_j T} - \tilde{u}_j \tilde{T}) \quad (2.78)$$

The ideal gas law, Eq. (2.46), becomes,

$$\bar{p} = \bar{\rho} R \tilde{T} \quad (2.79)$$

The turbulent stress τ_{ij} and the turbulent heat flux Q_j have to be modeled in order to close the system of equations. The quantity τ_{ij} represents the effect of the sub-grid scale velocity component on the evolution of the large-scale motion.

Using the decomposition defined by Eq. (2.69), the following expressions for τ_{ij} and Q_j are obtained

$$\tau_{ij} = -\bar{\rho} \left[\widetilde{\tilde{u}_i \tilde{u}_j} - \tilde{u}_i \tilde{u}_j + \widetilde{\tilde{u}_i u_j''} + \widetilde{u_i'' \tilde{u}_j} + \widetilde{u_i'' u_j''} \right] \quad (2.80)$$

$$Q_j = -\bar{\rho} \left[\widetilde{\tilde{u}_j \tilde{T}} - \tilde{u}_j \tilde{T} + \widetilde{\tilde{u}_j T''} + \widetilde{u_j'' \tilde{T}} + \widetilde{u_j'' T''} \right] \quad (2.81)$$

τ_{ij} can be further decomposed into 3 components respectively known as the Leonard stress L_{ij} , cross sub-grid scale stress C_{ij} , and the Reynolds sub-grid scale stress R_{ij} ,

$$\tau_{ij} = L_{ij} + C_{ij} + R_{ij} \quad (2.82)$$

where,

$$\begin{aligned} L_{ij} &= -\bar{\rho}(\widetilde{\tilde{u}_i \tilde{u}_j} - \tilde{u}_i \tilde{u}_j) \\ C_{ij} &= -\bar{\rho}(\widetilde{\tilde{u}_i u_j''} + \widetilde{u_i'' \tilde{u}_j}) \\ R_{ij} &= -\bar{\rho}(\widetilde{u_i'' u_j''}) \end{aligned} \quad (2.83)$$

Analogous to the decomposition of the SGS stress tensor, the SGS heat flux vector can also be decomposed into the respective Leonard, cross and Reynolds components

$$Q_j = Q_j^L + Q_j^C + Q_j^R \quad (2.84)$$

where

$$\begin{aligned} Q_j^L &= -\bar{\rho}(\widetilde{\tilde{u}_j \tilde{T}} - \tilde{u}_j \tilde{T}) \\ Q_j^C &= -\bar{\rho}(\widetilde{\tilde{u}_j T''} + \widetilde{u_j'' \tilde{T}}) \\ Q_j^R &= -\bar{\rho}(\widetilde{u_j'' T''}) \end{aligned} \quad (2.85)$$

L_{ij} and Q_j^L contain only the resolved scale variables and can be computed directly. In principle only C_{ij} , R_{ij} , Q_j^C and Q_j^R need to be modeled.

The description of turbulence has to be the same in all inertial frames of reference, and it is therefore essential that the property of Galilean invariance be satisfied by any model. Several models in the past, such as those by Biringen and Reynolds [1981], Bardina et al. [1983] and Moin and Kim [1982] did not exhibit this invariance. Speziale [1985] noticed that L_{ij} , and C_{ij} individually are not Galilean invariant, but that $L_{ij} + C_{ij}$ and R_{ij} are Galilean invariant. Consequently the total stress τ_{ij} ($= L_{ij} + C_{ij} + R_{ij}$) is also Galilean invariant. In this work the total stress τ_{ij} is modeled rather than each of the components individually.

It is noted, however, that there has been recent progress (Zang et al. [1993]; Salvetti and Banerjee [1995]) in approaches to the modeling of the SGS stress, and these are potential directions for future improvements to this study.

2.5 Sub-grid Scale Models

In the current work, all three terms were lumped together and modeled using the dynamic modeling procedure with the Smagorinsky model as the base model. It must be mentioned here that the dynamic model procedure can be used with any base model, such as the mixed subgrid-scale model (MSM) proposed by Zang et al. [1993]. The dynamic modeling procedure (often referred to as the “dynamic model”) was first proposed by Germano et al. [1991], and used the Smagorinsky model as the base model. The compressible extension to the incompressible dynamic model made by Moin et al. [1991], is used in this study.

2.5.1 Smagorinsky sub-grid scale model

Proposed over thirty years ago by Smagorinsky [1963], this subgrid scale model is still the most popular among researchers. As mentioned earlier, the new dynamic model is, strictly speaking a procedure based on the Smagorinsky formulation. The Smagorinsky model is an eddy-viscosity based model, and is based on the notion that the principal effects of the sub-grid scale stresses are increased transport and dissipation. A heuristic method, amongst others, to derive this model is to equate the production and dissipation of subgrid-scale turbulent kinetic energy. Turbulence theories can also be used to derive this model. The compressible flow version of the Smagorinsky model is given as

$$\tau_{ij} = \frac{1}{3}\tau_{kk}\delta_{ij} - 2\mu_T(\tilde{S}_{ij} - \frac{1}{3}\tilde{S}_{kk}\delta_{ij}) \quad (2.86)$$

where μ_T is the eddy-viscosity, and

$$\tilde{S}_{ij} = \frac{1}{2} \left(\frac{\partial \tilde{u}_i}{\partial x_j} + \frac{\partial \tilde{u}_j}{\partial x_i} \right) \quad (2.87)$$

is the Favre-filtered strain rate tensor, and τ_{kk} is the sub-grid scale turbulent kinetic energy. Unlike the case for incompressible flows, where τ_{kk} is absorbed into the pressure term, it needs to be explicitly modeled for compressible flows as the pressure is fixed by the equation of state. The model proposed by Yoshizawa [1986], described in a following section, is adopted.

For closure, μ_T is parameterized by equating the sub-grid scale energy production and dissipation, as mentioned above, to obtain,

$$\mu_T = C_s \bar{\rho} \Delta^2 \sqrt{2 \tilde{S}_{ij} \tilde{S}_{ij}} \quad (2.88)$$

where C_s is a model parameter to be specified, and Δ is the filter width which is typically assumed to be a function of the grid resolution. Few large eddy simulations are carried out with uniform grid resolution in three directions, and an average Δ is often used. For meshes with moderate anisotropies an appropriate average is the geometric mean (Scotti et al., 1993) $\Delta_{av} = (\Delta x \Delta y \Delta z)^{1/3}$, which has been confirmed to work well up to aspect ratios of 20:1 [Reynolds, 1990].

The Smagorinsky sub-grid scale model has been successfully used for channel flow simulations [Wang, 1995] and for channel flows with high heating and cooling [Dailey, 1997]. For such wall bounded flows it is necessary to damp the eddy-viscosity using an appropriate wall damping function. For example, the model proposed by Piomelli [1988] is presented,

$$\mu_T = C_s \bar{\rho} \Delta^2 [1 - \exp(-y^{+3}/A^{+3})]^{1/2} \sqrt{2 \tilde{S}_{ij} \tilde{S}_{ij}} \quad (2.89)$$

where A^+ is a constant typically equal to 25.

Some of the drawbacks of the Smagorinsky model are

- The model parameter C_s needs to be known *a priori*. C_s is dependent on the nature of the flow, and hence far from being universal.
- The model parameter does not decrease to zero at the walls, and appropriate wall damping functions need to be used.

2.5.2 Dynamic sub-grid scale models

The dynamic model [Germano et al., 1991] is, strictly speaking, a procedure rather than a model, and can employ any model as its base model. The model parameter C_s is calculated “dynamically” using spectral information from two different levels already part of the resolved solution. C_s is thus, a function of space and time. The eddy-viscosity asymptotically approaches zero near solid walls and in regimes where the flow is laminar. The dynamic model has been successfully used in channel flows [Wang, 1995] and in more complex flows such as the rearward facing step flow [Akselvoll and Moin, 1995].

For compressible flows, in addition to the eddy viscosity, the turbulent thermal diffusivity can be calculated dynamically. The extension of the dynamic model for compressible flows proposed by Moin et al. [1991] has been employed in this study.

2.5.2.1 Modeling of the SGS stress tensor

The dynamic model requires the definition of a new filtering operation where the filter width $\widehat{\Delta}$ is assumed to be greater than the grid filter width Δ . This is referred to as the “test” filter. Using $\tilde{f} = \overline{\rho f} / \bar{\rho}$, the SGS stress tensor expression can be manipulated as follows:

$$\tau_{ij} = \bar{\rho}(\overline{u_i u_j} - \tilde{u}_i \tilde{u}_j) \quad (2.90)$$

$$= \overline{\rho u_i u_j} - \frac{\overline{\rho u_i} \overline{\rho u_j}}{\bar{\rho}} \quad (2.91)$$

Defining the sub-test scale stress terms analogous to the sub-grid scale stress terms, one obtains

$$\mathcal{T}_{ij} = \overline{\overline{\rho u_i u_j}} - \frac{\overline{\overline{\rho u_i}} \overline{\overline{\rho u_j}}}{\widehat{\rho}} \quad (2.92)$$

The quantities τ_{ij} and \mathcal{T}_{ij} are related by the following identity of Germano [1992],

$$\mathcal{L}_{ij} = \mathcal{T}_{ij} - \widehat{\tau}_{ij} \quad (2.93)$$

$$= \left[\overline{\overline{\rho u_i u_j}} - \frac{\overline{\overline{\rho u_i}} \overline{\overline{\rho u_j}}}{\widehat{\rho}} \right] - \left[\overline{\rho u_i u_j} - \frac{\overline{\rho u_i} \overline{\rho u_j}}{\bar{\rho}} \right] \quad (2.94)$$

$$(2.95)$$

Noting that $\overline{\rho u_i} = \bar{\rho} \tilde{u}_i$, Eq. (2.94) can be simplified to

$$\mathcal{L}_{ij} = \overline{\tilde{\rho} \tilde{u}_i \tilde{u}_j} - \frac{\overline{\tilde{\rho} \tilde{u}_i} \overline{\tilde{\rho} \tilde{u}_j}}{\hat{\tilde{\rho}}} \quad (2.96)$$

Now, the sub-test scale turbulent stress term \mathcal{T}_{ij} is modeled similar to the sub-grid scale turbulent stress τ_{ij} ,

$$\mathcal{T}_{ij} = \frac{1}{3} \mathcal{T}_{kk} \delta_{ij} - 2\mu_T (\hat{\tilde{S}}_{ij} - \frac{1}{3} \hat{\tilde{S}}_{kk} \delta_{ij}) \quad (2.97)$$

using a Smagorinsky model with the same model parameter,

$$\mu_T = C_s \hat{\tilde{\rho}} \hat{\Delta}^2 \sqrt{2 \hat{\tilde{S}}_{ij} \hat{\tilde{S}}_{ij}} \quad (2.98)$$

$$= C_s \hat{\tilde{\rho}} \hat{\Delta}^2 |\hat{\tilde{S}}| \quad (2.99)$$

where $\sqrt{2 \hat{\tilde{S}}_{ij} \hat{\tilde{S}}_{ij}}$ is abbreviated as $|\hat{\tilde{S}}|$. For compressible flows, τ_{kk} and \mathcal{T}_{kk} also have to be modeled. The model proposed by Yoshizawa [1986] can be written as,

$$\tau_{kk} = 2C_I \bar{\rho} \Delta^2 |\tilde{S}|^2 \quad (2.100)$$

$$\mathcal{T}_{kk} = 2C_I \hat{\tilde{\rho}} \hat{\Delta}^2 |\hat{\tilde{S}}|^2 \quad (2.101)$$

Contracting Eq. (2.93) and substituting Eqs. (2.100) and (2.101) into the resulting expression and solving for C_I , one obtains,

$$C_I = \frac{1}{2\Delta^2} \frac{\overline{\tilde{\rho} \tilde{u}_k \tilde{u}_k} - \frac{\overline{\tilde{\rho} \tilde{u}_k} \overline{\tilde{\rho} \tilde{u}_k}}{\hat{\tilde{\rho}}}}{(\hat{\tilde{\rho}} \alpha^2 |\hat{\tilde{S}}|^2 - \bar{\rho} |\tilde{S}|^2)} \quad (2.102)$$

where α is the ratio of the filter widths $\hat{\Delta}/\Delta$.

Substituting Eqs. (2.86) and (2.97) into Eq. (2.93) and rearranging one gets,

$$\mathcal{L}_{ij} - \frac{1}{3} \mathcal{L}_{kk} \delta_{ij} = \left(\mathcal{T}_{ij} - \frac{1}{3} \mathcal{T}_{kk} \delta_{ij} \right) - \left(\hat{\tau}_{ij} - \frac{1}{3} \hat{\tau}_{kk} \delta_{ij} \right) \quad (2.103)$$

$$= -2C_s \Delta^2 \left\{ \alpha^2 \hat{\tilde{\rho}} |\hat{\tilde{S}}| \left(\hat{\tilde{S}}_{ij} - \frac{1}{3} \hat{\tilde{S}}_{kk} \delta_{ij} \right) - \hat{\rho} |\tilde{S}| \left(\tilde{S}_{ij} - \frac{1}{3} \tilde{S}_{kk} \delta_{ij} \right) \right\} \quad (2.104)$$

The above equation can be written down symbolically in a much simpler form as,

$$D_{ij} = -2C_s \Delta^2 P_{ij} \quad (2.105)$$

The above tensor equation represents five independent equations to determine a single constant, and thereby no value of C_s can be chosen to make it correct. Using the least squares approach to error minimization [Lilly, 1992], E is defined as the square of the error in Eq. (2.105),

$$E = (D_{ij} + 2C_s \Delta^2 P_{ij})^2 \quad (2.106)$$

Now, $\frac{\partial E}{\partial C_s} = 0$ implies

$$C_s = -\frac{1}{2\Delta^2} \frac{D_{ij} P_{ij}}{P_{lm} P_{lm}} \quad (2.107)$$

This value of C_s represents the minimum of E since $\frac{\partial^2 E}{\partial C_s^2} > 0$.

2.5.2.2 Modeling of the SGS heat flux vector

Using $\tilde{f} = \overline{\rho f} / \bar{\rho}$, the subgrid scale heat flux Q_j is manipulated,

$$Q_j = \bar{\rho} (\widetilde{u_j T} - \tilde{u}_j \tilde{T}) \quad (2.108)$$

$$= \overline{\rho u_j T} - \frac{\overline{\rho u_j} \overline{\rho T}}{\bar{\rho}} \quad (2.109)$$

The subgrid scale heat flux is modeled using an eddy-diffusivity model,

$$Q_j = -\bar{\rho} \alpha_\tau \frac{\partial \tilde{T}}{\partial x_j} = -\frac{\bar{\rho} \nu_\tau}{Pr_\tau} \frac{\partial \tilde{T}}{\partial x_j} \quad (2.110)$$

$$= -\frac{\bar{\rho} C_s \Delta^2 |\tilde{S}|}{Pr_\tau} \frac{\partial \tilde{T}}{\partial x_j} \quad (2.111)$$

where Pr_τ is the turbulent Prandtl number, and defined as the ratio of eddy-viscosity ν_τ to eddy-diffusivity α_τ . "Test" filtering the energy equation yields the sub-test scale heat flux vector,

$$Q_j = \widehat{\overline{\rho u_j T}} - \frac{\widehat{\overline{\rho u_j}} \widehat{\overline{\rho T}}}{\widehat{\bar{\rho}}} \quad (2.112)$$

which is modeled analogous to the subgrid-scale heat flux, using the *same* turbulent Prandtl number at the grid filter and test filter levels,

$$Q_j = -\frac{\widehat{\rho} C_s \widehat{\Delta}^2 |\widehat{S}|}{Pr_\tau} \frac{\partial \widehat{T}}{\partial x_j} \quad (2.113)$$

The resolved turbulent heat flux \mathcal{H}_j is related to the subgrid and subtest heat fluxes by the algebraic identity,

$$\begin{aligned} \mathcal{H}_j &= Q_j - \widehat{Q}_j \\ &= \left(\frac{\overline{\rho u_j \rho T}}{\widehat{\rho}} \right) - \frac{\overline{\rho u_j \rho T}}{\widehat{\rho}} \end{aligned} \quad (2.114)$$

$$= \overline{\rho \tilde{u}_j \tilde{T}} - \frac{\overline{\rho \tilde{u}_j \rho \tilde{T}}}{\widehat{\rho}} \quad (2.115)$$

Substitution of the models for Q_{ij} and Q_{ij} , from Eqs. (2.113) and (2.111), one obtains

$$H_j = -\frac{C_s}{Pr_\tau} F_j \quad (2.116)$$

where,

$$F_j = (\widehat{\rho} \widehat{\Delta}^2 |\widehat{S}| \frac{\partial \widehat{T}}{\partial x_j} - \overline{\rho \Delta^2 |\tilde{S}| \frac{\partial \tilde{T}}{\partial x_j}}) \quad (2.117)$$

Equation (2.116) represents a system of three independent equations in a single unknown.

Using the least squares approach to error minimization (as shown earlier) we get,

$$Pr_\tau = -C_s \frac{F_k F_k}{H_l F_l} \quad (2.118)$$

Thus, our system of equations is now closed. But it has been observed during numerical simulations that often the model constants calculated using the above approach have a large scatter with positive and negative values. This almost invariably makes the calculation unstable as observed by many other investigators. As a remedy for this, both the numerators and denominators were averaged along homogeneous directions so that the model constant now is a function of only the inhomogeneous directions. For flows without any homogeneous

directions, one can envisage a localized spatial average [Zang et al., 1993], but this behavior remains as the primary drawback of the dynamic model. Equation (2.107) can then be represented as,

$$C_s = -\frac{1}{2\Delta^2} \frac{\langle D_{ij} P_{ij} \rangle}{\langle P_{lm} P_{lm} \rangle} \quad (2.119)$$

where $\langle \rangle$ denotes averaging over homogeneous directions.

The dynamic model can be considered “input free” except for the factor α which is the test to grid filter width ratio. Germano et al. [1991] have found that a value of 2 gives the best results, but the ratio did not seem to have much effect in general. A value of 2 has been used in the present computations.

CHAPTER 3 NUMERICAL FORMULATION

The governing partial differential equations described in the previous chapter now need to be *discretized*. A discretization method approximates the differential equations by a system of linear algebraic equations for the variables at discrete locations in space and time. Several options exist for the choice of the discretization method. Methods like spectral schemes, boundary element methods, and cellular automata are used for special classes of problems, while others such as finite difference (FD), finite volume (FV) and finite element (FE) methods are generally used for most flow simulations. Spectral schemes have been used extensively for the direct and large eddy simulations of turbulent flows in simple geometric domains with periodic boundary conditions in all three coordinate directions. However, they cannot be easily adapted to complex flows, or flows where periodic boundary conditions cannot necessarily be imposed. Finite volume and finite difference methods have thus become increasingly popular for flow simulations in complex flows and geometries. The finite volume approach is chosen for this study, and is described in this chapter.

3.1 The Finite Volume Approach

The starting point for all FV methods is the integral form of the conservation equations. The domain of interest is subdivided into a finite number of contiguous, non-overlapping control volumes, and the conservation equations are enforced at the control volume (CV) level. A computational node is located at the centroid of each CV in a cell-centered scheme or at each of the corners of the CV in a cell-vertex scheme. The variables are calculated at

the computational nodes. Variable values at the CV surfaces are obtained by interpolation of the nodal values. Appropriate quadrature formulae are used to approximate surface and volume integrals. Thus, an algebraic equation for each CV, containing neighbor nodal values is obtained.

Any type of grid can be accommodated by the FV method, and hence is suitable for complex geometries. The CV boundaries are defined by the grid, and need not be related to a coordinate system. The FV method is conservative by construction, as long as the surface integrals are the same for the CVs sharing a boundary. The surface integrals represent convective and diffusive fluxes.

For any closed surface S enclosing a volume V , all conservation laws can be written in the following general form.

$$\frac{\partial}{\partial t} \int_V \phi dV + \oint_S \vec{F} \cdot d\vec{s} = \int_V B dV \quad (3.1)$$

where ϕ is the conserved quantity, \vec{F} is the flux vector at a point on the surface, $d\vec{s}$ is the surface normal at that point, and B could be a body force or, in general, a source term. The NS equations can also be cast in a similar form as,

$$\frac{\partial}{\partial t} \int_V \mathbf{W} dV + \oint_S (\mathbf{E}\vec{i} + \mathbf{F}\vec{j} + \mathbf{G}\vec{k}) \cdot d\vec{s} = \int_V \mathbf{B} dV \quad (3.2)$$

where \mathbf{W} is the vector of conserved variables, \mathbf{E} , \mathbf{F} , \mathbf{G} are the corresponding flux vectors in the \vec{i} , \vec{j} , and \vec{k} directions, and \mathbf{B} is a body force.

For the governing equations described in the last chapter, the following expansion of the vectors in Eq. (3.2) is obtained,

$$\mathbf{E} = \mathbf{E}_{inv} - \mathbf{E}_{vis} + \mathbf{E}_{tur} \quad (3.3)$$

$$\mathbf{F} = \mathbf{F}_{inv} - \mathbf{F}_{vis} + \mathbf{F}_{tur} \quad (3.4)$$

$$\mathbf{G} = \mathbf{G}_{inv} - \mathbf{G}_{vis} + \mathbf{G}_{tur} \quad (3.5)$$

where the subscripts '*inv*', '*vis*', and '*tur*' denote the inviscid (convective), viscous, and turbulent sub-grid scale stress contributions to the flux vectors, respectively. The vectors in

Eq. (3.2) are given by,

$$\mathbf{W} = \begin{bmatrix} \bar{\rho} \\ \bar{\rho}\tilde{u} \\ \bar{\rho}\tilde{v} \\ \bar{\rho}\tilde{w} \\ \bar{\rho}\tilde{T} \end{bmatrix} ; \quad \mathbf{B} = \begin{bmatrix} 0 \\ 0 \\ \frac{Ra}{2\epsilon Pr Re^2} \bar{\rho} \\ 0 \\ 0 \end{bmatrix} \quad (3.6)$$

$$\mathbf{E} = \underbrace{\begin{bmatrix} \bar{\rho}\tilde{u} \\ \bar{\rho}\tilde{u}^2 + \bar{p} \\ \bar{\rho}\tilde{u}\tilde{v} \\ \bar{\rho}\tilde{u}\tilde{w} \\ \bar{\rho}\tilde{u}\tilde{T} \end{bmatrix}}_{\mathbf{E}_{inv}} - \underbrace{\begin{bmatrix} 0 \\ \bar{\sigma}_{11} \\ \bar{\sigma}_{21} \\ \bar{\sigma}_{31} \\ -\bar{q}_1 \end{bmatrix}}_{\mathbf{E}_{vis}} + \underbrace{\begin{bmatrix} 0 \\ \tau_{11} \\ \tau_{21} \\ \tau_{31} \\ -Q_1 \end{bmatrix}}_{\mathbf{E}_{tur}} \quad (3.7)$$

$$\mathbf{F} = \underbrace{\begin{bmatrix} \bar{\rho}\tilde{v} \\ \bar{\rho}\tilde{v}\tilde{u} \\ \bar{\rho}\tilde{v}^2 + \bar{p} \\ \bar{\rho}\tilde{v}\tilde{w} \\ \bar{\rho}\tilde{v}\tilde{T} \end{bmatrix}}_{\mathbf{F}_{inv}} - \underbrace{\begin{bmatrix} 0 \\ \bar{\sigma}_{12} \\ \bar{\sigma}_{22} \\ \bar{\sigma}_{32} \\ -\bar{q}_2 \end{bmatrix}}_{\mathbf{F}_{vis}} + \underbrace{\begin{bmatrix} 0 \\ \tau_{12} \\ \tau_{22} \\ \tau_{32} \\ -Q_2 \end{bmatrix}}_{\mathbf{F}_{tur}} \quad (3.8)$$

$$\mathbf{G} = \underbrace{\begin{bmatrix} \bar{\rho}\tilde{w} \\ \bar{\rho}\tilde{w}\tilde{u} \\ \bar{\rho}\tilde{w}\tilde{v} \\ \bar{\rho}\tilde{w}^2 + \bar{p} \\ \bar{\rho}\tilde{w}\tilde{T} \end{bmatrix}}_{\mathbf{G}_{inv}} - \underbrace{\begin{bmatrix} 0 \\ \bar{\sigma}_{13} \\ \bar{\sigma}_{23} \\ \bar{\sigma}_{33} \\ -\bar{q}_3 \end{bmatrix}}_{\mathbf{G}_{vis}} + \underbrace{\begin{bmatrix} 0 \\ \tau_{13} \\ \tau_{23} \\ \tau_{33} \\ -Q_3 \end{bmatrix}}_{\mathbf{G}_{tur}} \quad (3.9)$$

For non-overlapping stationary hexahedral control volumes, the surface integral can be replaced by a summation over the six faces of a face-averaged flux times the cell face area and the volume integral by a volume-averaged quantity times the cell volume.

$$\frac{\partial \mathbf{W}}{\partial t} \Delta V + \sum_{n=1}^6 (\mathbf{E}\vec{i} + \mathbf{F}\vec{j} + \mathbf{G}\vec{k}) \cdot \Delta S_n = \mathbf{B} \Delta V \quad (3.10)$$

where \mathbf{W} and \mathbf{B} are now volume-averaged quantities, and \mathbf{E} , \mathbf{F} and \mathbf{G} are face-averaged quantities.

3.2 The Cell Centered Algorithm

Once the domain is discretized using non-overlapping cells, two ways of storing the vector of unknowns in terms of their physical location in the mesh are possible: the cell-centered approach and the cell-vertex approach. In the former, the unknowns are stored at the center of a CV and the fluxes on the CV faces are approximated by interpolating across the CV faces. In the cell-vertex method, the unknowns are stored at the CV vertices themselves and the fluxes on the CV faces are approximated by interpolating along the CV faces. Figure 3.1 details the two ways. Morton and Paisley [1989] have suggested that the trapezoidal integration along the cell boundary that results from a cell-vertex approach is more accurate on skewed meshes. It allows fewer number of spurious decoupling modes since it has a more compact stencil for the inviscid fluxes. The cell-vertex approach, however, suffers from the problem of disparity between the number of unknowns and the number of cell based equations that can be set up. The cell based residuals need to be distributed to the nodes in order to rectify this disparity. Now, only combinations of the cell based residuals will approach zero at convergence (for steady state problems), and consequently compactness of the stencil is destroyed. Based on the above argument, some of the advantages of the cell-vertex approach are mitigated. The viscous terms anyway require a larger stencil than the cell centered approach, thus making both approaches similar in their properties.

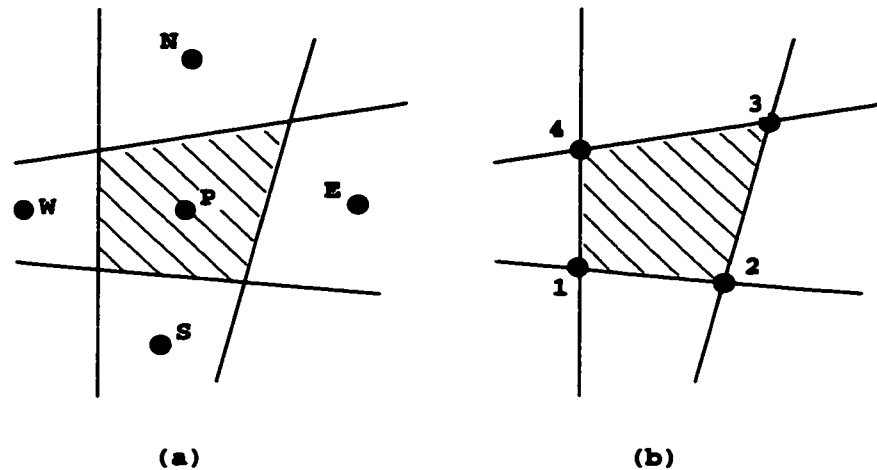


Figure 3.1 Geometry of flow variables (a) Cell-centered approach (b) Cell-vertex approach (Figure adapted from Narayanan [1998])

The cell centered approach has been more extensively used and tested in comparison to the cell vertex approach, which is one of the reasons why it is adopted in this study.

3.3 The Colocated Grid Approach

Turbulence research in general, and much of the LES work to date in particular, has been performed for the incompressible flow regime. Finite volume schemes for incompressible flows have traditionally used staggered grid approaches. In the staggered grid approach all the unknown variables are not stored at the same physical location, and this approach obviates the odd-even decoupling mechanism that is characteristic of colocated grid schemes. The problems associated with odd-even decoupling on colocated grids are difficult to eliminate without resorting to the addition of *ad hoc* artificial diffusion terms. Figures 3.2 and 3.3 show the arrangement of flow variables in the two approaches.

In the staggered grid approach, the velocity variables are stored at the mesh cell faces, and the momentum equations are solved by constructing separate control volumes around them. Pressure, density and other scalars are stored at the mesh cell center. With this arrangement, a compact stencil for the continuity equation is obtained that requires no

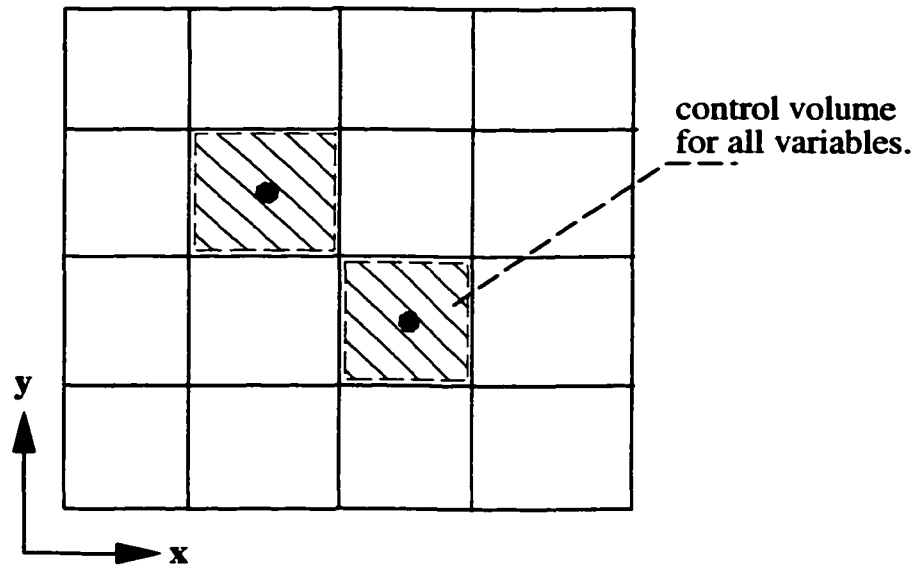


Figure 3.2 Arrangement of unknowns for the collocated grid approach (Figure adapted from Narayanan [1998])

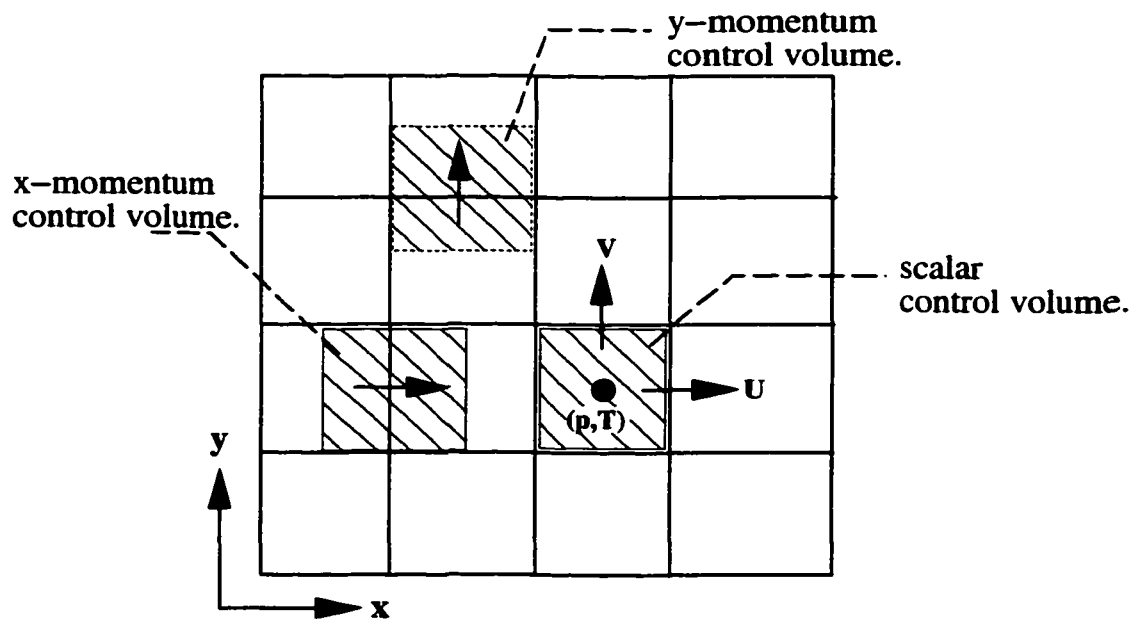


Figure 3.3 Arrangement of unknowns for the staggered grid approach (Figure adapted from Narayanan [1998])

interpolations. Interpolation is also not required for the pressure gradient terms in the momentum equations. A strong coupling between the pressure and velocity fields is achieved with this arrangement. The staggered grid approach is thus, very responsive to grid-level fluctuations. All the resolvable modes are uniquely captured, and accumulation of spurious energy at the grid level is prevented.

But staggered grid schemes become very awkward to generalize to complex geometries. From a discussion on this aspect by Zang et al. [1994], it is clear that the use of staggering for complex geometries leads to either high memory requirements [Zang et al., 1991; Meakin and Street, 1988], or inefficient solution methods [Rosenfeld et al., 1991], or complicated equations with additional source terms [Shyy and Vu, 1991]. It would not be wrong to add that use of staggered grids in the unstructured framework would also be very difficult.

In order to perform LES for geometries of practical interest, it is important to evaluate the applicability of colocated grid algorithms with suitable remedies for the odd-even decoupling problem.

Colocated grid algorithms dealing with low speed flows often suffer from the phenomenon of pressure-velocity decoupling which makes them unstable in many flow situations and, in general, unsuitable for LES in their standard form. One remedy, often used, is to introduce "artificial diffusion" terms that provide the necessary coupling. This method requires the specification of *ad hoc* constants that determine the amount of extra diffusion introduced. However, this is problem dependent and can cause excessive damping of the turbulent fluctuations as observed Dailey [1997] for the LES of a ribbed channel flow.

Narayanan [1998] successfully extended the momentum-interpolation (MI) correction proposed by Rhie and Chow [1983] to a fully coupled, dual time-stepping approach in a colocated grid framework. Two-dimensional laminar flow calculations and large eddy simulations of isotropic decaying turbulence were carried out on a colocated-grid using MI, and the results were in good agreement with experiments. However, for the LES of a plane channel flow, the penalty incurred in the allowable time step motivated the author to seek other methods

to tackle the odd-even coupling mechanism.

A sixth order compact filtering technique proposed by Lele [1992] was adopted, and has yielded excellent results. This approach was successfully used by Meng et al. [1999] in the large eddy simulation of a ribbed channel to prevent oscillations of the grid level frequencies. This procedure enabled the central difference scheme to remain stable, having little influence on the turbulence characteristics.

3.4 Cartesian Grid Limitation

In the Cartesian grid arrangement used in this work, the boundaries have nodes on them. These nodes are assumed to have zero volume, and separate boundary equations are solved to update the values at these nodes. Thus, fictitious or ghost cells outside the domain are not necessary in this approach. The boundary conditions will be described in a later section.

Stretched grids were used in this study, and an algebraic equation of the hyperbolic tangent type was used whenever grid stretching was deemed essential. The generating function is specified as

$$x_i = \frac{\tanh(a\xi_i)}{\tanh(a)} \quad (3.11)$$

where

$$\xi_i = -1 + 2 \frac{(i-1)}{(imax-1)} \quad \forall \quad 1 < i < imax \quad (3.12)$$

$$a = \frac{1}{2} \log \left[\frac{(1+b)}{(1-b)} \right] \quad \forall \quad 0 < b < 1 \quad (3.13)$$

The constant 'b' is an input parameter that controls the degree of grid stretching.

3.5 Spatial Discretization

In the Cartesian grid arrangement, the control volumes are rectangular parallelopeds, in general. Thus, the cell-face area vectors are in the direction of the respective coordinate axes.

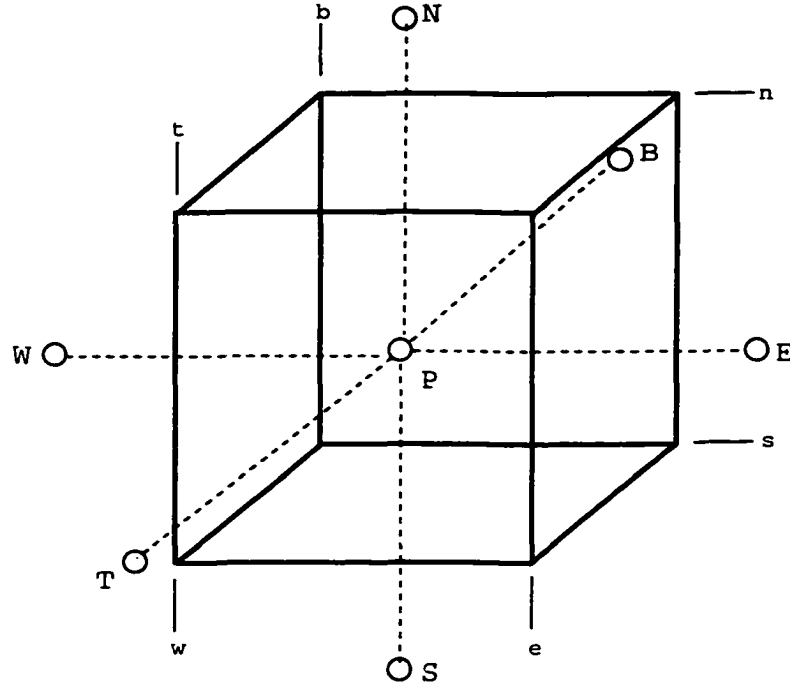


Figure 3.4 Nomenclature for discretization (Figure adapted from Narayanan [1998])

To facilitate further discussion, the nomenclature shown in Fig. 3.4 will be used. The point of interest will be denoted by P and its neighbors will be referred to as E, W, N, S, T, B . The cell faces will be referred to as e, w, n, s, t, b .

With the above simplifications, Eq. (3.10) can be written as,

$$\frac{\partial \mathbf{W}}{\partial t} \Delta V + (\mathbf{E}_e - \mathbf{E}_w) \Delta y \Delta z + (\mathbf{F}_n - \mathbf{F}_s) \Delta x \Delta z + (\mathbf{G}_t - \mathbf{G}_b) \Delta x \Delta y = \mathbf{B} \Delta V \quad (3.14)$$

where $\Delta V (= \Delta x \Delta y \Delta z)$ is the volume of the cell. Dividing by the volume, we get,

$$\frac{\partial \mathbf{W}}{\partial t} + \frac{1}{\Delta x} (\mathbf{E}_e - \mathbf{E}_w) + \frac{1}{\Delta y} (\mathbf{F}_n - \mathbf{F}_s) + \frac{1}{\Delta z} (\mathbf{G}_t - \mathbf{G}_b) = \mathbf{B} \quad (3.15)$$

In the following sections, the method used to approximate the cell-face fluxes is described. The calculation for the east face is chosen as an example, and extension to the other faces is straightforward.

3.6 Evaluation of Inviscid Fluxes

It is well known that colocated-grid central difference schemes are prone to spurious oscillations in the pressure and velocity fields that make them unstable, especially for high Reynolds number turbulent flows. Upwind schemes have been shown to be more robust as they have essentially a higher amount of diffusion, and remain stable over a wide range of flow regimes. Upwind schemes are also generally costlier in terms of computational effort. However, in the realm of turbulent simulations, upwind or upwind-biased schemes, owing to dissipation inherent in such schemes, have been shown to significantly affect the spectrum of the resolved structures [Mittal and Moin, 1997].

Based on conclusions of Narayanan [1998], Mittal [1996], and Mittal and Moin [1997], second- and fourth-order central difference schemes were deemed appropriate choices for carrying out large eddy simulations of the flows considered in this work.

3.6.1 Second and fourth-order central differences

To calculate the values of the primitive variable at the face, the second-order central difference scheme uses two points, one on each side of the face. Geometric weighting is necessary for non-uniform grid distributions. The east face value for a quantity 'u', for example, is calculated as,

$$u_e = \left(\frac{x_{i+1} - x_e}{x_{i+1} - x_i} \right) u_i + \left(\frac{x_e - x_i}{x_{i+1} - x_i} \right) u_{i+1} \quad (3.16)$$

Using the above formula, the primitive variables are interpolated onto the face, and the flux is then constructed from these interpolated values. For example, for the x-momentum equation,

$$\mathbf{E}_{e,inv} = \rho_e u_e^2 + p_e \quad (3.17)$$

A four-point Lagrangian interpolation formula is used for the fourth-order scheme. Two points on either side of a face are used, and this results in a five-point stencil for each cell.

The east face value, for example, can then be written as,

$$\begin{aligned}
u_e = & \left[\frac{(x_e - x_i)(x_e - x_{i+1})(x_e - x_{i+2})}{(x_{i-1} - x_i)(x_{i-1} - x_{i+1})(x_{i-1} - x_{i+2})} \right] u_{i-1} \\
& + \left[\frac{(x_e - x_{i-1})(x_e - x_{i+1})(x_e - x_{i+2})}{(x_i - x_{i-1})(x_i - x_{i+1})(x_i - x_{i+2})} \right] u_i \\
& + \left[\frac{(x_e - x_{i-1})(x_e - x_i)(x_e - x_{i+2})}{(x_{i+1} - x_{i-1})(x_{i+1} - x_i)(x_{i+1} - x_{i+2})} \right] u_{i+1} \\
& + \left[\frac{(x_e - x_{i-1})(x_e - x_i)(x_e - x_{i+1})}{(x_{i+2} - x_{i-1})(x_{i+2} - x_i)(x_{i+2} - x_{i+1})} \right] u_{i+2} \quad (3.18)
\end{aligned}$$

The flux at a cell face can also be calculated by interpolating the fluxes themselves from the neighboring points. For a second-order central difference scheme, the flux ($\mathbf{E}_{e,inv}$ for example) can be calculated as,

$$\mathbf{E}_{e,inv} = \left(\frac{x_{i+1} - x_e}{x_{i+1} - x_i} \right) \mathbf{E}_{i,inv} + \left(\frac{x_e - x_i}{x_{i+1} - x_i} \right) \mathbf{E}_{i+1,inv} \quad (3.19)$$

It is interesting to note that this method of flux computation, used by Wang [1995], was determined to be the one of primary causes of instability of the solution. Calculating the fluxes from primary variables interpolated onto the cell, as in Eq.(3.16), allowed the solution to remain stable.

The logic provided by Narayanan [1998] is summarized as follows:

- The fluxes are non-linear, and whenever a flux is calculated high wavenumber modes are generated due to this non-linear interaction. Wave numbers that are higher than the maximum resolvable wavenumber (Nyquist wavenumber) are aliased onto the resolved scales.
- In addition, any interpolation scheme has an associated truncation error which usually increases with wavenumber. Discussion on this aspect is presented in Narayanan [1998]. Owing to truncation, the interpolated primary variables have much less energy in their high wavenumber resolvable modes. The higher frequencies generated due to the non-linear interactions are thus, very weak.

- In the case where the fluxes are interpolated, the aliased modes could be much stronger, depending on the type of interpolation used. For central difference schemes which have no mechanism of controlling aliasing errors at high wave numbers, this could lead to eventual instability.

3.7 Viscous Flux Calculation

Owing to the fact that the viscous operator is elliptic in nature, it is always approximated using a central difference formulation. A second-order gradient approximation as given below was used in the case of the 2CD scheme. The derivative $\partial u/\partial x$ at the east face, for example, was approximated as,

$$\left(\frac{\partial u}{\partial x}\right)_e = \frac{u_{i+1} - u_i}{x_{i+1} - x_i} \quad (3.20)$$

For the 4CD scheme, the velocity gradients are approximated at the cell faces using fourth-order central differencing as described below. The general four-point Lagrangian interpolation formula for a quantity 'u' can be written as,

$$u = \phi_{i-1}u_{i-1} + \phi_i u_i + \phi_{i+1}u_{i+1} + \phi_{i+2}u_{i+2}, \quad \forall \quad x_{i-1} \leq x \leq x_{i+2} \quad (3.21)$$

where ϕ_{i-1} , ϕ_i , ϕ_{i+1} and ϕ_{i+2} are interpolation functions that are the same as the corresponding coefficients in Eq. (3.18) with x_e replaced by x . The quantity $\partial u/\partial x$ at the east face can then be written as,

$$\left(\frac{\partial u}{\partial x}\right)_e = \left(\frac{\partial \phi_{i-1}}{\partial x}\right)_e u_{i-1} + \left(\frac{\partial \phi_i}{\partial x}\right)_e u_i + \left(\frac{\partial \phi_{i+1}}{\partial x}\right)_e u_{i+1} + \left(\frac{\partial \phi_{i+2}}{\partial x}\right)_e u_{i+2} \quad (3.22)$$

However, since it would be very cumbersome to implement a fourth-order approximation for the viscous fluxes involving cross derivative terms (like $\partial^2 v/\partial x \partial y$), and the modeled sub-grid scale turbulent stresses, a second-order approximation was used to calculate these terms. This is not expected to seriously affect the overall accuracy of the formulation since the magnitude of these terms is expected to be small in the flows of interest. A more careful treatment might be necessary for other complex flows.

3.8 Unsteady Terms and Preconditioning

At low Mach numbers, typical compressible NS formulations tend to become very stiff. As the Mach number tends to zero, the acoustic wave speed tends to infinity. A large difference in the eigenvalues of the system, thus results. The time step gets severely restricted since the allowable time step is inversely proportional to the maximum eigenvalue. The computation of low Mach number flows, thus becomes practically impossible.

Traditionally, very low speed or nearly incompressible flows are computed by solving the incompressible form of the NS equations. But in this case, the continuity equation does not have a time derivative or unsteady term in which the pressure (or density) appears. Therefore it is not possible to solve the system of equations by time advancement in a coupled manner. This situation can be remedied in two ways.

The most popular approach is to solve the momentum equation and the continuity equation in a decoupled manner. Using the continuity and the momentum equations, a Poisson equation for pressure can be derived. The solution algorithm can be set up as follows.

- Using a guessed pressure and velocity field (initial conditions), the momentum equations are solved to get updated velocities.
- Using the new velocities the pressure Poisson equation is solved iteratively, until a converged pressure field is obtained.
- The above steps are repeated until a solution satisfying both the continuity and momentum equations is obtained.

This method was used by Harlow and Welch [1965]. The SIMPLE algorithm developed by Patankar and Spalding [1972] is a similar method, which solves a pressure correction equation instead. The pressure corrections are related to velocity corrections and thus the velocities obtained by solving the momentum equations are also corrected after solving the pressure

correction equation. A revision of the above method called SIMPLER (SIMPLE revised) has also been proposed [Patankar, 1981] which has better convergence properties than SIMPLE.

Another interesting method of solving the incompressible NS equations, albeit in a coupled fashion, is the artificial compressibility method proposed by Chorin [1967]. In this approach, an artificial time derivative term is added to the continuity equation which vanishes at steady state. The nature of the system of equations is altered from an originally elliptic-parabolic system to a hyperbolic system. This makes it feasible to solve the system of equations using any regular time dependent approach. This method has also been successfully used, and, in terms of computational effort is comparable to the other methods. Artificial (or pseudo) time derivative terms can also be added to the unsteady momentum equations which vanish at convergence at each time step, and the original NS equations are recovered.

This artificial compressibility method falls under the purview of the general technique of preconditioning. Preconditioning involves changing the transient nature of the system of equations for efficiently solving the equations, in a way that the original system is recovered at convergence.

To alleviate the stiffness problem of the compressible form of the NS equations at low Mach numbers, a generalized preconditioning technique is applied to change the nature of the system of equations. It was demonstrated by Pletcher and Chen [1993] that essentially incompressible results can be obtained for flows with very low Mach numbers. The convergence of the algorithm was found to be independent of the Mach number. Thus, Eq. (3.15) with the above modification would be written as,

$$[\Gamma'] \frac{\partial \mathbf{W}}{\partial \tau} + [I] \frac{\partial \mathbf{W}}{\partial t} + \frac{1}{\Delta x} (\mathbf{E}_e - \mathbf{E}_w) + \frac{1}{\Delta y} (\mathbf{F}_n - \mathbf{F}_s) + \frac{1}{\Delta z} (\mathbf{G}_t - \mathbf{G}_b) = \mathbf{B} \quad (3.23)$$

where, τ is the pseudo time, and $[\Gamma']$ is the preconditioning matrix that will be described later.

The time derivative terms (pseudo and physical) are discretized differently. Since the pseudo time term vanishes at convergence, only a first-order backward discretization is used.

The physical time term is approximated using a second-order backward discretization. The time integration was performed in a fully implicit manner. The unsteady terms can then be written as,

$$\frac{\partial \mathbf{W}}{\partial \tau} = \frac{\mathbf{W}^{n+1,k+1} - \mathbf{W}^{n+1,m}}{\Delta \tau} \quad (3.24)$$

and

$$\frac{\partial \mathbf{W}}{\partial t} = \frac{3\mathbf{W}^{n+1,k+1} - 4\mathbf{W}^n + \mathbf{W}^{n-1}}{2\Delta t} \quad (3.25)$$

where the superscripts n and k denote the physical and pseudo time levels respectively. Using the above discretizations, Eq. (3.23) can be written as,

$$\begin{aligned} & [\Gamma'] \frac{\mathbf{W}^{n+1,k+1} - \mathbf{W}^{n+1,m}}{\Delta \tau} + [I] \frac{3\mathbf{W}^{n+1,k+1} - 4\mathbf{W}^n + \mathbf{W}^{n-1}}{2\Delta t} \\ & + \frac{1}{\Delta x} (\mathbf{E}_e^{k+1} - \mathbf{E}_w^{k+1}) + \frac{1}{\Delta y} (\mathbf{F}_n^{k+1} - \mathbf{F}_s^{k+1}) + \frac{1}{\Delta z} (\mathbf{G}_t^{k+1} - \mathbf{G}_b^{k+1}) = \mathbf{B}^{k+1} \end{aligned} \quad (3.26)$$

Equation (3.26) represents the discretized equation that needs to be solved. It was also found that for best convergence, different pseudo time steps could be used for the continuity equation and momentum equations, obviously, without affecting the final converged solution.

3.9 Primitive Variables and Linearization

Traditionally, for compressible NS formulations the conserved variables, $[\rho, \rho u, \rho v, \rho w, E_t]$, are chosen as the primary unknowns. In fact, the conserved variables are not always the optimal choice and other sets of variables may be used without incurring any penalty [Chwalowski and Taylor, 1991]. Primitive variables $[p, u, v, w, T]$, as the primary unknowns, are typically used for preconditioned codes [Pletcher and Chen, 1993; Choi and Merkle, 1993], such as the one used in this study. The variation of pressure is generally significant for all flow regimes and hence preferred to density. Shuen et al. [1992] have also shown that at low Mach numbers, the computation of pressure from the equation of state with codes using conserved

variables could result in significant round off errors. It has been demonstrated by Chen and Pletcher [1991] that accurate results can be obtained for a wide range of Mach numbers with a primitive variable approach. For the aforementioned reasons, primitive variables were chosen in this study.

Denoting the vector of primitive variables as \mathbf{U} , Eq. (3.26) can be rewritten as,

$$[\Gamma] \frac{\mathbf{U}^{n+1,k+1} - \mathbf{U}^{n+1,m}}{\Delta\tau} + [T] \frac{3\mathbf{U}^{n+1,k+1} - 4\mathbf{U}^n + \mathbf{U}^{n-1}}{2\Delta t} + \frac{1}{\Delta x}(\mathbf{E}_e^{k+1} - \mathbf{E}_w^{k+1}) + \frac{1}{\Delta y}(\mathbf{F}_n^{k+1} - \mathbf{F}_s^{k+1}) + \frac{1}{\Delta z}(\mathbf{G}_t^{k+1} - \mathbf{G}_b^{k+1}) = \mathbf{B}^{k+1} \quad (3.27)$$

where, $[T]$ is the Jacobian matrix ($= \partial \mathbf{W} / \partial \mathbf{U}$) which can be expanded as,

$$[T] = \begin{bmatrix} \frac{1}{R\bar{T}} & 0 & 0 & 0 & -\frac{\bar{p}}{R\bar{T}^2} \\ \frac{\tilde{u}}{R\bar{T}} & \frac{\bar{p}}{R\bar{T}} & 0 & 0 & -\frac{\bar{p}\tilde{u}}{R\bar{T}^2} \\ \frac{\tilde{v}}{R\bar{T}} & 0 & \frac{\bar{p}}{R\bar{T}} & 0 & -\frac{\bar{p}\tilde{v}}{R\bar{T}^2} \\ \frac{\tilde{w}}{R\bar{T}} & 0 & 0 & \frac{\bar{p}}{R\bar{T}} & -\frac{\bar{p}\tilde{w}}{R\bar{T}^2} \\ \frac{1}{R} & 0 & 0 & 0 & 0 \end{bmatrix} \quad (3.28)$$

At this time, it is appropriate to define the preconditioning matrix $[\Gamma]$ as given below,

$$[\Gamma] = \begin{bmatrix} \frac{1}{\bar{T}} & 0 & 0 & 0 & -\frac{\bar{p}}{R\bar{T}^2} \\ \frac{\tilde{u}}{\bar{T}} & \frac{\bar{p}}{R\bar{T}} & 0 & 0 & -\frac{\bar{p}\tilde{u}}{R\bar{T}^2} \\ \frac{\tilde{v}}{\bar{T}} & 0 & \frac{\bar{p}}{R\bar{T}} & 0 & -\frac{\bar{p}\tilde{v}}{R\bar{T}^2} \\ \frac{\tilde{w}}{\bar{T}} & 0 & 0 & \frac{\bar{p}}{R\bar{T}} & -\frac{\bar{p}\tilde{w}}{R\bar{T}^2} \\ 1 & 0 & 0 & 0 & 0 \end{bmatrix} \quad (3.29)$$

It can be seen that $[\Gamma]$ is similar to $[T]$ except that the first column has been multiplied by the non-dimensional gas constant, R . As the Mach number approaches zero, all the elements in the first column of $[T]$ tend to zero, thus, making it singular. This is because the non-dimensional gas constant is proportional to $1/M^2$. So, multiplying the first column by R remedies the situation. It is also necessary to initialize the pressure to a value having the same order of magnitude as the non-dimensional gas constant, R , for the diagonal elements to be dominant.

Equation (3.27) is a system of non-linear algebraic equations. In order to solve for the primary unknowns using linear algebra, the non-linear terms have to be linearized. For this work, the Newton linearization procedure was used and the terms were linearized with respect to the solution at the previous pseudo time level ($\mathbf{U}^{n+1,k}$). Also, during linearization the equations were written in the "delta" form with the change in the values (i.e. the deltas) becoming the unknowns being solved for. The Newton linearization can be illustrated for a flux vector, \mathbf{E} , as below,

$$\begin{aligned}\mathbf{E}(\mathbf{U}^{k+1}) &= \mathbf{E}(\mathbf{U}^{k+1} + \delta\mathbf{U}) \\ &\approx \mathbf{E}(\mathbf{U}^k) + \left(\frac{\partial\mathbf{E}}{\partial\mathbf{U}}\right)^k \delta\mathbf{U}\end{aligned}\quad (3.30)$$

where, $\delta\mathbf{U}$ is the update that is solved for and $\partial\mathbf{E}/\partial\mathbf{U}$ is the Jacobian matrix.

Carrying out this process for the terms in Eq. (3.27) it can be written as,

$$\begin{aligned}&\left(\frac{1}{\Delta\tau}[\Gamma] + \frac{1}{\Delta t}[T]\right)\delta\mathbf{U} + \sum_{k=1}^3 \frac{1}{\Delta x_k}[\mathbf{A}]^k \delta\mathbf{U}_k \\ &+ \sum_{k=1}^3 \frac{1}{\Delta y_k}[\mathbf{B}]^k \delta\mathbf{U}_k + \sum_{k=1}^3 \frac{1}{\Delta z_k}[\mathbf{C}]^k \delta\mathbf{U}_k = -\mathbf{R}\end{aligned}\quad (3.31)$$

where $[\mathbf{A}]$, $[\mathbf{B}]$, and $[\mathbf{C}]$ are the Jacobian matrices of the flux vectors $[\mathbf{E}]$, $[\mathbf{F}]$, and $[\mathbf{G}]$, respectively, and are the sums of both the inviscid and viscous flux Jacobians written symbolically as,

$$[\mathbf{A}] = [\mathbf{A}_{inu}] + [\mathbf{A}_{vis}]$$

$$[\mathbf{B}] = [\mathbf{B}_{inv}] + [\mathbf{B}_{vis}] \quad (3.32)$$

$$[\mathbf{C}] = [\mathbf{C}_{inv}] + [\mathbf{C}_{vis}]$$

In this linearization process, some terms like the cross derivative viscous stresses and sub-grid scale stresses were lagged (using the values from the previous pseudo time level) to reduce the computational effort involved in setting up the Jacobian matrices. The molecular viscosity was also lagged. It is expected that this will not slow down the convergence as their net contribution is presumed to be small. The full form of the various Jacobians is given in Appendix A.

The quantity \mathbf{R} is the residual vector given by,

$$\begin{aligned} \mathbf{R} = & \frac{3\mathbf{U}^{n+1,k} - 4\mathbf{U}^n + \mathbf{U}^{n-1}}{2\Delta t} \\ & + \frac{1}{\Delta x}(\mathbf{E}_e^k - \mathbf{E}_w^k) + \frac{1}{\Delta y}(\mathbf{F}_n^k - \mathbf{F}_s^k) + \frac{1}{\Delta z}(\mathbf{G}_t^k - \mathbf{G}_b^k) - \mathbf{B}^k \end{aligned} \quad (3.33)$$

Upon comparison with Eq. (3.26), it is observed that the residual vector, \mathbf{R} , represents the discrete form of the NS equations at the previous pseudo time level. At convergence, $\delta\mathbf{U}$ approaches zero and the residual approaches zero, thus satisfying the required discrete form of the NS equations. Hence, it is often the case that the left hand side is discretized using a lower-order approximation as compared to the right hand side. This means that as long as the solution converges, higher-order accuracy is recovered. Typically, the left hand side is discretized using second-order approximations yielding a seven-point stencil. This also explains the summation indices going from 1 to 3 in Eq. (3.31) as the stencil of the left hand discretization is three in each direction.

3.10 Coupled Strongly Implicit Procedure

In order to solve the above linear algebraic system of equations, the coupled strongly implicit procedure (CSIP) of Stone [1968] and Weinstein et al. [1969] was used. This is an approximate LU factorization technique and is an iterative solver.

To illustrate this method briefly, we can write Eq. (3.31) in the following form,

$$\begin{aligned} & A_{i-1,j,k}^w \delta \mathbf{U}_{i-1,j,k} + A_{i,j-1,k}^s \delta \mathbf{U}_{i,j-1,k} + A_{i,j,k-1}^b \delta \mathbf{U}_{i-1,j,k-1} + A_{i,j,k}^w \delta \mathbf{U}_{i,j,k} \\ & + A_{i+1,j,k}^e \delta \mathbf{U}_{i+1,j,k} + A_{i,j,k+1}^n \delta \mathbf{U}_{i,j+1,k} + A_{i,j,k+1}^t \delta \mathbf{U}_{i,j,k+1} = R_{i,j,k} \end{aligned} \quad (3.34)$$

where $A^w \cdots A^t$ are the net coefficient matrices and $\delta \mathbf{U}$ is the vector of unknowns at any point. This set of equations for the whole domain can be written in matrix notation as,

$$[\mathcal{A}] \Delta \mathcal{U} = \mathcal{R} \quad (3.35)$$

The matrix $[\mathcal{A}]$ is a banded septa-diagonal matrix, with each element being a 5×5 block for a three-dimensional problem.

In order to factor the matrix $[\mathcal{A}]$ into lower and upper triangular matrices, an auxiliary matrix $[\mathcal{P}]$ is added to it.

$$[\mathcal{A} + \mathcal{P}] \Delta \mathcal{U} = [\mathcal{P}] \Delta \mathcal{U} + \mathcal{R} \quad (3.36)$$

Since the norm of $[\mathcal{P}]$ is small and it further decreases to zero at convergence, it can be dropped from the right hand side. Representing $[\mathcal{A} + \mathcal{P}]$ in terms of lower and upper triangular matrices ($[\mathcal{L}]$ and $[\mathcal{U}]$) we get,

$$[\mathcal{L}] [\mathcal{U}] \Delta \mathcal{U} = \mathcal{R} \quad (3.37)$$

Details regarding selection of the auxiliary matrix can be found in the above mentioned references. Equation (3.37) can then be solved using forward and backward substitution sweeps.

3.11 Convergence Criteria

For the large eddy simulations, the number of pseudo time iterations was limited such that the L_2 norm of the velocity correction would fall by at least 2 to 3 orders of magnitude. The L_2 norms of pressure and temperature corrections were also checked to make sure that they also reduced by approximately the same orders of magnitude.

3.12 Boundary Conditions

In the Reynolds averaged Navier-Stokes (RANS) approach, since only the time-mean quantities are resolved, the difficulty in prescribing appropriate boundary conditions is not much more than for laminar flow problems. The additional difficulty arises in specifying boundary and initial conditions for the extra turbulent quantities that are being solved for (for example k and ϵ , in the popular two-equation model).

On the other hand with the LES approach, specifying the boundary conditions for the primary unknowns itself is a significant challenge, as the goal is to resolve a spectrum of different turbulent scales. The nature of the turbulence in the domain of interest is obviously greatly influenced by the nature of incoming and/or free-stream turbulence, thus, making it necessary to characterize their features. Unlike the RANS approach, the boundary conditions have to be necessarily time dependent since LES computations are essentially unsteady. In some cases, where the problem is of an initial-value type, it becomes necessary to generate an initial field with artificial fluctuations approximating realistic turbulence. This problem gets aggravated when the flow is more complicated and is inhomogeneous and anisotropic. Prescription of good initial and boundary conditions is still a challenge in LES research. The following section addresses this topic in detail.

3.13 Navier-Stokes Characteristic Boundary Conditions (NSCBC)

A large number of direct and large eddy simulations have used periodic boundary conditions in two or more directions. Upon assumption of periodicity, the computational domain is folded on itself and no boundary conditions are actually required. However, the assumption of periodicity is a limitation on the applications of such simulations. Treatments of inflow and outflow situations without the assumption of periodicity have been smaller in number. Large eddy and direct numerical simulations of compressible formulations and flows depend strongly on the boundary conditions and their treatment. The constraints imposed on the

boundary condition formulations by these simulations, as given in Poinso and Lele [1992], are:

1. Accurate control of wave reflections for compressible formulations of the Navier-Stokes equations is required at the boundaries of the computational domain, unlike the case of steady state computations where in waves have to be eliminated and the behavior of the boundaries is not of interest as long as a steady state result can be obtained. Numerical dissipation often contributes to elimination of waves but in general it is not clear what mechanisms contribute to elimination of waves in different algorithms. Direct and large eddy simulations seek to minimize numerical viscosity, and therefore acoustic waves need to be dealt with by implementation of better non-reflecting or absorbing boundary conditions.
2. Experimental evidence suggests the existence of a strong coupling between acoustic waves and many mechanisms encountered in turbulent flows. Some examples are:
 - (a) Flow instabilities and their growth in non-reacting shear layers (Bechert and Stahl [1988], Ho and Nosseir [1981], Tang and Rockwell [1983])
 - (b) Interactions between turbulent combustion and acoustic waves (Poinso et al. [1987], Poinso and Candel [1987])

Accurate control of the behavior of the computational boundaries is crucial in the simulation of the aforementioned phenomena. Consideration of supersonic outlets eliminates the prescription of variables at the downstream (or outlet) boundary, nevertheless this does not eliminate the upstream propagation of spurious numerical waves. Evidence to the strong numerical coupling mechanisms between the inlet and outlet boundaries leading to non-physical oscillations for the one-dimensional advection equation has been presented by Vichnevetsky and Bowles [1982].

3. For the Euler equations, exact boundary conditions ensuring well-posedness have been derived (Kreiss [1970], Engquist and Majda [1977], Gustafsson and Olinger [1982]). However, for the Navier-Stokes equations the determination of well-posedness for a given set of boundary conditions can only be assessed in simple cases (Gustafsson and Sundström [1978], Olinger and Sundström [1978]).
4. Physical boundary conditions (boundary conditions that specify the known physical behavior of one or more dependent variables) have to be supplemented by additional conditions, called “numerical” boundary conditions (necessary for the numerical method while not being explicitly given by the physics of the problem) to solve for variables that are not specified by the boundary conditions. The numerical conditions have to be viewed as compatibility relations necessitated by the choice of the numerical method and not as boundary conditions. The computational results, thus depend on both the physical and numerical conditions used at the boundaries.

Poinsot and Lele [1992] used theoretical results on the well-posedness of Navier-Stokes boundary conditions (Strikwerda [1977], Dutt [1988]) to develop a precise and robust method to specify boundary conditions satisfying the above constraints. The method was derived using the following criteria:

1. Relax smoothly from the Navier-Stokes equations to the Euler equations if the viscosity reduces to zero. Allow control of different waves that crossed the boundaries
2. Suppress arbitrariness in the construction of boundary conditions by avoiding extrapolation procedures [Moretti, 1981].
3. Specify the number of boundary conditions for the Navier-Stokes equations as given by theoretical analyses of well-posedness (Strikwerda [1977], Dutt [1988])

Detailed description of the principle of the method, strategies to impose characteristic boundary conditions for Euler and Navier-Stokes equations and examples of implementation are

provided in Poinso and Lele [1992]. Essential steps to provide Navier-Stokes characteristic boundary conditions for the domain in consideration are described in the following section drawing heavily upon the work of Poinso and Lele [1992].

3.13.1 Steps to provide NSCBC conditions

3.13.1.1 Inviscid Characteristic Analysis

Recast the system of NS equations, using characteristic analysis to modify the hyperbolic terms corresponding to waves propagating in the direction of interest. For example, if one wants to impose characteristic boundary conditions at the outlet of the backward-facing step geometry as shown, then the equations must be recast modifying the hyperbolic terms corresponding to waves propagating in the x direction. For a spatially developing boundary layer if one wants to impose NSCBC conditions at the top "wall" - then the hyperbolic terms corresponding to the waves propagating in the y direction have to be modified. For completeness, the system of governing equations in this study are recalled:

$$\frac{\partial \bar{p}}{\partial t} + \frac{\partial \bar{p} \tilde{u}_j}{\partial x_j} = 0 \quad (3.38)$$

$$\frac{\partial \bar{p} \tilde{u}_i}{\partial t} + \frac{\partial \bar{p} \tilde{u}_i \tilde{u}_j}{\partial x_j} = -\frac{\partial \bar{p}}{\partial x_i} + \frac{\partial \bar{\sigma}_{ij}}{\partial x_j} - \frac{\partial \tau_{ij}}{\partial x_j} \quad (3.39)$$

$$\frac{\partial}{\partial t}(\bar{\rho} \tilde{T}) + \frac{\partial}{\partial x_j}(\bar{\rho} \tilde{u}_j \tilde{T}) = -\frac{\partial \bar{q}_j}{\partial x_j} - \frac{\partial Q_j}{\partial x_j} \quad (3.40)$$

The boundary located at $x = L$ (Fig. 3.5) is considered. Using characteristic analysis

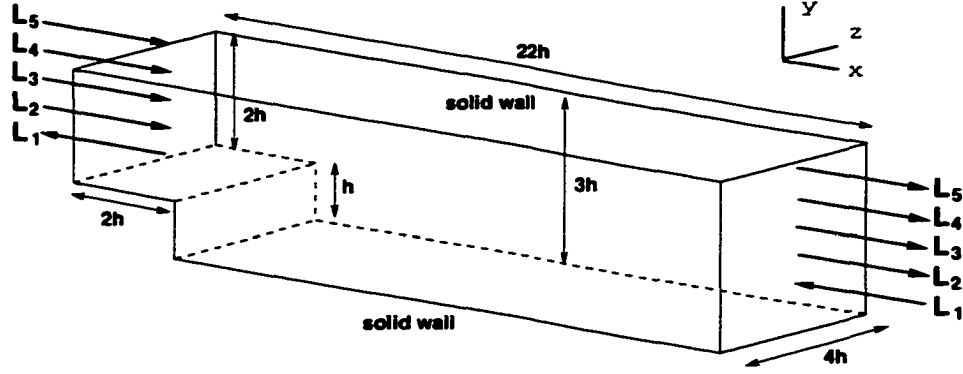


Figure 3.5 Waves entering and leaving the backward-facing step domain

[Thompson, 1987], the system of equations is recast as:

$$\frac{\partial \bar{p}}{\partial t} + d_1 + \frac{\partial \bar{\rho} \tilde{u}_2}{\partial x_2} + \frac{\partial \bar{\rho} \tilde{u}_3}{\partial x_3} = 0 \quad (3.41)$$

$$\frac{\partial \bar{\rho} \tilde{u}_1}{\partial t} + u_1 d_1 + \rho d_3 + \frac{\partial \bar{\rho} \tilde{u}_1 \tilde{u}_j}{\partial x_j} = \frac{\partial \bar{\sigma}_{1j}}{\partial x_j} - \frac{\partial \tau_{1j}}{\partial x_j} \quad (3.42)$$

$$\frac{\partial \bar{\rho} \tilde{u}_2}{\partial t} + u_2 d_1 + \rho d_4 + \frac{\partial \bar{\rho} \tilde{u}_2 \tilde{u}_j}{\partial x_j} = \frac{\partial \bar{\sigma}_{2j}}{\partial x_j} - \frac{\partial \tau_{2j}}{\partial x_j} - \frac{\partial \bar{p}}{\partial x_2} \quad (3.43)$$

$$\frac{\partial \bar{\rho} \tilde{u}_3}{\partial t} + u_3 d_1 + \rho d_5 + \frac{\partial \bar{\rho} \tilde{u}_3 \tilde{u}_j}{\partial x_j} = \frac{\partial \bar{\sigma}_{3j}}{\partial x_j} - \frac{\partial \tau_{3j}}{\partial x_j} - \frac{\partial \bar{p}}{\partial x_3} \quad (3.44)$$

$$\frac{\partial}{\partial t}(\bar{\rho} \tilde{T}) + Ec \frac{d_2}{(\gamma - 1)} + \frac{\partial}{\partial x_j}(\bar{\rho} \tilde{u}_2 \tilde{T}) + \frac{\partial}{\partial x_j}(\bar{\rho} \tilde{u}_3 \tilde{T}) = -\frac{\partial \bar{q}_j}{\partial x_j} - \frac{\partial Q_j}{\partial x_j} \quad (3.45)$$

The system of equations above, contains terms normal to the x_1 boundary (d_1 to d_5), derivatives parallel to the x_1 boundary like $\frac{\partial(\bar{\rho} \tilde{u}_2 \tilde{u}_2)}{\partial x_2}$ and local viscous terms. The vector \mathbf{d} is given by characteristic analysis [Thompson, 1987] and can be expressed as

$$\mathbf{d} = \begin{pmatrix} d_1 \\ d_2 \\ d_3 \\ d_4 \\ d_5 \end{pmatrix} = \begin{bmatrix} \frac{1}{c^2} \left[\mathcal{L}_2 + \frac{1}{2}(\mathcal{L}_5 + \mathcal{L}_1) \right] \\ \frac{1}{2}(\mathcal{L}_5 + \mathcal{L}_1) \\ \frac{1}{2\rho c}(\mathcal{L}_5 - \mathcal{L}_1) \\ \mathcal{L}_3 \\ \mathcal{L}_4 \end{bmatrix} = \begin{bmatrix} \frac{\partial \bar{\rho} \tilde{u}_1}{\partial x_1} \\ \frac{\partial(c^2 \bar{\rho} \tilde{u}_1)}{\partial x_1} + (1 - \gamma) \tilde{u}_1 \frac{\partial \bar{p}}{\partial x_1} \\ u_1 \frac{\partial \tilde{u}_1}{\partial x_1} + \frac{1}{\rho} \frac{\partial \bar{p}}{\partial x_1} \\ \tilde{u}_1 \frac{\partial \tilde{u}_2}{\partial x_1} \\ \tilde{u}_1 \frac{\partial \tilde{u}_3}{\partial x_1} \end{bmatrix} \quad (3.46)$$

where the \mathcal{L}_i 's are the amplitude variations of characteristic waves associated with each characteristic velocity λ_i . These velocities are given by [Thompson, 1987]

$$\lambda_1 = \tilde{u}_1 - c \quad (3.47)$$

$$\lambda_2 = \tilde{u}_1 \quad (3.48)$$

$$\lambda_3 = \tilde{u}_1 \quad (3.49)$$

$$\lambda_4 = \tilde{u}_1 \quad (3.50)$$

$$\lambda_5 = \tilde{u}_1 + c \quad (3.51)$$

where

$$c = \sqrt{\gamma RT} \quad (3.52)$$

λ_1 is the acoustic velocity in negative x_1 direction, λ_2 is the convective velocity, λ_3 is the velocity at which \tilde{u}_2 is advected in the x_1 direction, λ_4 is the velocity at which \tilde{u}_3 is advected in the x_1 direction, and λ_5 is the acoustic velocity in the positive x_1 direction. The \mathcal{L}_i 's are given by

$$\mathcal{L}_1 = \lambda_1 \left(\frac{\partial \bar{p}}{\partial x_1} - \bar{\rho} c \frac{\partial \tilde{u}_1}{\partial x_1} \right) \quad (3.53)$$

$$\mathcal{L}_2 = \lambda_2 \left(c^2 \frac{\partial \bar{p}}{\partial x_1} - \frac{\partial \bar{p}}{\partial x_1} \right) \quad (3.54)$$

$$\mathcal{L}_3 = \lambda_3 \left(\frac{\partial \tilde{u}_2}{\partial x_1} \right) \quad (3.55)$$

$$\mathcal{L}_4 = \lambda_4 \left(\frac{\partial \tilde{u}_3}{\partial x_1} \right) \quad (3.56)$$

$$\mathcal{L}_5 = \lambda_5 \left(\frac{\partial \bar{p}}{\partial x_1} + \bar{\rho} c \frac{\partial \tilde{u}_1}{\partial x_1} \right) \quad (3.57)$$

A physical interpretation of the \mathcal{L}_i 's is provided by Poinsot and Lele [1992] by looking at the linearized Navier-Stokes equations for one-dimensional inviscid acoustic waves. For example, the upstream propagating wave associated to the velocity λ_1 is considered. If p' and u' are the pressure and velocity perturbations, then the wave amplitude given by

$$A_1 = p' - \rho c u' \quad (3.58)$$

is conserved along the characteristic line

$$x - \lambda_1 t = \text{constant} \quad (3.59)$$

so that

$$\frac{\partial A_1}{\partial t} + \lambda_1 \frac{\partial A_1}{\partial x_1} = 0 \quad (3.60)$$

$$\Rightarrow \frac{\partial A_1}{\partial t} + \mathcal{L}_1 = 0 \quad (3.61)$$

Thus, at a given location $-\mathcal{L}_1$ represents the variation in time of the wave amplitude, $(\frac{\partial A_1}{\partial t})$, and therefore termed *amplitude variation* of the characteristic waves crossing the boundary.

The system of equations, as recast, are expressed in terms of wave amplitude variations crossing the boundaries and thereby provide better insight in the derivation of boundary conditions.

It is important to note that with regards to advancing the solution in time on the boundaries using the system of recast equations, most quantities can be estimated using interior points. Parallel terms of the type $\frac{\partial(\bar{\rho} \tilde{u}_2)}{\partial x_2}$, $\frac{\partial(\bar{\rho} \tilde{u}_3)}{\partial x_3}$ can be obtained on the boundary at the same level of approximation as the interior since they do not involve derivatives normal to the boundary. The derivatives normal to the boundary are the set of d_i 's given as functions of the \mathcal{L}_i 's. Of these \mathcal{L}_i 's, the ones corresponding to information propagating from the inside of the domain to the outside can be calculated using interior points and one-sided differences. For the waves propagating into the domain, however, two situations exist:

1. Those where some information about the outside domain is known such that these amplitude variations may be determined. In such cases, an asymptotic solution may be used to describe the solution between the boundary and infinity. For example, if a satisfactory estimate of all gradients at the outlet boundary can be made, as in the case of a self-similar solution for a shear layer, then the \mathcal{L}_i 's can be estimated from these gradients using Eqs. (3.54 - 3.57).

2. Those where such information is unavailable. This is usually the case, and exact values of the incoming wave amplitude variations cannot be obtained. The approach used in the NSCBC technique to obtain such information is by the examination of a local one-dimensional inviscid (LODI) problem.

3.13.1.2 The local one-dimensional inviscid relations

Neglecting transverse and viscous terms in the system of recast equations, Eqs. (3.41 - 3.45), at each point on the boundary yields equations that allow us to infer values for the wave amplitude variations. These relations are viewed as compatibility relations between the choices made for the physical boundary conditions and the amplitudes of the waves crossing the boundary. In terms of the primitive variables, the LODI system is

$$\frac{\partial \bar{p}}{\partial t} + \frac{1}{c^2} \left[\mathcal{L}_2 + \frac{1}{2}(\mathcal{L}_5 + \mathcal{L}_1) \right] = 0 \quad (3.62)$$

$$\frac{\partial \bar{p}}{\partial t} + \frac{1}{2}(\mathcal{L}_5 + \mathcal{L}_1) = 0 \quad (3.63)$$

$$\frac{\partial \tilde{u}}{\partial t} + \frac{1}{2\rho c}(\mathcal{L}_5 - \mathcal{L}_1) = 0 \quad (3.64)$$

$$\frac{\partial \tilde{v}}{\partial t} + \mathcal{L}_3 = 0 \quad (3.65)$$

$$\frac{\partial \tilde{w}}{\partial t} + \mathcal{L}_4 = 0 \quad (3.66)$$

These relations can be combined to express time derivatives of other quantities of interest such as the temperature (\tilde{T}), entropy (s), and enthalpy (h), since they can be expressed in terms of primitive variables as

$$s = C_v \log \frac{\bar{p}}{\bar{\rho}^\gamma} \quad (3.67)$$

$$h = \frac{1}{2} \tilde{u}_i^2 + C_p \tilde{T} \quad (3.68)$$

When boundary conditions are imposed in terms of gradients, it is possible to derive other forms of LODI relations by manipulating Eqs. (3.54 - 3.57) and all gradients normal to the

boundary can be expressed as

$$\frac{\partial \bar{p}}{\partial x_1} = \frac{1}{c^2} + \left[\frac{\mathcal{L}_2}{\tilde{u}_1} + \frac{1}{2} \left(\frac{\mathcal{L}_5}{\tilde{u}_1 + c} + \frac{\mathcal{L}_1}{\tilde{u}_1 - c} \right) \right] \quad (3.69)$$

$$\frac{\partial \bar{p}}{\partial x_1} = \frac{1}{2} \left(\frac{\mathcal{L}_5}{\tilde{u}_1 + c} + \frac{\mathcal{L}_1}{\tilde{u}_1 - c} \right) \quad (3.70)$$

$$\frac{\partial \tilde{u}_1}{\partial x_1} = \frac{1}{2\bar{\rho}c} \left(\frac{\mathcal{L}_5}{\tilde{u}_1 + c} + \frac{\mathcal{L}_1}{\tilde{u}_1 - c} \right) \quad (3.71)$$

$$\frac{\partial \tilde{T}}{\partial x_1} = \frac{\tilde{T}}{\bar{\rho}c^2} + \left[\frac{-\mathcal{L}_2}{\tilde{u}_1} + \frac{1}{2}(\gamma - 1) \left(\frac{\mathcal{L}_5}{\tilde{u}_1 + c} + \frac{\mathcal{L}_1}{\tilde{u}_1 - c} \right) \right] \quad (3.72)$$

Most physical boundary conditions have a counterpart LODI relation, such as the imposition of constant pressure (setting $\frac{\partial \bar{p}}{\partial t} = 0$, in Eq. (3.63) at the inlet should be accompanied by setting $\mathcal{L}_5 = -\mathcal{L}_1$ to fix the amplitude variation of the wave \mathcal{L}_5 entering the domain. Note that the LODI relations are used only to estimate the incoming wave amplitude variations, and that the boundary variables will be advanced in time using the system of equations, Eqs. (3.41 - 3.45), and the viscous and parallel terms will effectively be taken into account.

3.13.1.3 NSCBC strategy for the NS equations

As an example, we consider the case of a subsonic outlet boundary with an imposed static pressure. The procedure consists of the following steps:

1. For each inviscid physical boundary condition on this boundary, the corresponding conservation equations from the system of equations, Eqs. (3.41 - 3.45), are eliminated. For the constant pressure outlet, \bar{p} is specified and Eq. (3.45) is eliminated.
2. For each inviscid boundary condition, the corresponding LODI relation is used to express the unknown \mathcal{L}_i 's (corresponding to incoming waves) as a function of the known \mathcal{L}_i 's (corresponding to outgoing waves). The only incoming wave for the case of specified outlet pressure is \mathcal{L}_1 , and LODI relation Eq. (3.63) implies

$$\mathcal{L}_1 = -\mathcal{L}_5 - 2 \frac{dP}{dt} \quad (3.73)$$

where $p(x_1 = L, x_2, x_3, t) = P(x_2, x_3, t)$. \mathcal{L}_5 can be computed from interior points using one-sided differences and \mathcal{L}_1 is the amplitude variation of the acoustic wave entering the domain through the outlet at a velocity of $\lambda_1 = \bar{u}_1 - c$, and is given by Eq. (3.73).

3. The remaining conservation equations of the system, Eqs. (3.41 - 3.45) are combined with the values of the \mathcal{L}_i 's obtained from Step 2 to compute all variables of interest not given by the inviscid boundary conditions. For the case in consideration here, the density and velocities will be given by Eqs. (3.41, 3.43, 3.44, 3.45), where Eq. (3.73) is used to evaluate the incoming amplitude variation.

Three other conditions have to be added, as suggested by Strikwerda [1977]. Several choices were tested by Poinso and Lele [1992] and they recommend the following choice:

$$\frac{\partial \tau_{12}}{\partial x_1} = 0 \quad (3.74)$$

$$\frac{\partial \tau_{13}}{\partial x_1} = 0 \quad (3.75)$$

$$\frac{\partial q_1}{\partial x_1} = 0 \quad (3.76)$$

i.e., setting spatial derivatives of the tangential viscous stresses and the normal heat flux to zero.

The specific implementations for the boundary conditions used for the backward-facing step geometry in this study will be addressed in the following section.

3.14 Boundary Conditions for the Flow Past a Backward-Facing Step

Boundary conditions used for the LES of the backward-facing step (Fig. 3.5) need to be prescribed in the

1. Streamwise direction:

(a) at the inflow, $\frac{x}{h} = -2$

(b) at the outflow, $\frac{x}{h} = 20$

2. Wall-normal direction:

(a) top wall, $\frac{y}{h} = 2$

(b) bottom wall, $\frac{y}{h} = -1$

3. Spanwise direction

(a) at $\frac{z}{h} = 0$

(b) at $\frac{z}{h} = 1.28 \pi h$

3.14.1 Streamwise boundary conditions

1. Inflow:

$$\tilde{u}_1(-2, x_2, x_3, t) = u(x_2, x_3, t) \quad (3.77)$$

$$\tilde{u}_2(-2, x_2, x_3, t) = v(x_2, x_3, t) \quad (3.78)$$

$$\tilde{u}_3(-2, x_2, x_3, t) = w(x_2, x_3, t) \quad (3.79)$$

where $u(x_2, x_3, t)$, $v(x_2, x_3, t)$, $w(x_2, x_3, t)$ are the velocities in a $x - z$ plane stored from the large eddy simulation of the turbulent flow in a plane channel (see Section 4.3).

At the inlet, in order to enforce a constant mass flow rate, a constant density condition was used

$$\bar{\rho} = \text{constant} \quad (3.80)$$

$$\Rightarrow \frac{\bar{p}}{RT} = \text{constant} \quad (3.81)$$

Upon linearization of the above expression using a Newton linearization approach, one obtains

$$\frac{1}{R\bar{T}} \Delta \bar{p} - \frac{\bar{p}}{R\bar{T}^2} \Delta T = 0 \quad (3.82)$$

The pressure was extrapolated from the interior at the inlet using a zeroth order extrapolation.

2. **Outflow:** In the case of subsonic flows, waves reflecting on regions far from the computational domain where some static pressure p_∞ is specified are responsible for conveying information from the outside of the domain to the interior. This information helps the flow determine the mean pressure. Hence, partially non-reflecting boundary conditions as opposed to perfectly non-reflecting boundary conditions are desirable. Imposing the static pressure at the outlet, $p = p_\infty$ leads to a well-posed problem which, however, creates acoustic wave reflections. We would like to provide some physical information on the mean static pressure p_∞ so that the problem remains well-posed. After the waves have left the computational domain, the pressure at each point at the outlet is expected to be close to p_∞ . The following steps of the NSCBC procedure provide such conditions at the outflow boundary.

- (a) The physical boundary condition is that the static pressure at infinity is imposed. Since this condition does not fix any of the dependent variables in the system, all the conservation equations of the system, Eqs. (3.41 - 3.45) are retained. We also note that four characteristic waves, $\mathcal{L}_2, \mathcal{L}_3, \mathcal{L}_4, \mathcal{L}_5$ leave the computational domain and \mathcal{L}_1 enters the domain at the speed of $\lambda_1 = \bar{u}_1 - c$.
- (b) The condition of constant pressure at infinity is used to obtain the amplitude variation \mathcal{L}_1 of the incoming wave. If the outlet pressure is not close to p_∞ , reflected waves will enter the domain through the outlet to bring the mean pressure to a value close to p_∞ . Thus, a simple way to ensure well posedness [Poinsot and

Lele, 1992] is:

$$\mathcal{L}_1 = K(p - p_\infty) \quad (3.83)$$

$$\text{where } K = \frac{\sigma(1 - M^2)c}{L} \quad (3.84)$$

where M is the maximum Mach number in the flow, σ is a constant, L is a characteristic size of the domain, and K is a constant. For $\sigma = 0$, the amplitude of reflected waves is set to zero, and perfectly non-reflecting conditions are thus obtained. The viscous conditions require that the spatial derivatives of the tangential stresses τ_{12} , τ_{13} , and normal heat flux q_1 be set to zero.

- (c) All other \mathcal{L}_i 's can be estimated from interior points and the system of equations, Eqs. (3.41 - 3.45) are used to advance the solution in time on the boundary.

3.14.2 Wall-normal boundary conditions

1. Top and bottom walls:

- (a) Isothermal no-slip wall At the isothermal no-slip wall, all the velocities and the normal pressure gradient are set to zero.

$$\tilde{u} = 0 \quad (3.85)$$

$$\tilde{v} = 0 \quad (3.86)$$

$$\tilde{w} = 0 \quad (3.87)$$

$$\tilde{T} = 1 \quad (3.88)$$

$$\frac{\partial p}{\partial y} = 0 \quad (3.89)$$

- (b) Adiabatic no-slip wall The equations from an inviscid characteristic analysis now need to be derived corresponding to waves in the wall normal direction. The final

form of the equations is

$$\frac{\partial \bar{\rho}}{\partial t} + \frac{\partial \bar{\rho} \tilde{u}_1}{\partial x_1} + d_1 + \frac{\partial \bar{\rho} \tilde{u}_3}{\partial x_3} = 0 \quad (3.90)$$

$$\frac{\partial \bar{\rho} \tilde{u}_1}{\partial t} + \frac{\partial \bar{\rho} \tilde{u}_1 \tilde{u}_1}{\partial x_1} + u_1 d_1 + \rho d_3 + \frac{\partial \bar{\rho} \tilde{u}_1 \tilde{u}_3}{\partial x_3} = \frac{\partial \bar{\sigma}_{1j}}{\partial x_j} - \frac{\partial \tau_{1j}}{\partial x_j} - \frac{\partial \bar{p}}{\partial x_1} \quad (3.91)$$

$$\frac{\partial \bar{\rho} \tilde{u}_2}{\partial t} + \frac{\partial \bar{\rho} \tilde{u}_2 \tilde{u}_1}{\partial x_1} + u_2 d_1 + \rho d_4 + \frac{\partial \bar{\rho} \tilde{u}_2 \tilde{u}_3}{\partial x_3} = \frac{\partial \bar{\sigma}_{2j}}{\partial x_j} - \frac{\partial \tau_{2j}}{\partial x_j} \quad (3.92)$$

$$\frac{\partial \bar{\rho} \tilde{u}_3}{\partial t} + \frac{\partial \bar{\rho} \tilde{u}_3 \tilde{u}_1}{\partial x_1} + u_3 d_1 + \rho d_5 + \frac{\partial \bar{\rho} \tilde{u}_3 \tilde{u}_3}{\partial x_3} = \frac{\partial \bar{\sigma}_{3j}}{\partial x_j} - \frac{\partial \tau_{3j}}{\partial x_j} - \frac{\partial \bar{p}}{\partial x_3} \quad (3.93)$$

$$\frac{\partial}{\partial t}(\bar{\rho} \tilde{T}) + \frac{\partial}{\partial x_j}(\bar{\rho} \tilde{u}_1 \tilde{T}) + Ec \frac{d_2}{(\gamma - 1)} + \frac{\partial}{\partial x_j}(\bar{\rho} \tilde{u}_3 \tilde{T}) = -\frac{\partial \bar{q}_j}{\partial x_j} - \frac{\partial Q_{ej}}{\partial x_j} \quad (3.94)$$

At an adiabatic no-slip wall, all velocity components vanish and the heat flux is zero.

$$\tilde{u} = 0 \quad (3.95)$$

$$\tilde{v} = 0 \quad (3.96)$$

$$\tilde{w} = 0 \quad (3.97)$$

$$q_2 = -k \frac{\partial \tilde{T}}{\partial y} = 0 \quad (3.98)$$

The steps of the NSCBC procedure are:

- i. Since the velocities \tilde{u} , \tilde{v} , \tilde{w} are fixed ($= 0$), Eqs. (3.42, 3.43, 3.44) are not needed.
- ii. From LODI relations 3.64, 3.65, 3.66,

$$\mathcal{L}_1 = \mathcal{L}_5 \quad (3.99)$$

$$\mathcal{L}_3 = 0 \quad (3.100)$$

$$\mathcal{L}_4 = 0 \quad (3.101)$$

$$(3.102)$$

Also, from Eq. (3.55), $\mathcal{L}_2 = 0$, since the normal velocity \tilde{v} equal to zero.

iii. \mathcal{L}_5 can be computed from interior points and \mathcal{L}_1 is set equal to \mathcal{L}_5 in the system of Eqs. (3.90 - 3.94). The continuity equation is reduced as follows:

$$\frac{\partial \bar{\rho}}{\partial t} + d_1 = 0 \quad (3.103)$$

$$\frac{\partial \bar{\rho}}{\partial t} + \frac{\mathcal{L}_5}{c^2} = 0 \quad (3.104)$$

$$\frac{\partial \bar{\rho}}{\partial t} + \frac{1}{c^2} \left[(\tilde{v} + c) \left(\frac{\partial \bar{\rho}}{\partial y} + \bar{\rho} c \frac{\partial \tilde{v}}{\partial y} \right) \right] = 0 \quad (3.105)$$

$$\frac{\partial \bar{\rho}}{\partial t} + \frac{1}{c} \frac{\partial \bar{\rho}}{\partial y} + \bar{\rho} \frac{\partial \tilde{v}}{\partial y} = 0 \quad (3.106)$$

and the energy equation to:

$$\frac{\partial \bar{\rho} \tilde{T}}{\partial t} + Ec \frac{\mathcal{L}_5}{\gamma - 1} = 0 \quad (3.107)$$

$$\frac{\partial \bar{\rho} \tilde{T}}{\partial t} + Ec \left[\frac{c}{\gamma - 1} \frac{\partial \bar{\rho}}{\partial y} + \frac{\bar{\rho} c^2}{\gamma - 1} \frac{\partial \tilde{v}}{\partial y} \right] = 0 \quad (3.108)$$

(c) No-slip wall with specified heat flux For the case of a wall with specified heat flux, the modification to the above equation would be in the right hand side to account for the heat flux term, as follows:

$$\frac{\partial \bar{\rho} \tilde{T}}{\partial t} + Ec \left[\frac{c}{\gamma - 1} \frac{\partial \bar{\rho}}{\partial y} + \frac{\bar{\rho} c^2}{\gamma - 1} \frac{\partial \tilde{v}}{\partial y} \right] = -\frac{\partial q_2}{\partial x_2} \quad (3.109)$$

3.14.3 Spanwise boundary conditions

Periodic boundary conditions were used in the spanwise direction for the velocities, pressure and temperature.

CHAPTER 4 LES OF ISOTHERMAL TURBULENT FLOW

4.1 Introduction

The finite volume LES formulation described in the earlier chapter is used to simulate the isothermal turbulent flow past a backward facing step. The geometry of the domain of interest, initial and boundary conditions, and relevant simulation details will be described in the following sections of this chapter. Inflow conditions for the turbulent flow past the backward facing step were provided by supplying planes of data stored from an independent fully developed turbulent channel flow simulation described in Section 4.3. Results from this simulation are compared to experimental data, and an analysis of these results will be presented in Section 4.5.

4.2 Problem Description

The flow of interest is the isothermal turbulent flow past a single-sided backward-facing step as shown in Fig. 4.1. All dimensions are normalized by the step height, h . The computational case was designed to match the experimental setup of Kasagi and Matsunaga [1995] as closely as possible. The experiments of Kasagi and Matsunaga [1995] are amongst the latest available results in the literature for a backward facing step flow, and more importantly the condition upstream of the step was well defined as a fully developed turbulent channel flow. This was done to ensure that no calculation would suffer from incompleteness or ambiguity in the upstream boundary conditions. The height of the backward-facing step was

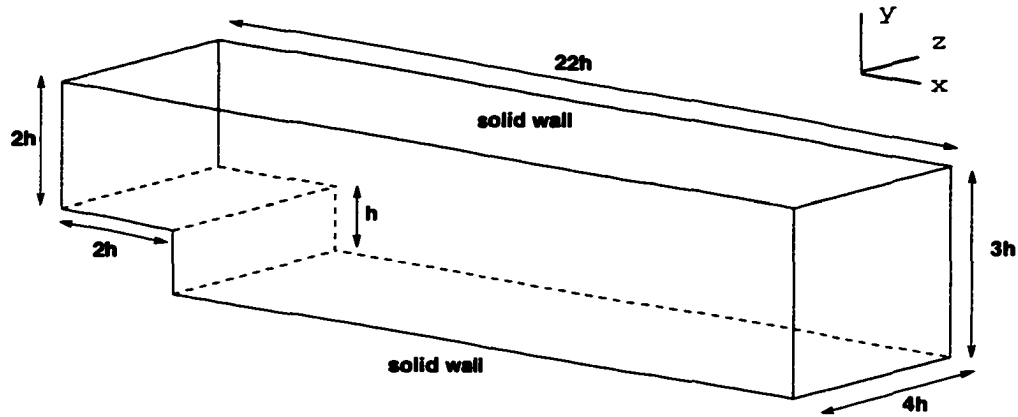


Figure 4.1 Backward-facing step geometry

41 mm, and the upstream section had a height of 82 mm. The resulting expansion ratio was 1.5. The Reynolds number based on the upstream centerline velocity and the step height, $Re_h (= \frac{U_{ref} h}{\nu})$ was 5540. The temperature of the water in the experimental setup, and the temperature of the air in the numerical simulations was maintained at 293K. Reference values of other relevant variables were $U = 2.063$ m/s, $k = 25.74 \times 10^{-3}$ W/m K, $h = 0.041$ m, $\nu = 15.27 \times 10^{-6}$ m²/s, and $\rho = 1.194$ kg/m³.

In the experiments, the outflow boundary was located at about 165 step heights, and the spanwise width was 20 step heights. Constructing an exact computational counterpart would result in an extremely expensive calculation, and is unnecessary; the onus therefore shifts to the provision of carefully constructed boundary conditions, as discussed in the earlier chapter. Based on previous backward-facing step studies (Friedrich and Arnal [1990], Akselvoll and Moin [1995], Le and Moin [1994]), it was determined that the outflow boundary condition for the computational case would be located at 20 step heights and a spanwise width of 4 step heights would be chosen. The outflow boundary was located far enough so as not to hinder the development of the separation bubble and the subsequent growth of the boundary layer flow. Compressible formulations of the NS equations, unlike incompressible formulations, allow for finite acoustic speeds and are therefore prone to acoustic wave reflections from approximate treatments of boundaries or from inappropriate choices of their location.

Acoustic wave reflections are effectively controlled through the implementation of the Navier-Stokes characteristic boundary conditions [Poinsot and Lele, 1992]. The spanwise width was chosen to be sufficiently large to allow for vortex stretching since vorticity dynamics plays an important role in the sustenance and production of turbulence. Evidence from previous studies suggests that lack of sufficient resolution in the spanwise direction might have contributed to lack of agreement between experimental results and numerical calculations. The use of periodic boundary conditions in the spanwise direction for the computational case is justifiable on the basis that the mean flow is negligible in that direction.

For large eddy and direct numerical simulations the prescription of accurate initial and “realistic” inflow conditions is often crucial to the success of the simulation. The importance of realistic turbulent inflow conditions cannot be overemphasized for the case of spatially developing flows such as the case of the backward facing step flow, unlike the channel flow, where periodic boundary conditions can be specified.

In this study, accurate inflow conditions were made available by way of large eddy simulation of the turbulent flow in a plane channel. The plane channel geometry corresponds to the upstream section of the backward-facing step. For each time step of the backward-facing step simulation, a plane of data stored from the channel simulation was supplied suitably upstream of the step, at a distance of 2 step heights, to allow for adjustment of the variables to the new flow conditions. The large eddy simulation of the turbulent plane channel flow is described in the following section.

4.3 Large Eddy Simulation of Turbulent Flow in a Channel

Large eddy simulations of the turbulent flow in a channel were performed in order to address the following issues:

1. development of a stable colocated grid scheme

2. provision of “realistic” inflow conditions for the backward facing step

Wang [1995] conducted a comparison of various central difference (second-order, fourth-order) and upwind schemes, both in the staggered and colocated grid frameworks. In the colocated-grid framework, the central difference schemes were unstable for the “simple” turbulent incompressible planar channel flow. For more complex flows, even the upwind colocated-grid scheme was not able to sustain the computation long enough. On the other hand, the staggered grid algorithms performed satisfactorily for the incompressible channel flow case. The central difference schemes produced better results than the upwind schemes in terms of the mean and the statistical quantities. Again, for more complex flows, the staggered central difference schemes were found to be unstable. The combination of upwinding and the staggered grid seemed to give the most robust algorithm for the simulations.

The issue of the instability of the central difference schemes observed by Wang [1995] for his large eddy simulations of a planar channel was successfully addressed by Narayanan [1998] (see Section 3.6). The cause was traced to the method used to compute the cell-face convective fluxes. It was found that calculating the cell-face fluxes using interpolated values of the primitive variables was more effective in controlling the aliasing errors. With this improvement, channel flow simulations have been performed using both the second-order and the fourth-order central difference colocated-grid schemes. Sixth-order compact filtering [Lele, 1992] was used to contain oscillations from pressure-velocity decoupling peculiar to colocated grid schemes; however, in the case of the turbulent channel flow such oscillations were not found and hence there was no need to “switch on” the filtering mechanism. In addition to validation of the central difference schemes, these channel flow simulations were of significant value in having provided inflow conditions for the backward facing step.

4.3.1 Problem description, simulation details, and results

The computational case was designed to match the inlet section of the experimental case performed by Kasagi and Matsunaga [1995]. The streamwise, wall normal and spanwise dimensions of the channel are $2\pi\delta \times 2\delta \times \pi\delta$ respectively, where δ is the channel half height. The Reynolds number based on the channel half height and centerline velocity was 5540. Periodic boundary conditions were used in the streamwise and spanwise directions, and no-slip conditions at the top and bottom walls.

Often, for turbulent channel flow simulations, the streamwise pressure gradient parameter is adjusted [Benocci and Pinelli, 1990] at each time step to provide the desired mass flow rate as

$$\beta^{n+1} = \beta^n - \frac{1}{\Delta t} \left[\left(\frac{\dot{m}}{A_c} \right)^0 - 2 \left(\frac{\dot{m}}{A_c} \right)^n + \left(\frac{\dot{m}}{A_c} \right)^{n-1} \right] \quad (4.1)$$

where \dot{m}^n is the average mass flow rate for the channel at time level n , Δt is the physical time step, and A_c is the cross-flow area of the channel. The average mass flow rate is given by

$$\frac{\dot{m}}{A_c} = \frac{1}{L_y L_z} \int_{-1}^1 \langle \rho u \rangle_{x,z} dy \quad (4.2)$$

where $\langle \rangle_{x,z}$ denotes an ensemble average in the streamwise and spanwise directions. The desired mass flow rate is given by $\left(\frac{\dot{m}}{A_c} \right)^0$.

The Mach number for the flow was 0.006, and the non-dimensional real time step used was 0.03, with 6-8 pseudo time steps being used within each real time step. Uniform grid spacing was used in the streamwise and spanwise directions, while a hyperbolic tangent stretching (see Sec. 3.4) scheme was used for the grid spacing in the wall-normal direction. The grid resolution in regular coordinates and wall coordinates, based on the experimental friction velocity u_τ of 0.052, or $Re_\tau = 290$, is given in Table 4.3.1.

The nondimensional experimental value of the friction velocity, u_τ , upstream of the step was 0.052, while a value of 0.05 was obtained from the simulations with the fine grid resolu-

Table 4.1 Grid spacing

Grid	Streamwise spacing		Spanwise spacing		Wall-normal spacing			
	Δx	Δx^+	Δz	Δz^+	Δy	Δy_{min}^+	Δy	Δy_{max}^+
65 × 65 × 65	0.096	28.043	0.0483	14.007	0.0058	1.682	0.0496	14.384
81 × 81 × 81	0.077	22.495	0.0387	14.007	0.0041	1.189	0.0414	12.006
48 × 31 × 48	0.130	37.960	0.0654	18.980	0.0073	2.117	0.1318	38.220

tion. Results from the simulation are compared to the DNS results of Kim et al. [1987] and the experimental results of Kasagi and Matsunaga [1995] and those of Niederschulte et al. [1990]. The DNS results were obtained by Kim et al. [1987] from the solution of the incompressible unsteady Navier-Stokes equations using about 4×10^6 grid points ($192 \times 129 \times 160$ in x, y, z) for a channel with nondimensional lengths of 4π , 2, and 2π in the streamwise, wall-normal and spanwise directions, respectively. The Reynolds number Re_δ was 2,800 where $Re_\delta = \frac{u_b \delta}{\nu_b}$ where u_b is the bulk velocity and ν_b is the viscosity based on bulk properties. The experiments of Niederschulte et al. [1990] were performed specifically for comparison with Kim et al. [1987] direct numerical simulations, and the flow parameters were therefore similar. The experimental results of Kasagi and Matsunaga [1995] are those from the upstream channel section of the backward-facing step setup, unlike the simulations that are of an independent channel. An obvious influence upstream due to the presence of the step in the case of the experimental results is therefore expected (Note: For the mean streamwise velocity, experimental results of Kasagi and Matsunaga [1995] are not shown owing to some difficulties in manipulating the data). The mean streamwise velocity profiles are shown in wall coordinates in Fig. 4.2. The mean velocity u is normalized by the friction velocity u_τ ($= \sqrt{\frac{\tau_w}{\rho_w}}$) to yield the mean velocity in wall coordinates, u^+ . The law of the wall and the log law are represented on the plot in dash-dot lines. Good agreement between the results from the fine grid simulations, the experiments of Niederschulte et al. [1990] and the DNS results of Kim et al. [1987] is observed.

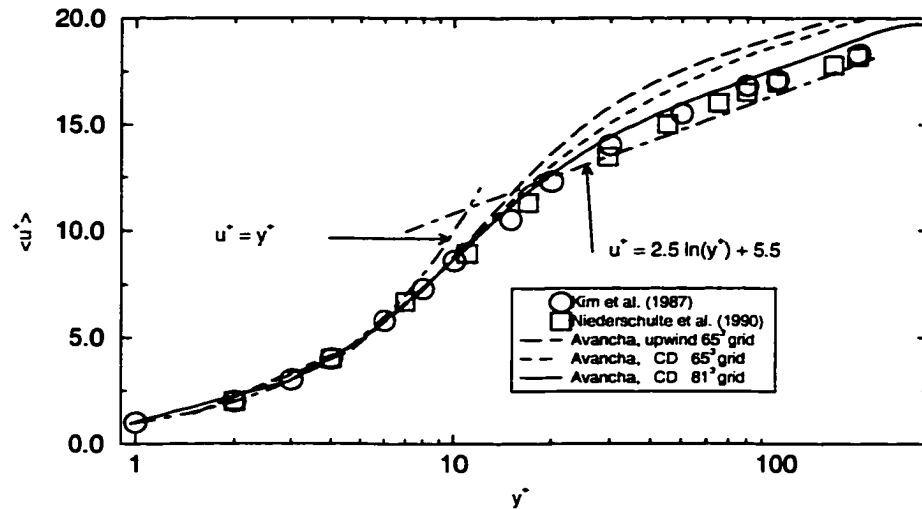


Figure 4.2 Law of the wall plot

The root mean square velocity fluctuations are shown in Figs. 4.3, 4.4, 4.5. For the streamwise velocity fluctuations, good agreement between the results from the fine grid simulations and the experiments of Kasagi and Matsunaga [1995] and Niederschulte et al. [1990], and the DNS results of Kim et al. [1987] is observed. However, with the wall-normal and spanwise RMS velocity fluctuations, the characteristic underprediction, especially at the center of the channel is observed. As mentioned earlier, the experimental results of Kasagi and Matsunaga [1995] are obviously influenced by the presence of the step downstream.

Planes of data from this fully developed turbulent channel flow simulation were stored for 1000 time steps and were used to supply inflow conditions for the step.

4.4 Simulation Details: Flow Past a Backward-Facing Step

A grid resolution of $72 \times 46 \times 48$ was used in the streamwise, wall normal and spanwise directions for the post step section. The upstream channel resolution was $16 \times 31 \times 48$. While the grid was uniform in the spanwise direction, it was stretched in the streamwise and wall normal directions using a hyperbolic tangent stretching as described in Sec. 3.4. Owing to the significant computational expenses involved, simulations on different grid resolutions

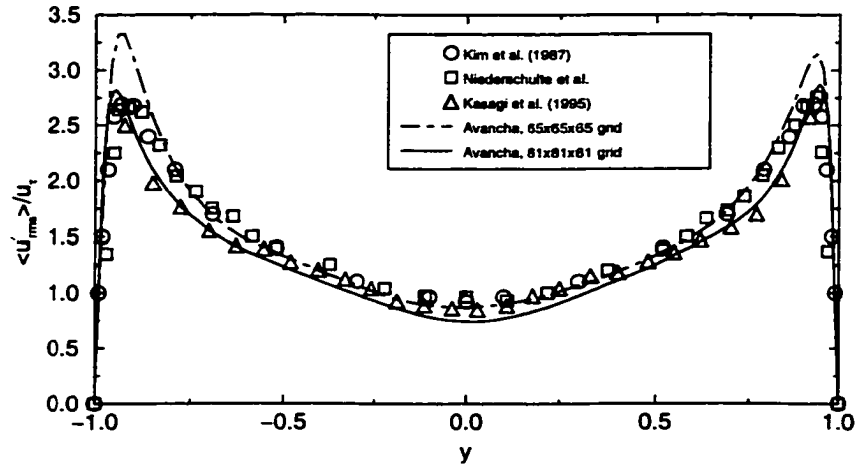


Figure 4.3 Streamwise RMS velocity profile

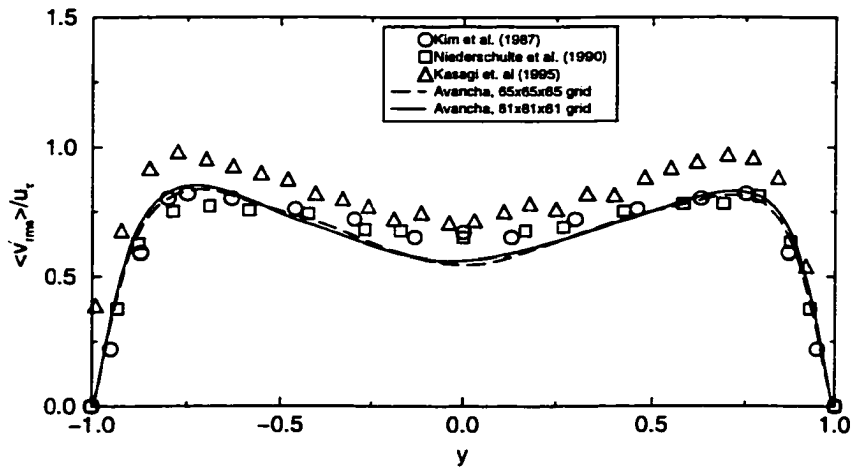


Figure 4.4 Wall-normal RMS velocity profile

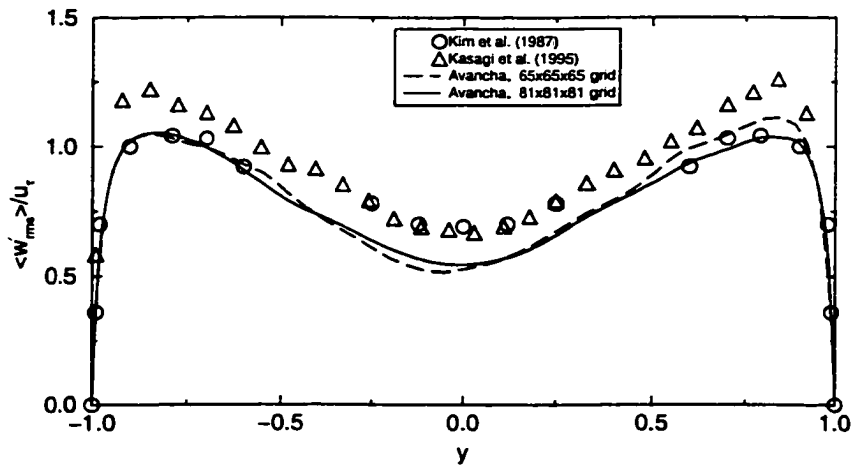


Figure 4.5 Spanwise RMS velocity profile

Table 4.2 Grid resolution used by Akselvoll and Moin [1995]

Case ID	N_x	N_y	N_z
DMX1	70	48	32
DMBA	112	48	32
DMX2	230	48	32
DMZ1	112	48	16
DMY1	112	29	32

were unaffordable. However, the literature was reviewed thoroughly and the grid resolution used for this study was arrived at after a careful consideration of the results from large eddy simulations conducted by Akselvoll and Moin [1995]. The backward-facing step geometry in their study was the lower half of a double-sided backward facing step, with an expansion ratio of 1.2. The Reynolds number was 5100 based on the step height h , and the inlet freestream velocity.

They tested different grid resolutions as shown in Table 4.4, and found that decreasing the number of points, in the wall-normal direction (case DMY1) as compared to the case DMX1, adversely affected results in the recirculation region. This is in contrast to only a minor improvement, in the mean velocity profiles and turbulent statistics, when the number of points in the streamwise direction was doubled or tripled (cases DMBA and DMX2). They further concluded that the accuracy of the LES with the case DMX1 was most likely adequate for practical engineering purposes. Their conclusions and results played an important role in the choice of the grid resolution for this study.

Planes of inflow data were interpolated from an originally computed turbulent channel flow on a $81 \times 81 \times 81$ grid. A non-dimensional physical time step of 0.03 was used for the simulations, and turbulent statistics were accumulated for roughly 5000 time steps - corresponding to 7 flow through times. Using the same non-dimensional real time step as used for the turbulent channel flow simulations eliminated the need for any interpolation

in time of the database of inflow conditions. A Mach number of 0.006 was used. The Navier-Stokes boundary condition strategy was employed to provide boundary conditions at all boundaries (see Sec. 3.14). Periodic boundary conditions were employed in the spanwise direction. Pressure velocity decoupling was effectively curbed by use of a sixth-order compact filtering procedure [Lele, 1992].

4.5 Results and Discussion

4.5.1 Mean velocity distributions

The streamwise, wall normal and spanwise mean velocity distributions from the simulation are in excellent agreement with experimental distributions for streamwise locations available in the database, as shown in Figs. 4.7, 4.8 and 4.9. A steep vertical gradient of the velocity can be observed immediately downstream of separation, which weakens towards the reattachment point. In the recirculating region behind the step, the streamwise velocities have appreciable negative values close to wall at $x/h = 2 \sim 4$, the maximum reverse flow velocity being $0.24 U_c$, as compared to $0.2 U_c$ in the experiment. Owing to the shear layer developing behind the step, the wall normal mean velocity distribution attains negative and positive peak values, the peak negative value being about $0.08 U_c$ at $x/h = 3.5$ and $y/h = 0.1$. Farther downstream, the wall normal mean velocity distribution becomes uniformly negative. The mean spanwise velocities are very close to zero. Along the entire streamwise distance, the mass flow rate is constant to within $\pm 2\%$ and there is no appreciable streamwise bulk flow acceleration due to the developing wall boundary layers. From a plot of the mean streamline (Fig. 4.6), the center of the recirculating region can be inferred to be located at $x/h \sim 2$. The contour levels on the mean streamline plot indicate magnitudes of the streamwise velocity. The experimental results of Kasagi and Matsunaga [1995], however, place the center of the recirculating region at $x/h \sim 3$. The reason for this discrepancy is not very clear, since the mean reattachment point from the simulation is $6.1 x/h$ as

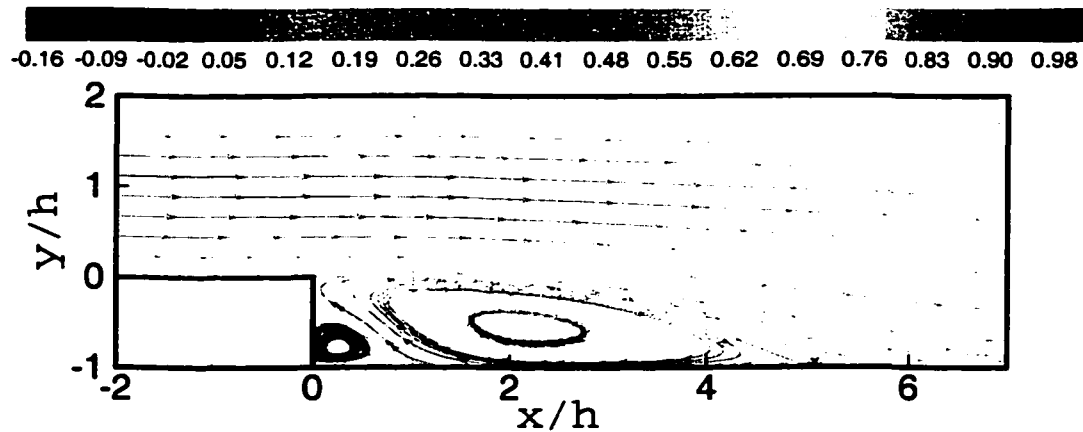


Figure 4.6 Streamline of mean velocity

opposed to that from the experiments, of $6.51 x/h$ - a disagreement of about 7%. A secondary recirculating region - near the corner of the step, in both the experiments and the simulations are nearly at the same locations.

4.5.2 Reattachment length

For the flow past a backward facing step, the point of flow separation is fixed at the step shoulder; the fact that the reattachment point is a function of time is clearly elucidated in Fig. 4.10. Eaton and Johnston [1980] found that the “flapping” of the shear layer normal to the wall causes its impingement point to move slowly back and forth over a range of ± 1 step height. Friedrich and Arnal [1990] also observed this behavior in their simulations. The oscillatory behavior of this reattachment location is observed from a study of the animation of streamwise velocity.

Le and Moin [1994] argue that the growth of large scale structures from the rolling of the shear layer and their subsequent collapse is the reason for the saw tooth shape of the x_r vs. t plot. The sudden drop in x_r is indicative of the collapse of a large scale structure, and a single reattachment point cannot be well defined, but small fragments of forward and reverse flow regions are scattered from $(x_r)_{min}$ to $(x_r)_{max}$ for all such occurrences. This

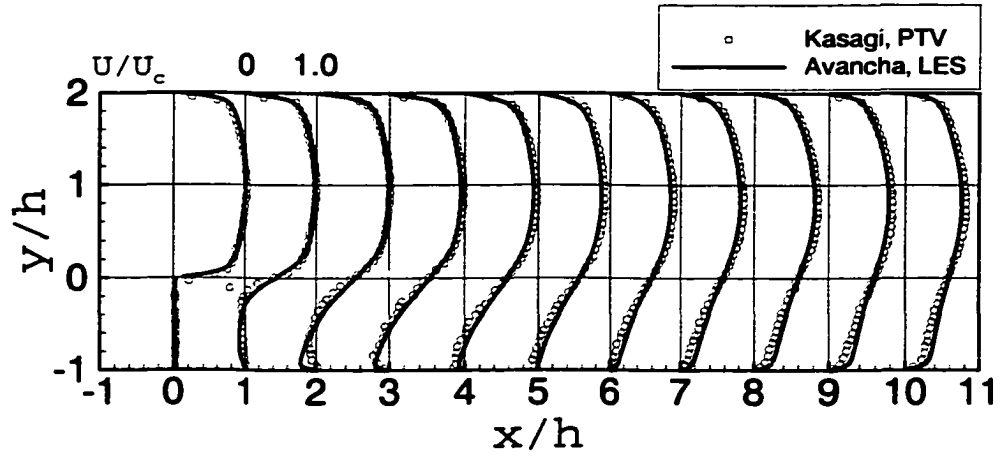


Figure 4.7 Streamwise mean velocity profiles

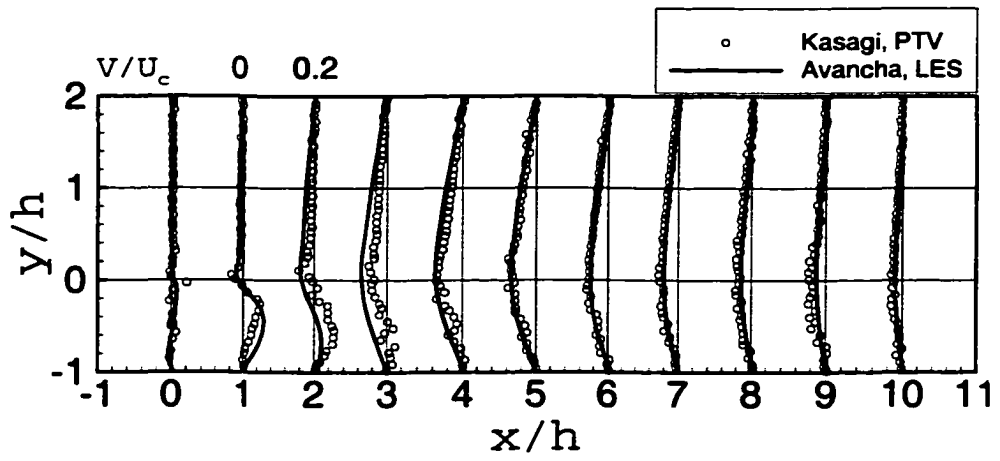


Figure 4.8 Wall-normal mean velocity profiles

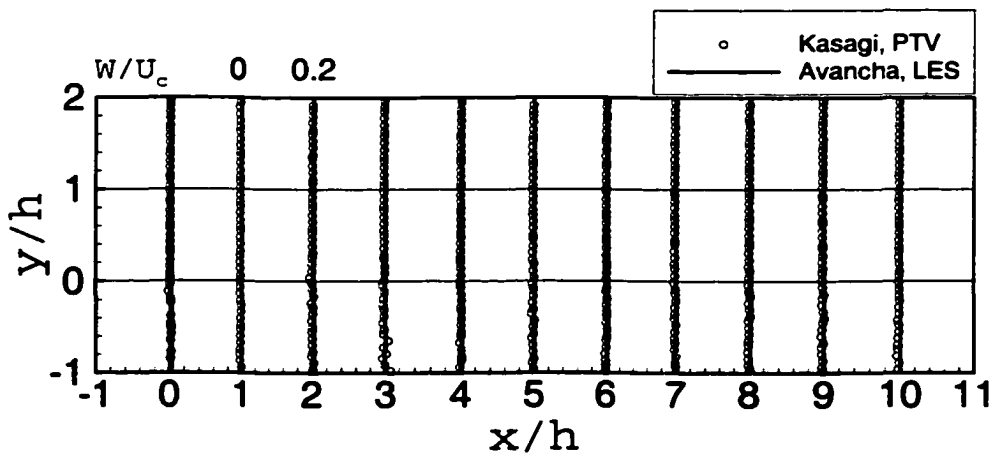


Figure 4.9 Spanwise mean velocity profiles

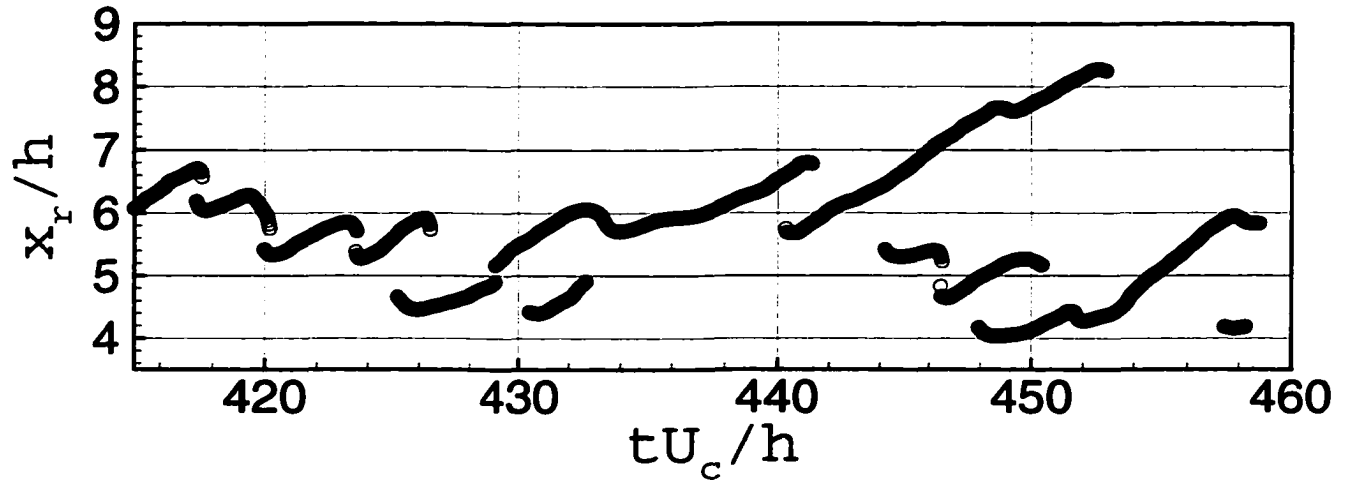


Figure 4.10 Temporal variation of the spanwise average reattachment locations

plot is essentially a distance vs. time plot, and the linear slopes of the reattachment location indicate that this location is traveling a constant speed, and a drop in this location is seen every time there is a collapse of the large scale structure.

4.5.3 Spanwise averaged coefficients of friction and pressure

The coefficient of friction along the lower wall of the domain is defined as $C_f = \frac{2 \tau_w}{\rho U_{ref}^2}$. The reattachment length x_r , found from the figure at the point where the coefficient of friction goes to zero, is a value close to 6.0. Using a probability density function approach, the reattachment length is predicted to be a value of 6.1. The coefficient of skin friction takes on negative values in the recirculating region, before starting to climb back up after reattachment, before fully recovering about 3 ~ 4 step heights beyond the mean reattachment point. From the C_f profile, we can infer that the shear stress assumes a large value in the reattachment region, and Vogel and Eaton [1984] cite this observation to reaffirm the fact that the recirculation flow is not a “dead-air” region, though it could probably be treated as such for some limited purposes. The coefficient of pressure, C_p is defined as $\frac{2(\bar{p} - p_{ref})}{\rho U_{ref}^2}$.

The pressure at the corner of the step is used as the reference. The pressure coefficient on the step wall decreases till about $x/h = 2$, and then increases rapidly in the reattachment zone and flattens out nearly 3 ~ 4 step heights downstream of the mean reattachment point.

4.5.4 Velocity fluctuations and turbulent kinetic energy

Root mean square (RMS) velocity fluctuations (also referred to, in literature, as “turbulent intensities”) are shown in Figs. 4.13, 4.14, 4.15, and show excellent agreement between the experimental results and the simulations. All of these profiles show an increase in the peak values and a broadening of the turbulence region as the shear layer grows [Eaton and Johnston, 1980]. However, in the region of reattachment and farther downstream, a decay in the turbulence intensities is observed. Eaton and Johnston [1980] observed that the location of the peak starts somewhere about $y/h = 0.0$ (corresponding to $y/h = 1.0$ for their geometry), and dips down toward the wall in the reattachment zone before moving back to $y/h = 0.0$ downstream of reattachment. This behavior is attributed to the “flapping” vertical motion of the shear layer. The streamwise RMS fluctuation close to the step shoulder resembles the upstream channel flow and has two peaks. The streamwise RMS fluctuation experiences significant change on the step side in contrast to the opposite wall, as can be inferred from Figure 4.13. It reaches a peak value of close to $0.21 U_c$ at $y/h = 0$ and $x/h = 0.5$. The wall normal RMS fluctuation distribution is qualitatively similar to the streamwise fluctuation and it reaches a peak value of about $0.12 U_c$ close to $x/h = 1.0$ and $y/h = 0$. In terms of magnitude, $u_{rms} > w_{rms} > v_{rms}$, a trend that is very similar to the channel flow. From inspection of the RMS fluctuations in the recirculation region near the wall, it is observed that w_{rms} component is the greatest, as also borne out by the experiments [Kasagi and Matsunaga, 1995], and was first reported by Itoh and Kasagi [1989]. The nondimensional turbulent kinetic energy was calculated from $0.5*(u_{rms}^2 + v_{rms}^2 + w_{rms}^2)$, and a contour plot

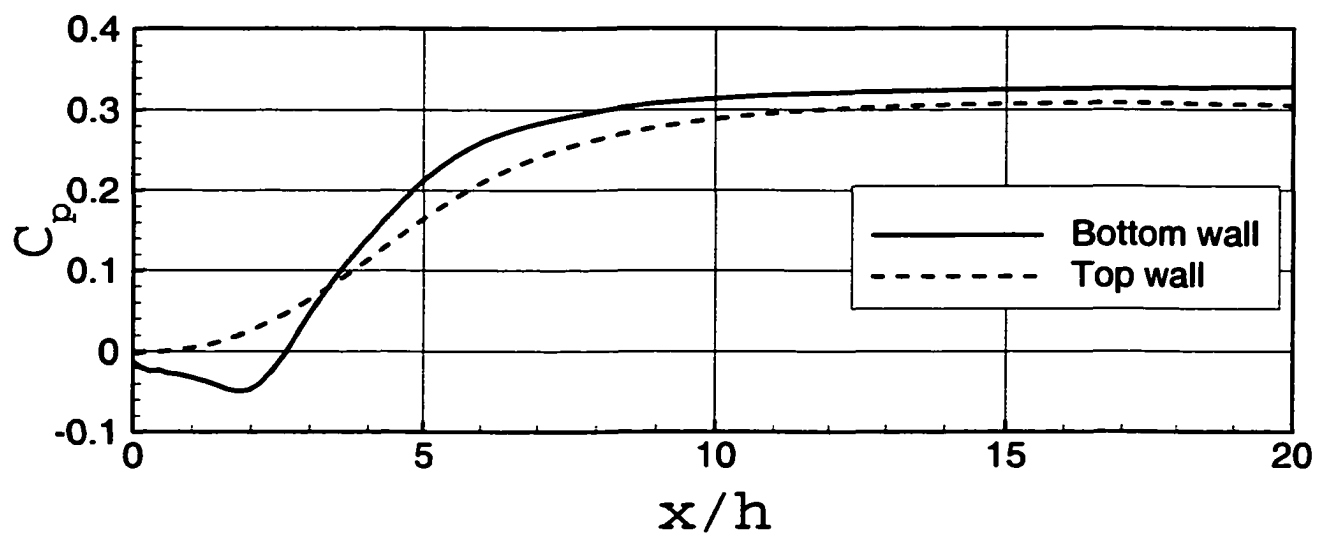


Figure 4.11 Coefficient of pressure

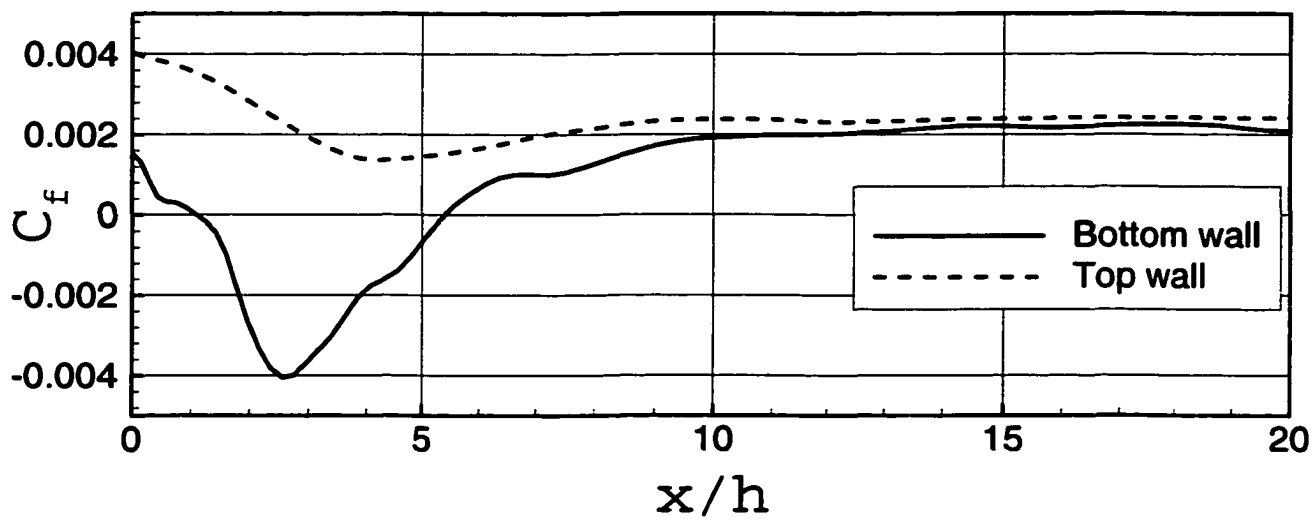


Figure 4.12 Coefficient of friction

is shown in Fig. 4.16.

4.5.5 Reynolds shear stresses

The three Reynolds shear stress components are shown in Figs. 4.17, 4.18 and 4.19. The $-\langle u'v' \rangle$ component appears to be in greater disagreement with experimental results in the recirculation region than elsewhere, and the reason behind this discrepancy is not clear. Kasagi and Matsunaga [1995] have indicated that the uncertainties associated with the shear stress were relatively higher in the recirculation region than in other regions of the flow, and is a possible explanation for the disagreement. The other two components are negligible, as confirmed by the experiment.

4.5.6 Triple velocity correlations

Spanwise averaged triple velocity correlations were calculated and compared with those from the experimental database. All 10 components of the triple velocity correlations are shown in Figs. 4.20- 4.29. It may be noted that four of them $\langle u'u'w' \rangle$, $\langle u'v'w' \rangle$, $\langle v'v'w' \rangle$, and $\langle w'w'w' \rangle$ are negligible, as confirmed by the experiment, and corroborate with the fact that in a 2D flow, these components should indeed be zero. Of the non-negligible components, while some of them have opposite signs, they all exhibit a similar behavior qualitatively: they have peaks on opposite sides of the shear layer, and the peaks on the upper side are greater than the peaks on the lower side.

4.5.7 Effect of subgrid scale model

In order to determine the contribution of the subgrid scale model to the shear stress, the following norm [Akselvoll and Moin, 1995], $e(x)$, was defined:

$$e(x) = 100 \times \left[\frac{\int_y \langle \tau_{12} \rangle_{tz}^2}{\int_y \langle u'v' \rangle_{tz}^2} \right]^{1/2}. \quad (4.3)$$

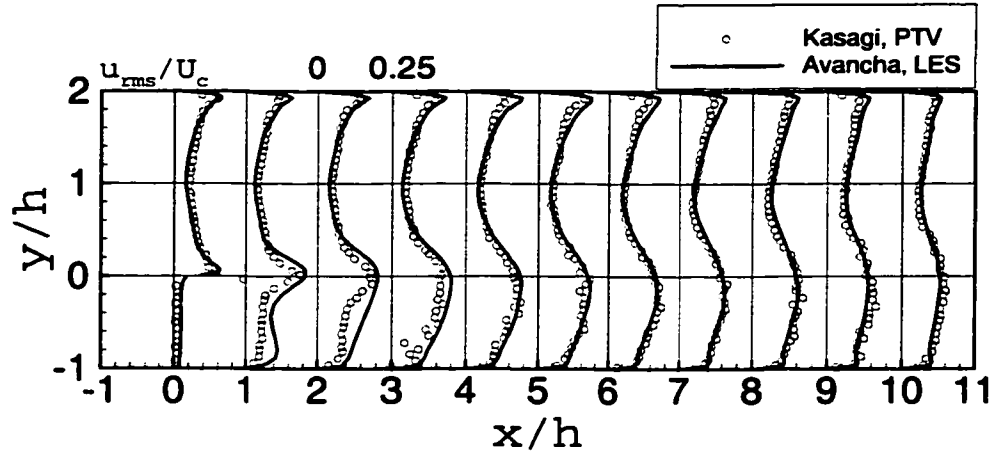


Figure 4.13 Streamwise RMS velocity profiles

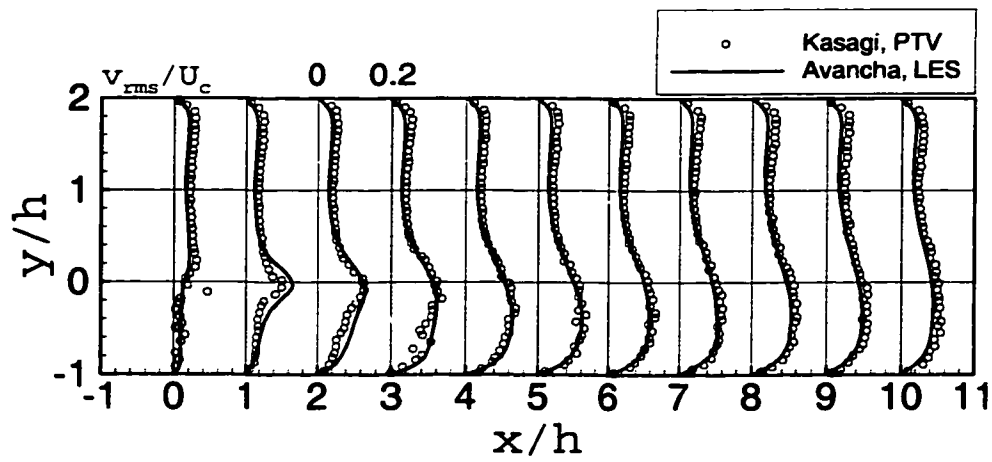


Figure 4.14 Wall-normal RMS velocity profiles

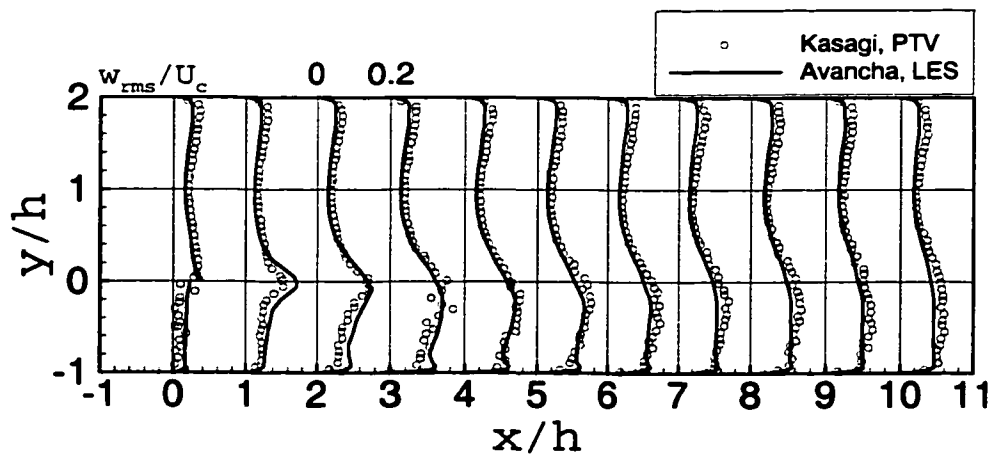


Figure 4.15 Spanwise RMS velocity profiles

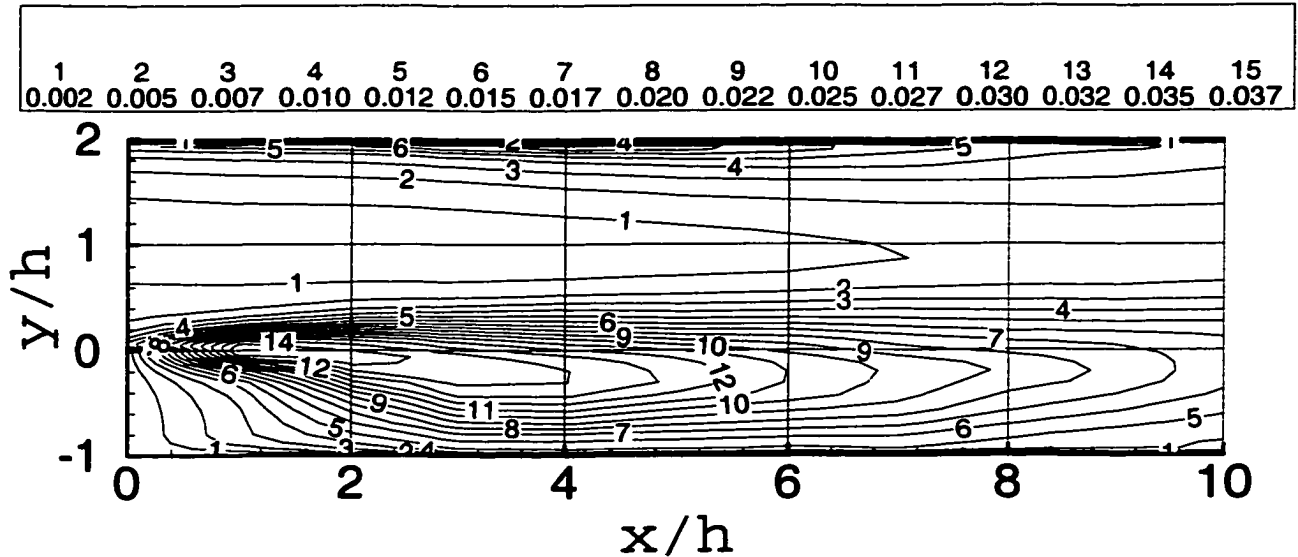


Figure 4.16 Contour lines of turbulent kinetic energy

Figure 4.30 is a measure of the ratio of the subgrid scale shear stress to the resolved turbulent shear stress plotted versus the streamwise distance. It is observed that the contribution of the subgrid scale stress to the resolved shear stress is about 5% at the step and decreases to about 2% downstream, indicating that the SGS model plays an important role in the earlier part of the shear layer. Another function $I(x)$ was defined to compute the ratio of the subgrid scale dissipation to molecular dissipation:

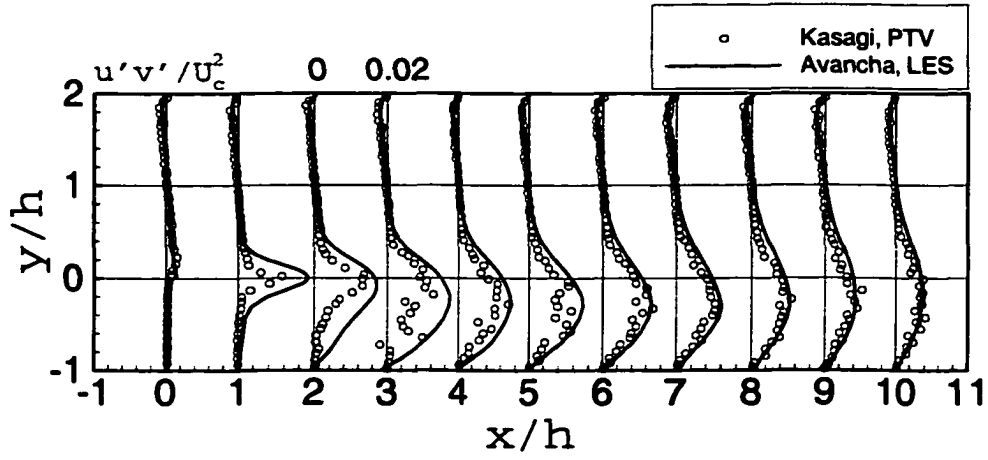
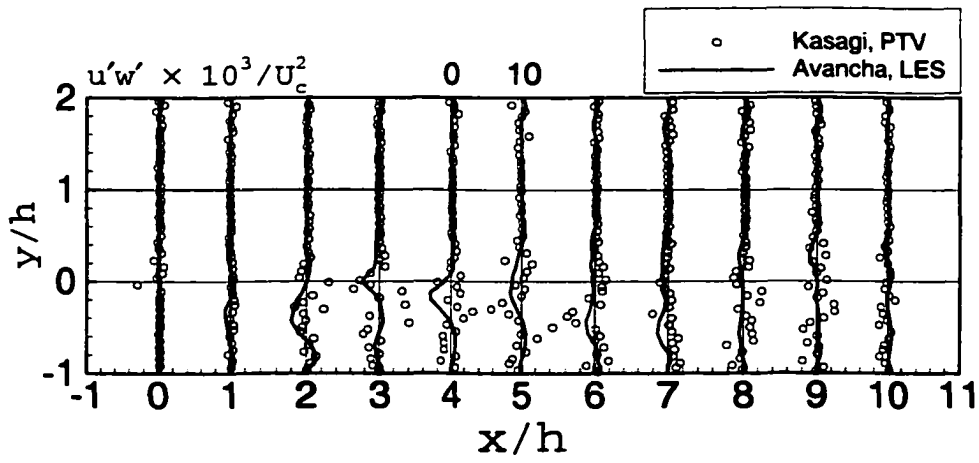
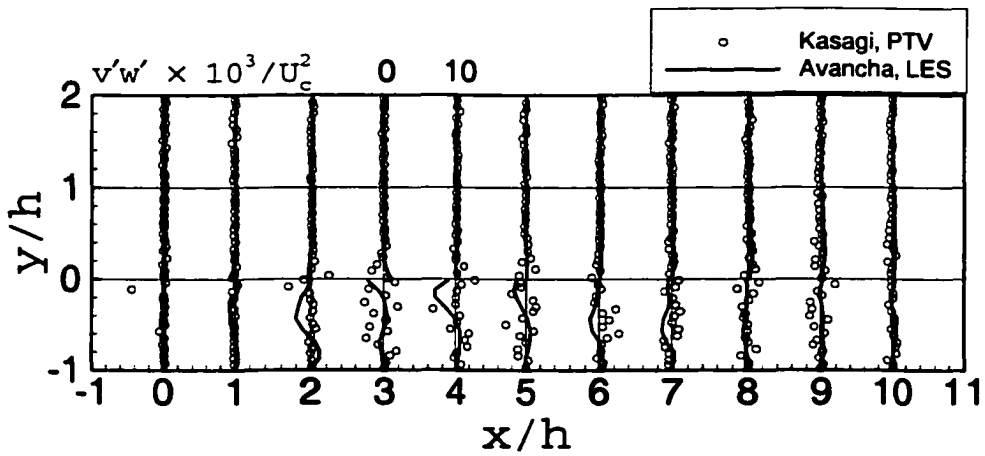
$$I(x) = \left[\frac{\int_y \langle \rho \epsilon_{SGS} \rangle_{tz} dy}{\int_y \langle \rho \epsilon_m \rangle_{tz} dy} \right] \quad (4.4)$$

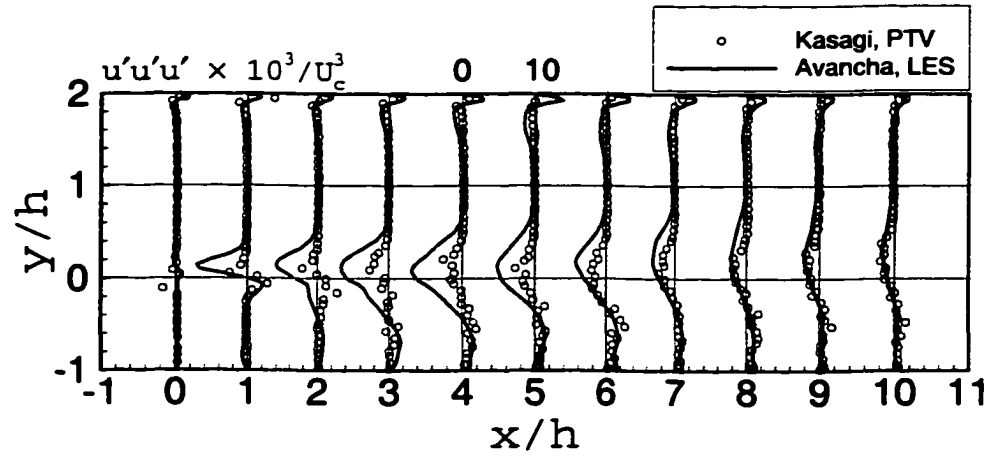
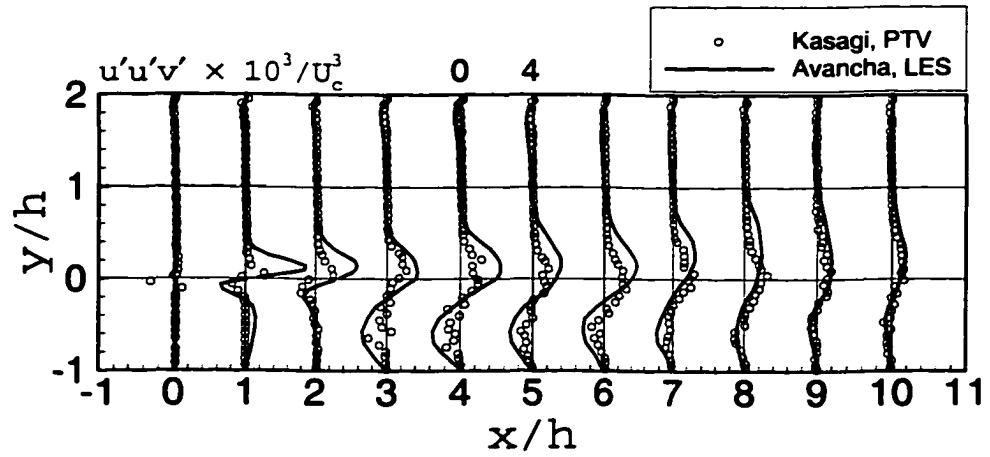
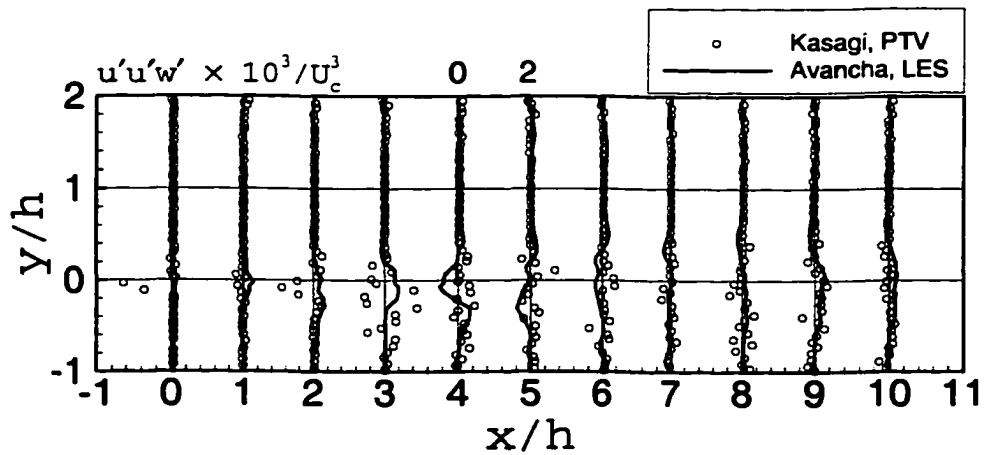
where

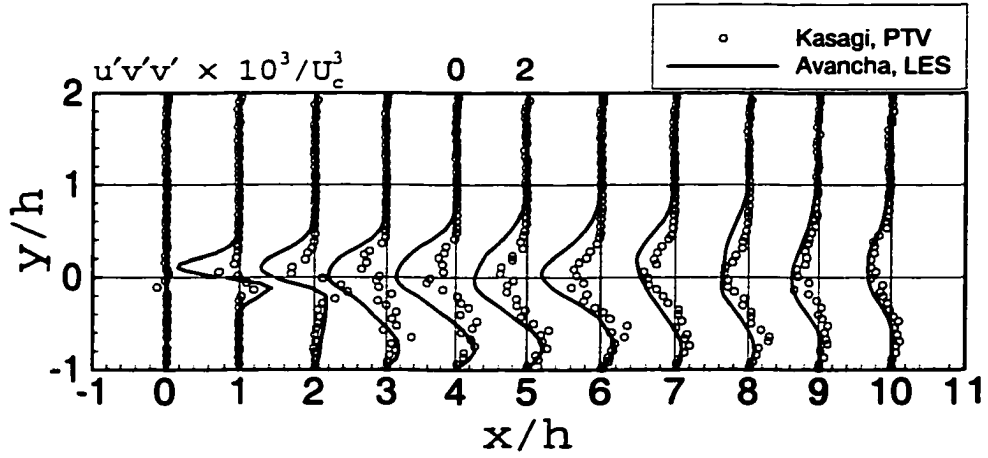
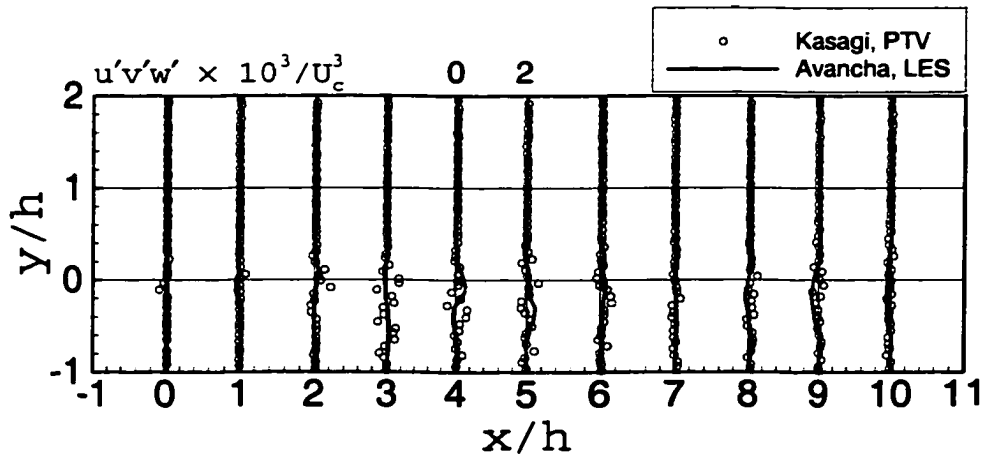
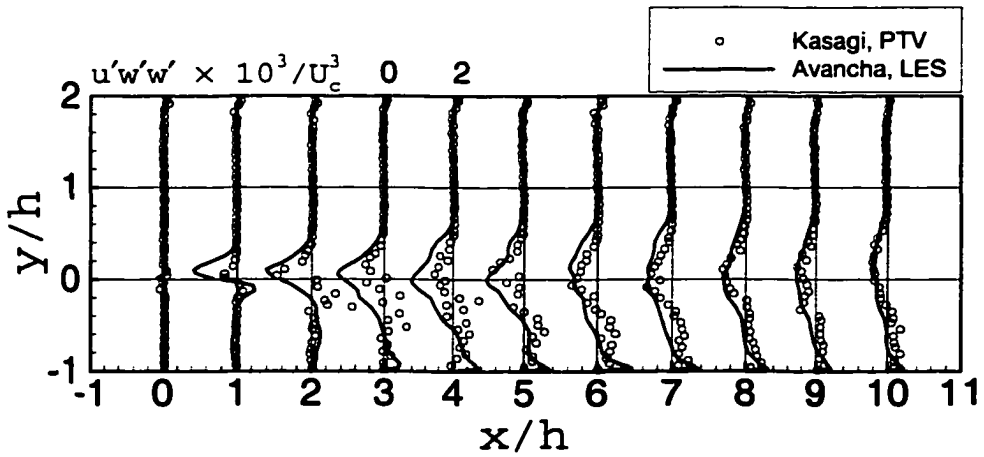
$$\rho \epsilon_{SGS} = \mu_t |\tilde{S}|^2 \quad (4.5)$$

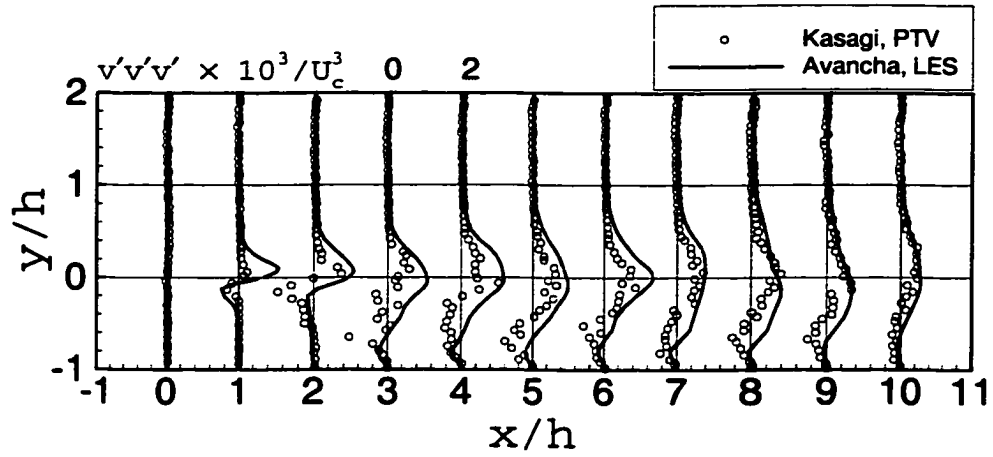
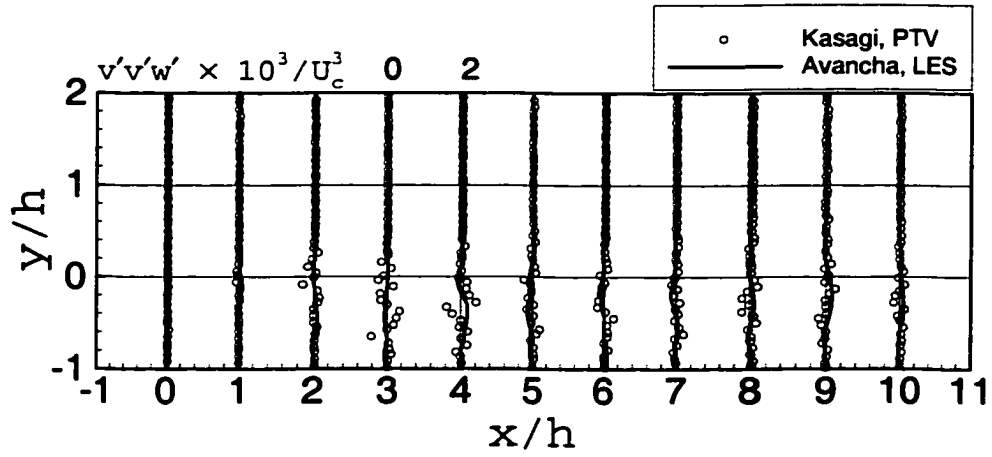
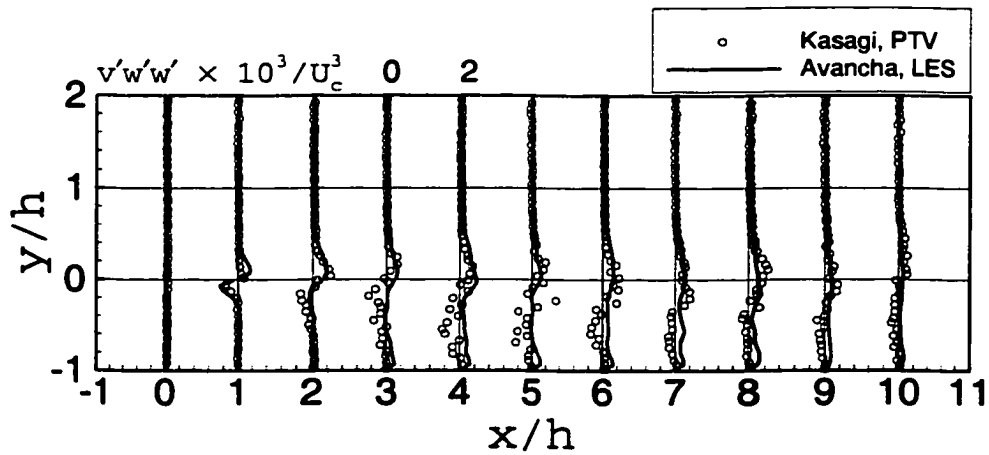
$$\rho \epsilon_m = \frac{\mu}{Re} |\tilde{S}|^2 \quad (4.6)$$

Figure 4.31 is a plot of the ratio of $\langle \rho \epsilon_{SGS} \rangle_{tz}$ to $\langle \rho \epsilon_m \rangle_{tz}$ averaged over the cross sectional area and plotted versus the streamwise distance. The contribution of the subgrid scale model to the resolved dissipation is maximum upstream of reattachment and drops

Figure 4.17 Reynolds shear stress: $-\langle u'v' \rangle_{tz}$ Figure 4.18 Reynolds shear stress: $-\langle u'w' \rangle_{tz}$ Figure 4.19 Reynolds shear stress: $-\langle v'w' \rangle_{tz}$

Figure 4.20 Skewness profiles: $\langle u'u'u' \rangle_{tz}$ Figure 4.21 Skewness profiles: $\langle u'u'v' \rangle_{tz}$ Figure 4.22 Skewness profiles: $\langle u'u'w' \rangle_{tz}$

Figure 4.23 Skewness profiles: $\langle u'v'v' \rangle_{tz}$ Figure 4.24 Skewness profiles: $\langle u'v'w' \rangle_{tz}$ Figure 4.25 Skewness profiles: $\langle u'w'w' \rangle_{tz}$

Figure 4.26 Skewness profiles: $\langle v'v'v' \rangle_{tz}$ Figure 4.27 Skewness profiles: $\langle v'v'w' \rangle_{tz}$ Figure 4.28 Skewness profiles: $\langle v'w'w' \rangle_{tz}$

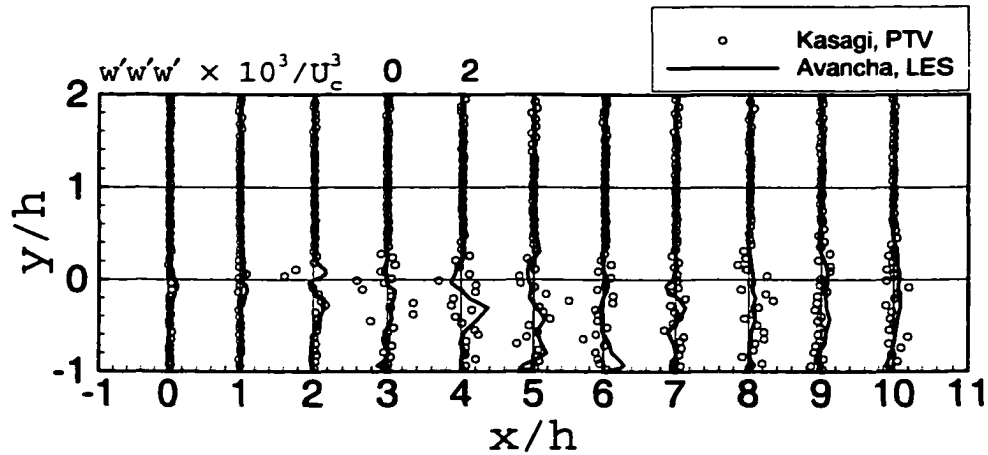


Figure 4.29 Skewness profiles: $\langle w'w'w' \rangle_{tz}$

to about a quarter of its value farther downstream. Finally, Fig 4.32 shows the streamwise distribution of the dynamic model coefficient.

4.6 Significance of the Study

A stable colocated-grid finite volume scheme using second/fourth order central differences has been developed. Large eddy simulations, using the colocated-grid scheme, of the turbulent channel flow have been performed in order to provide inflow conditions for the backward facing step. Pressure-velocity decoupling has been eliminated by use of the sixth order compact filtering that effectively damps oscillations at the grid level frequencies while having little influence on the turbulence characteristics of the flow. An outflow boundary condition for the step designed to control spurious reflections was imposed at the exit of the step. Having successfully simulated the turbulent flow past the backward facing step at $Re=5540$, attention will now be turned to extending this study to one involving significant heat transfer. Although heat transfer results have been reported in the literature, available results for separated and reattaching flows are limited. Reattaching flows cause large variations of local heat transfer coefficient as well as augment overall heat transfer. Available experimen-

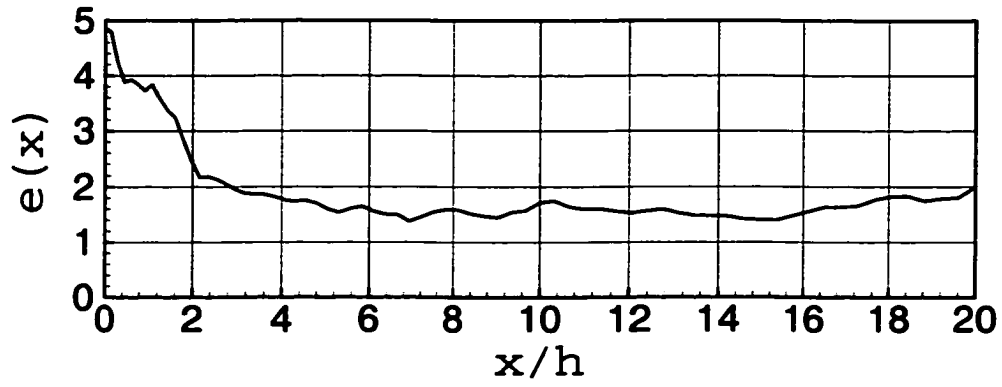
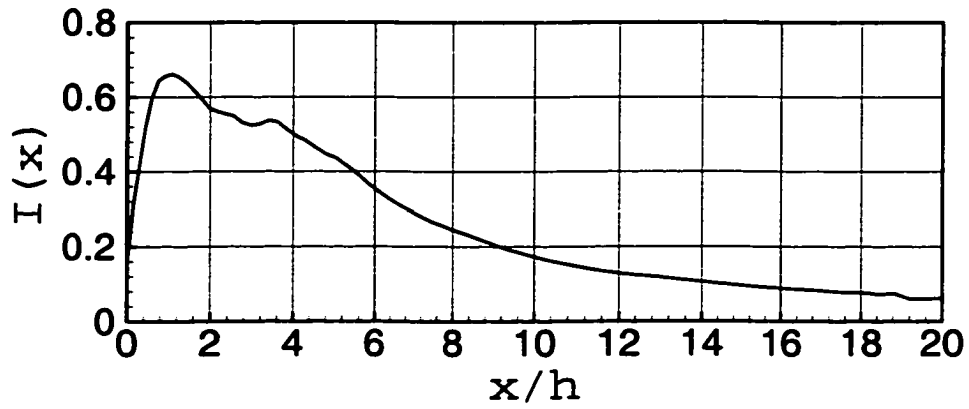
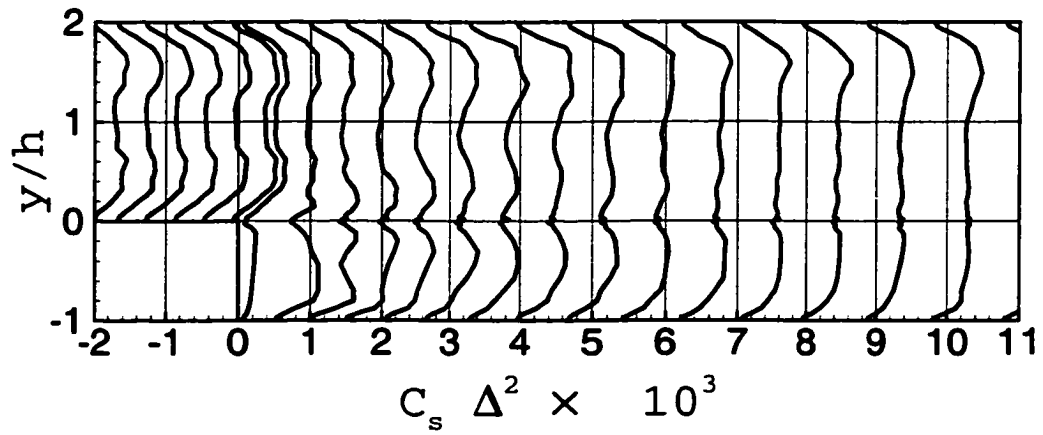
Figure 4.30 Plot of $e(x)$ Figure 4.31 Plot of $I(x)$ 

Figure 4.32 Streamwise profiles of the dynamic model coefficient

tal data are small in number, as indicated by Vogel and Eaton [1985]. Experiments are also constrained by practical limitations to impose moderate heat flux levels, not quite close to the levels that are usually found in practical applications. As a result, the influence of heat transfer in regions of separated and reattaching flow is not well understood. In numerical simulations, it is possible to include desired heat flux levels, and temperature gradients, and therefore it is important for calculations to take a lead role in influencing current design methods. These large eddy simulations of the backward facing step flow will provide valuable data to evaluate and improve current two equation turbulence models like the $k - \epsilon$ and $k - \omega$ models.

CHAPTER 5 LES OF TURBULENT FLOW WITH HEAT TRANSFER AND PROPERTY VARIATIONS

5.1 Introduction

Results from the large eddy simulation of the isothermal flow past a backward-facing step were presented in the previous chapter. In this chapter, steps involved in carrying out simulations of turbulent flow for the same geometry with heat transfer, achieved through a uniform heat flux condition, will be discussed. Results and analysis of the effects of heat transfer and property variations on the turbulent separating and reattaching flow for this geometry will then be presented.

5.2 Problem Description and Simulation Details

The flow of interest is the turbulent flow past a single-sided backward-facing step subjected to a uniform wall heat flux that is specified to the bottom wall immediately downstream of the step. All other walls were kept insulated (adiabatic). The geometry of the step is the same as the one used for the isothermal large eddy simulations. The geometry used for the isothermal simulations was retained with the expectation that results from the LES would motivate new experimental work, in light of advances being made in measurement methods, to include the effects of heat transfer. More importantly, using the same geometry permits the use of the planes of channel flow data for inflow conditions, initial conditions for the heat transfer cases become easily available from the isothermal simulations, and result in

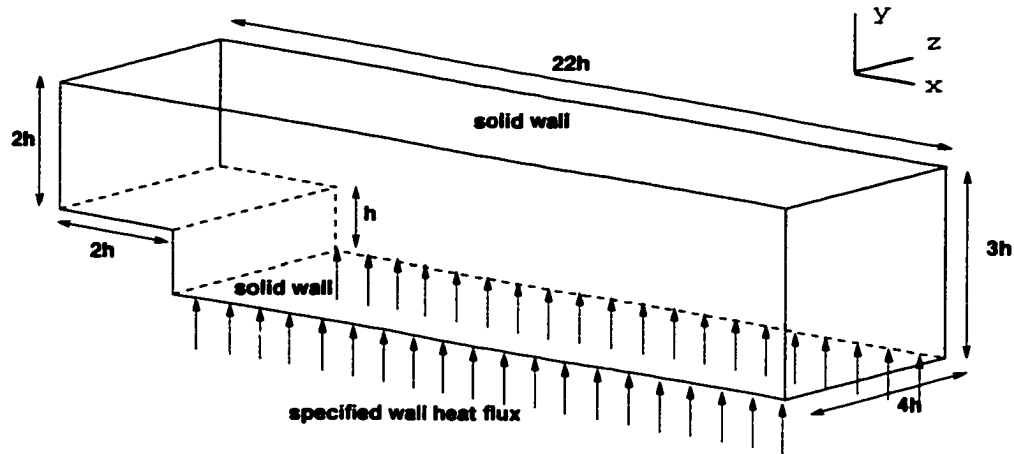


Figure 5.1 Backward-facing step geometry

significant savings in computer resources.

The grid resolution and stretching patterns used for the isothermal simulations were retained. A grid resolution of $72 \times 46 \times 48$ was used in the streamwise, wall normal and spanwise directions for the post step section. The upstream channel resolution was $16 \times 31 \times 48$. While the grid was uniform in the spanwise direction, it was stretched in the streamwise and wall normal directions using a hyperbolic tangent stretching as described in Sec. 3.4. The inflow and outflow were treated as in the case of the isothermal simulations. The top and bottom wall upstream of the step, the top wall downstream of the step, and the step face wall were treated as no-slip adiabatic (insulated) walls (see Sec. 3.14.2). The bottom wall downstream of the step is treated as a no-slip wall with a specified wall heat flux, as described in Sec. 3.14.2. Turbulent inflow conditions for each time step of the simulation were provided by planes of data stored from an independent LES of a channel flow with the same Reynolds number and time step, as in the case of the isothermal simulations. A Mach number of 0.006 and a non-dimensional physical time step of 0.03 were used for the simulations, and turbulent statistics were accumulated for roughly 10,000 time steps - corresponding to 14

flow through times. Reference values of relevant variables are given below:

$$\begin{array}{lll}
 U = 2.063 \text{ m/s} & L = h = 0.041 \text{ m} & T = 293.0 \text{ K} \\
 k = 25.74 \times 10^{-3} \text{ W/m K} & \nu = 15.27 \times 10^{-6} \text{ m}^2/\text{s} & \rho = 1.194 \text{ kg/m}^3 \\
 C_p = 1006.0 \text{ J/kg K} & R = 286.85 \text{ J/kg K} & \frac{C_p}{C_v} = \gamma = 1.4
 \end{array}$$

Note: The reference velocity shown above is the upstream centerline velocity. The thermal conductivity, kinematic viscosity and density of air are obtained at the reference temperature of 293 K.

Simulations with three different wall heat flux values of 1.0 kW/m², 2.0 kW/m², 3.0 kW/m² were carried out, to study the effect of increasing wall heat flux. The heat flux was non-dimensionalized as :

$$q_w = \frac{q_w^*}{\left[\frac{k_{ref} T_{ref}}{L_{ref}} \right]} \quad (5.1)$$

where q_w^* is the dimensional heat flux, and q_w takes on the values of 5.44, 10.87, and 16.30, for the three different wall heat flux cases, respectively. An alternate normalization is also possible,

$$Q^+ = \frac{q_w^*}{\rho_{ref} U_{ref} C_p T_{ref}} \quad (5.2)$$

where Q^+ takes on values of 0.0014, 0.0028, and 0.0042, for dimensional heat flux values of 1.0 kW/m², 2.0 kW/m², 3.0 kW/m², respectively.

The effects of buoyancy (see Appendix C) and radiation are neglected.

5.3 Results and Discussion

5.3.1 Mean velocity and mean temperature distributions

Mean streamwise, wall-normal and spanwise velocity profiles are shown in Figures 5.2, 5.3, 5.4 and are in good agreement with the experimental results of Kasagi and Matsunaga

[1995]. The mean streamwise velocity profiles demonstrate the growth of the shear layer by entrainment of fluid, and its subsequent contact with the wall at the reattachment point. As pointed out in the earlier chapter, the reattachment point is defined as the length between from the step face to the point of zero mean skin friction and that the reattachment point is not fixed but oscillates over a distance of ± 1 step height. The mean wall-normal velocity profiles, downstream of $x/h \sim 2$, are negative and imply that the shear layer is bending toward the wall. Downstream of reattachment, the mean wall-normal velocity is small and indicates the development of a wall-bounded flow [Vogel and Eaton, 1984]. Integration of the streamwise mass flow across the channel height shows that the mass flow rate variations are within 2%, and that the conservation of mass is satisfied very well.

Mean temperature profiles, normalized as $\frac{(T - T_{ref})}{T_{ref}}$ are shown in Fig. 5.5. Expanded plots of the mean temperature profiles are shown in Figs. 5.6 and 5.7. Significant gradients in temperature are confined to the near-wall region along the length of the downstream section - most of the temperature drop appears to occur within a fraction of the step height from the bottom wall. The only region away from the wall where significant mean temperature gradients are observed is immediately downstream of the step. These gradients can be attributed to the activity of the secondary corner eddy as well as the larger recirculation eddy that are responsible for pushing up (as evidenced by the positive wall-normal velocity profiles near the step up to $x/h \sim 2$) warm packets of fluid while simultaneously relatively "colder" packets of fluid are introduced into the same region by the shear layer. It can be observed from looking at these profiles that the gradients get larger with increasing heat flux. It can also be inferred from the mean temperature profiles, and subsequently confirmed from the animations of temperature, that convective mixing effects prohibit temperature gradients in other regions of the flow. Downstream of reattachment, the growth of the thermal boundary layer is clearly discernible from examining the spread of the mean temperature gradients in Figs. 5.6 and 5.7. Vogel and Eaton [1984] also indicate that it might require well over 50 step heights for the downstream flow to reach a fully developed state.

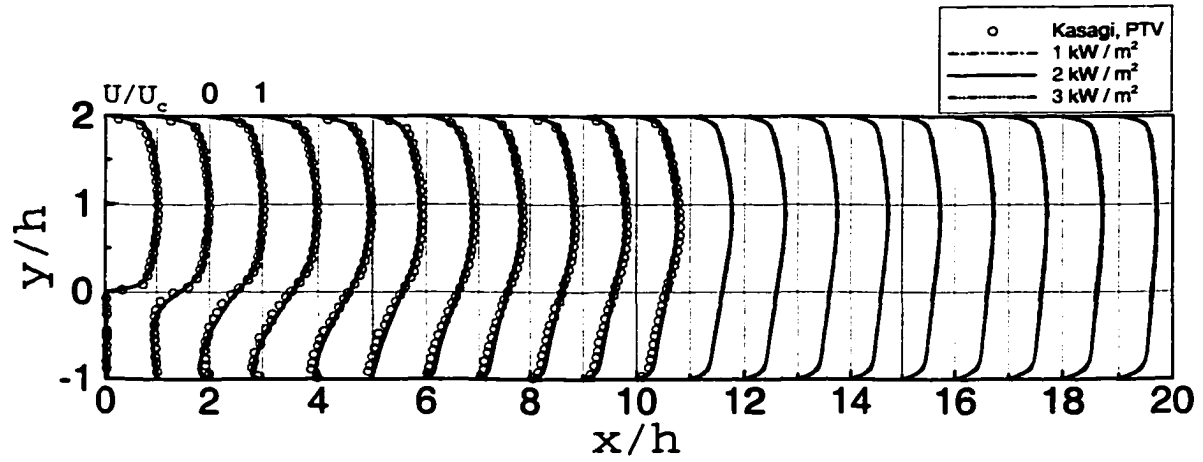


Figure 5.2 Mean streamwise velocity

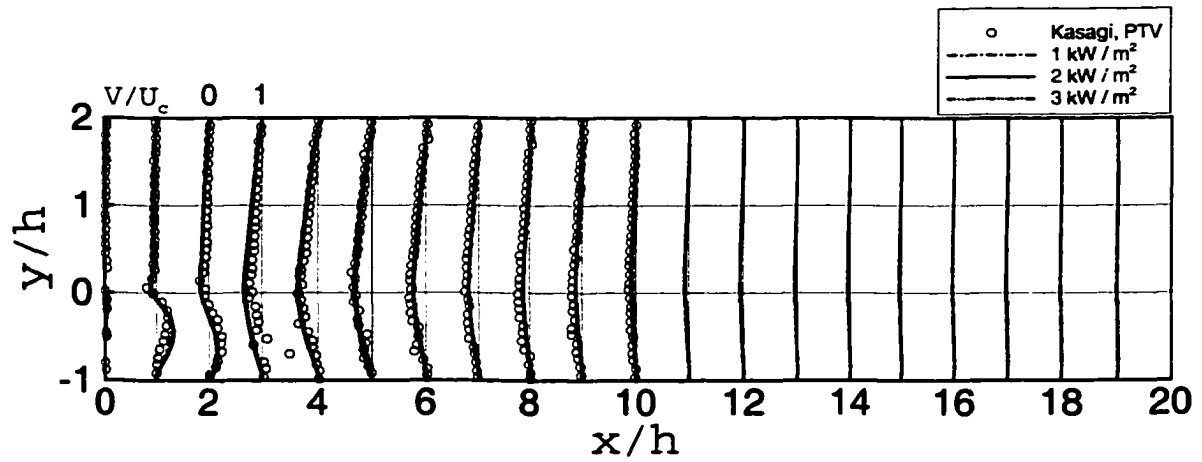


Figure 5.3 Mean wall-normal velocity

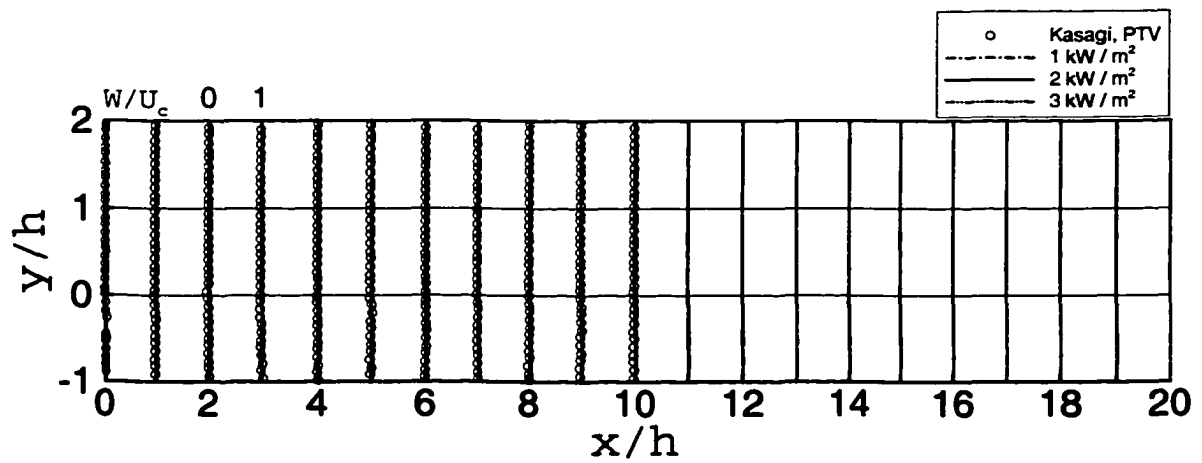


Figure 5.4 Mean spanwise velocity

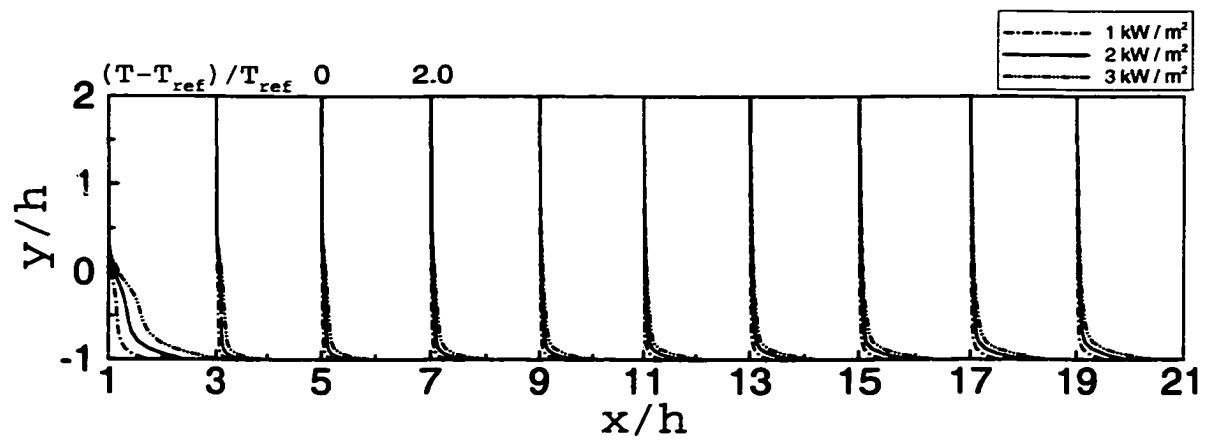


Figure 5.5 Mean temperature

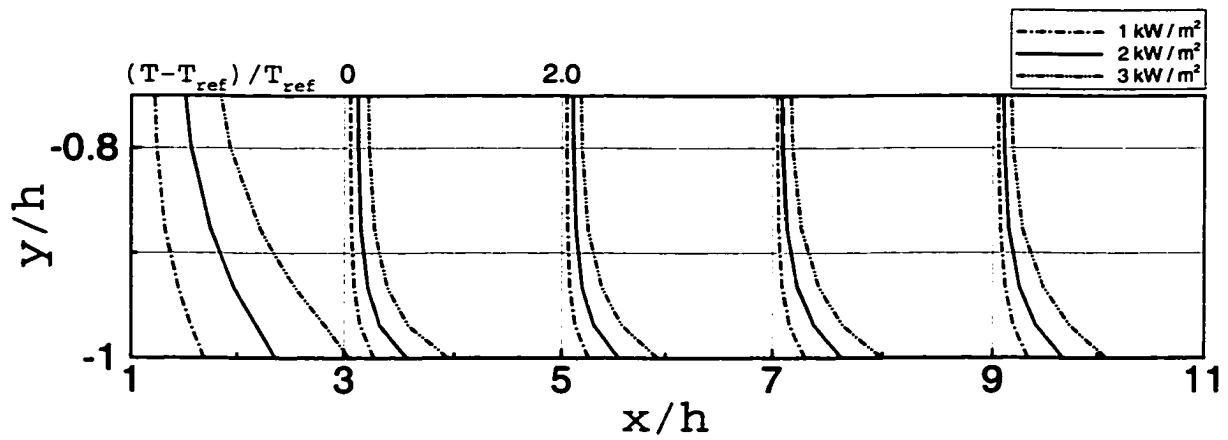


Figure 5.6 Mean temperature

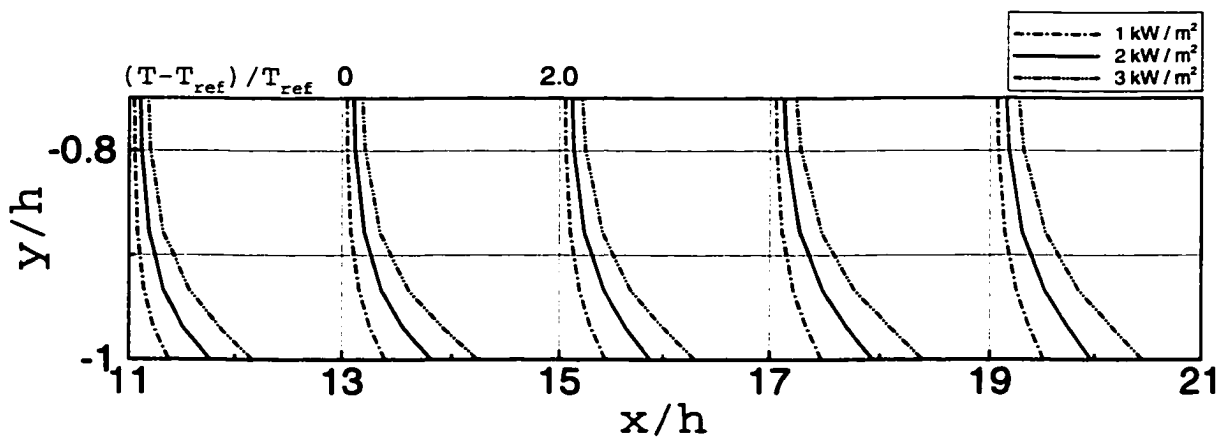


Figure 5.7 Mean temperature

The heat flux levels of 1.0 kW/m², 2.0 kW/m², 3.0 kW/m² supplied to the surface downstream of the step, yield maximum $\langle T_{wall} \rangle_{zt} / \langle T_{bulk} \rangle_{zt}$ ratios of about 1.7, 2.3, and 2.9 respectively, where the bulk temperature is given by:

$$T_{bulk} = \frac{\int_y \int_z \rho u C_v T dy dz}{\int_y \int_z \rho u C_v dy dz} \quad (5.3)$$

The bulk temperature profiles (Fig. 5.8) are in good agreement with analytical estimates based on an overall energy balance for the uniform heat flux condition (see Appendix B). The wall temperatures (Fig. 5.9) show a dramatic increase downstream of the step, reaching their peak values in the neighborhood of the streamwise distance of $x/h \sim 2$. This increase in wall temperature is accompanied by a decrease in convective heat transfer (as evidenced by the Nusselt number profiles in Fig. 5.10), and suggests that the air in this zone is almost in a “stagnant” state. A good estimate of heat transfer is the Nusselt number, Nu , which provides a ratio of convective heat transfer to conductive heat transfer and is computed as:

$$Nu = \frac{h L_y}{k_{bulk}} \quad (5.4)$$

where

$$h = \frac{q_w}{T_{wall} - T_{bulk}} \quad (5.5)$$

and L_y is the step height h . In the neighborhood of $x/h \sim 0.5$, Nu attains its minimum value for the three different heat flux cases - an indication that the dominant mode of heat transfer in this region, close to the step face, is through conduction. Evidence to support this suggestion is obtained by the relatively thicker viscous sub-layer close to the step that can be inferred from inspection of the mean temperature profiles in wall coordinates.

Away from the step face, the wall temperature profiles drop significantly, accompanied by a steep rise in the Nusselt number profiles that suggest increased heat transfer due to convection. The Nusselt number profiles attain a maximum slightly upstream of reattachment, which is in agreement with Vogel and Eaton [1984], as opposed to several other studies that

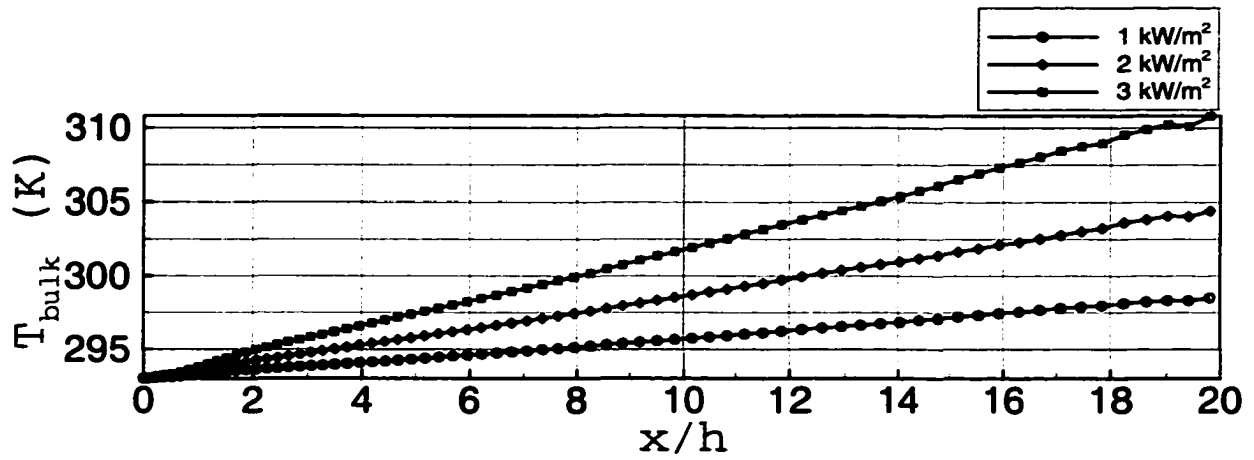


Figure 5.8 Bulk temperature

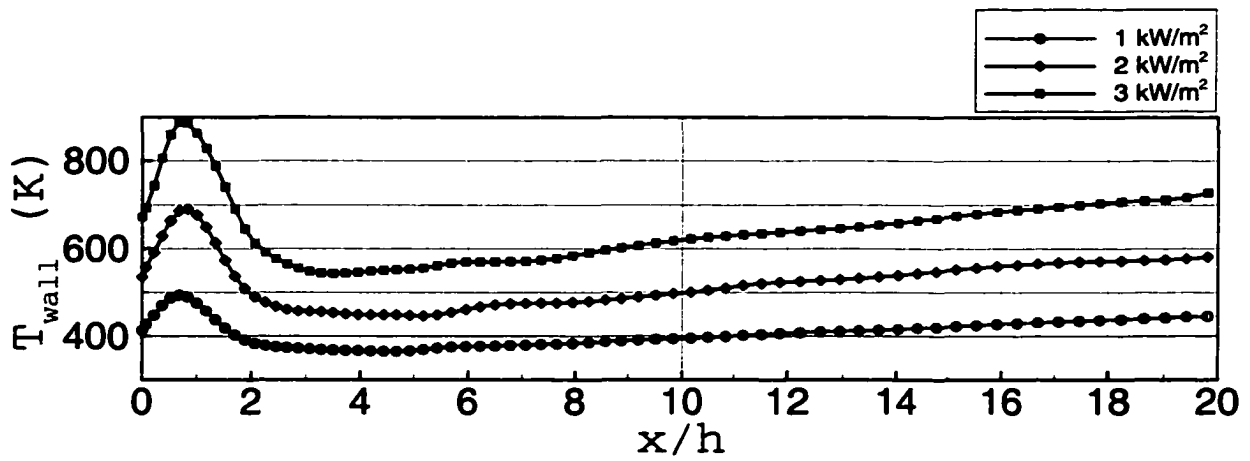


Figure 5.9 Wall temperature

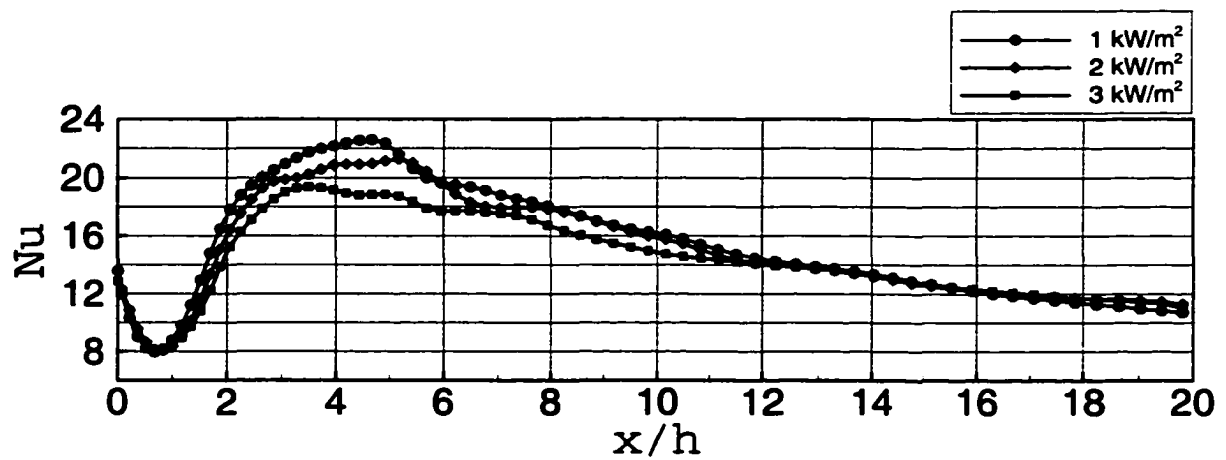


Figure 5.10 Nusselt number

have assumed the location of the peak Nusselt number to coincide with the mean reattachment point. The peak Nu is maximum for the 1.0 kW/m² case, followed by the 2.0 kW/m² and the 3.0 kW/m² cases. The location of the peak Nusselt numbers are within roughly 1.5 step heights of each other.

Farther downstream, in the region of reattachment, the impinging shear layer is responsible for the depression in the wall temperature around reattachment. A linear increase of the wall temperatures downstream of reattachment that corresponds to the growth of the thermal boundary layer is observed, and a monotonic decrease in the Nusselt number profiles is strong evidence of reduced heat transfer due to convective mixing. The Nusselt number profiles resemble the flat plate boundary layer behavior, and in fact, lie on top of each other. As indicated earlier, it is expected to require well over 50 step heights for the downstream flow to reach a fully developed state.

Profiles of the mean streamwise velocity and temperature in wall coordinates (indicated by the '+' superscripts for y , u and T) where

$$u^+ = \frac{u}{u_\tau}; \quad u_\tau = \sqrt{\frac{\tau_w}{\rho_w}} \quad (5.6)$$

$$y^+ = \frac{\delta_y u_\tau}{\nu_w} \quad (5.7)$$

$$T^+ = \frac{T}{T_\tau}; \quad T_\tau = \frac{q_w}{\rho_w C_p u_\tau} \quad (5.8)$$

and semi-local coordinates (indicated by the '*' superscripts for y , u and T) where

$$u^* = \frac{u}{u_\tau^*}; \quad u_\tau^* = \sqrt{\frac{\tau_w}{\rho(y)}} \quad (5.9)$$

$$y^* = \frac{y u_\tau}{\nu(y)} \quad (5.10)$$

$$T^* = \frac{T}{T_\tau^*}; \quad T_\tau^* = \frac{q_w}{\rho(y) C_p u_\tau^*} \quad (5.11)$$

have been plotted for various streamwise stations, starting from immediately downstream of the step until the exit station. The linear law, $u^+ = y^+$ and the log-law, $2.5 \ln y^+ + 5.5$ for the velocity and the thermal linear law, $T^+ = Pr y^+$ and the thermal log-law $T^+ =$

$2.78 \ln y^+ + 2.09$ are also shown on the plots. In view of the substantial mean density variations expected with the heat flux values in this study, we wanted to consider the effect of scaling the mean velocity and temperature using semi-local coordinates.

The 'law of the wall' and its thermal counterpart clearly do not hold within the recirculating region. Vogel and Eaton [1984] have demonstrated that the flow under the recirculation bubble resembles a Falkner-Skan flow more than it does the turbulent 'law of the wall'. Downstream of reattachment, with the development of the velocity and thermal boundary layers, we observe that the mean profiles tend towards the 'law of the wall' and complete agreement can only be expected when the downstream flow reaches a fully developed state for the velocity and temperature.

However, some very important conclusions regarding the dominant thermal transport mechanism within the recirculating region can be drawn from a study of the mean velocity and temperature profiles plotted in the wall and semi-local coordinates. The region over which $y^+ = u^+$, or $y^+ = T^+$ is called the viscous sub-layer and is a region where the flow is considered to be laminar. This viscous sub-layer is responsible for most of the thermal resistance in the flow Vogel and Eaton [1984]. Where the viscous sub-layer is thick (estimated by a visual examination of the plots, as to first point of departure from the $y^+ = u^+$, or $y^+ = T^+$ curves), the Nusselt and Stanton numbers fall, indicative of reduced convective mixing effects. Correspondingly, where the viscous sub-layer is at its thinnest, the Nusselt and Stanton numbers are at their peak values. The Stanton number takes on a minimum close to the step at about $x/h = 1.0$; and one-to-one correspondence between this behavior of the Stanton number and the thickness of the viscous sub-layer can be made from observation of the thermal 'law of the wall' plots at the streamwise stations of $x/h = 0.07$ until the streamwise station of $x/h = 1.0$. This correspondence can be observed by continuing to track these profiles at the subsequent streamwise stations, where a thickening of the viscous sub-layer takes place until the streamwise station of $x/h = 3.07$, beyond which the viscous sub-layer again demonstrates a pattern of thinning until the streamwise station of $x/h =$

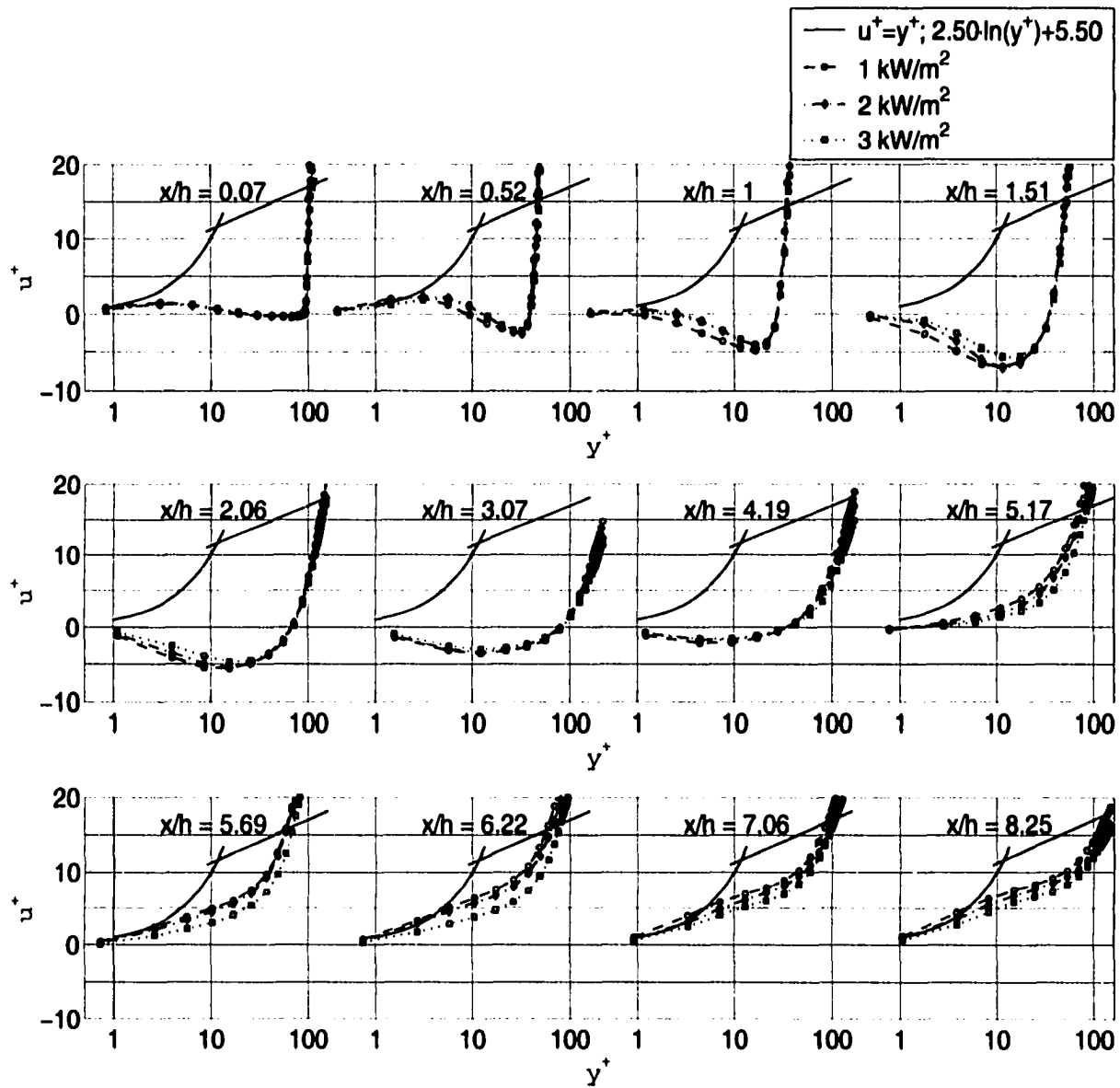


Figure 5.11 Mean streamwise velocity in wall coordinates

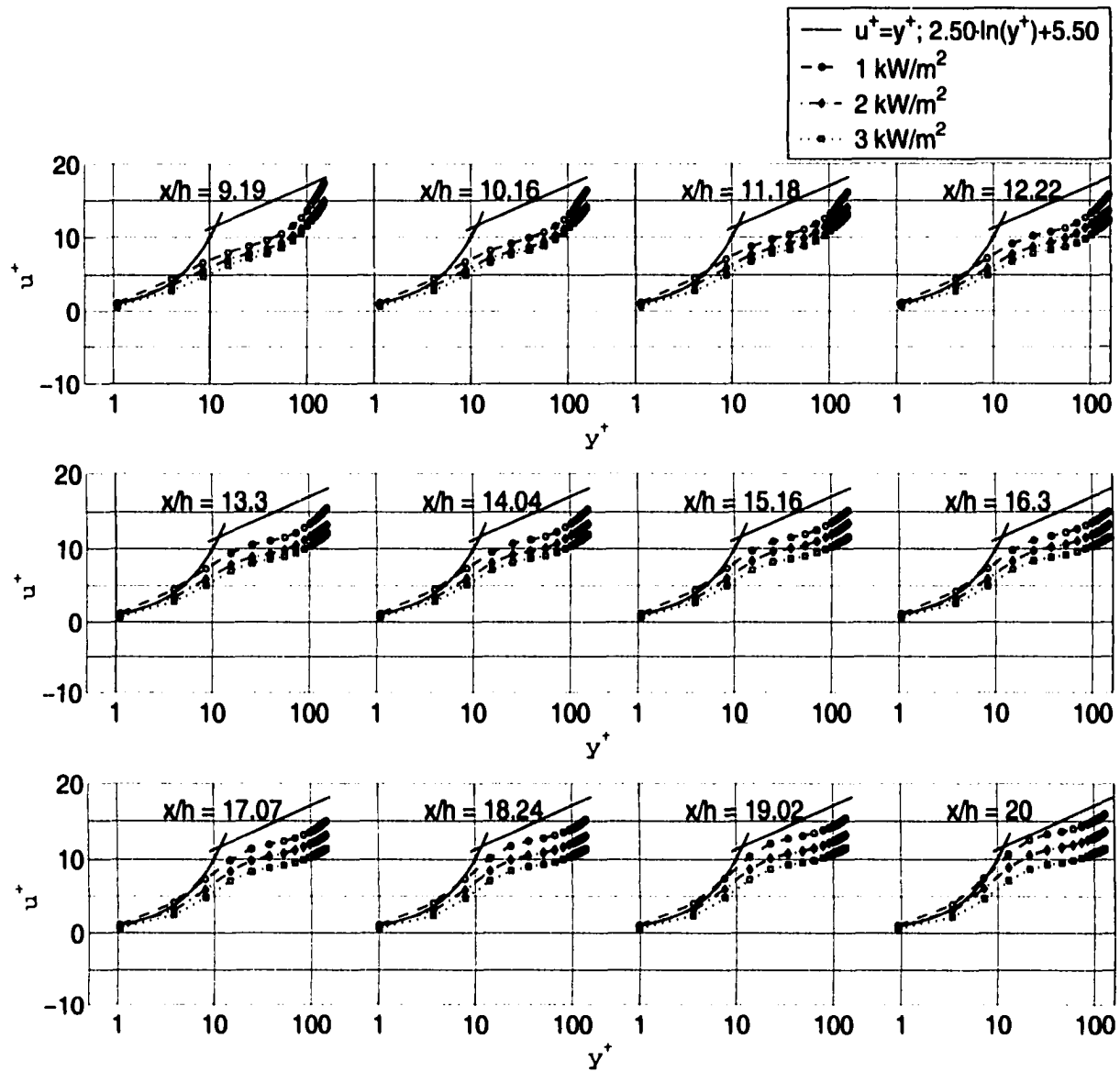


Figure 5.12 Mean streamwise velocity in wall coordinates

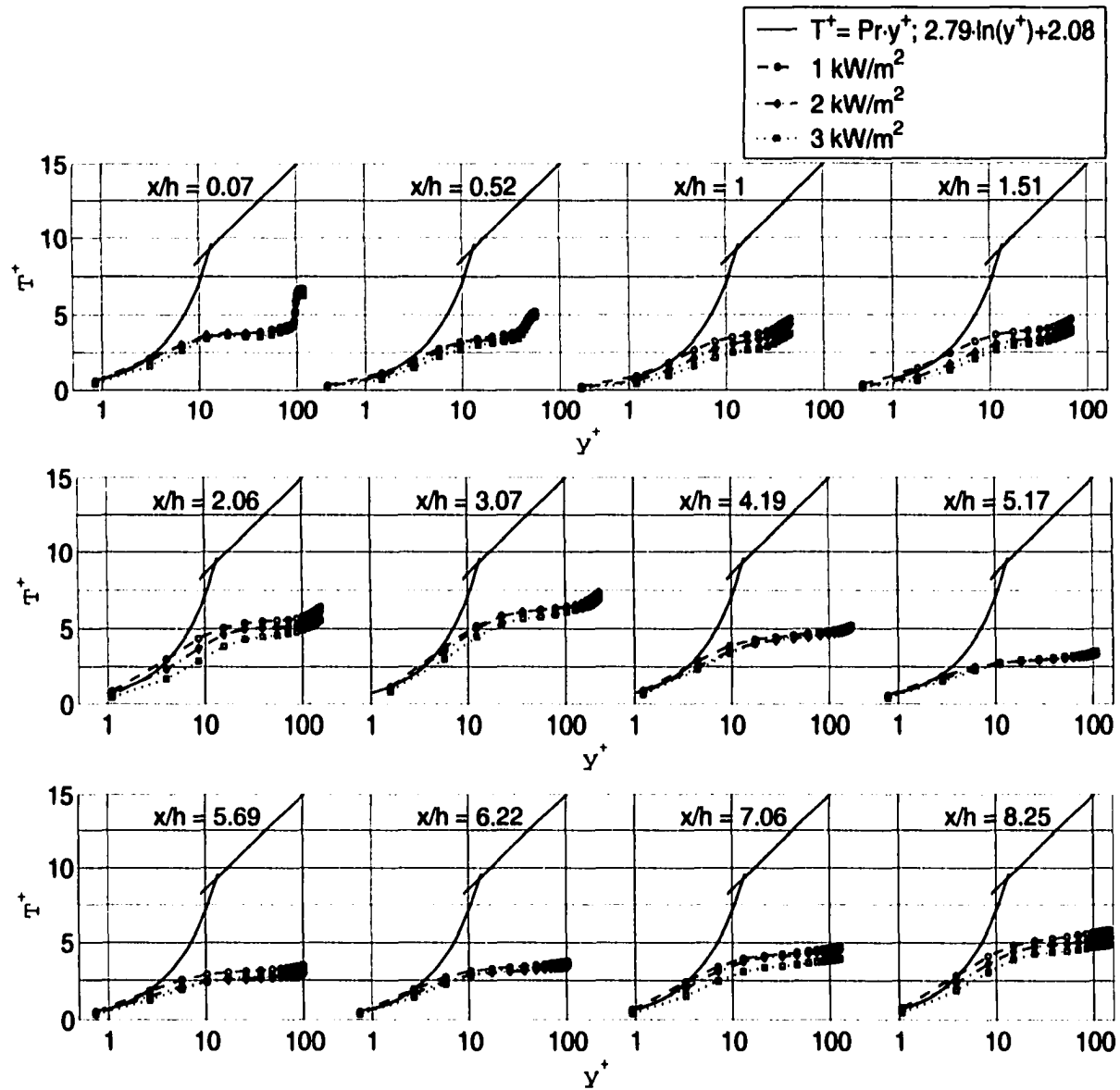


Figure 5.13 Mean temperature in wall coordinates

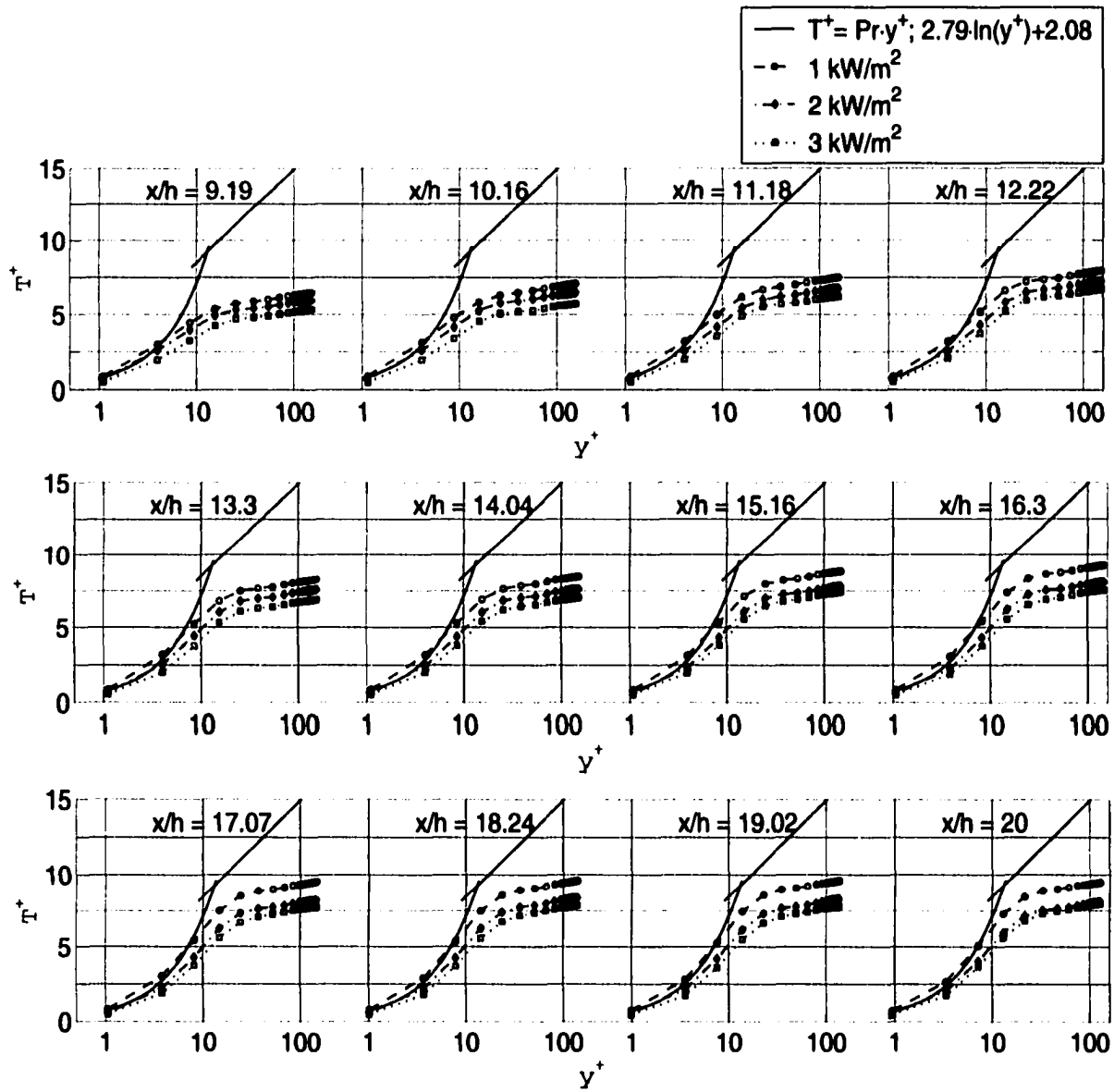


Figure 5.14 Mean temperature in wall coordinates

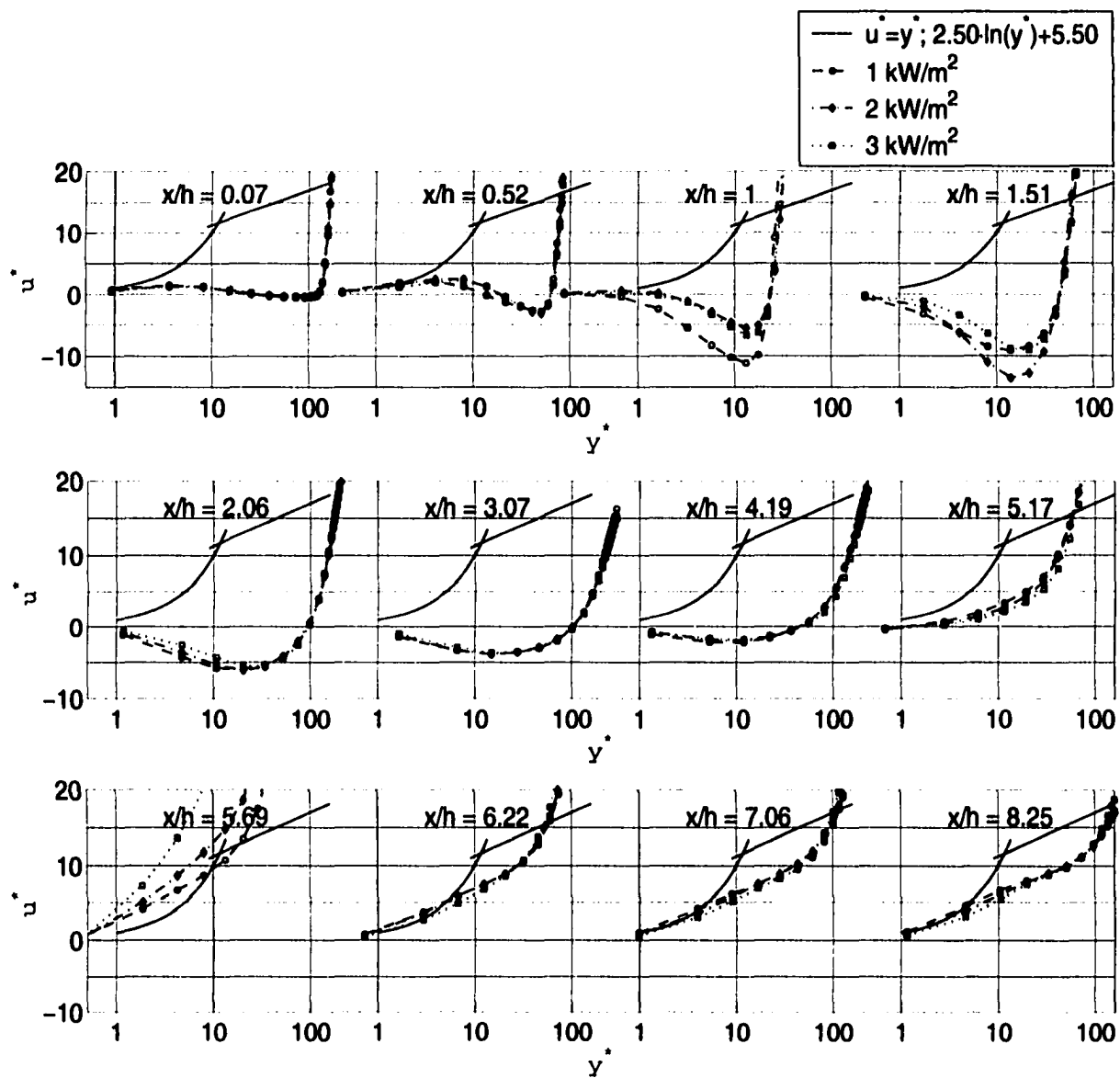


Figure 5.15 Mean streamwise velocity in semi-local coordinates

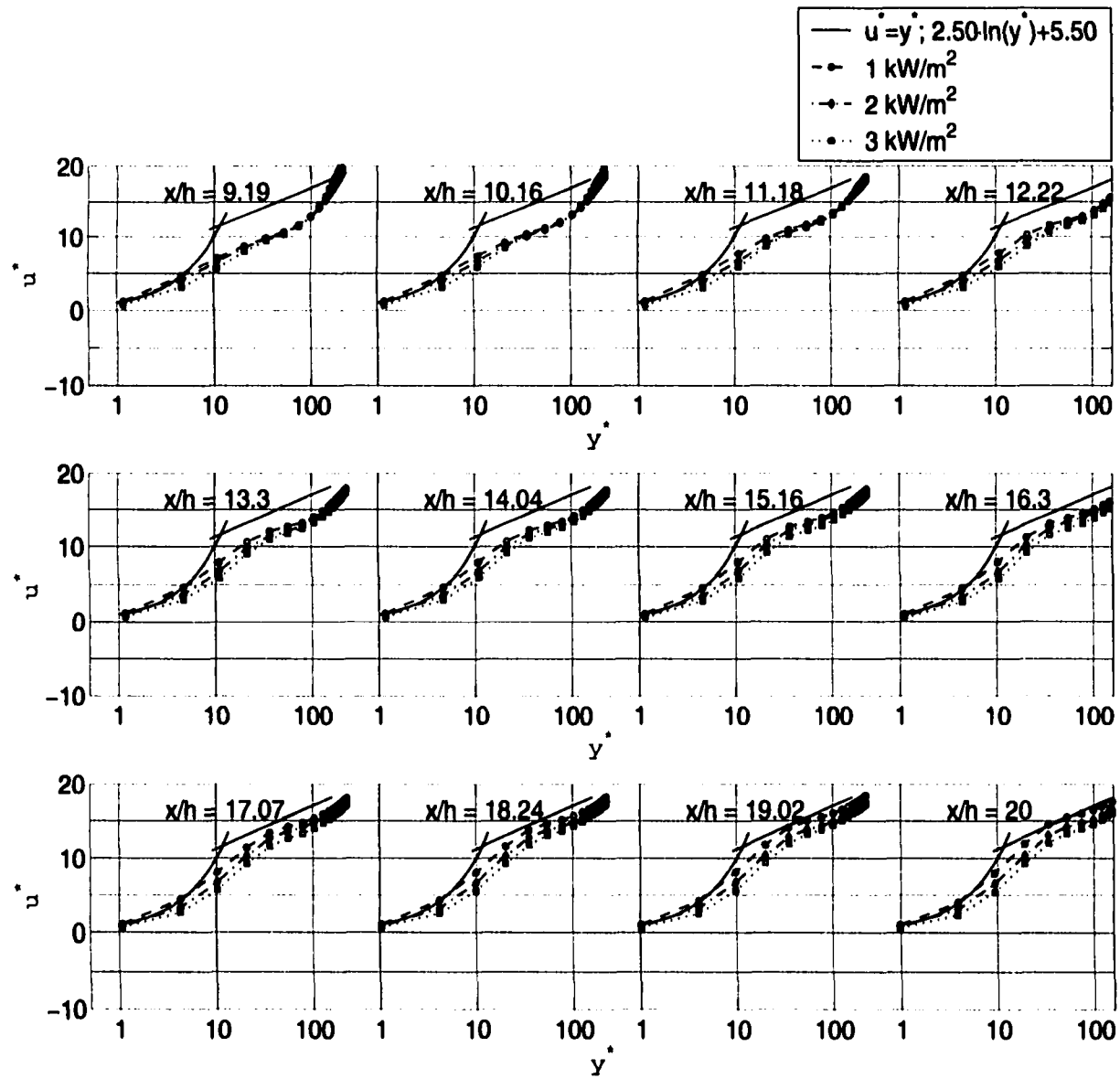


Figure 5.16 Mean streamwise velocity in semi-local coordinates

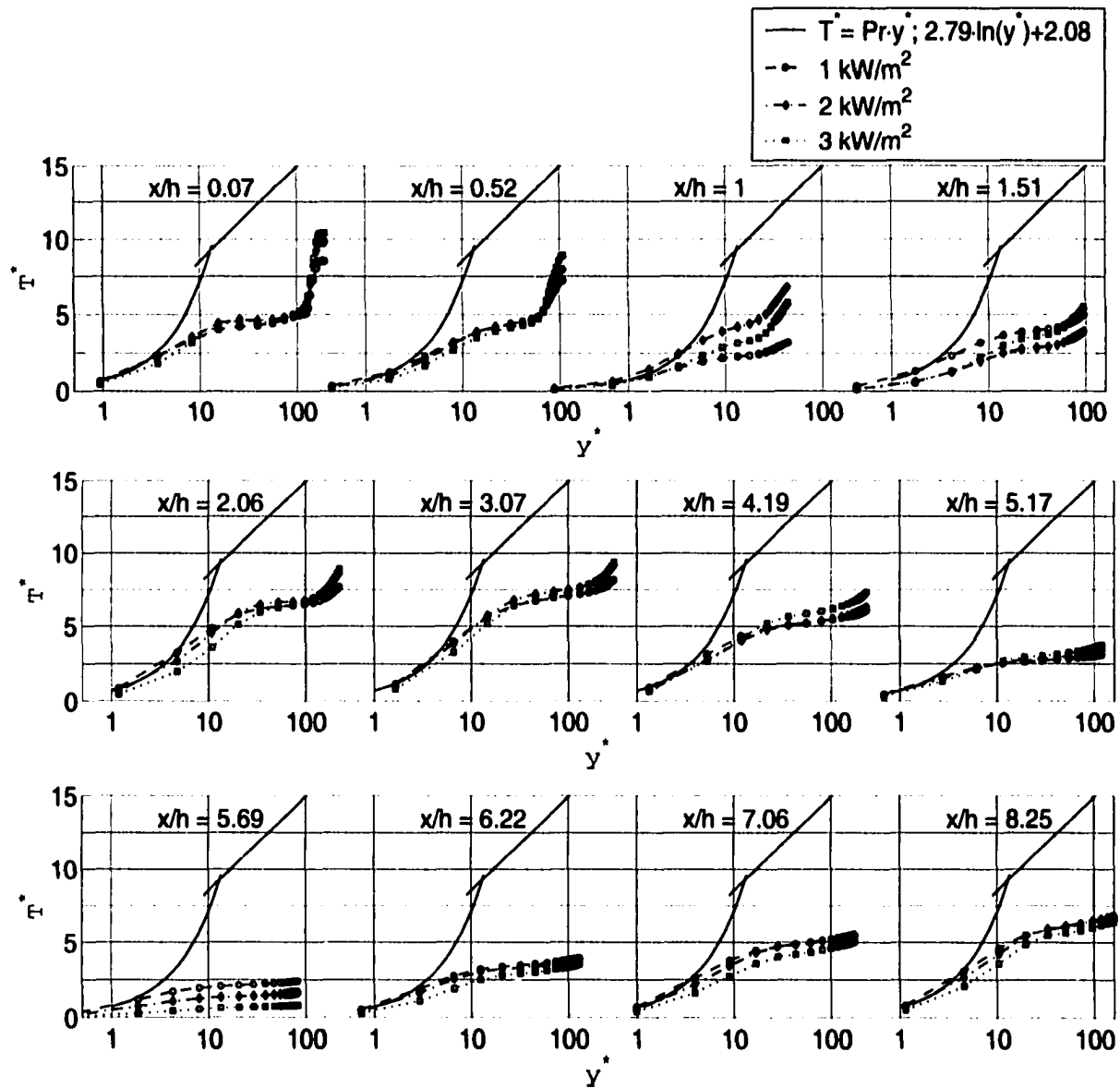


Figure 5.17 Mean temperature in semi-local coordinates

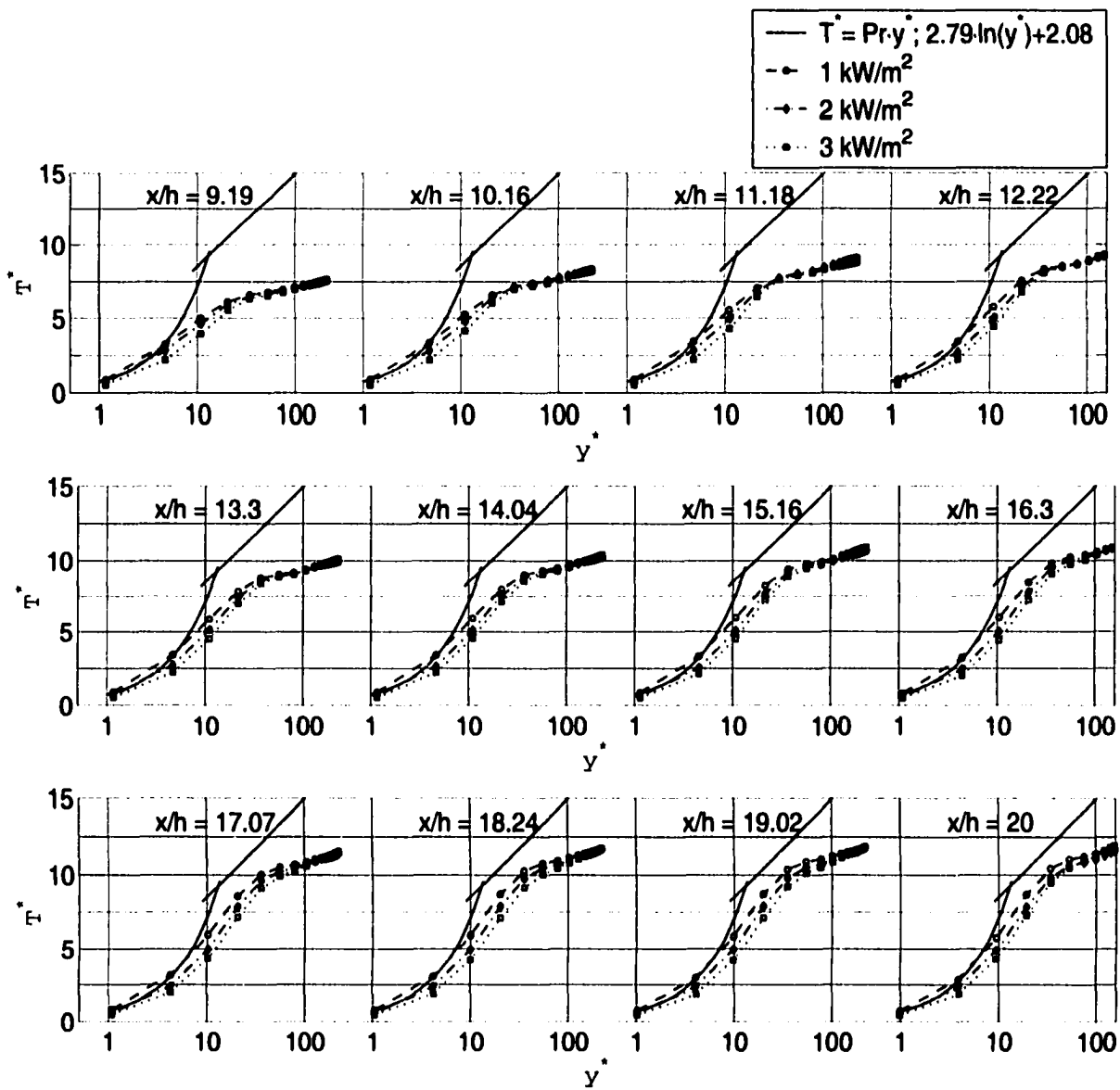


Figure 5.18 Mean temperature in semi-local coordinates

6.22. No further thinning of the viscous sub-layer can be observed at stations beyond $x/h = 6.22$, and this is keeping with the growth of the thermal boundary layer. The similarity between heat transfer and momentum transfer in flat-plate boundary layer flows has been termed the Reynolds analogy. For a constant free stream velocity, constant wall temperature, $Pr \approx 1$, and no unheated starting length, the rate of heat transfer is related to skin friction coefficient by

$$St = \frac{C_f}{2} \quad (5.12)$$

where $St = \frac{Nu}{Re Pr}$. Equation 5.12 itself is often called the Reynolds analogy. From a practical engineering stand point the Reynolds analogy offers the advantage that one can estimate the heat transfer, without further experimentation or calculations, from momentum transfer calculations alone should the momentum-heat transfer similarity be valid for the flow of interest. From inspection of the Stanton number profiles (Fig. 5.19) and the mean skin-friction profiles (Fig. 5.20) we can conclude that the Reynolds analogy does not hold in the recirculating region of the flow. Close to the step, both the Stanton number and skin-friction coefficient are small in magnitude and show a downward trend; the Stanton number attains its minimum close to the step and this implies a low level of convective heat transfer in this region. It is at these points of minimum Stanton number that the wall temperature (Fig. 5.9) takes on the maximum values. Rapid change in both St and C_f is observed in recirculating region. The skin-friction coefficient drops by three times the value at the step for the 3.0 kW/m^2 case, before starting to rise to zero at reattachment; the Stanton number rises from its minimum close to the step and attains a peak value upstream of reattachment suggesting a gradual increase in heat transfer due to convective mixing. Downstream of reattachment the two profiles start to resemble their flat-plate boundary layer counterparts.

While the Reynolds analogy does not hold in the mean sense in the recirculation region, it is possible that it might hold in an instantaneous sense. For this to be true, one would expect the mean Stanton number to be correlated with the time average of the absolute skin-

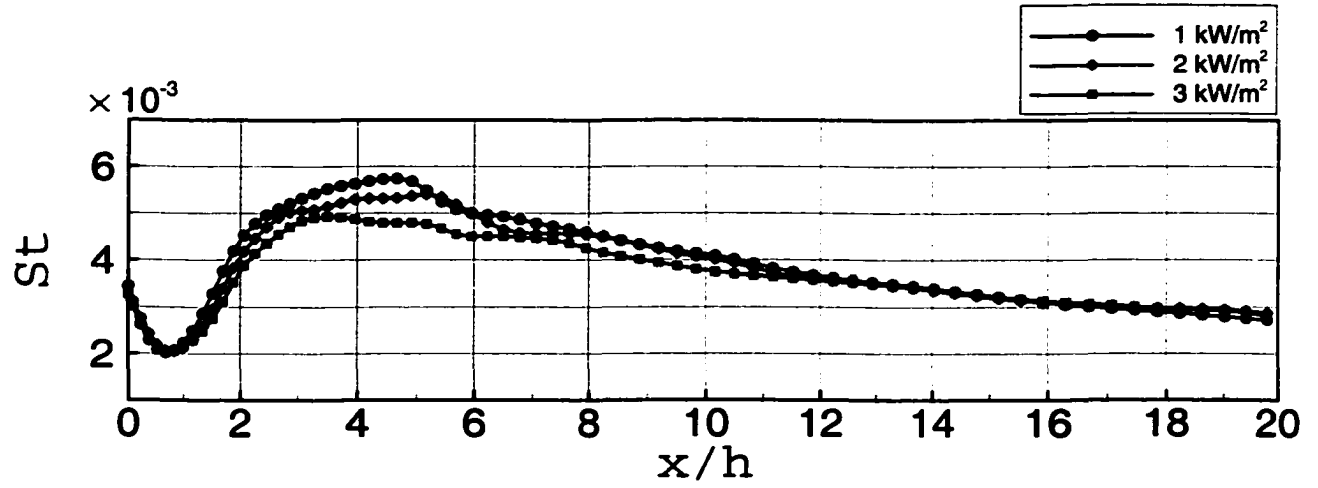


Figure 5.19 Mean Stanton number

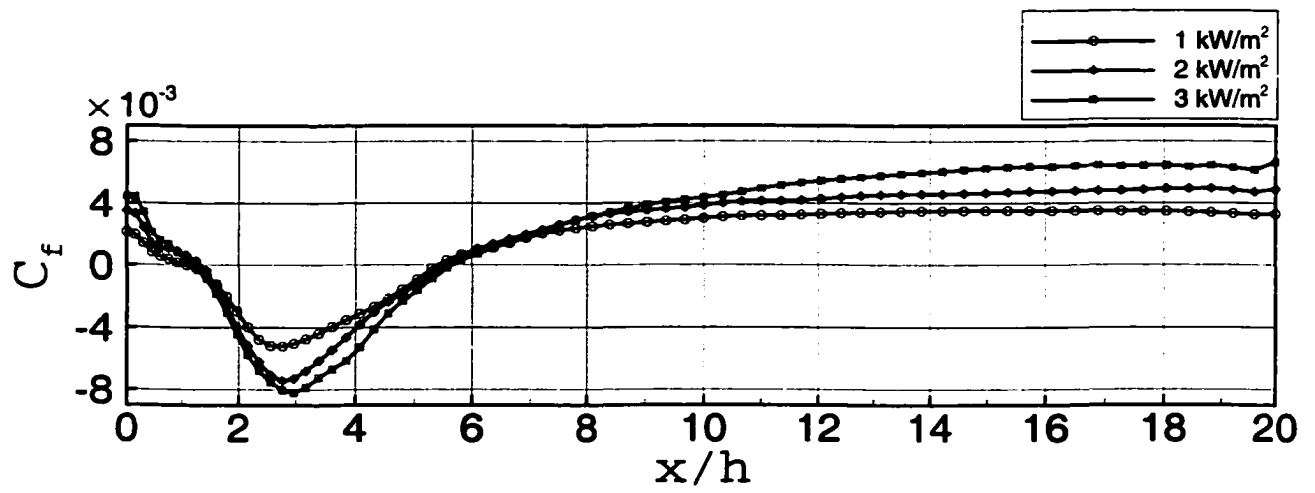


Figure 5.20 Mean skin-friction

friction coefficient, $|C_f|$. Comparing Figs. 5.19 and 5.22, it is seen that close to the step, the absolute value of the skin-friction coefficient and the Stanton number show downward trends and start to climb at nearly the same streamwise location. At roughly $x/h \sim 3$, the absolute value of the skin-friction coefficient and Stanton number diverge strongly from each other, nevertheless maintaining their positive values. It is in this sense of measure of sign, that the Stanton number agrees better with the absolute value of the skin-friction coefficient than it does with the mean skin-friction coefficient Vogel and Eaton [1984].

It is very interesting to note that the mean Stanton number profiles (Fig. 5.19) show a more striking similarity with the fluctuating skin-friction coefficient profiles (Fig. 5.23), than they do with the average absolute skin-friction coefficient (Fig. 5.22). The fluctuating skin-friction coefficient is computed as:

$$C'_f = \sqrt{(\langle C_f \rangle_z - C_f)^2} \quad (5.13)$$

and subsequently a span- and time-averaged value $\langle C'_f \rangle_{zt}$ is computed. The Stanton number profiles and the skin-friction coefficient show a downward trend close to the step, before the subsequent peak values upstream of reattachment. At reattachment itself, however, both the profiles have started to relax from the peak values. Vogel and Eaton [1984] indicate that this strong similarity of behavior in the fluctuating skin-friction coefficient and the Stanton number profiles underscores the importance of the near-wall region in determining the heat transfer rate. They also point out that the high degree of correlation between the fluctuating skin-friction coefficient and the Stanton number suggests that the correct velocity scale governing the strength of convective effects in the reattachment zone must be related to the velocity fluctuations rather than the mean velocity.

5.3.2 Velocity and temperature fluctuations

The root mean square (RMS) velocity fluctuations from the simulations with the different wall heat fluxes show excellent agreement with the experimental results. It must be recalled

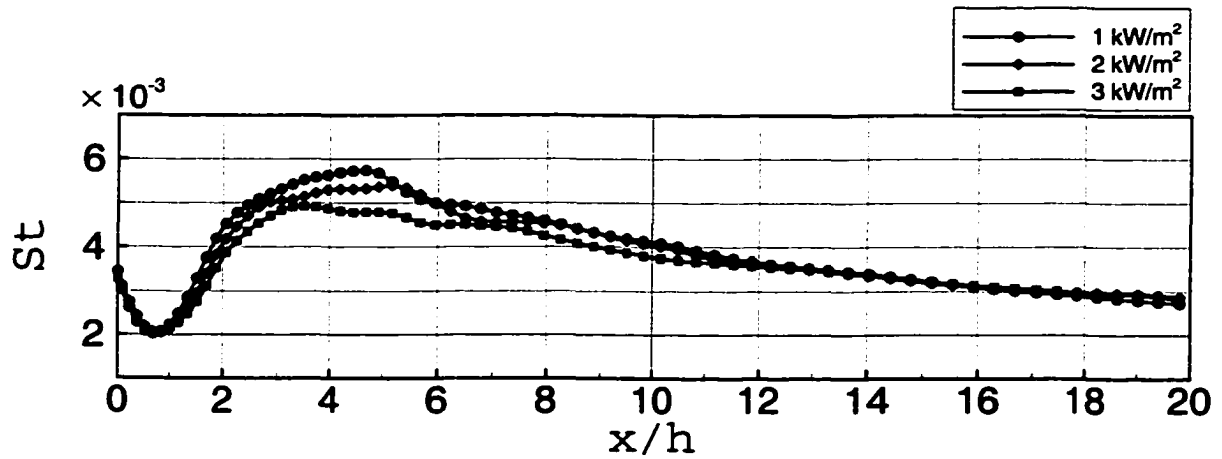


Figure 5.21 Mean Stanton number

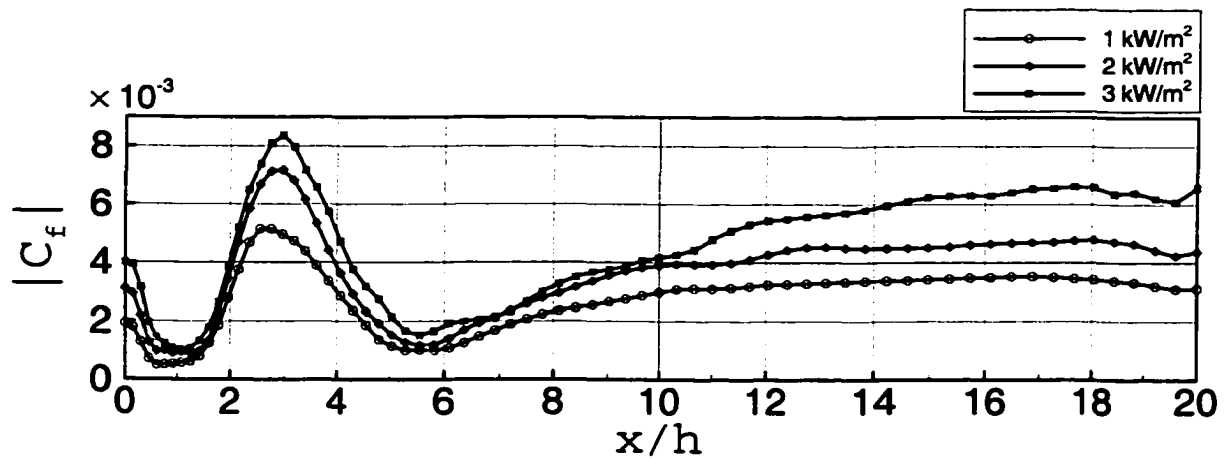


Figure 5.22 Average of absolute skin-friction coefficient

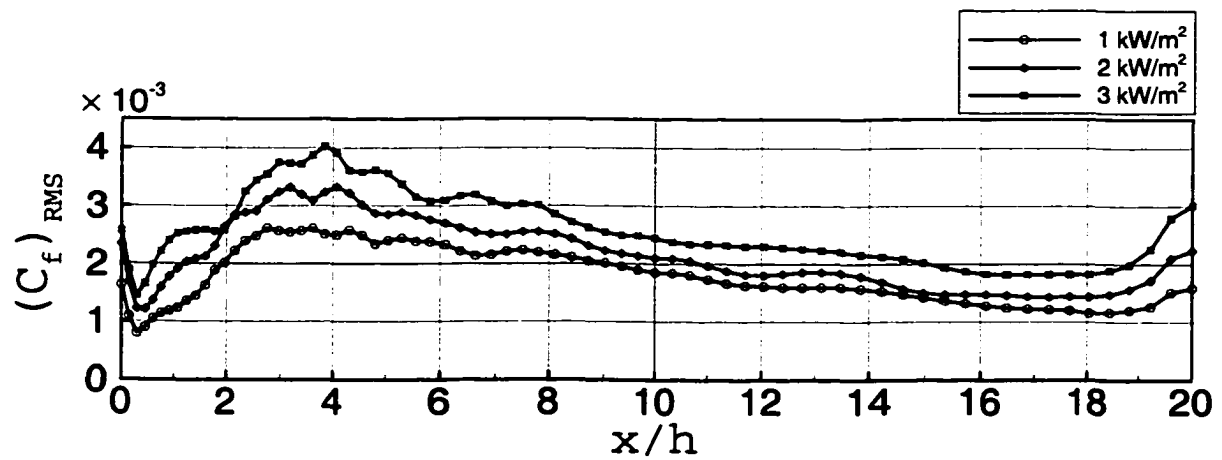


Figure 5.23 Fluctuating skin-friction coefficient

that there is no heat transfer involved in the experiments. For a detailed discussion of the behavior of the RMS fluctuations, see Sec. 4.5.4.

The level of temperature fluctuations depends on the local length scales of velocity and temperature [Vogel and Eaton, 1984]. If the temperature gradient is small, then large velocity fluctuations are necessary to create large temperature fluctuations. If the temperature gradient is large, then even small velocity fluctuations can result in large temperature fluctuations. The RMS temperature fluctuations are shown in Fig. 5.27. Expanded plots of the RMS temperature fluctuations are shown in Figs. 5.28 and 5.29. The highest level of temperature fluctuations is close to the step face, downstream of separation. The magnitude of the fluctuations across the shear layer decreases downstream of separation. These fluctuations in temperature are a result of “warm” fluid being transported upwards away from the wall, as evidenced by the positive wall-normal velocity, being exposed to “cooler” fluid being entrained into the same region by the separating shear layer. A gradual decrease of the temperature fluctuations away from the bottom wall can be observed, although we can observe an increase in the depth of penetration of these fluctuations. The peak levels in the temperature fluctuations, however, remain confined to the near wall region for all streamwise stations. It also obvious that the temperature fluctuations show an increase in magnitude with increasing values of wall heat flux.

The higher mean temperature gradients coupled with the velocity fluctuations result in large temperature fluctuations close to the step face. Farther downstream, the mean temperature gradients are confined to the near wall region and with a concentration of velocity fluctuations close to the wall, the temperature fluctuations are greatest near the wall. Downstream of reattachment, the mean temperature gradients show a greater spread away from the wall, and the fluctuations in temperature follow this spread. Essentially, the velocity fluctuations, the flow turbulence, play an important role in giving rise to fluctuations in temperature. For a flow constant in temperature, one would not expect to see any temperature fluctuations regardless of turbulence levels [Vogel and Eaton, 1984].

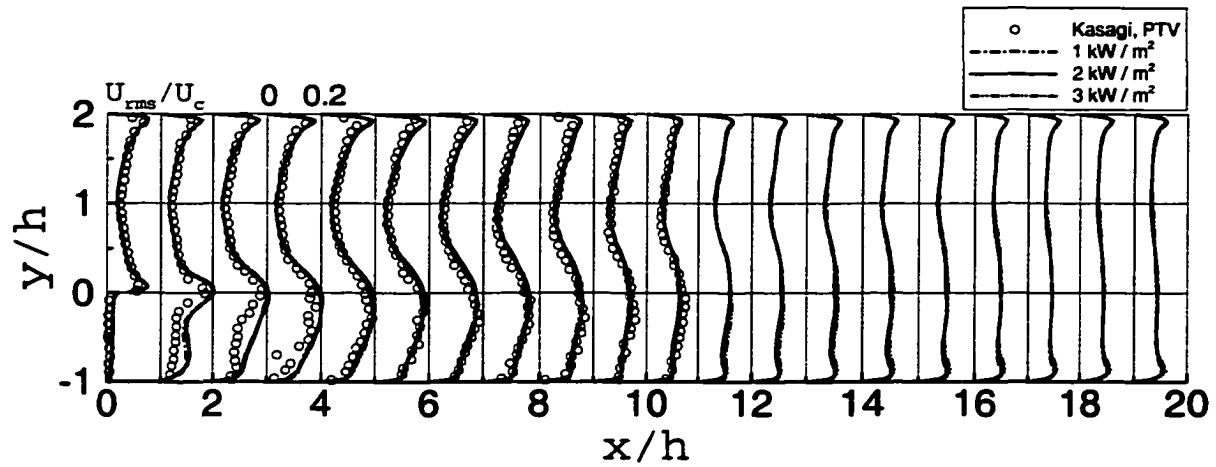


Figure 5.24 Streamwise RMS velocity fluctuations

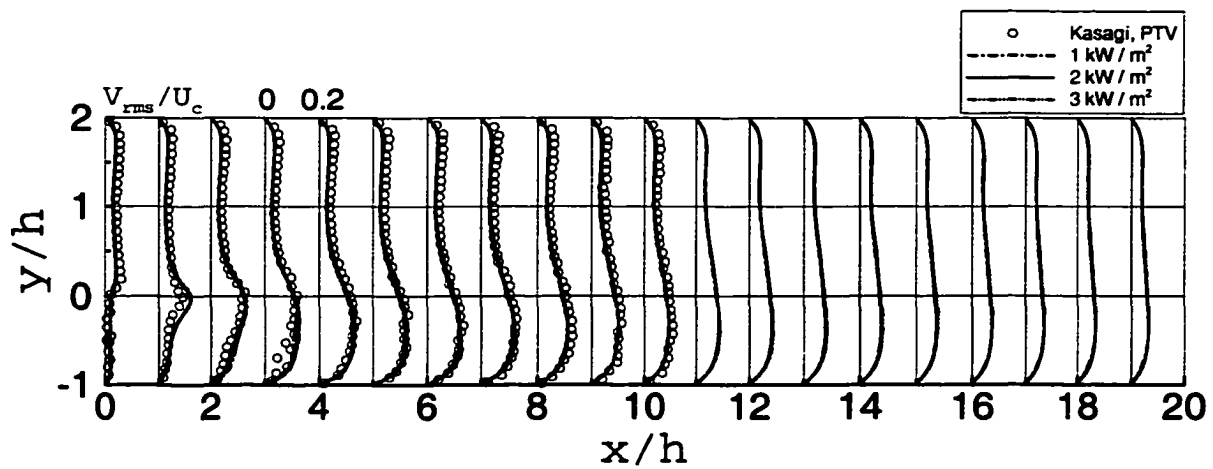


Figure 5.25 Wall-normal RMS velocity fluctuations

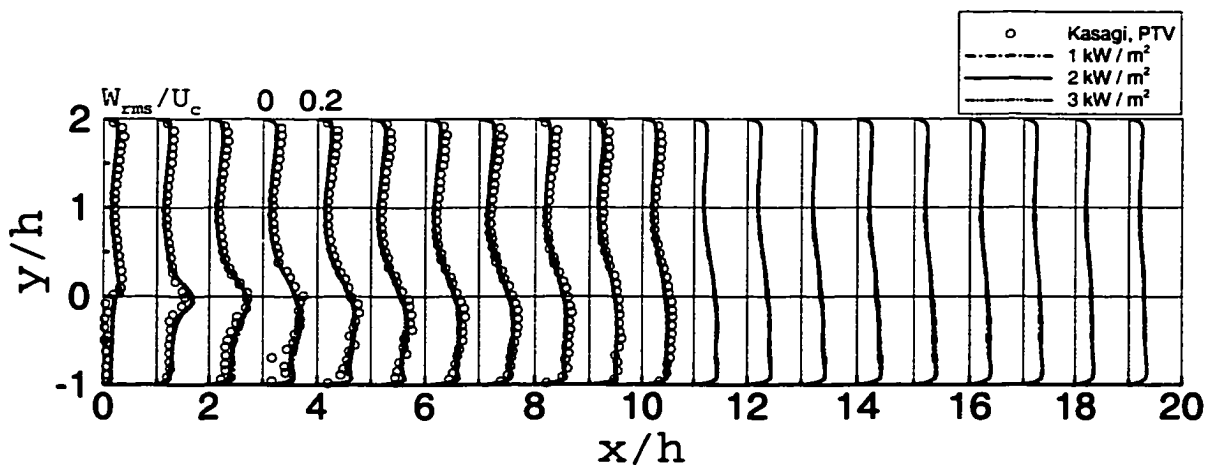


Figure 5.26 Spanwise RMS velocity fluctuations

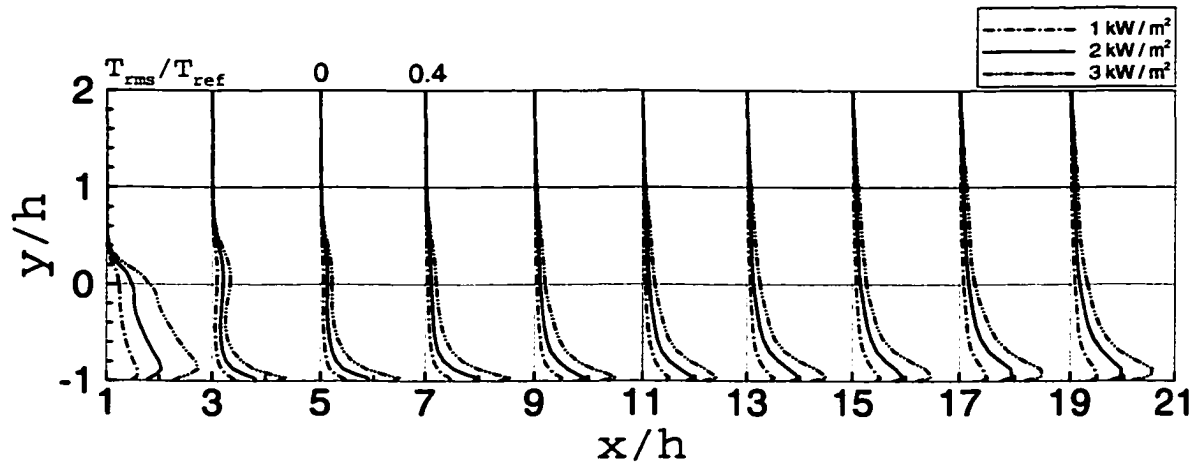


Figure 5.27 RMS temperature fluctuations

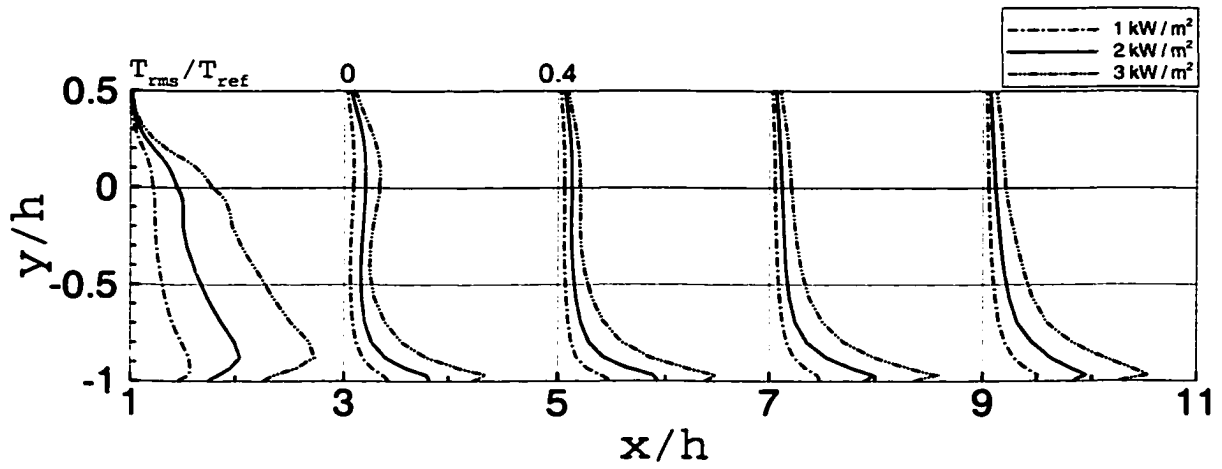


Figure 5.28 RMS temperature fluctuations

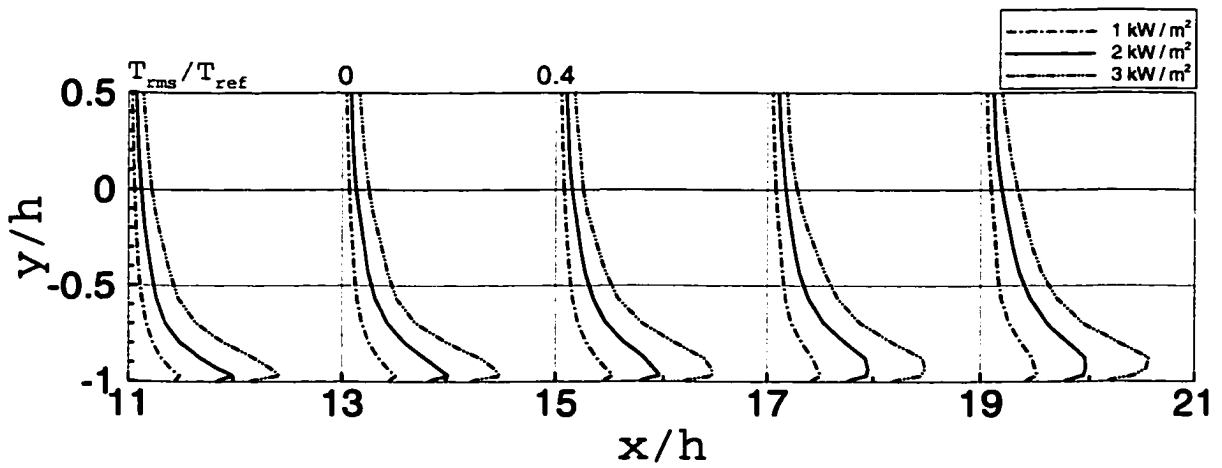


Figure 5.29 RMS temperature fluctuations

5.3.3 Cross-correlations of the velocity and temperature fluctuations

The cross-correlations of the velocity and temperature fluctuations $\langle \rho u'' T'' \rangle_{zt}$, $\langle \rho v'' T'' \rangle_{zt}$, $\langle \rho w'' T'' \rangle_{zt}$, shown in Figs. 5.30, 5.31, 5.32, represent the streamwise, wall-normal and spanwise turbulent heat flux components based on Favre-averaged fluctuations. For a comparison between the turbulent heat fluxes based on Reynolds- and Favre-averaged fluctuations see Appendix D. The transport of energy across the shear layer immediately downstream of the step is through the wall-normal turbulent heat flux, $\langle \rho v'' T'' \rangle_{zt}$ (also referred to as normal component of turbulent transport in Vogel and Eaton [1984]). This turbulent heat flux drops sharply on the warmer side of the shear layer (possibly indicating that the transport of energy here is by a mechanism other than the wall-normal velocity fluctuations) before it increases in the near-wall region (where the temperature fluctuations are larger than elsewhere owing to the large temperature gradients in combination with all components of velocity fluctuations). It is interesting to note that, at this same streamwise station, the streamwise turbulent heat flux $\langle \rho u'' T'' \rangle_{zt}$ shows a positive peak in the near-wall region and negative peak on the warmer side of the shear layer. The behavior of the streamwise turbulent heat flux, close to the step face, is a result of the non-negligible gradients of temperature and streamwise velocity fluctuations. The temperature gradients in streamwise direction are possibly due to the interplay between “colder” packets of fluid being entrained by the shear layer at separation and the “warmer” packets of fluid traveling upstream within the recirculation bubble. Farther downstream, a decrease in the vertical turbulent heat flux is observed, going away from the wall. However, as the thermal boundary layer develops and grows the turbulence levels are higher, and the magnitude of the vertical and streamwise turbulent heat fluxes successively increase traveling downstream. The depth to which these turbulent fluxes penetrate also increases downstream.

It is also important to note that Vogel and Eaton [1984] have indicated that the streamwise turbulent heat flux is negligible as compared to the wall-normal turbulent heat flux.

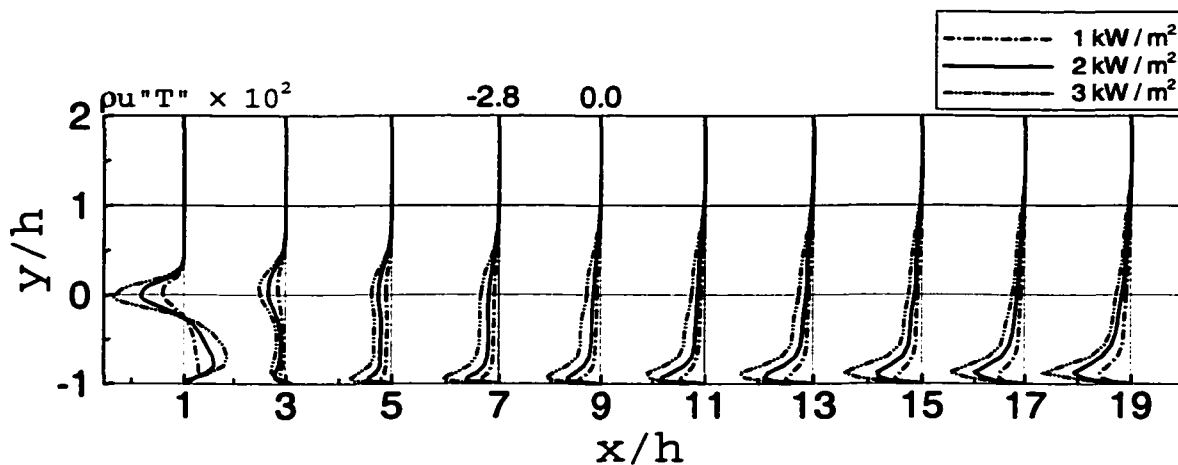


Figure 5.30 Streamwise turbulent heat flux

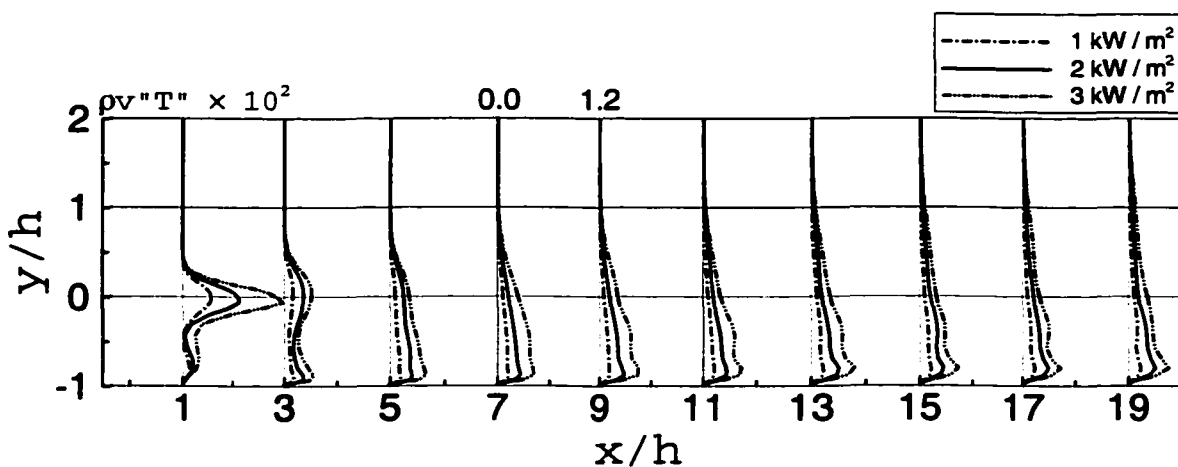


Figure 5.31 Wall-normal turbulent heat flux

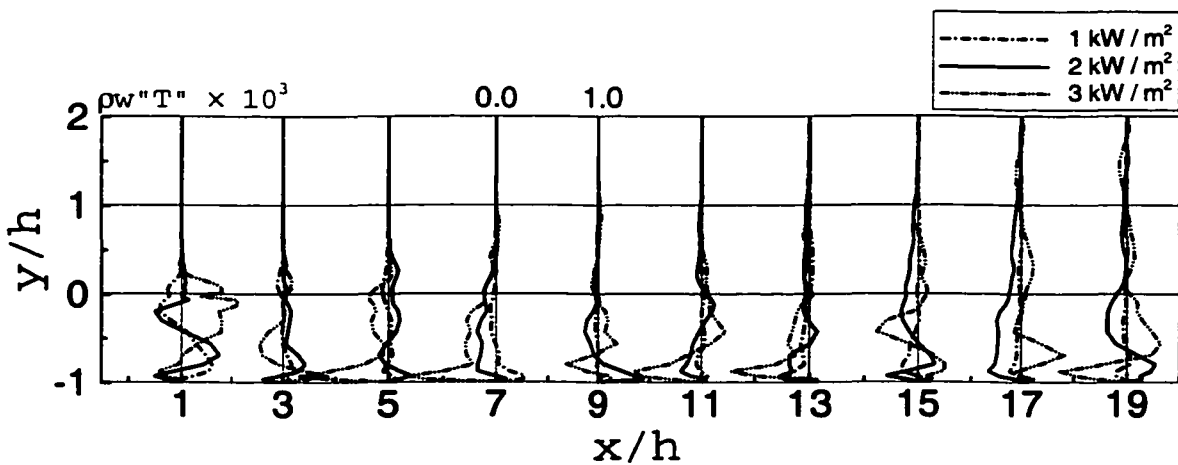


Figure 5.32 Spanwise turbulent heat flux

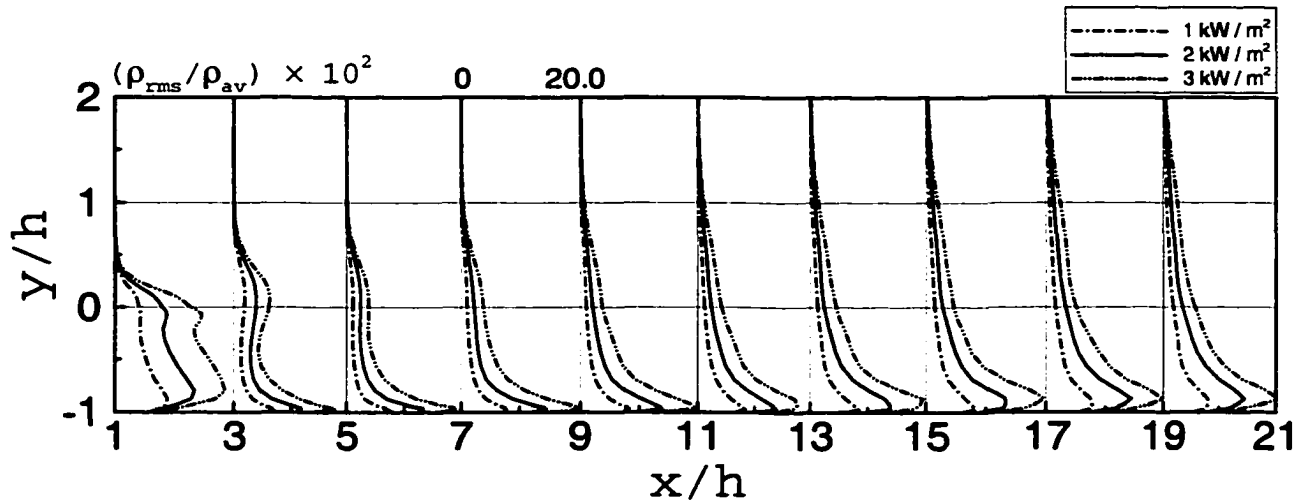


Figure 5.33 RMS density fluctuations

However, we show that while the streamwise turbulent heat flux, as in Fig. 5.30, is indeed smaller in magnitude than the wall-normal turbulent heat flux, Fig. 5.31, nevertheless it is non-negligible. The heat flux levels, and consequently the temperature gradients, in this work are an order of magnitude greater than in their study (130 W/m^2), and the Reynolds numbers are three to five times smaller. These are probable reasons for their observation of negligible streamwise turbulent heat flux in comparison with the vertical turbulent heat flux.

The spanwise turbulent heat flux was also computed and no specific conclusions can be drawn other than the fact that the transport of energy is much smaller through this mode of transport.

5.3.4 Density fluctuations

Root mean square density fluctuations, expressed as a percentage of the local span- and time-averaged density ρ_{av} , of up to 20 % are observed in Fig. 5.33. At the peak wall temperatures for the three heat flux cases, the viscosity and thermal conductivity are roughly about 20%, 40% and 60% greater than the values at the inlet, which are at the reference temperature of 293 K, thus demonstrating the need for property variations to be considered

in calculations involving high heat fluxes. For example, considering the expressions for the skin-friction coefficient, friction velocity, Nusselt number

$$C_f = \frac{2 \tau_w}{\rho U_{ref}^2} \quad (5.14)$$

$$Nu = \frac{h L_y}{k_{bulk}} \quad (5.15)$$

$$u_\tau = \sqrt{\frac{\tau_w}{\rho_w}}; \quad \tau_w = \mu \frac{\partial u}{\partial y} \quad (5.16)$$

and recalling that μ and k are functions of temperature whose variation is given by the power-law form of Sutherland's formula [Schlichting, 1979].

$$\frac{\mu^*}{\mu_{ref}} = \left(\frac{T^*}{T_{ref}} \right)^{0.71} \quad (5.17)$$

$$\frac{k^*}{k_{ref}} = \left(\frac{T^*}{T_{ref}} \right)^{0.71} \quad (5.18)$$

substantial change in the computed values of these quantities, as in Figs. 5.22, 5.10 amongst others, is observed for variations in the thermal conductivity and dynamic viscosity, especially for the range of wall temperatures as observed in Fig. 5.9. Figures 5.35 and 5.34 show the variation in the dimensional values of μ and k based on Sutherland's law. All the calculations included in the review by Abrous and Emery [1996] have used wall heat flux values of 5.0 kW/m² and relied on the assumption of constant properties, and it is our contention that it is important to consider the effects of property variations.

5.4 Summary

Large eddy simulations to study the heat transfer and fluid dynamics of the turbulent reattaching flow past a backward-facing step have been successfully conducted. The choice of the formulation enabled the inclusion of property variations, and facilitated the study at low Mach numbers.

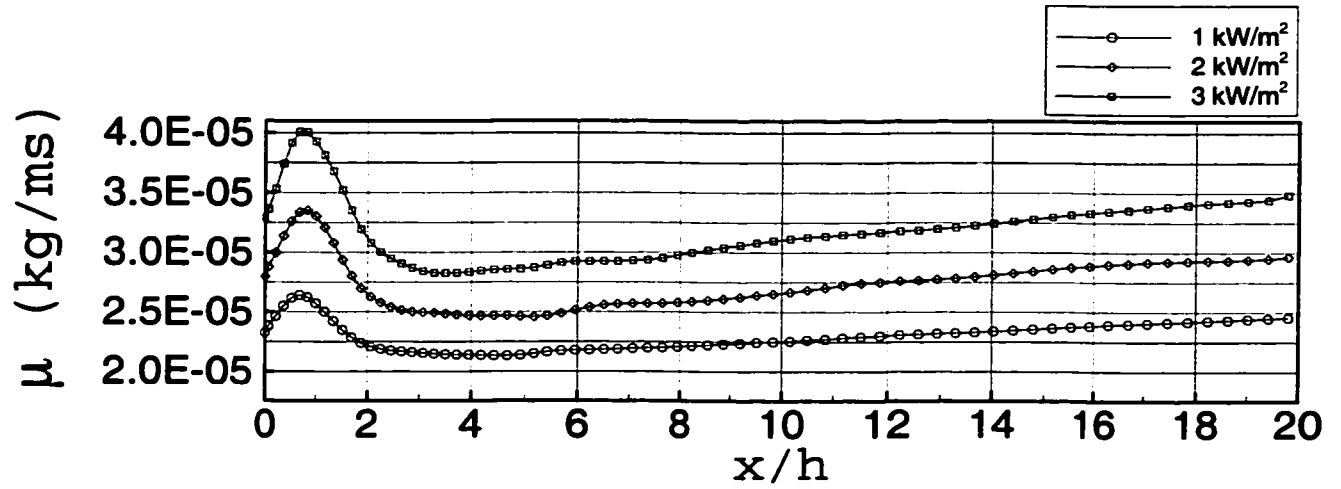


Figure 5.34 Variation in dynamic viscosity

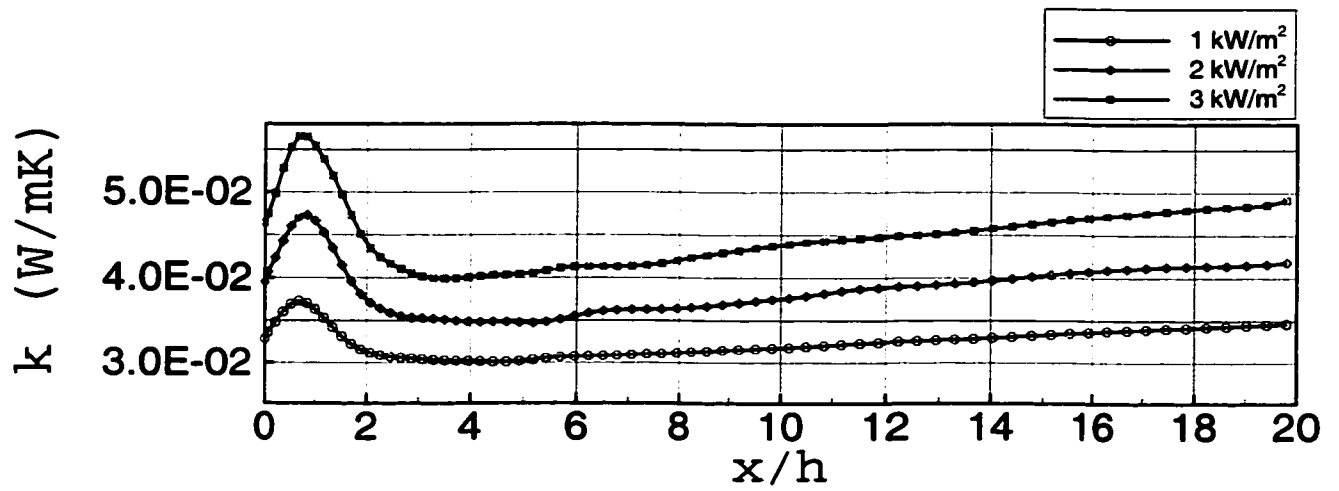


Figure 5.35 Variation in thermal conductivity

The mean velocity profiles are in good agreement with the isothermal experimental results of Kasagi and Matsunaga [1995]. The mean temperature profiles are in good qualitative agreement with Vogel and Eaton [1984]. The law of the wall for the mean streamwise velocity or the mean temperature do not hold in the recirculation region, nor in the recovery region; however, farther downstream of reattachment the mean velocity and temperature tend toward their respective law of the wall profiles. Gradients in mean temperature are confined to the region close to the wall along the length of the downstream section except close to the step where they also exist across the separating shear layer, and near the secondary recirculation eddy. Bulk temperature profiles are in excellent agreement with analytical estimates. Dramatic variation of the wall temperatures in the recirculation region is observed with a steep increase in wall temperature close to the step accompanied by a decrease in convective heat transfer.

The peak heat transfer rate occurs slightly upstream of reattachment. The viscous sub-layer is responsible in controlling the rate of conduction heat transfer, and a strong correlation can be observed between the Nusselt/Stanton numbers and the thickness of the viscous sub-layer; where the viscous sub-layer is at its thickest, the Nusselt/Stanton numbers are at their minimum values. While the Reynolds analogy for the mean flow is not valid for a flow with separation and reattachment, the possibility of a "instantaneous" Reynolds analogy corroborates with the observations of Vogel and Eaton [1984]. The Stanton number profiles correlate strongly with the fluctuating skin-friction coefficient profiles. The RMS velocity fluctuations are in good agreement with the isothermal experimental results of Kasagi and Matsunaga [1995]. The RMS temperature fluctuations are greater close to the wall, and can be observed to spread away from the wall with the growth of the thermal boundary layer. Streamwise and wall-normal turbulent heat fluxes, indicative of thermal energy transport due to turbulence, are of the same order of magnitude. RMS density fluctuations of up to 20% are observed, as are significant variations in viscosity and thermal conductivity.

CHAPTER 6 CONCLUSIONS AND RECOMMENDATIONS

A summary of the dissertation, and significant contributions from this study are presented in Section 6.1. Recommendations for future work are presented in Section 6.2.

6.1 Summary and Contributions

A robust colocated-grid finite volume scheme, using a non-linear filter to suppress numerical oscillations, for the large eddy simulation of complex turbulent flows with heat transfer and property variations was developed and tested. The finite volume procedure solves the Favre-filtered Navier-Stokes equations in a fully-implicit manner with second- or fourth-order central differences for the convective terms and fourth-order central differences for the viscous terms. Time derivative preconditioning was incorporated and it enabled the computation of low-Mach number (essentially incompressible) flows with density variations using a fully coupled compressible formulation. The compressible extension [Moin et al., 1991] to the incompressible dynamic subgrid scale modeling procedure [Germano et al., 1991] has been used to account for effects of the smaller scales on the large scale flow.

The starting point for this work was a code developed by Wang [1995] that had problems associated with the instability of the central difference schemes, subsequently addressed by Narayanan [1998], and issues related to pressure-velocity decoupling, peculiar to colocated-grid schemes. While Narayanan [1998] adapted the momentum-interpolation correction [Rhie and Chow, 1983] to laminar flows and the large eddy simulation of isotropic decaying turbulence, a severe penalty in the time step was incurred that discouraged its use in the simulation

of the turbulent flow past a backward facing step.

The Navier-Stokes characteristic boundary condition (NSCBC) [Poinsot and Lele, 1992] method to provide boundary conditions for direct and large eddy simulations of compressible viscous flows was successfully implemented and tested.

The aforementioned finite volume procedure for large eddy simulations, and boundary conditions strategy were utilized in the simulation of the isothermal turbulent flow past a backward-facing step. The LES formulation demonstrated the ability to capture the complex flow physics encountered in this geometry very well. Good agreement with the experimental results for the mean flow, and the turbulent statistics was obtained. The use of the sixth-order compact filter [Lele, 1992] to curb oscillations peculiar to colocated grid schemes, at the grid-level frequencies, without affecting the realistic turbulent fluctuations was successfully demonstrated.

Having tested the capability of the formulation for the isothermal turbulent flow, large eddy simulations of turbulent flows with significant heat transfer, achieved by specifying a constant wall heat flux, resulting in property variations were carried out for the same geometry. Results from the simulation are in very good qualitative agreement with the experimental results of Vogel and Eaton [1984].

Significant contributions, and important results of this study are indicated below.

1. Development of a second-order accurate, cell-centered, colocated grid, fully coupled compressible formulation employing central differences for the large eddy simulation of a complex turbulent flow such as the flow past a backward-facing step with significant heat transfer and property variations.

While large eddy simulations have been carried out for the turbulent flow in this geometry, this is first known to include the effects of heat transfer and property variations. Most treatments of the turbulent flow for this geometry with heat transfer have utilized incompressible formulations with the assumption of constant properties in the

framework of RANS type approaches that have met with limited success.

2. Provided an understanding of the relevant heat transfer mechanisms in turbulent separated and reattaching flows by way of large eddy simulation. To the best of the author's knowledge, results from these simulations are the first known to support several results from the experimental studies carried out by Vogel and Eaton [1984]. RANS methods have proved inadequate and have yielded rather inconsistent results [Abrous and Emery, 1996] for the skin friction, location of the peak Nusselt number and peak wall temperatures, and the shape of the Nusselt number profiles.

Key results from the large eddy simulations conducted include:

- (a) With increasing heat flux, the effects of conduction heat transfer start to dominate convective mixing effects; the role of the viscous sub-layer in controlling the conduction heat transfer is ascertained through examination of the mean streamwise velocity and mean temperature profiles in wall and semi-local coordinates.
- (b) While the Reynolds analogy clearly does not exist for a recirculating flow in the mean sense, it is interesting to note that it might hold in an instantaneous sense. The mean Stanton number and the RMS skin-friction coefficient show a striking similarity of behavior.
- (c) Vogel and Eaton [1984] indicated that the streamwise turbulent heat flux was negligible in comparison to the wall-normal turbulent heat flux. However, in this study, it has been shown that the two are of the same order of magnitude.
- (d) RMS density variations, as a percentage of the local span- and time-averaged density, of up to 20% for a wall heat flux of 3.0kW/m^2 are observed. At the peak wall temperatures for the three heat flux cases, the viscosity and the thermal conductivity are roughly 20%, 40% and 60% greater than at their inlet values (where the temperature is 293.0 K), respectively. A need for considering the

effects of property variations where similar levels of heat fluxes are used is thus, clearly demonstrated.

3. Implemented and tested the Navier-Stokes characteristic boundary condition (NSCBC) method designed by Poinso and Lele [1992] for the large eddy simulations carried out in this study. This enables the computation of other complex and spatially developing flows where periodic boundary conditions are not applicable.
4. Developed and tested a version of the large eddy simulation code suitable for distributed memory architecture machines such as the SGI Origin2000. However, there appear to be some obstacles in achieving a good degree of efficiency and these issues have been identified. (See Appendix 3)

6.2 Recommendations for Future Work

With specific reference to this study and geometry the following are key recommendations:

1. Attempt simulations with finer grid resolution to determine if there are major changes in the prediction of turbulence intensities and heat fluxes distribution, skin-friction, Nusselt and Stanton numbers and other relevant quantities.
2. Consider the effects of varying the Reynolds number for the same heat flux values as in this study.
3. Many of the RANS studies, indicated in Chapter 1 involved heat flux levels of 5.0 kW/m². It would be interesting to attempt simulations using those heat flux levels, but it may be important to consider buoyancy effects at those heat flux levels, depending upon the flow Reynolds number.
4. Consideration of the effects of rotation on the turbulent heat transfer for this geometry.

5. It would be very interesting to attempt simulations with constant temperature wall boundary conditions in contrast to the constant wall heat flux conditions used in this study.

**APPENDIX A JACOBIAN MATRICES FOR FAVRE FILTERED
SYSTEM OF EQUATIONS**

$$[A_{inv}] = \begin{bmatrix} \frac{\tilde{u}}{R\tilde{T}} & \frac{\bar{p}}{R\tilde{T}} & 0 & 0 & -\frac{\bar{p}\tilde{u}}{R\tilde{T}^2} \\ \frac{\tilde{u}^2}{R\tilde{T}} & 2\frac{\bar{p}\tilde{u}}{R\tilde{T}} & 0 & 0 & -\frac{\bar{p}\tilde{u}^2}{R\tilde{T}^2} \\ \frac{\tilde{u}\tilde{v}}{R\tilde{T}} & \frac{\bar{p}\tilde{v}}{R\tilde{T}} & \frac{\bar{p}\tilde{u}}{R\tilde{T}} & 0 & -\frac{\bar{p}\tilde{u}\tilde{v}}{R\tilde{T}^2} \\ \frac{\tilde{u}\tilde{w}}{R\tilde{T}} & \frac{\bar{p}\tilde{w}}{R\tilde{T}} & 0 & \frac{\bar{p}\tilde{u}}{R\tilde{T}} & -\frac{\bar{p}\tilde{u}\tilde{w}}{R\tilde{T}^2} \\ \frac{\tilde{u}}{R} & \frac{\bar{p}}{R} & 0 & 0 & 0 \end{bmatrix} \quad (\text{A.1})$$

$$[B_{inv}] = \begin{bmatrix} \frac{\tilde{v}}{R\tilde{T}} & 0 & \frac{\bar{p}}{R\tilde{T}} & 0 & -\frac{\bar{p}\tilde{u}}{R\tilde{T}^2} \\ \frac{\tilde{v}\tilde{u}}{R\tilde{T}} & \frac{\bar{p}\tilde{v}}{R\tilde{T}} & \frac{\bar{p}\tilde{u}}{R\tilde{T}} & 0 & -\frac{\bar{p}\tilde{v}\tilde{u}}{R\tilde{T}^2} \\ \frac{\tilde{v}^2}{R\tilde{T}} & 0 & 2\frac{\bar{p}\tilde{v}}{R\tilde{T}} & 0 & -\frac{\bar{p}\tilde{v}^2}{R\tilde{T}^2} \\ \frac{\tilde{v}\tilde{w}}{R\tilde{T}} & 0 & \frac{\bar{p}\tilde{w}}{R\tilde{T}} & \frac{\bar{p}\tilde{v}}{R\tilde{T}} & -\frac{\bar{p}\tilde{v}\tilde{w}}{R\tilde{T}^2} \\ \frac{\tilde{v}}{R} & 0 & \frac{\bar{p}}{R} & 0 & 0 \end{bmatrix} \quad (\text{A.2})$$

$$[C_{inv}] = \begin{bmatrix} \frac{\tilde{w}}{R\tilde{T}} & 0 & 0 & \frac{\bar{p}}{R\tilde{T}} & -\frac{\bar{p}\tilde{w}}{R\tilde{T}^2} \\ \frac{\tilde{w}\tilde{u}}{R\tilde{T}} & \frac{\bar{p}\tilde{w}}{R\tilde{T}} & 0 & \frac{\bar{p}\tilde{u}}{R\tilde{T}} & -\frac{\bar{p}\tilde{w}\tilde{u}}{R\tilde{T}^2} \\ \frac{\tilde{w}\tilde{v}}{R\tilde{T}} & 0 & \frac{\bar{p}\tilde{w}}{R\tilde{T}} & \frac{\bar{p}\tilde{v}}{R\tilde{T}} & -\frac{\bar{p}\tilde{w}\tilde{v}}{R\tilde{T}^2} \\ \frac{\tilde{w}^2}{R\tilde{T}} & 0 & 0 & 2\frac{\bar{p}\tilde{w}}{R\tilde{T}} & -\frac{\bar{p}\tilde{w}^2}{R\tilde{T}^2} \\ \frac{\tilde{w}}{R} & 0 & 0 & \frac{\bar{p}}{R} & 0 \end{bmatrix} \quad (\text{A.3})$$

$$[A_{vis}] = \begin{bmatrix} 0 & 0 & 0 & 0 & 0 \\ 0 & \frac{\mu}{Re} \frac{\partial}{\partial x} & 0 & 0 & 0 \\ 0 & 0 & \frac{\mu}{Re} \frac{\partial}{\partial x} & 0 & 0 \\ 0 & 0 & 0 & \frac{\mu}{Re} \frac{\partial}{\partial x} & 0 \\ 0 & 0 & 0 & 0 & \frac{k}{Re Pr} \frac{\partial}{\partial x} \end{bmatrix} \quad (\text{A.4})$$

$$[B_{vis}] = \begin{bmatrix} 0 & 0 & 0 & 0 & 0 \\ 0 & \frac{\mu}{Re} \frac{\partial}{\partial y} & 0 & 0 & 0 \\ 0 & 0 & \frac{\mu}{Re} \frac{\partial}{\partial y} & 0 & 0 \\ 0 & 0 & 0 & \frac{\mu}{Re} \frac{\partial}{\partial y} & 0 \\ 0 & 0 & 0 & 0 & \frac{k}{Re Pr} \frac{\partial}{\partial y} \end{bmatrix} \quad (\text{A.5})$$

$$[C_{vis}] = \begin{bmatrix} 0 & 0 & 0 & 0 & 0 \\ 0 & \frac{\mu}{Re} \frac{\partial}{\partial z} & 0 & 0 & 0 \\ 0 & 0 & \frac{\mu}{Re} \frac{\partial}{\partial z} & 0 & 0 \\ 0 & 0 & 0 & \frac{\mu}{Re} \frac{\partial}{\partial z} & 0 \\ 0 & 0 & 0 & 0 & \frac{k}{Re Pr} \frac{\partial}{\partial z} \end{bmatrix} \quad (\text{A.6})$$

APPENDIX B AN ESTIMATE OF FLUID BULK TEMPERATURE

The following expression from Incropera and DeWitt [1990] (Chapter 8, Eq.8.40) may be used to obtain an expression for the bulk temperature gradient in the streamwise direction:

$$\frac{dT_B}{dx} = \frac{q_w P}{\dot{m} C_p} = \frac{q_w (L_z * L_{ref})}{\left[\int_y \int_z \rho u dy dz \right] \rho_{ref} U_{ref} L_{ref}^2} \quad (B.1)$$

where $U_{ref} = 2.063$ m/s, $L_{ref} = 0.041$ m, $\rho_{ref} = 1.194$ kg/m³ and $C_p = 1006.0$ J/kg K. The non-dimensional mass flow rate, \dot{m} , obtained from the isothermal simulation was 6.96, and the non-dimensional spanwise length L_z was 4.02. The bulk temperature gradient is:

$$\frac{dT_B}{dx} = q_w \times 0.005698 \quad (B.2)$$

For different wall heat flux values, the bulk temperature gradients and the bulk temperatures are calculated ($T_{ref} = 293.0$ K) and shown in Table B.1.

Table B.1 Estimates of certain quantities for different heat flux values

No.	Wall heat flux (q_w)	dT_B/dx	$(\Delta T_B)_{x/h=20}$	$(T_B)_{x/h=20}$	T_B/T_{ref}
1	5000	28.49	23.36	316.36	1.08
2	4000	22.79	18.69	311.69	1.06
3	3000	17.09	14.02	307.02	1.04
4	2000	11.40	9.35	302.35	1.03
5	1000	5.70	4.67	297.67	1.01

APPENDIX C AN ESTIMATE OF BUOYANCY EFFECTS

The ratio of the Grashof number Gr to the square of the Reynolds number Re is considered to be the relevant dimensionless parameter to determine whether the effects of free convection need to be considered [Incropera and DeWitt, 1990]. They state that the combined effects of free and forced convection must be considered when $\frac{Gr}{Re^2} \approx 1$. If the inequality $\frac{Gr}{Re^2} \ll 1$ is satisfied, free convection effects may be neglected. This ratio is given as:

$$\frac{Gr}{Re^2} = \frac{g\beta\Delta T L_{ref}}{U_{ref}^2} \quad (C.1)$$

Relevant quantities in order to estimate the effects of buoyancy are given in the table below. In the third column, the bulk temperature at the location of the peak wall temperature is designated as T_b . The fourth column contains the difference between the wall and bulk temperatures at the same location, and the average of the two temperatures is used to compute β shown in the fifth column.

Table C.1 Estimates of certain quantities to determine buoyancy effects

No.	Wall heat flux (q_w)	$(T_w)_{peak}$	T_b	$(T_w - T_b)$	$\beta (= \frac{1}{\frac{T_w + T_b}{2}})$	$\frac{Gr}{Re^2}$
1	1000	1.685	1.000	0.685	1.343	0.048
2	2000	2.357	1.000	1.357	1.678	0.076
3	3000	3.032	1.001	2.031	2.016	0.095

APPENDIX D COMPARISON OF TURBULENT TRANSPORT TERMS BASED ON REYNOLDS- AND FAVRE-AVERAGED FLUCTUATIONS

The following material has drawn upon the study of data from the direct numerical simulation of a compressible channel flow by Huang et al. [1995].

Nomenclature and definitions:

$$\langle \rangle \quad : \quad \text{Reynolds averaging} \quad (\text{D.1})$$

$$\{ \} \quad : \quad \text{Favre averaging} = \left(\text{for a variable } \phi, \{ \phi \} = \frac{\langle \rho \phi \rangle}{\langle \rho \rangle} \right) \quad (\text{D.2})$$

$$\phi' \quad : \quad \text{Turbulent fluctuations with respect to Reynolds averaging} \quad (\text{D.3})$$

$$\phi'' \quad : \quad \text{Turbulent fluctuations with respect to Favre averaging} \quad (\text{D.4})$$

Using the above definitions, we obtain:

$$\rho' \quad = \quad \rho - \langle \rho \rangle \quad (\text{D.5})$$

$$u_i'' \quad = \quad u_i - \{ u_i \} \quad (\text{D.6})$$

$$T'' \quad = \quad T - \{ T \} \quad (\text{D.7})$$

$$\langle p \rangle \quad = \quad \langle \rho \rangle R \{ T \} = \langle \rho \rangle R \langle T \rangle + R \langle \rho' T' \rangle \quad (\text{D.8})$$

$$= \quad \langle \rho \rangle R (\langle T \rangle - \langle T'' \rangle) \quad (\text{D.9})$$

$$\{ u_i'' u_j'' \} \quad = \quad \frac{\langle \rho u_i'' u_j'' \rangle}{\langle \rho \rangle} \quad (\text{D.10})$$

We also note that $\langle \phi \rangle = 0$, $\langle \rho \phi'' \rangle = 0$ and $\langle \phi'' \rangle \neq 0$. The relationship between Reynolds-

and Favre-averaged quantities for velocities and temperature can be deduced as follows:

$$\langle \phi \rangle = \phi - \phi' \quad (\text{D.11})$$

$$\{ \phi \} = \phi - \phi'' \quad (\text{D.12})$$

Subtracting one equation from the other, and Reynolds-averaging, we obtain

$$\langle \phi \rangle - \{ \phi \} = \langle \phi'' \rangle \quad (\text{D.13})$$

$$= -\frac{\langle \rho' \phi' \rangle}{\langle \rho \rangle} \quad (\text{D.14})$$

$$= -\frac{\langle \rho' \phi'' \rangle}{\langle \rho \rangle} \quad (\text{D.15})$$

Relationships between the Reynolds- and Favre-averaged values for turbulent shear stresses and turbulent heat fluxes can be written as:

$$\{ u_i'' u_i'' \} = \langle u_i' u_j' \rangle - \langle u_i'' \rangle \langle u_j'' \rangle + \frac{\langle \rho' u_i' u_j' \rangle}{\langle \rho \rangle} \quad (\text{D.16})$$

$$\{ u_i'' T'' \} = \langle u_i' T' \rangle - \langle u_i'' \rangle \langle T'' \rangle + \frac{\langle \rho' u_i' T' \rangle}{\langle \rho \rangle} \quad (\text{D.17})$$

The above expressions can be rewritten, using Eq. D.10, as

$$\frac{\langle \rho u_i'' u_j'' \rangle}{\langle \rho \rangle} = \langle u_i' u_j' \rangle - \langle u_i'' \rangle \langle u_j'' \rangle + \frac{\langle \rho' u_i' u_j' \rangle}{\langle \rho \rangle} \quad (\text{D.18})$$

$$\frac{\langle \rho u_i'' T'' \rangle}{\langle \rho \rangle} = \langle u_i' T' \rangle - \langle u_i'' \rangle \langle T'' \rangle + \frac{\langle \rho' u_i' T' \rangle}{\langle \rho \rangle} \quad (\text{D.19})$$

Examining the DNS data for a compressible channel flow Huang et al. [1995] determined that $\langle \rho' u' v' \rangle$ and $\langle \rho' u' T' \rangle$ were at least one order of magnitude larger than $\langle \rho \rangle \langle u'' \rangle \langle v'' \rangle$ and $\langle \rho \rangle \langle u'' \rangle \langle T'' \rangle$, respectively. Then, contracting Eqs. D.18 and D.19 for $i = 1, j = 2$, we obtain

$$\langle \rho u'' v'' \rangle = \langle \rho \rangle \langle u' v' \rangle + \langle \rho' u' v' \rangle \quad (\text{D.20})$$

$$\approx \langle \rho u' v' \rangle \quad (\text{D.21})$$

$$\langle \rho v'' T'' \rangle = \langle \rho \rangle \langle v' T' \rangle + \langle \rho' v' T' \rangle \quad (\text{D.22})$$

$$\approx \langle \rho v' T' \rangle \quad (\text{D.23})$$

The following plots will demonstrate that the above assumptions are indeed valid.

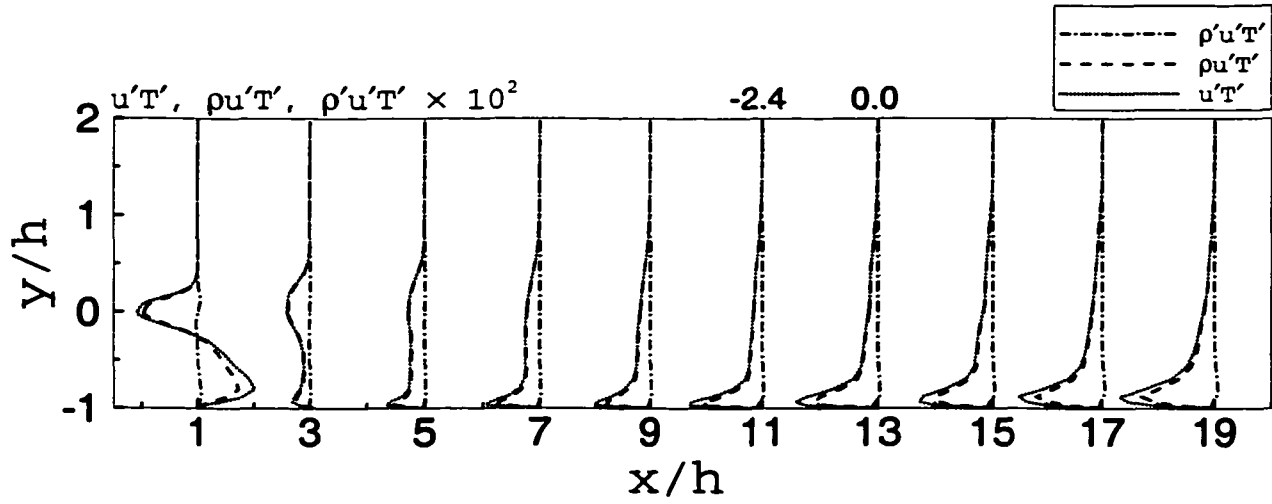


Figure D.1 Streamwise turbulent heat flux

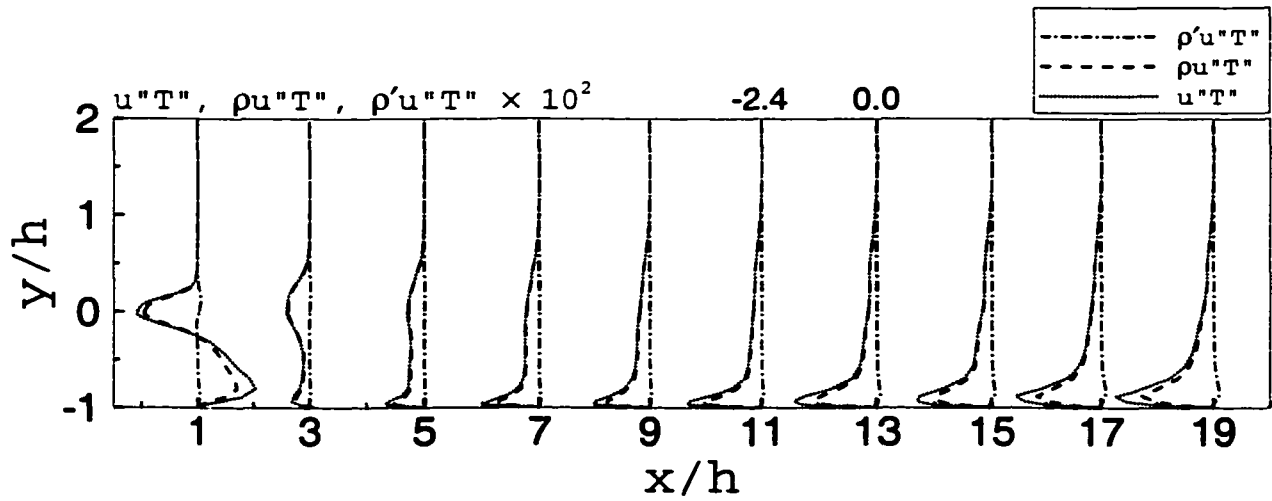


Figure D.2 Streamwise turbulent heat flux

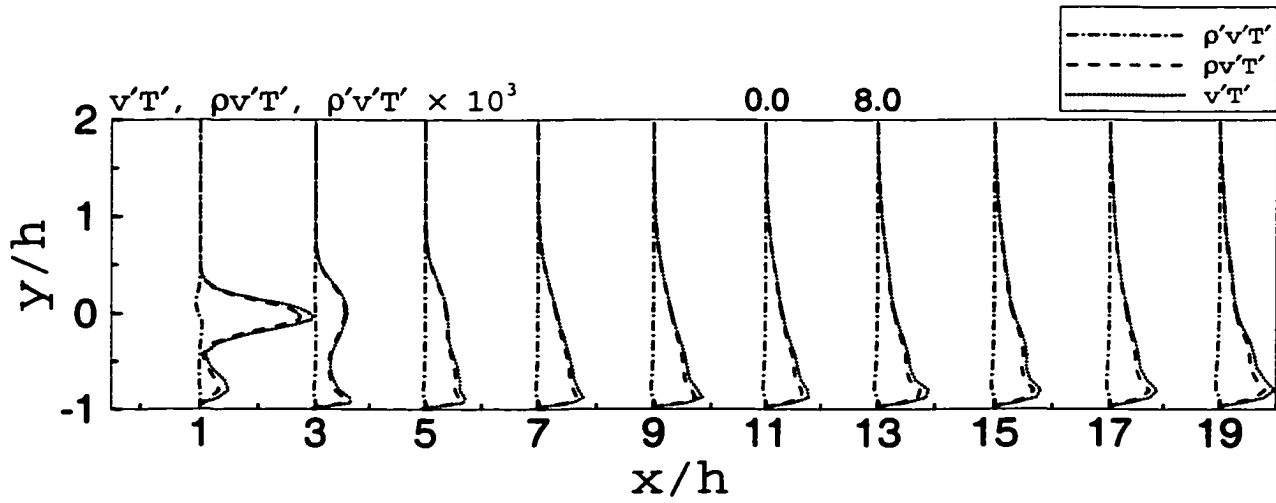


Figure D.3 Wall-normal turbulent heat flux

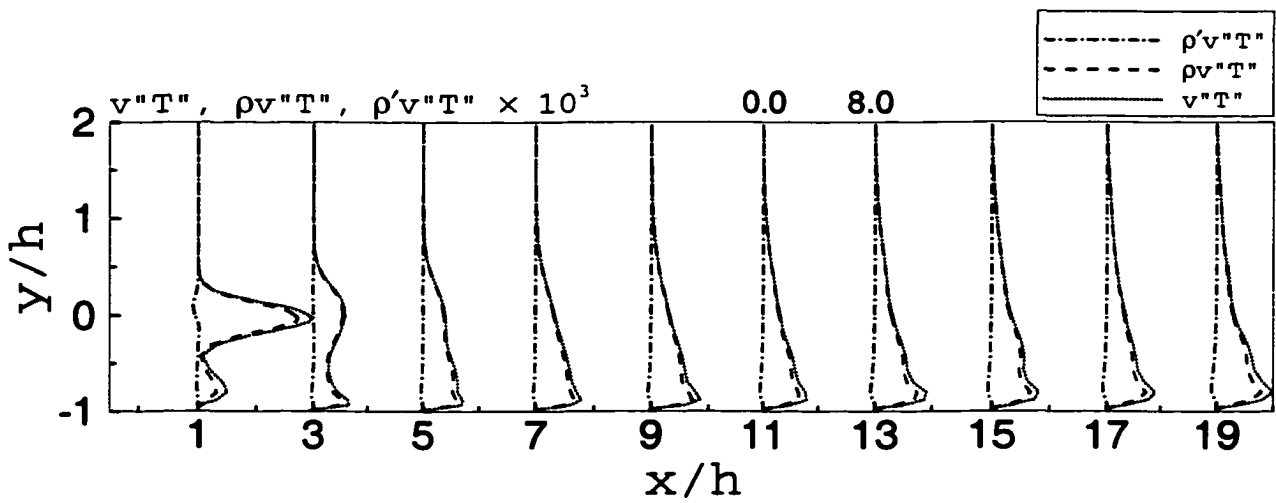


Figure D.4 Wall-normal turbulent heat flux

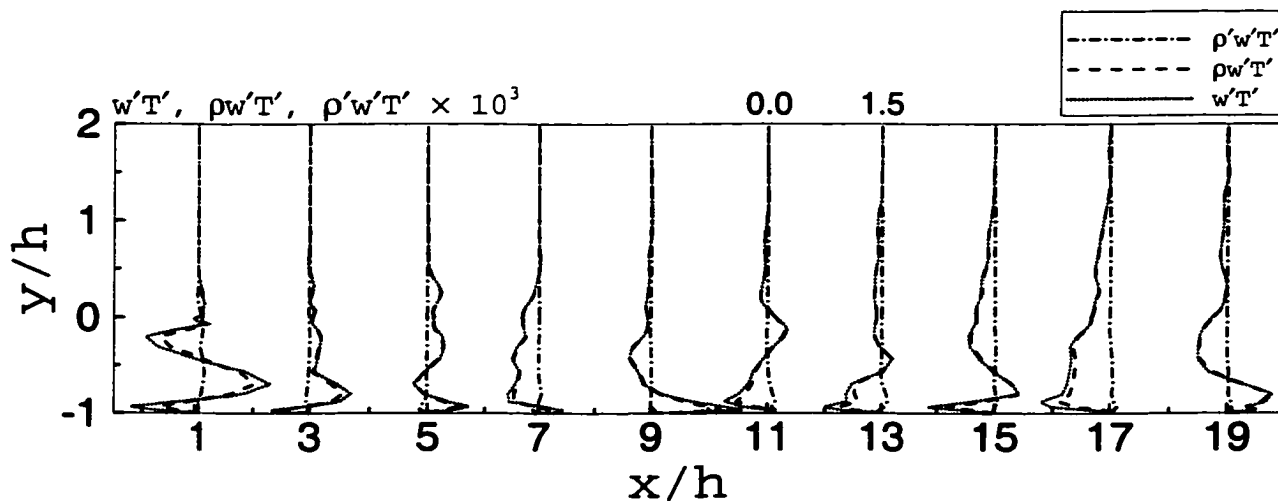


Figure D.5 Spanwise turbulent heat flux

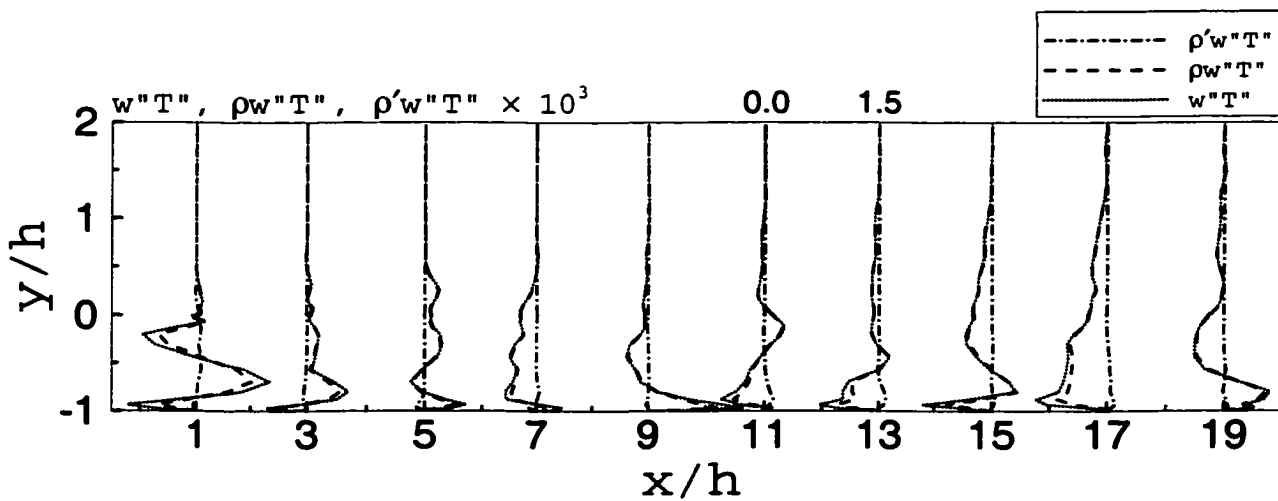


Figure D.6 Spanwise turbulent heat flux

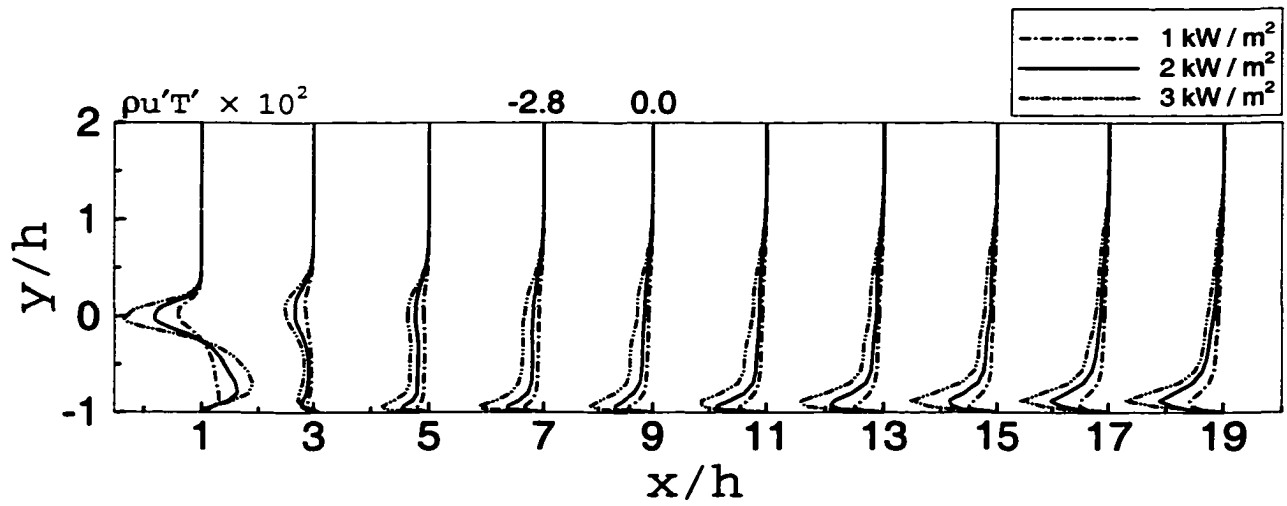


Figure D.7 Streamwise turbulent heat flux

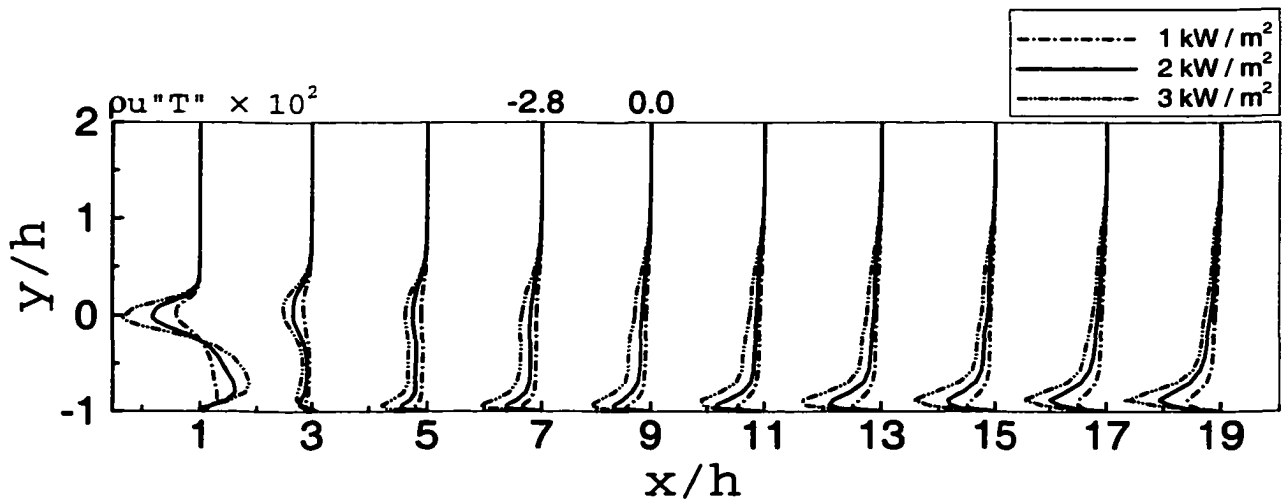


Figure D.8 Streamwise turbulent heat flux

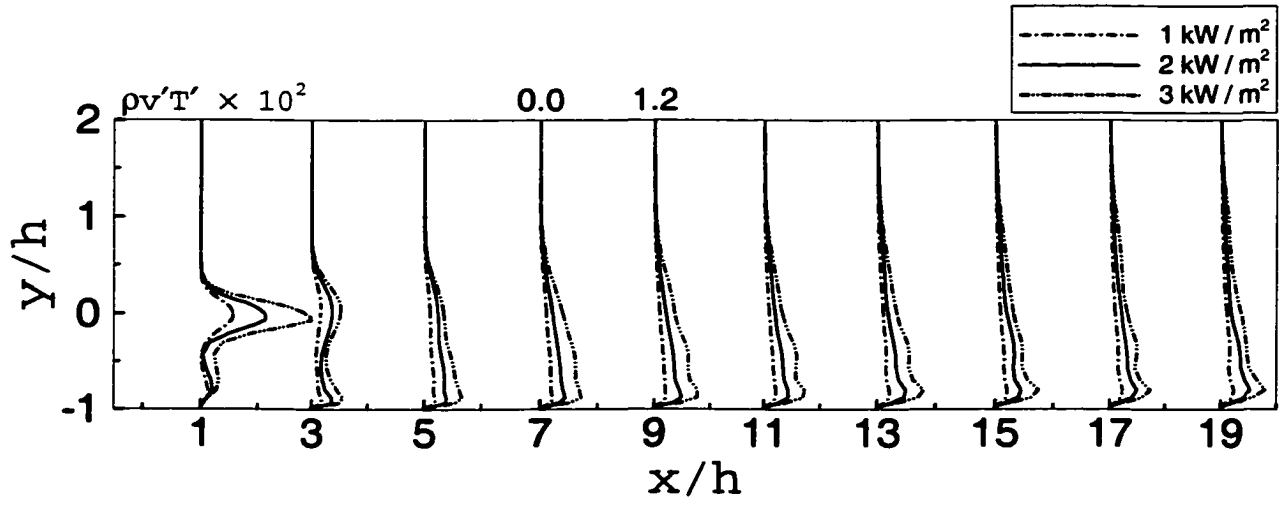


Figure D.9 Wall-normal turbulent heat flux

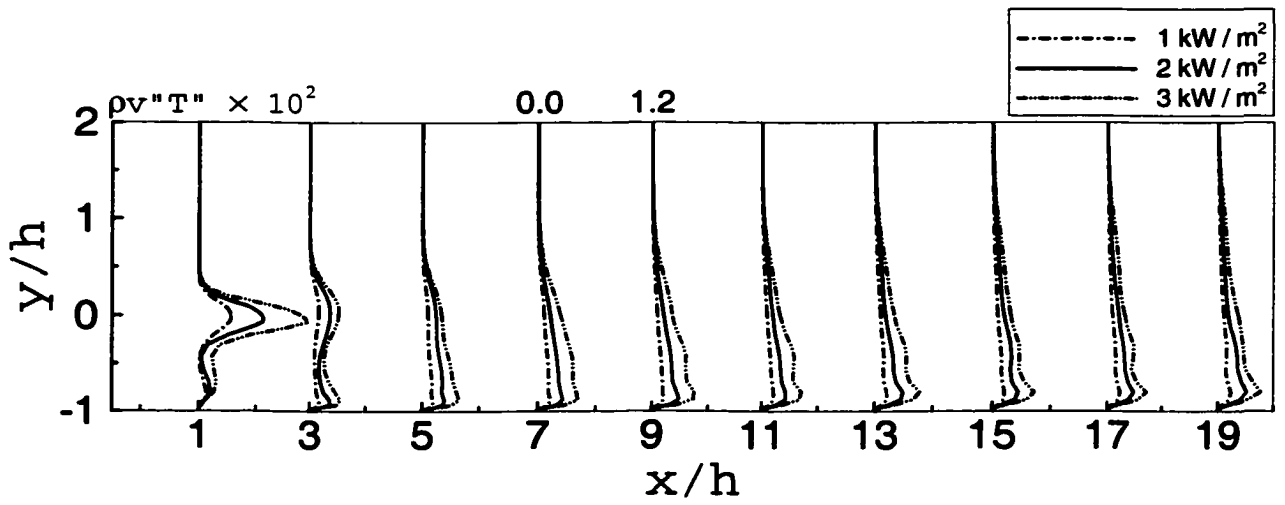


Figure D.10 Wall-normal turbulent heat flux

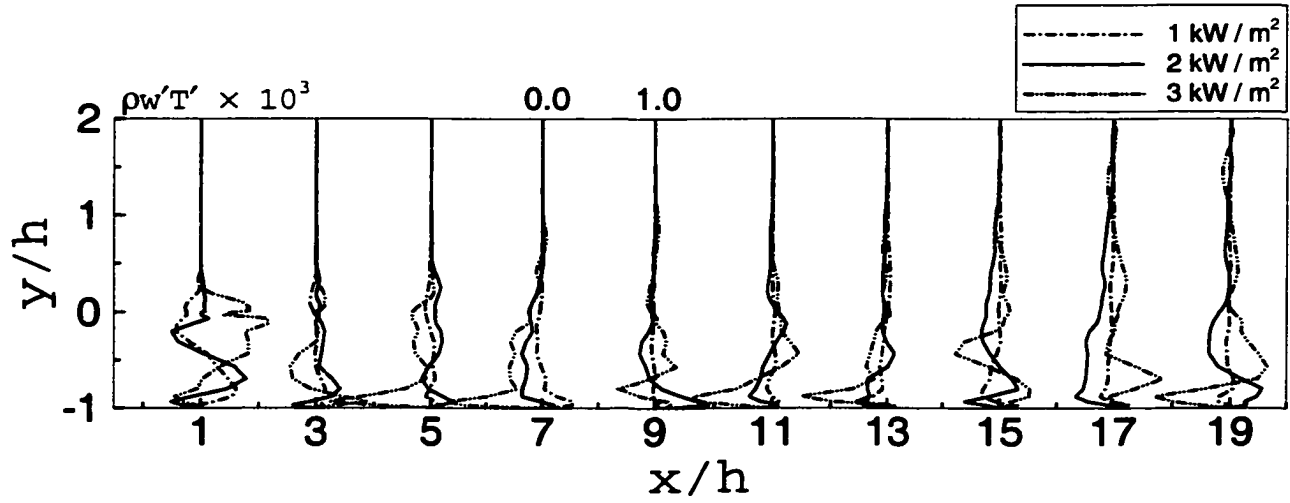


Figure D.11 Spanwise turbulent heat flux

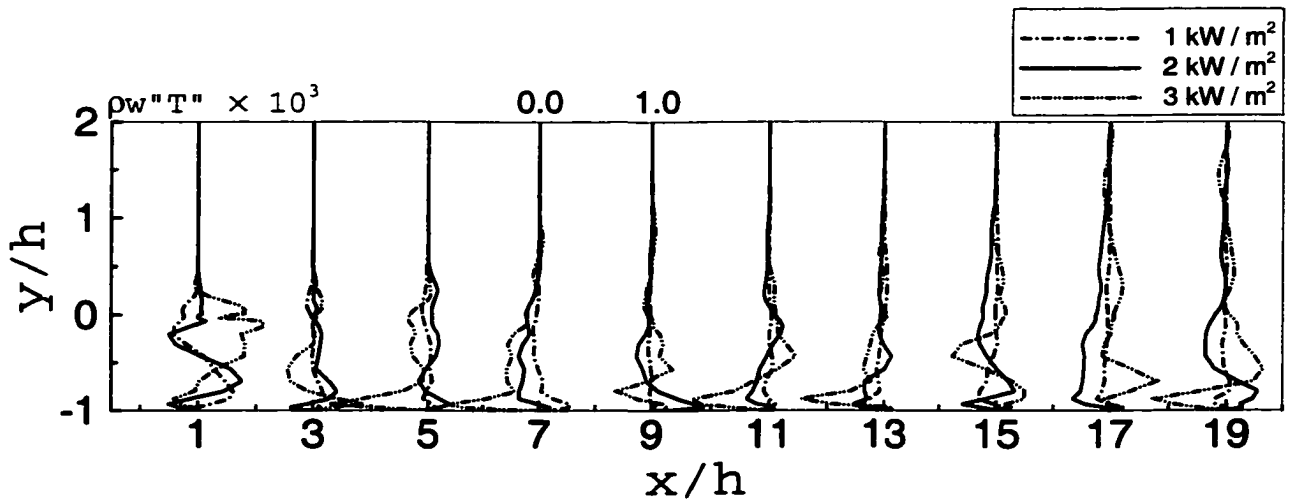


Figure D.12 Spanwise turbulent heat flux

APPENDIX E PARALLELIZATION AND OPTIMIZATION OF A LARGE EDDY SIMULATION CODE USING OpenMP FOR SGI Origin2000 PERFORMANCE

A paper published in the *Proceedings of the 11th International Conference on Parallel Computational Fluid Dynamics, Williamsburg, VA*

Punyam Satya-narayana ¹, Ravikanth Avancha², Philip Mucci³, Richard Pletcher⁴

Abstract

A multi-block, colocated-grid, finite volume code, developed by researchers at Iowa State University for the large eddy simulation (LES) of complex turbulent flows, is the focus of attention. This code, written in FORTRAN, has been well optimized for use on vector processor machines such as the CRAY C90/T90. Increasing popularity and availability of relatively cost-effective machines using the RISC based NUMA architecture such as the Origin2000 are making it necessary to migrate codes from the CRAY C90/T90. It is well known that CFD codes are among the toughest class of problems to port and optimize for RISC based NUMA architecture [1]. Strategies adopted towards the creation of a shared memory version of the code and its optimization are discussed in detail. Large eddy simulations of the turbulent flow in a channel are then performed on an Origin2000 system, and the corresponding results

¹Raytheon Systems Company, ARL MSRC, 939-I Beards Hill Rd, Suite #191, Aberdeen MD 21001

²Department of Mechanical Engineering, Iowa State University, Ames IA 50011

³Computer Science Department, University of Tennessee, Knoxville TN 37996

⁴Department of Mechanical Engineering, Iowa State University, Ames IA 50011

compared with those from simulations on a CRAY T90, to check for their accuracy. Scaling studies from the parallel version are also presented, demonstrating the importance of cache optimization on NUMA machines.

Large Eddy Simulation Code

Large eddy simulation (LES) is currently one of the popular approaches for the numerical simulation of turbulent flows. Turbulent flows are inherently time dependent and three-dimensional in nature. They also have a continuous spectrum of relevant length scales that need to be accurately captured unlike other multiple scale problems which have a finite number of relevant scales. For any flow, the large significant length scales are related to the domain size, and the small scales are related to the dissipative eddies, where the viscous effects become predominant. In LES, the motion of the large-scale structures is computed and the nonlinear interactions with the smaller scales are modeled. LES relies on the assumption that small scales of motion are nearly isotropic and independent of the geometry, and hence can be approximated by a simple universal model. Although the small scales are modeled in LES, significant computer resources are required to accurately capture the large, energy-carrying length scales.

The LES of a fully developed turbulent channel flow is performed in order to provide "realistic" turbulent inflow conditions for the simulation of the flow past a backward-facing step. It is the objective of this paper to parallelize the LES code dealing with the turbulent channel flow. Upon successful parallelization of this code, the methodology will be extended to perform the LES of the flow past a backward facing step, a more complex flow that is characteristic of practical application areas. Within the framework of a fairly simple geometry, the turbulent flow past a backward facing step consists of distinctly different flow regimes: boundary layers, a mixing layer, flow separation, reattachment, and recovery, in the presence of a strong adverse pressure gradient.

A coupled finite volume procedure is used to solve the compressible Favre filtered Navier-Stokes equations. The procedure is fully implicit, and second-order accurate in time. The advective terms can be discretized in one of three ways: second-order central differences, fourth-order central differences or QUICK-type upwind differences. The viscous terms are discretized using fourth-order central differences. Time derivative preconditioning is incorporated to alleviate the stiffness and related convergence problems that occur at low Mach numbers [2]. The aforementioned system of algebraic equations is solved using Stone's strongly implicit procedure (SIP). The details of the numerical procedure are described in [3].

Large eddy simulation is essentially an unsteady, three-dimensional computation; super-computing resources become necessary in order to carry out these computations. Efficient use of these expensive computing resources motivates parallelization and optimization studies such as that carried out in this work.

Over the past few years, the high performance computing community has had to expend significant effort to keep in phase with the evolution of high performance computers. This is especially so when market pressures, technological breakthroughs, and the dual demands of the scientific community (ever increasing problem size and the need to minimize wall-clock time) evolve the machine architecture and compiler technology all too often. In the United States, a case in point is the dwindling vendor interest in the once popular vector machines, following successful performance by the new shared/distributed memory machines with sophisticated memory hierarchies. This new direction in high performance computers, combining elements of both shared and distributed memory, is requiring scientists to devote a significant amount of time porting their codes and more fundamentally, necessitating change in their programming style. Often scientists are working with legacy codes that require major efforts to port, in order to fully utilize the performance potential of the HPC machines [4].

In this paper, we attempt to address two questions most often asked by the scientific community when faced with a legacy code in hand (in this case, the LES code), a new

HPC machine on the horizon (NUMA Origin2000), and the eventual de-commissioning of a popular workhorse machine (CRAY C90/T90):

1. How long does it take to port and optimize the code?
2. How does one utilize the tools available to parallelize the code for good performance on the new machines?

We identify three different approaches in porting the LES code to utilize the computational potential of the new machines [5]:

1. reliance on vendor-supplied (automatic) parallelizing compilers [6],
2. use of the industry standard OpenMP parallel programming interface [7;8] to produce a Single Processor Multiple Data (SPMD) style parallel code, and
3. use of an emerging tool, called CAPTools, to produce a Message Passing Interface (MPI) style message passing parallel code.

Optimization and Parallelization Strategy

The vector LES code optimized for a Cray C90/T90 is ported to the Origin2000 following the SGI guidelines by first going through Single Processor Optimization and Tuning (SPOT) and then through Multiprocessor Tuning (MUT). SPOT and MUT involved several steps. Starting with the existing tuned code, SPOT meant

1. getting the right answer (comparing with benchmark physics results at every step, Figure E.1)
2. finding out where to tune (using SGI's Speedshop, prof, and pixie tools)
3. letting the compiler do the work (using various levels of optimization, -O2, -O3, and -Ofast)

4. tuning for cache performance (using Speedshop experiments, loop fusion, do loop index ordering for FORTRAN arrays)

In the next step, MUT involved

1. parallelization of the code (using PFA, the loop level automatic parallelization compiler, and OpenMP style SPMD paradigm)
2. bottleneck identification (using `prof` and `ssrun`)
3. fixing of false sharing (with the help of the `perfex` tool)
4. tuning for data placement (enclosing initialization in a parallel region or using data distribution directives)
5. performance analysis at every step

We used a relatively small, $32 \times 32 \times 32$ grid for initial work and debugging purposes, for faster turn around time. Larger scale problems with 64 and 81 dimensions were used for scaling studies, which will be discussed in Section E. In the following sections we describe the performance of the vector code on the CRAY C90/T90 and its subsequent optimization for cache reuse on the Origin2000.

CRAY T90 LES Code

Extensive reference was made to CRAY Research publications [9;10] to develop an optimized LES code for the CRAY T90. A vectorized version of the coupled strongly implicit procedure (CSIP) solver was developed and was the key to obtaining good performance on the CRAY T90. Figures E.1 and E.2 show good agreement between the simulations and experiments/simulations from available literature.

Table E.1 contains timings, and MFLOPS for different grids with either a single processor or multitasking enabled. The numbers in the “%CPU obtained” column indicate the actual

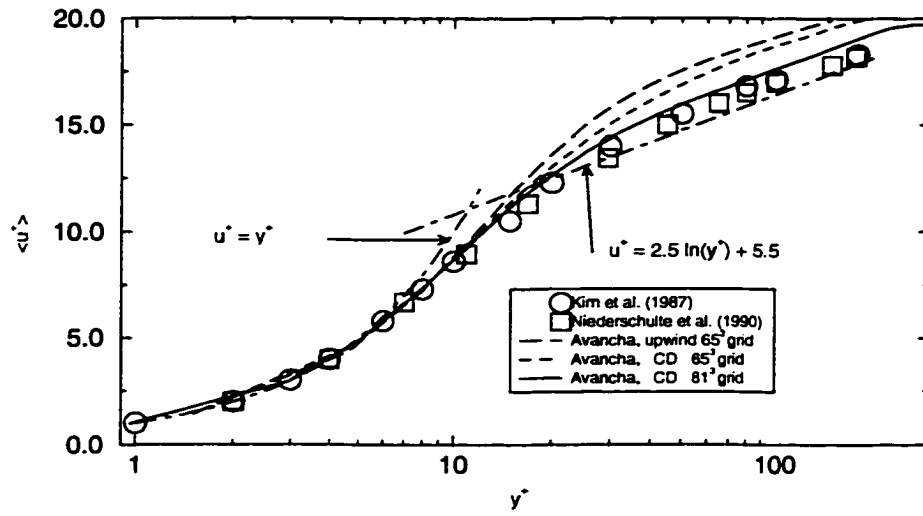


Figure E.1 Law of the wall plot

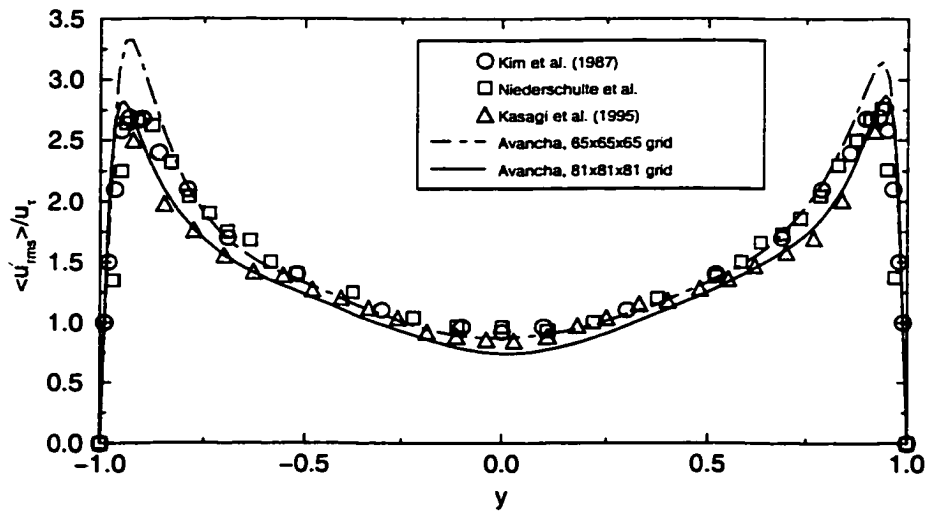


Figure E.2 Streamwise rms statistics

Table E.1 Code Performance on the CRAY T90

Flag	Grid	Processors	Wallclock secs	% CPU Obtained	User CPU secs	Vector Length	MFLOPS
A	21 × 21 × 21	1	10.824	94.5	10.195	34	273
A	45 × 45 × 45	1	86.683	69.0	60.362	66	455
B	45 × 45 × 45	4	41.505	162.0	67.053	65	410
A	81 × 81 × 81	1	583.364	51.0	297.699	97	540
B	81 × 81 × 81	4	162.730	193.5	314.085	95	511
B	81 × 81 × 81	6	342.663	94.5	322.419	95	499
B	81 × 81 × 81	8	348.514	93.0	323.630	95	497
B	81 × 81 × 81	12	108.733	295.5	320.870	95	501
B	81 × 81 × 81	14	340.704	96.0	324.625	95	495

Notes:

FORTTRAN compiler: CF90; Number of iterations: 60

Flag A: `-dp -Ovector3,scalar3,inline3 -Oaggress`

Flag B: `-dp -Ovector3,scalar3,inline3,task3,taskinner -Oaggress`

CPU allocation for the job, where 100% is equal to a single, dedicated processor. It can be seen from Table E.1 that the use of multiple processors (as in the case of 4 and 12 for the 81 × 81 × 81 case, and 4 for the 45 × 45 × 45 case) results in significantly lower wall-clock time to carry out the same number of iterations. Scaling the wall-clock time with actual CPU allocation, we find that turn around time is inversely proportional to the number of processors available. By adopting an effective parallelization strategy, the transition from the CRAY T90 to the Origin2000 is expected to be highly beneficial. Since each Origin2000 processor is less powerful than a CRAY T90 processor, it is extremely important to obtain parallel efficiency in order to achieve good overall performance. The challenges in porting and optimizing CFD codes to cache based RISC systems such as the Origin2000 are clearly outlined in [1].

Single CPU optimization

SpeedShop (SGI) tools [12] `ssrun` and `prof` were used to instrument pc sampling and ideltime experiments. Continuous monitoring of CPU time in conjunction with `prof` (`-heavy -1` options) analysis identified the bottlenecks and cache problems. We made sure that high CPU utilization was achieved during the entire modification process. The results are given in Table 2. With efficient collaboration between the authors over a seven day period [11] the most expensive routines were identified; in order to make the code “cache-friendly”, array dimensions in the entire code (containing about 45 subroutines) were rearranged, i.e. `array_name(i,j,k,nx,ny) → array_name(nx,ny,i,j,k)`; do loop indices were rearranged to attain stride one access for FORTRAN arrays; and routines were rewritten to minimize cache-misses and maximize cache-line reuse.

More specifically, within the most expensive subroutine `csip5v.f`, an in-house LU decomposition solver :

1. array dimensions were rearranged for efficient cache use
2. indirect address arrays were merged for data locality, i.e.,
`indi(ip,isurf), indj(ip,isurf), indk(ip,isurf) → ind(i,ip,isurf)`
3. do loops were unrolled and array references were kept to proximity

Single processor optimization performance is given in Table E.2 for different compiler options. Single CPU optimization shows that cache misses went down by a factor of 3 with a proportionate reduction in TLB misses. One observation is that the optimized code for a single Origin2000 processor is still slower than the optimized version on the CRAY T90, by a factor of 3. This is indicative of the respective performance capabilities of the two different processors.

Table E.2 Single CPU performance on the Origin2000

Flag	Grid	Processors	CPU sec	L2 cache misses sec	TLB misses sec	MFLOPS
A	21 × 21 × 21	1	209	23.2	27.00	8.40
B	21 × 21 × 21	1	110	22.5	22.50	24.30
C	21 × 21 × 21	1	28	9.3	0.73	57.24

Notes:

FORTRAN Compiler: f77 MIPSpro Version 7.2; Number of iterations: 60

Flag A: Vector Code, no optimization

Flag B: Vector Code, -Ofast

Flag C: Optimized Single CPU code, -Ofast

Parallelization

The parallel environment on the Origin2000 allows one to follow various paradigms to achieve parallelization, as follows:

- automatic parallelization using the MIPSpro FORTRAN compiler;
- loop-level parallelism;
- single program multiple data (SPMD) style of parallelism;
- use of low level parallel threads;
- message passing using parallel virtual machine (PVM) or MPI;
- use of the Portland Group's High Performance FORTRAN compiler (HPF); and
- use of commercial tools that parallelize the code, supposedly with minimal code modifications by the user.

In this paper we select the automatic parallelization option of the MIPSpro compiler (Power FORTRAN Analyzer: PFA), the OpenMP interface, and MPI using CAPTools (a computer aided parallelization toolkit that translates sequential FORTRAN programs into message passing SPMD codes). They are discussed in brief in the following sections. First impressions of the performance of LES code on the Origin2000 NUMA machines are reported and compared with the performance of the serial code on the T90. We find that CAPTools can significantly reduce the programmer's burden. However, the use of CAPTools can make the code unreadable and might demand that the user master its communication interface in addition to MPI. We defer CAPTools results to a future article due to limited scope of the paper and space.

Power FORTRAN Analyzer

This option is available to the users of the compiler and can be invoked using compiler flags - the code need not be modified. Although no analysis of the code is required by the user, the PFA option usually parallelizes the code at the individual loop level. The compiler automatically places directives in front of each parallelizable loop and does not parallelize the loops with data dependencies. This results in some part of the code, often a significant portion, being serial. The serial component of the code leads to poor scaling beyond 8 processors. Results for a $32 \times 32 \times 32$ grid are shown in Figure E.3.

The need for cache optimization can be inferred from Figure E.3. We note that PFA was compiled with aggressive optimization flag -03, whereas the OMP version was compiled with -02 option. Aggressive optimization flag -03, did not complete due to compiler runtime errors and hence the difference in speed between PFA and OMP versions.

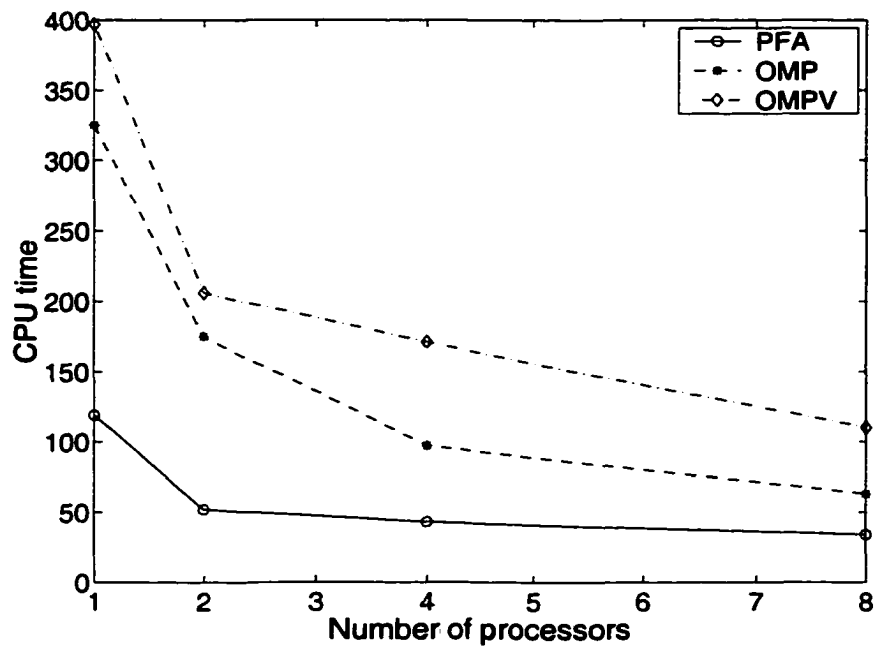


Figure E.3 Scalability chart for $32 \times 32 \times 32$ grid showing wall-clock time for PFA, OpenMP (optimized) and OpenMP (pure vector code). Comparison of OMP and OMPV shows the need for cache optimization; for 8 processors the CPU time drops by a factor of 2 if optimized code is used.

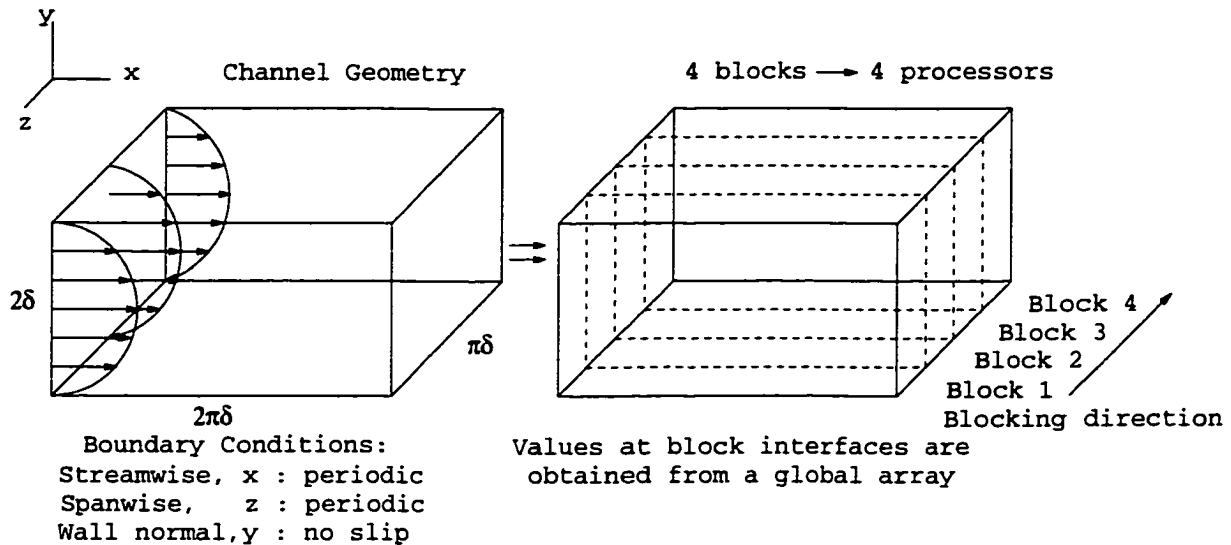


Figure E.4 Channel geometry showing partitioned blocks tasked to processors

OpenMP

The LES code is parallelized using the SPMD style of OpenMP parallel programming (as opposed to loop level parallelism) that relies heavily on domain decomposition. While domain decomposition can result in good scalability, it does transfer the responsibility of decomposition from the computer to the user. Once the problem domain is decomposed, the same sequential algorithm is followed, but the program is modified to handle multiple sub-domains. The data that are local to a sub-domain are specified as PRIVATE or THREADPRIVATE. THREADPRIVATE is used for sub-domain data that need file scope or are used in common blocks. The THREADPRIVATE blocks are shared among the subroutines but private to the thread itself. This type of programming is similar in spirit to message passing in that it relies on domain decomposition. Message passing is replaced by shared data that can be read by all the threads thus avoiding communication overhead. Synchronization of writes to shared data is required. For a Cartesian grid, the domain decomposition and geometry are shown in Figure E.4.

Data initialization is parallelized using one parallel region for better data locality among

active processors. This method overcomes some of the drawbacks of first-touch policy adopted by the compiler. If the data are not distributed properly, the first-touch policy may distribute the data to a remote node, incurring a remote memory access penalty. The main computational kernel is embedded in the time advancing loops. The time loops are treated sequentially due to obvious data dependency, and the kernel itself is embedded in a second parallel region. Within this parallel region, the computational domain is divided into blocks in the z-direction, as shown in Figure E.4, which allows each block to be tasked to a different processor.

Several grid sizes were considered; the scalability chart is shown in Figure E.5 and a typical load balance chart (using MFLOPS as an indicator) is shown in Figure E.6. We see performance degradation near 8 processors for the $32 \times 32 \times 32$ grid and 16 processors for the $81 \times 81 \times 81$ grid. Less than perfect load balancing is seen due to the remnant serial component in two subroutines. We observe linear speedup up to 4 processors across all the grid sizes and the large memory case levels off at 8 processors. The SPMD style of parallelization shows an encouraging trend in scalability. A detailed analysis with fully cache optimized and parallelized code will be presented elsewhere.

Summary

In summary, the CRAY C90/T90 vector code is optimized and parallelized for Origin2000 performance. A significant portion of our time is spent in optimizing `csip5v.f`, an in-house LU decomposition solver, which happens to be the most expensive subroutine. The FORTRAN subroutine is modified by changing the order of nested do loops so that the innermost index is the fastest changing index. Several arrays in `csip5v.f` are redefined for data locality, and computations are rearranged to optimize cache reuse.

Automatic parallelization, PFA, scales comparably to SPMD style OpenMP parallelism, but performs poorly for larger scale sizes and when more than 8 processors are used. SPMD

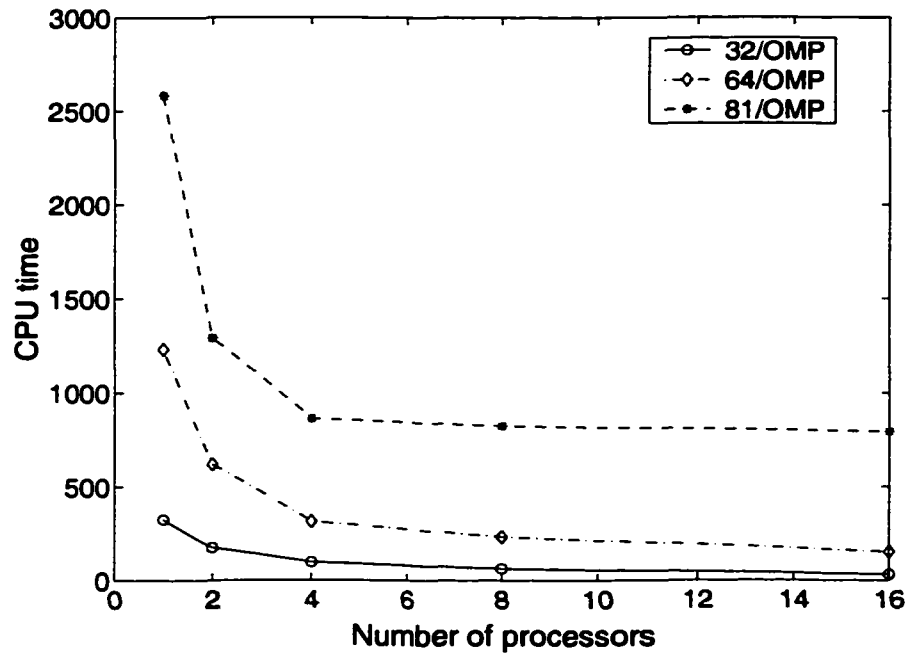


Figure E.5 Scalability chart for 32^3 , 64^3 and 81^3 grids

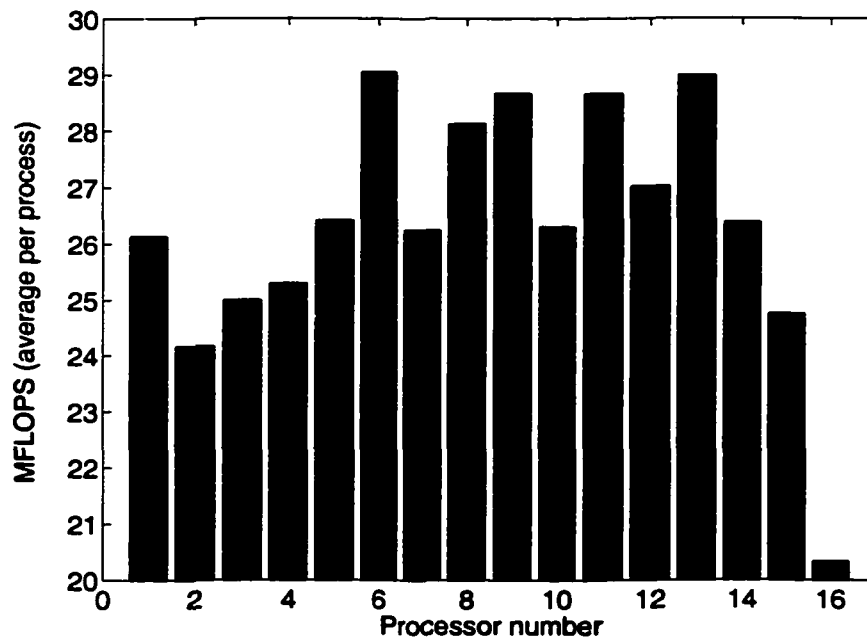


Figure E.6 SGI MFLOPS across all processors for OpenMP LES code for 81^3 grid

style OpenMP parallelization scales well for the $81 \times 81 \times 81$ grid, but shows degradation due to the serial component in still unoptimized subroutines. These subroutines contain data dependencies and will be addressed in a future publication. Finally, we report an important observation, for the $32 \times 32 \times 32$ grid presented here, that cache optimization is crucial for achieving parallel efficiency on the SGI Origin2000 machine.

Acknowledgment

The current research was partially supported by the Air Force Office of Scientific Research under Grant F49620-94-1-0168 and by the National Science Foundation under grant CTS-9414052. The use of computer resources provided by the U.S. Army Research Laboratory Major Shared Resource Center and the National Partnership for Advanced Computational Infrastructure at the San Diego Supercomputing Center is gratefully acknowledged.

References

1. Taft, J., Initial SGI Origin2000 tests show promise for CFD codes, *NAS News*, Volume 2, Number 25, July-August 1997.
2. Pletcher, R. H. and Chen, K.-H., On solving the compressible Navier-Stokes equations for unsteady flows at very low Mach numbers, AIAA Paper 93-3368, 1993.
3. Wang, W.-P., Coupled compressible and incompressible finite volume formulations of the large eddy simulation of turbulent flows with and without heat transfer, Ph.D. thesis, Iowa State University, 1995.
4. Jin, H., Haribar, M., and Yan, J., Parallelization of ARC3d with Computer-Aided Tools, *NAS Technical Reports*, Number NAS-98-005, 1998.

5. Frumkin, M., Haribar, M., Jin, H., Waheed, A., and Yan, J., A comparison of automatic parallelization tools/compiler on the SGI Origin2000, *NAS Technical Reports*.
6. *KAP/Pro Toolset for OpenMP*, <http://www.kai.com>
7. *OpenMP Specification*. <http://www.openmp.org>, 1999.
8. Menon, R., *OpenMP Tutorial*. SuperComputing, 1999.
9. *Optimizing Code on Cray PVP Systems*, Publication SG-2912, Cray Research Online Software Publications Library.
10. *Guide to Parallel Vector Applications*, Publication SG-2182, Cray Research Online Software Publications Library.
11. Satya-narayana, P., Mucci, P. and Avancha, R., Optimization and parallelization of a CRAY C90 code for ORIGIN performance: What we accomplished in 7 days. *Cray Users Group Meeting*, Denver, USA 1998.
12. *Origin 2000(TM) and Onyx2(TM) Performance Tuning and Optimization Guide*. Document Number 007-3430-002. SGI Technical Publications.

BIBLIOGRAPHY

- Abe, K., Kondoh, T., and Nagano, Y. (1994). A new turbulence model for predicting fluid flow and heat transfer in separating and reattaching flows – I. Flow field calculations. *International Journal of Heat and Mass Transfer*, 37(1):137–151.
- Abe, K., Kondoh, T., and Nagano, Y. (1995). A new turbulence model for predicting fluid flow and heat transfer in separating and reattaching flows – II. Thermal field calculations. *International Journal of Heat and Mass Transfer*, 38(8):1467–1481.
- Abrous, A. and Emery, A. F. (1996). Benchmark computational results for turbulent backward facing step flow with heat transfer. In *National Heat Transfer Conference*, volume 9 of *Heat Transfer Division - Vol. 331*, New York. ASME.
- Adams, E. W., Johnston, J. P., and Eaton, J. K. (1984). Experiments on the structure of turbulent reattaching flow. Report MD-43, Thermosciences Division, Department of Mechanical Engineering, Stanford University.
- Akselvoll, K. and Moin, P. (1995). Large eddy simulation of turbulent confined coannular jets and turbulent flow over a backward facing step. Report TF-63, Department of Mechanical Engineering, Stanford University, Stanford, CA.
- Armaly, B. F., Durst, F., and Kottke, V. (1981). Momentum, heat and mass transfer in backward facing step flows. In *Proceedings of the Third Symposium on Turbulent Shear Flows*. University of California, Davis.

- Arnal, M. and Friedrich, R. (1991). On the effects of spatial resolution and subgrid-scale modeling in large eddy simulation of a recirculating flow. In *Proceedings of the Ninth GAMM Conference on Numerical Methods in Fluid Mechanics*, Lausanne.
- Arnal, M. and Friedrich, R. (1992). Large eddy simulation of a turbulent flow with separation. In *Turbulent Shear Flows 8*, pages 169–187, Munich. Elsevier Science.
- Aung, W. and Goldstein, R. J. (1972a). Heat transfer in a turbulent separated flow downstream of a rearward facing step. *Israel Journal of Technology*, 10(1-2):35–44.
- Aung, W. and Goldstein, R. J. (1972b). Temperature distribution and heat transfer in a transitional separated shear layer. In *Proceedings of the Fourth International Heat Transfer Conference*.
- Aung, W. and Watkins, C. (1978). Heat transfer mechanisms in separated forced convection. In *Turbulent Forced Convection in Channels and Bundles: Theory and Applications to Heat Exchangers*, Turkey.
- Avanchara, R. V. R. and Pletcher, R. H. (2000). Large eddy simulation of the turbulent flow past a backward facing step. *AIAA Paper*, (2000-0542).
- Bardina, J., Ferziger, J. H., and Reynolds, W. C. (1983). Improved turbulence models based on large eddy simulation of homogeneous, incompressible, turbulent flows. Report TF-19, Mechanical Engineering Department, Stanford University, Stanford, California.
- Bechert, D. and Stahl, B. (1988). Excitation of instability waves in free shear layers. part 2. experiments. *Journal of Fluid Mechanics*, 186:63.
- Benocci, C. and Pinelli, A. (1990). The role of the forcing term in the large eddy simulation of equilibrium channel flow. In Rodi, W. and Ganic, E. N., editors, *Engineering Turbulence Modeling and Measurements*, pages 287–296, New York. Elsevier Science.

- Biringen, S. and Reynolds, W. C. (1981). Large eddy simulation of the shear-free turbulent boundary layer. *Journal of Fluid Mechanics*, 103:53–63.
- Cebeci, T. and Smith, A. M. O. (1974). *Analysis of Turbulent Boundary Layers*. Academic Press, New York.
- Chen, K.-H. and Pletcher, R. H. (1991). Primitive variable, strongly implicit calculation procedure for viscous flows at all speeds. *AIAA Journal*, 29:1241–1249.
- Chieng, G. C. and Launder, B. (1980). On the calculation of turbulent heat transport downstream from an abrupt pipe expansion. *Numerical Heat Transfer*, 3:189–207.
- Choi, Y. H. and Merkle, C. L. (1993). The application of preconditioning in viscous flows. *Journal of Computational Physics*, 105:207–223.
- Chopin (1996). Turbulent flow and heat transfer in a backward facing step using the FLO-TRAN CFD program. In *National Heat Transfer Conference*, volume 9 of *Heat Transfer Division - Vol. 331*, New York. ASME.
- Chorin, A. J. (1967). A numerical method for solving incompressible viscous flow problems. *Journal of Computational Physics*, 2:12–26.
- Chwalowski, P. and Taylor, A. C. (1991). Use of a generalized set of field variables in fluid flow calculations. *AIAA Paper*, (91-0240).
- Ciofalo, M. and Collins, M. W. (1989). $k - \epsilon$ predictions of heat transfer in turbulent recirculating flows using an improved wall treatment. *Numerical Heat Transfer, Part B*, 15:21–47.
- Collins, M. W. (1983). Heat transfer predictions for turbulent flow downstream of an abrupt pipe expansion. HTFS/Harwell Research Symposium, University of Bath.
- Currie, I. G. (1974). *Fundamental Mechanics of Fluids*. McGraw Hill, New York.

- Dailey, L. D. (1997). *Large Eddy Simulation of Turbulent Flows With Variable Property Heat Transfer Using a Compressible Finite Volume Formulation*. PhD dissertation, Iowa State University, Ames, IA.
- Durst, F. and Schmitt, F. S. (1985). Experimental study of high Reynolds number backward facing step flow. In *Proceedings of the Fifth Symposium on Turbulent Shear Flows*. Cornell University, Ithaca, NY.
- Dutt, P. (1988). Stable boundary conditions and difference schemes for Navier-Stokes equations. *SIAM Journal of Numerical Analysis*, 25(2):245–267.
- Eaton, J. K. and Johnston, J. P. (1980). Turbulent flow reattachment: An experimental study of the flow and structure behind a backward facing step. Report MD-39, Thermosciences Division, Department of Mechanical Engineering, Stanford University.
- Engquist, B. and Majda, A. (1977). Absorbing boundary conditions for the numerical simulation of waves. *Mathematics of Computation*, 31(139):629–651.
- Favre, A. (1983). Turbulence: Space-time statistical properties and behavior in supersonic flows. *Physics of Fluids*, 26:2851–2863.
- Fletcher, L. S., Briggs, D. G., and Page, R. H. (1974). Heat transfer in separated and reattached flows: An annotated review. *Israel Journal of Technology*, 12:236–261.
- Friedrich, R. and Arnal, M. (1990). Analysing turbulent backward facing step flow with the lowpass-filtered Navier-Stokes equations. *Journal of Wind Engineering and Industrial Aerodynamics*, 35:101–128.
- Germano, M. (1992). Turbulence: The filtering approach. *Journal of Fluid Mechanics*, 238:325–336.
- Germano, M., Piomelli, U., Moin, P., and Cabot, W. H. (1991). A dynamic subgrid-scale eddy viscosity model. *Physics of Fluids A*, 3:1760–1765.

- Ghosal, S., Lund, T. S., Moin, P., and Akselvoll, K. (1994). A dynamic localization model for large eddy simulation of turbulent flows. *Journal of Fluid Mechanics*, 282:1–27.
- Gooray, A., Watkins, C. B., and Aung, W. (1981). Numerical calculation of turbulent heat transfer downstream of a rearward-facing step. In *Proceedings of the Second International Conference of Numerical Methods in Laminar and Turbulent Flow*, pages 639–651, Venice, Italy. Pineridge Press, Swansea, U.K.
- Griaznov and Sengupta, S. (1996). Computations using FIRE code for flow behind a backward facing step. In *National Heat Transfer Conference*, volume 9 of *Heat Transfer Division - Vol. 331*, New York. ASME.
- Gustafsson, B. and Oliger, J. (1982). Stable boundary approximations for implicit time discretizations for gas dynamics. *SIAM Journal on Scientific and Statistical Computing*, 4:408–421.
- Gustafsson, B. and Sundström, A. (1978). Incompletely parabolic problems in fluid dynamics. *SIAM Journal of Applied Mathematics*, 35:343–357.
- Harlow, F. H. and Welch, J. E. (1965). Numerical calculation of time-dependent viscous incompressible flow of fluid with free surface. *Physics of Fluids*, 8:2182–2189.
- Ho, C. M. and Nasseir, N. (1981). Dynamics of an impinging jet – 1. The feedback phenomenon. *Journal of Fluid Mechanics*, 105:119–142.
- Holloway, J. L. (1958). Smoothing and filtering of time series and space fields. *Advances in Geophysics*, 4:351–389.
- Hong, Armaly, B. F., and Chen, T. S. (1996). Numerical simulation of turbulent flow and heat transfer over a backward facing step – A benchmark problem. In *National Heat Transfer Conference*, volume 9 of *Heat Transfer Division - Vol. 331*, New York. ASME.

- Horstman, R. H., Cochran, R. J., and Emery, A. F. (1996). Solutions of turbulent backward facing step flow with heat transfer using the finite volume method. In *National Heat Transfer Conference*, volume 9 of *Heat Transfer Division - Vol. 331*, New York. ASME.
- Huang, P. G., Coleman, G. N., and Bradshaw, P. (1995). Compressible turbulent channel flow - A close look using DNS data. *AIAA Paper*, (1995-0584).
- Incropera, F. P. and DeWitt, D. P. (1990). *Fundamentals of Heat and Mass Transfer*. Wiley, New York, 3rd edition.
- Itoh, N. and Kasagi, N. (1989). Turbulence measurement in a separated and reattaching flow over a backward facing step with the three dimensional particle tracking velocimeter. *Journal of the Flow Visualization Society of Japan*, 34:245–248.
- Jovic, S. and Driver, D. M. (1995). Backward facing step measurement at low Reynolds number $Re_h = 5000$. Technical Memorandum 108807, NASA, Ames Research Center, Moffett Field, CA 94305.
- Kasagi, N. and Matsunaga, A. (1995). Three-dimensional particle-tracking velocimetry measurement of turbulence statistics and energy budget in a backward facing step flow. *International Journal of Heat and Fluid Flow*, 16:477–485.
- Kim, J., Kline, S. J., and Johnston, J. P. (1980). Investigation of a reattaching turbulent shear layer: Flow over a backward facing step. *Journal of Fluids Engineering*, 102(3):302–308.
- Kim, J., Moin, P., and Moser, R. (1987). Turbulence statistics in fully developed channel flow at low reynolds numbers. *Journal of Fluid Mechanics*, 177:133–166.
- Kobayashi, T. and Tagashi, S. (1996). Comparison of turbulence models applied to backward facing step flow. *JSME International Journal*, 39(3):453–460.

- Kottke, V. (1984). Heat, mass and momentum transfer in separated flows. *International Journal of Chemical Engineering*, 24(1):86–94.
- Kreiss, H.-O. (1970). Initial boundary value problems for hyperbolic systems. *Communications in Pure and Applied Mathematics*, 22:277–298.
- Le, H. and Moin, P. (1994). Direct numerical simulation of turbulent flow over a backward facing step. Report TF-58, Department of Mechanical Engineering, Stanford University, Stanford, CA.
- Lele, S. K. (1992). Compact finite difference schemes with spectral-like resolution. *Journal of Computational Physics*, 103:16–42.
- Leonard, A. (1974). Energy cascade in large eddy simulations of turbulent flows. *Advances in Geophysics*, 18 A:237–248.
- Lilly, D. K. (1992). A proposed modification of the Germano subgrid-scale closure method. *Physics of Fluids A*, 4:633–635.
- Meakin, R. L. and Street, R. L. (1988). Simulation of environmental flow problems in geometrically complex domains. *Computational Methods in Applied Mechanics and Engineering*, 68:151–175.
- Meng, N., Pletcher, R. H., and Simons, T. (1999). Large eddy simulation of a turbulent channel flow with rib-roughened wall. *AIAA Paper*, (1999-0423).
- Métais, O. and Lesieur, M. (1992). Spectral large eddy simulation of isotropic and stably stratified turbulence. *Journal of Fluid Mechanics*, 239:157–194.
- Mittal, R. (1996). Progress on the large eddy simulation of flow past a circular cylinder. In *Annual Research Briefs*, pages 233–241. Center for Turbulence Research, Stanford University.

- Mittal, R. and Moin, P. (1997). Suitability of upwind-biased finite difference schemes for large-eddy simulation of turbulent flows. *AIAA Journal*, 35(8):1415–1417.
- Moin, P. and Kim, J. (1982). Numerical investigation of turbulent channel flow. *Journal of Fluid Mechanics*, 118:341–377.
- Moin, P., Squires, K., Cabot, W., and Lee, S. (1991). A dynamic subgrid-scale model for compressible turbulence and scalar transport. *Physics of Fluids A*, 3:2746–2757.
- Moretti, G. (1981). A physical approach to the numerical treatment of boundaries in gas dynamic. In *Proceedings of Numerical Boundary Condition Procedures Symposium*, volume CP-2201 of *NASA Ames Symposium*, pages 73–97.
- Mori, Y., Uchida, Y., and Sakai, K. (1986). A study of the time and spatial structure of heat transfer performances near the reattaching point of separated flows. In *Proceedings of the Eighth International Heat Transfer Conference*, pages 1083–1088.
- Morinishi, Y. and Kobayashi, T. (1990). Large eddy simulation of backward facing step flow. In Rodi, W. and Martelli, M., editors, *Engineering Turbulence Modeling and Experiments*, page 245, New York. Elsevier Science.
- Morton, K. W. and Paisley, M. F. (1989). A finite volume scheme with shock fitting for the steady Euler equations. *Journal of Computational Physics*, 80:168–203.
- Nagano, Y., Tagawa, M., and Niimi, M. (1989). An improvement of the $k-\epsilon$ turbulence model (the limiting behavior of wall and free turbulence and the effect of adverse pressure gradient). *JSME Journal Series B*, (55):1008–1015.
- Narayanan, C. (1998). Colocated-grid finite volume formulation for the large eddy simulation of incompressible and compressible turbulent flows. Master's thesis, Iowa State University, Ames, IA.

- Neto, A. S., Grand, D., Métais, O., and Lesieur, M. (1993). A numerical investigation of coherent vortices in turbulence behind a backward facing step. *Journal of Fluid Mechanics*, 256:1–25.
- Niederschulte, M. A., Adrian, R. J., and Hanratty, T. J. (1990). Measurements of turbulent flow in a channel at low reynolds numbers. *Experiments in Fluids*, 9:222–230.
- Oliger, J. and Sundström, A. (1978). Theoretical and practical aspects of some initial boundary value problems in fluid dynamics. *SIAM Journal of Applied Mathematics*, 35:419–446.
- Osied, K., Kim, S. E., and Choudhury, D. (1996). Turbulent heat transfer in a backstep geometry - Benchmark calculations using FLUENT. In *National Heat Transfer Conference*, volume 9 of *Heat Transfer Division - Vol. 331*, New York. ASME.
- Patankar, S. V. (1981). A calculation procedure for two-dimensional elliptic situations. *Numerical Heat Transfer*, 4:409–425.
- Patankar, S. V. and Spalding, D. B. (1972). A calculation procedure for heat, mass and momentum transfer in three-dimensional parabolic flows. *International Journal of Heat and Mass Transfer*, 15:1787–1806.
- Piomelli, U. (1988). *Models for Large Eddy Simulations of Turbulent Channel Flows Including Transpiration*. PhD dissertation, Stanford University, Stanford, California.
- Pletcher, R. H. and Chen, K.-H. (1993). On solving the compressible Navier-Stokes equations for unsteady flows at very low Mach numbers. *AIAA Paper*, (93-3368).
- Poinsot, T. J. and Candel, S. (1987). Vortex-driven acoustically coupled combustion instabilities. *Journal of Fluid Mechanics*, pages 265–292.
- Poinsot, T. J. and Lele, S. K. (1992). Boundary conditions for direct simulations of compressible viscous flows. *Journal of Computational Physics*, 101:104–129.

- Poinsot, T. J., Trounev, A. C., Veynante, D. P., Candel, S. M., and Esposito, E. J. (1987). Vortex-driven acoustically coupled combustion instabilities. *Journal of Fluid Mechanics*, 177:265–292.
- Reynolds, W. C. (1990). The potential and limitations of direct and large eddy simulations. In Lumley, J. L., editor, *Whither Turbulence? Turbulence at the Crossroads*, volume 357 of *Lecture Notes in Physics*, pages 313–342. Springer-Verlag, Berlin.
- Rhie, C. M. and Chow, W. L. (1983). Numerical study of the turbulent flow past an airfoil with trailing edge separation. *AIAA Journal*, 21(11):1525–1532.
- Rodi, W. (1976). A new algebraic relation for calculating the Reynolds stress. *ZAMM*, 56:219.
- Rogallo, R. S. and Moin, P. (1984). Numerical simulation of turbulent flows. *Annual Review of Fluid Mechanics*, 16:99–137.
- Rosenfeld, M., Kwak, D., and Vinokur, M. (1991). A fractional step solution method for the unsteady incompressible Navier-Stokes equations in generalized coordinate systems. *Journal of Computational Physics*, 94:102–137.
- Salvetti, M. V. and Banerjee, S. (1995). A priori tests of a new dynamic subgrid-scale model for finite-difference large-eddy simulations. *Physics of Fluids*, 7(11):2831.
- Schlichting, H. (1979). *Boundary Layer Theory*. McGraw-Hill, New York, 2nd edition.
- Schumann, U. (1977). Realizability of Reynolds-stress turbulence models. *Physics of Fluids*, 20(5):721–725.
- Seban, R. A. (1964). Heat transfer to the turbulent separated flows of air downstream of a step in the surface of a plate. *Transactions of ASME, Series C (Journal of Heat Transfer)*, 86:259–264.

- Seban, R. A. (1966). The effect of suction and injection on the heat transfer and flow in a turbulent separated airflow. *Journal of Heat Transfer*, 88:276–284.
- Seban, R. A., Amery, A., and Levy, A. (1959). Heat transfer to separated and reattached subsonic turbulent flows obtained downstream of a surface step. *Journal of Aerospace Sciences*, 26(12):809–814.
- Shuen, J. S., Chen, K. H., and Choi, Y. (1992). A time-accurate algorithm for chemical non-equilibrium viscous flows at all speeds. *AIAA Paper*, (92-3639).
- Shyy, W. and Vu, T. C. (1991). On the adoption of velocity variable and grid system for fluid flow computation in curvilinear coordinates. *Journal of Computational Physics*, 92:82–105.
- Smagorinsky, J. (1963). General circulation experiments with the primitive equations. Part I. The basic experiment. *Monthly Weather Review*, 91:99–164.
- Spalart, P. R. (1988). Direct numerical simulation of a turbulent boundary layer up to $Re_\theta = 1410$. *Journal of Fluid Mechanics*, 187:61–98.
- Speziale, C. G. (1985). Galilean invariance of subgrid-scale stress models in the large-eddy simulation of turbulence. *Journal of Fluid Mechanics*, 156:55–62.
- Stone, H. L. (1968). Iterative solution of implicit approximations of multidimensional partial differential equations. *SIAM Journal of Numerical Analysis*, 5:531–558.
- Strikwerda, J. C. (1977). Initial boundary value problems for incompletely parabolic systems. *Communications in Pure and Applied Mathematics*, 30:797–822.
- Tang, T. and Rockwell, D. (1983). Instantaneous pressure fields at a corner associated with vortex impingement. *Journal of Fluid Mechanics*, 126:187.
- Thangam, S. and Speziale, C. G. (1992). Turbulent flow past a backward facing step: A critical evaluation of two-equation models. *AIAA Journal*, 30:1314–1320.

- Thompson, K. W. (1987). Time dependent boundary conditions for hyperbolic systems. *Journal of Computational Physics*, 68:1–24.
- Tropea, C. (1982). *Die Turbulente Strömung in Flachkanälen und Offenen Gerinnen*. PhD dissertation, University of Karlsruhe.
- Vichnevetsky, R. and Bowles, J. B. (1982). Fourier analysis of numerical approximation of hyperbolic equations. *SIAM*.
- Vogel, J. C. and Eaton, J. K. (1984). Heat transfer and fluid mechanics measurements in the turbulent reattaching flow behind a backward facing step. Report MD-44, Thermosciences Division, Department of Mechanical Engineering, Stanford University.
- Vogel, J. C. and Eaton, J. K. (1985). Combined heat transfer and fluid dynamic measurements downstream of a backward facing step. *Journal of Heat Transfer*, 107:922–929.
- Wang, W.-P. (1995). *Coupled Compressible and Incompressible Finite Volume Formulation for the Large Eddy Simulation of Turbulent Flow With and Without Heat Transfer*. PhD dissertation, Iowa State University, Ames, IA.
- Weinstein, H. G., Stone, H. L., and Kwan, T. V. (1969). Iterative procedure for solution of systems of parabolic and elliptic equations in three dimensions. *I & E C Fundamentals*, 8:281–287.
- Yakhot, V. and Orszag, S. A. (1986). Renormalization group analysis of turbulence. I. Basic theory. *Journal of Scientific Computing*, 1(1):3–51.
- Yim, I. K. and Armaly, B. F. (1996). Turbulent heat transfer over a backward facing step: Solution to a benchmark problem. In *National Heat Transfer Conference*, volume 9 of *Heat Transfer Division - Vol. 331*, New York. ASME.

- Yoshizawa, A. (1982). Statistical evaluation of the triple velocity correlation and the pressure-velocity correlation in shear turbulence. *Journal of the Physical Society of Japan*, 51(7):2326.
- Yoshizawa, A. (1986). Statistical theory for compressible turbulent shear flows, with the application to subgrid modeling. *Physics of Fluids A*, 5:3186–3196.
- Yoshizawa, A. (1989). Subgrid scale modeling with a variable length scale. *Physics of Fluids A*, 1(7):1293–1295.
- Zang, Y., Street, R. L., and Koseff, J. R. (1991). A composite-multigrid method for solving unsteady incompressible navier-stokes equations in complex geometries. In Taylor, C. et al., editors, *Proceedings of the Seventh International Conference on Numerical Methods in Laminar and Turbulent Flow*, number 87-1107, page 1485, Stanford, CA.
- Zang, Y., Street, R. L., and Koseff, J. R. (1993). A dynamic mixed subgrid-scale model and its application to turbulent recirculation flows. *Physics of Fluids A*, 5:3186–3196.
- Zang, Y., Street, R. L., and Koseff, J. R. (1994). A non-staggered grid, fractional step method for time-dependent incompressible Navier-Stokes equations in curvilinear coordinates. *Journal of Computational Physics*, 114:18–33.

ACKNOWLEDGEMENTS

I would like to take this opportunity to express my thanks to those who helped me with various aspects of conducting research and those with who I shared the experiences of graduate school.

Foremost, I would like to thank Dr. Pletcher for his valuable guidance, insight and continued financial support during the entire course of my graduate studies. It would be hard to forget questions like "So, where have we pushed the envelope in this study? ", "How have we helped advance the frontiers of knowledge ?" - these have helped shape my perspectives on scientific research.

The current research was partially supported by the Air Force Office of Scientific Research under Grant F49620-94-1-0168 and by the National Science Foundation under grants CTS-9414052 and CTS-9806989. The use of computer resources provided by the National Partnership for Advanced Computational Infrastructure at the San Diego Supercomputing Center and University of Minnesota Supercomputing Institute are gratefully acknowledged.

I would like to thank Dr. Gerald Colver, Dr. Ganesh Rajagopalan, Dr. John Tannehill, and Dr. Gene Takle for having consented to be on my doctoral committee.

I have benefited greatly from interactions with my friend Chidu, with who I often discussed various aspects of this research, thanks to talk. I am indebted to Anil for his help with several plots and all of the animations; his expertise in MATLAB proved very invaluable. I would also like to thank my fellow graduate students for an atmosphere of camaraderie and fellowship downstairs at the CFD laboratory: Lyle, Prantik, Rob, Todd, John (Iselin), Ning, Joon, Xiaofeng, Steve, Charles, Liuyang, Anup, John (Mammoser), and Nan.

I have interacted with so many people at Iowa State, both at a personal and professional level, and would like to thank them for having made my stay in Ames a memorable one. One of those personal contacts, was my wife: Manjula. I have much to thank for her patience, love, and support.

Finally, I would like to thank my parents and my brother for their encouragement, love and support.